Aerodynamics

DLR Deutsches Zentrum für Luft- und Raumfahrt e.V. in der Helmholtz-Gemeinschaft

Master of Science Thesis

Flutter Behaviour of a Laminar Supercritical Airfoil

A Numerical Investigation into the Influence of Boundary Layer Transition

A.C.L.M. van Rooij

February 9, 2012

Faculty of Aerospace Engineering · Delft University of Technology

TU Delft

Flutter Behaviour of a Laminar Supercritical Airfoil

A Numerical Investigation into the Influence of Boundary Layer Transition

Master of Science Thesis

For obtaining the degree of Master of Science in Aerospace Engineering at Delft University of Technology

A.C.L.M. van Rooij

February 9, 2012

Faculty of Aerospace Engineering · Delft University of Technology

Delft University of Technology

Delft University Of Technology
Department Of
Aerodynamics and Wind Energy

The undersigned hereby certify that they have read and recommend to the Faculty of Aerospace Engineering for acceptance a thesis entitled **"Flutter Behaviour of a Laminar Supercritical Airfoil"** by **A.C.L.M. van Rooij** in partial fulfillment of the requirements for the degree of **Master of Science**.

Dated: February 9, 2012

Graduation Committee:

Prof. dr. ir. drs. H. Bijl

Dr. ir. B.W. van Oudheusden

Dr. S.J. Hulshoff

Dr. R.P. Dwight

Summary

Today a lot of attention is paid to the development of environmental friendly technologies. In the aircraft industry, emissions need to be reduced as well. Fuel can be saved by ensuring that the flow over the wings of the aircraft is completely or partly laminar. A laminar boundary layer creates less skin friction drag than a turbulent boundary layer. It is however more prone to separation. Nevertheless, at the cruise speeds of transport aircraft a laminar boundary layer can be beneficial (because of the small angle of attack). At these speeds a shock wave can however be present on the airfoil at off-design conditions. This shock wave can cause a local separation of the boundary layer, if the pressure gradient is however not too strong, the flow will reattach after the shock and hence the drag of the aircraft will be reduced. During flight disturbances in the flow can set the aircraft into motion. This motion can be damped or amplified. The boundary between these types of motion is called the flutter boundary. This boundary is an important constraint of the flight envelope of aircraft. The influence of boundary layer transition on the flutter behaviour of transonic aircraft has not been investigated yet, therefore a first step has been taken in this thesis. The objective of this thesis is to: Investigate the influence of laminar to turbulent boundary layer transition on the flutter boundary and damping characteristics of a supercritical laminar airfoil (the CAST-10 airfoil) in transonic flow using numerical simulations. In order to do so numerical simulations are performed with the CAST-10 airfoil with two RANS codes: the DLR TAU code and the ANSYS CFX code. The DLR TAU code uses the e^N-method for transition prediction, whereas CFX uses the $\gamma - Re_\theta$ transition model. Steady and unsteady flow simulations have been performed with both codes. The steady flow simulations are used to initialise the unsteady flow simulations. In these unsteady flow simulations, the airfoil is forced to perform a sinusoidal pitching or plunging motion. The response of the airfoil to these applied motions serves as input to a flutter program, which uses the k-method to compute the flutter boundary. Simulations with both free and fixed transition are carried out. In case of fixed transition, transition was fixed at the leading edge of the airfoil.

During wind tunnel tests with the CAST-10 airfoil it was found that the airfoil deformed itself. This deformation is different for each Mach number and angle of attack. CFD simulations that take into account this deformation show excellent agreement with the

experimental results. At subsonic Mach number the deformation is less severe and therefore simulation results obtained with the undeformed airfoil agree reasonably well with the experimental results.

When the freestream flow is subsonic, the pressure distributions obtained from steady flow simulations with the original CAST-10 airfoil with fixed as well as with free transition, show only minor differences. When the freestream flow becomes transonic, the shock wave seems to fix the location of boundary layer transition. Differences between the CFD codes are most pronounced in the free transition and transonic fully turbulent cases. The lift-versus-angle of attack graphs shows highly non-linear behaviour in case of free boundary layer transition for both CFD codes. Quasi-steady flow simulations used to determine the lift-curve slope show that the lift-curves slope increases when the Mach number is increased. At some point a maximum occurs however. This maximum is located at a $M = 0.74125$ in case of free boundary layer transition and at $M = 0.755$ when boundary layer transition is fixed at the leading edge of the airfoil. In case of free boundary layer transition, the lift-curve slope reaches a value that is twice as high as in case of a fully turbulent boundary.

The unsteady flow simulations performed with TAU show that, in case of free transition, the transition location does not vary harmonically for all Mach numbers, since the amplitude of the forced motion is so small that the mesh is not able to capture all variations in transition onset location. The major differences between free and fixed transition occur in the response of the moment coefficient. Higher harmonical components are present in the airfoil's response when transition is free. The magnitude of moment coefficient shows clearly different behaviour as a function of the reduced frequency when the fixed and free transition cases are compared. Furthermore, the phase lag of the moment coefficient is much larger for both pitch and plunging mode. Unsteady pitching simulations performed with CFX (fully turbulent boundary layer) show similar behaviour for the lift coefficient as those with TAU, only the mean lift coefficient is different. The hysteresis loops of the moment coefficient show differences in magnitude and phase angle. The lift and moment coefficient responses obtained from both codes are however clearly different in case of free boundary layer transition. A possible explanation for the differences in the fully turbulent case, is the bad convergence of the CFX results. In case of free boundary layer transition, the differences in the transition locations predicted by the CFD codes are thought to be responsible for the differences in the hysteresis loops. The damping curves obtained from unsteady flow simulations with TAU, clearly show that flutter occurs at much lower flutter indices (non-dimensional parameter that includes the effects of velocity, altitude and structural density on flutter) in case of free boundary layer transition.

From this thesis it can be concluded that there is a clear difference in the flutter behaviour of an airfoil with a partly laminar boundary layer and with a fully turbulent boundary layer. The transonic dip in the flutter boundary is located at a $M = 0.741875$ in case of free transition, whereas when the boundary layer is fully turbulent it is located at $M = 0.755$. Furthermore, the flutter index at which flutter occurs is much lower at the transonic dip (0.08 versus 0.13 for a fully turbulent boundary layer). Hence, boundary layer transition has a large influence on the flutter boundary. These statements should however be treated with caution, as future investigations need to prove if this behaviour of the flutter boundary is correctly predicted. The range of flutter indices achieved is realistic as can be observed from comparison with flutter boundaries obtained from wind

tunnel experiments (with another supercritical airfoil). The quasi-steady lift-curve slope versus Mach number graph can give a first estimation of the location and the width of the transonic dip. The depth of the dip can however not be obtained from quasi-steady flow simulations. The larger phase lag of the pitching airfoil's lift coefficient response might be an explanation for the lower transonic dip in case of free boundary layer transition.

This thesis served as the first step in the investigation of the influence of free boundary layer transition on the flutter boundary of an aircraft. In future investigations more attention needs to be paid to the difference between the results obtained with the different CFD codes, as well as to the non-linear lift-curve slope behaviour. Also, further investigations are necessary with other (more realistic) airfoils and wings or even half-aircraft models. Furthermore, it is also important to perform wind tunnel experiments in order to verify the results obtained from numerical calculations.

Acknowledgements

This Master thesis forms the last part of my Master Aerospace Engineering at the Faculty of Aerospace Engineering of Delft University of Technology. It has been performed at the Institute of Aeroelasticity of the German Aerospace Center (DLR) in Göttingen. I would like thank Dr. rer. nat. R. Voss for the opportunity to carry out my thesis at DLR and for his advice. Furthermore, I'm also grateful to my daily supervisor at the German Aerospace Center, Dr. ir. W. Wegner and to my academic supervisor Dr. ir. B.W. van Oudheusden, for their guidance and advice and to drs. G. Voss for his help with the TAU code. It has been a very interesting period and I have learned a lot. Furthermore, I would like to thank all other members of the Institute of Aeroelasticity for creating a nice working environment as well. Last, but definitely not least, I would like to thank my parents, sisters, other family and friends, who have supported and encouraged me during my whole studies.

Göttingen, Germany
February 9, 2012

A.C.L.M. van Rooij

Contents

List of Figures

List of Tables

Nomenclature

Latin Symbols

A	Area	m^2
a	Amplitude of a disturbance	various
A_0	Aerodynamic forces matrix	various
a	Amplitude of a disturbance at x_i	various
$B(k)$	Matrix of eigenvalue system	various
c	Airfoil chord length	m
C_L	Lift coefficient (3D)	-
C_{stiff}	Mesh stiffness exponent	-
c_d	Drag coefficient	-
c_f	Skin friction coefficient	-
c_l	Lift coefficient (2D)	-
c_{m_y}	Moment coefficient	-
c_p	Pressure coefficient	-
c_p	Specific heat at constant pressure	J/K
c_r	Wave speed	m/s
D	Damping matrix	various
d	Distance between control volume node and boundary	m
d	Distance from the nearest boundary	m
d	Distance from the wall	m
d	Logarithmic decrement	-
D_k	Destruction term of the k-equation	$kg/m/s^3$

D_ω	Destruction term of the ω-equation	$kg/m^3/s^2$
$\tilde{D}_k$	Modified destruction term of the k-equation	$kg/m/s^3$
E	Total energy	J
e	Internal energy	J
E_γ	Destruction or relaminarisation term	$kg/m^3/s$
Fi	Flutter index	-
F_{length}	Transition length function	-
F_1	Blending function	-
f	Frequency	Hz
f_w	Wall-blockage function	-
g	Spot production rate per unit area	s^{-1}/m^2
H	Shape factor	-
H	Total enthalpy	J
h	Enthalpy	J
h	Vertical displacement	m
h_0	Amplitude of plunging motion	m
i	Imaginary unit	-
I_α	Mass moment of inertia	kgm^2
K	Stiffness matrix	various
k	Reduced frequency	-
k	Thermal conductivity	W/m/K
k	Turbulent Kinetic Energy	m^2/s^2
K_h	Vertical spring stiffness	N/m
K_α	Torsional spring stiffness	Nm/rad
L	Characteristic length	m
L	Lift	N
l	Characteristic length scale of the mean flow	m
L_0	Quasi-steady lift	N
M	Mach number	-
M	Mass matrix	various
m	Magnitude	-
m	Mass	kg
M_{EA}	Moment about the elastic axis	Nm
N	Amplification factor	-
N_T	Number of timesteps per period	-
p	Pressure	N/m^2
P_k	Production term of the TKE equation	$kg/m/s^2$
Pr	Prandtl number	-

P_{γ_1}	Transition source term	$kg/m^3/s$
P_{θ_t}	Production source term	$kg/m^3/s$
P_ω	Production term of the ω-equation	kg/m
$\tilde{P_k}$	Modified production term of the k-equation	$kg/m/s^3$
q	Dynamic pressure	$kg/m/s^2$
q	Heat flux	$J/m^2/s$
R	Dependence volume	m^3
r_α	Radius of gyration about EA	-
Re	Reynolds number	-
Re_v	Strain-rate Reynolds number	-
Re_x	Reynolds number based on x-location	-
Re_{x_i}	Reynolds number at which the spatially growing waves become unstable	-
Re_θ	Momentum thickness Reynolds number	-
$\overline{Re}_{\theta_t}$	Transition onset momentum-thickness Reynolds number	-
S	Absolute value of the strain rate	s^{-1}
S	Surface area	m^2
s	Streamwise coordinate	m
S_α	Static moment due to gravity	Nm
$\hat{S}$	Modified magnitude of vorticity	s^{-1}
T	Period	s
T	Temperature	K
t	Airfoil thickness	m
t	Time	s
Tu	Turbulence intensity	-
U	Mean flow velocity in x-direction	m/s
u	Velocity in x-direction	m/s
U_0	Characteristic velocity of the mean flow	m/s
u_τ	Friction velocity	m/s
u^+	Non-dimensional velocity	-
v	Velocity in y-direction	m/s
W	Work	Nm
w	Velocity in z-direction	m/s
x	Cartesian x-coordinate	m
x_α	Non-dimensional distance between EA and center of mass	-
x_0	Non-dimensional distance between EA and quarter-chord point	-
y	Cartesian y-coordinate	m
y	Distance from nearest wall	m
y^+	Non-dimensional wall distance	-

z	Cartesian z-coordinate	m

Greek Symbols

α	Angle of attack	°or rad
α	Wave number	m^{-1}
$\alpha_{\text{corrected}}$	Reduced angle of attack	°
β	Propagation speed of a wave	m/s
γ	Intermittency factor	-
γ	Ratio of specific heats	-
Γ_{disp}	Mesh stiffness	m^{-1}
δ	Boundary layer thickness	m
δ	Damping	-
δ	Displacement relative to the previous mesh location	m
Δt	Timestep	s
ΔU	Amplitude of the velocity	m/s
Δz	Difference between tunnel off and tunnel on contour of the airfoil	m
$\Delta\alpha$	Difference between the angle of attack in the wind tunnel and the angle of attack that fits best to the experimental results	°
δ_h	Plunge-damping coefficient	-
δ_α	Pitch-damping coefficient	-
δ^*	Displacement thickness	m
ϵ	Dissipation rate	m^2/s^3
η	Frequency parameter	-
θ	Momentum thickness	m
θ	Rotation angle of the deformed airfoil	°
Λ	Pohlhausen parameter	-
λ	Eigenvalue	-
λ	Lamé coefficient	kg/m/s
λ	Wave length	m
λ_θ	Pressure gradient parameter	-
μ	Dynamic viscosity	kg/m/s
μ	Mass ratio	-
$\hat{\mu}$	Modified turbulent dynamic viscosity	kg/m/s
ν	Kinematic viscosity	m^2/s
$\hat{\nu}$	Modified turbulent kinematic viscosity	m^2/s
ξ	Local pressure gradient	N/m^3
ξ	Uncoupled frequency ratio	-

ρ	Density	kg/m^3
τ_w	Wall shear stress	N/m^2
$\bar{\bar{\tau}}$	Stress tensor	N/m^2
ϕ	Flow variable	various
ϕ	Initial wave amplitude	m^2/s
ϕ	Phase angle	$^\circ$
χ	Ratio of modified turbulent to laminar kinematic viscosity	-
ψ	Stream function	m^2/s
ω	Angular frequency	rad/s
ω	Specific dissipation rate	s^{-1}
ω_h	Uncoupled natural bending frequency	s^{-1}
ω_α	Uncoupled natural torsional frequency	rad/s

Subscripts

0	Initial state
0	Mean value
$bestfit$	Best fit to wind tunnel experiments
$crit$	Critical
d	Divergence
def	Deformation
e	Boundary layer edge
eff	Effective
f	Flutter
h	Derivative w.r.t. vertical distance
i	Einstein summation index
i	Imaginary part
i	Instability
$inlet$	Inlet condition
j	Einstein summation index
l	Laminar
m	Amplitude
max	Maximum
min	Minimum
r	Real part
rot	Rotation
sim	Simulation
T	Turbulent

$_t$	Transition
$_{te}$	Trailing edge
$_{wt}$	Wind tunnel
$_\alpha$	Derivative w.r.t. angle of attack
$_\infty$	Freestream condition

Abbreviations

AUSM	Advection Upstream Splitting Method
CFD	Computational Fluid Dynamics
CFRP	Carbon-Fiber-Reinforced Plastic
DLR	Deutsches Zentrum für Luft- und Raumfahrt
DOF	Degree of Freedom
EA	Elastic Axis
FV	Finite Volume
LCTM	Local Correlation-based Transition Model
NACA	National Advisory Committee for Aeronautics
NOII	Number of inner iterations
NOTPP	Number of timesteps per period
RANS	Reynolds-Averaged Navier-Stokes
SST	Shear-Stress Transport
TKE	Turbulent Kinetic Energy
TWG	Transonic Wind tunnel Göttingen
AIAA	American Institute of Aeronautics and Astronautics

Other Symbols

$\bar{}$	Mean
$\dot{}$	First time derivative
$\ddot{}$	Second time derivative
$\hat{}$	Amplitude
$\tilde{}$	Favre average
$\vec{}$	Vector quantity
$\prime$	Real part
$\prime$	Fluctuation (Reynolds)
$\prime\prime$	Imaginary part
$\prime\prime$	Fluctuation (Favre)
$\lvert\ \rvert$	Magnitude

Chapter 1

Introduction

1.1 Background and relevance

Nowadays it is important to develop environmental friendly technologies. Therefore people try to find ways to reduce the footprint of technological developments such as airplanes. This can be achieved by using alternative fuels on the long term. On the short term other measures are necessary however. A short-term measure would be to reduce the drag of an aircraft, in order to reduce the emissions. This drag reduction can be accomplished by the use of light weight structures for example or by increasing the extent of the laminar flow over the wing. In order to postpone laminar-to-turbulent boundary layer transition, a so-called laminar wing can be used, which has a curvature such that a large part of the boundary layer on the airfoil is laminar. As a laminar boundary layer creates less skin friction drag, the total drag of the aircraft is reduced when a laminar airfoil is used.

The typical flight speeds of large transport aircraft are just below the speed of sound in the transonic speed regime. In this regime local supersonic areas are present above (or at large transonic Mach numbers also below) the airfoil. To decelerate the flow down to freestream speed a shock wave is present, which gives rise to wave drag. This can be circumvented by shaping the airfoil such that a favourable pattern of expansion and shock waves is present on the airfoil, which cancel each out. This interaction is depicted in figure 1.1. Airfoils which exhibit this favourable interaction are called "supercritical airfoils". They have a relatively flat upper surface and the maximum thickness point is located further aft than in case of a conventional airfoil, such that at design conditions no or only a weak shock wave is present on the airfoil, reducing the wave drag almost to zero.

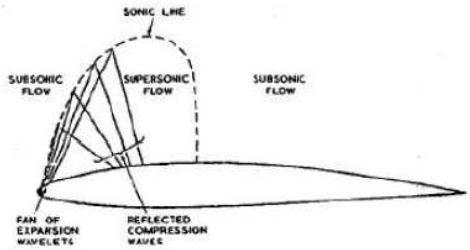

Figure 1.1: Flow development on a supercritical airfoil (adapted from Obert [2009])

When the Mach number, angle of attack or Reynolds number is slightly different from the design condition however, the flow pattern on a supercritical airfoil can change significantly and even a strong shock wave can be present. Figure 1.2 illustrates these effects by showing the flow patterns around the NLR 7301 airfoil at its design condition and at some off-design conditions.

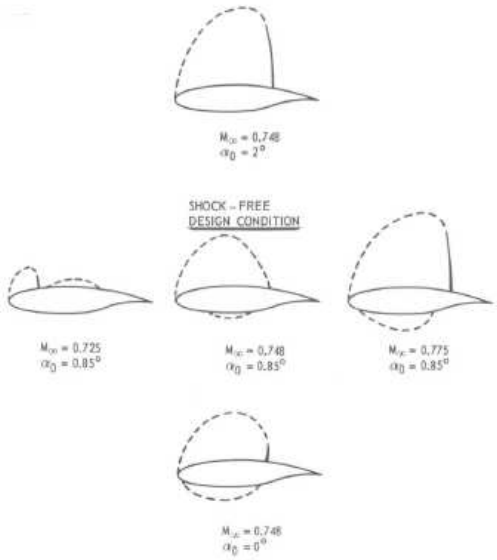

Figure 1.2: Flow patttern of the NLR 7301 airfoil at design and slightly off-design conditions (Tijdeman [1977])

A laminar boundary layer has a low skin friction drag and is therefore preferred over a turbulent boundary layer in cruise flight. The disadvantage of a laminar boundary layer is however that it tends to separate from the surface earlier than a turbulent boundary layer would do. In cruise the angle of attack is however small, such that no trailing-edge separation occurs. A local separation bubble can however be present, mostly boundary layer transition then occurs inside this bubble. In transonic flow the boundary layer interacts with the shock wave, which is present on the airfoil at off-design conditions. When the boundary layer is laminar at the interaction, it might become turbulent during the interaction with the shock wave (through a separation bubble). Furthermore, the shock wave will be located further downstream during a laminar shock/boundary layer interaction in comparison to a turbulent shock/boundary layer interaction at the same freestream speed (Becker et al. [2007]).

Disturbances in the air around the aircraft can cause it to vibrate, when the amplitude of this motion grows over time, flutter occurs. The flutter boundary represents the boundary between a stable and an unstable (growing amplitude) flow-induced motion of the aircraft. When it is surpassed this can have disastrous effects. The flutter boundary is influenced by the structural properties of the wing, as well as by the speed of the aircraft and the atmospheric conditions, that is, the flight altitude. Figure 1.3 shows an example of a flutter boundary. In the transonic regime the flutter boundary is found to exhibit the so-called "transonic dip". That is, the speed at which flutter occurs is significantly reduced at transonic Mach numbers. This is caused by the shock wave(s) on the airfoil. During the motion of the aircraft the shock wave(s) will move and cause a change in the force distribution on the wing, which will change the aircraft's stability with respect to flutter (O. O. Bendiksen [2011]).

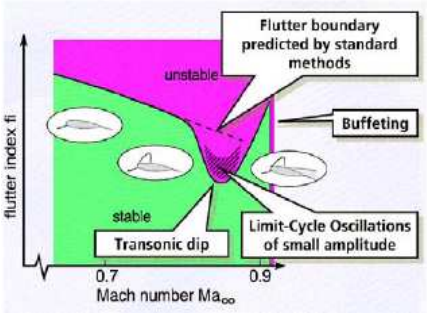

Figure 1.3: Flutter boundary (R. Voss et al. [2011])

The use of a laminar wing must however not lead to a reduction in the capabilities of aircraft. Therefore, the influence of a large laminar extent of the boundary layer on the performance of aircraft needs to be investigated. The flutter boundary is one of the most important constraints of the flight envelope of an aircraft. It is still unknown what the influence of boundary layer transition on the location and depth of the transonic dip in the flutter boundary will be. Hence, it is important to investigate the effect of boundary layer transition on the flutter boundary of a laminar wing.

1.2 Thesis objective and set-up

Since the influence of a partly laminar boundary layer on the flutter behaviour of an aircraft has not been investigated yet, a first step will be made in this thesis by using a laminar supercritical airfoil to investigate this influence. Therefore the objective of this thesis is to:

"Investigate the influence of laminar to turbulent boundary layer transition on the flutter boundary and damping characteristics of a supercritical laminar airfoil (the CAST-10 airfoil) in transonic flow using numerical simulations"

In order to do this quickly numerical simulations are performed with the CAST-10 airfoil, which is a supercritical airfoil developed by Dornier (Kühl & Zimmer [1974]). Characteristic of this airfoil is furthermore that the flow stays laminar over a large part of the

chord on both upper and lower surface. Figure 1.4 shows this airfoil together with some of its characteristics as well as its theoretical design point. Further details of this airfoil and its coordinates can be found in Appendix A.

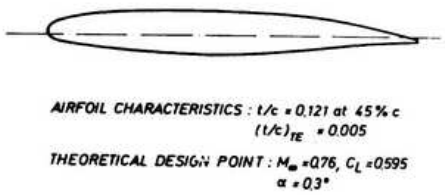

Figure 1.4: Original CAST-10 airfoil (Stanewsky et al. [1988])

Steady and unsteady CFD simulations are performed with the DLR TAU code as well as with ANSYS CFX. Both CFD codes use the principle of the Reynolds-Averaged Navier-Stokes (RANS) equations. The prediction of boundary layer transition is performed by two different models. In the DLR TAU code the e^N-method is used, whereas the ANSYS CFX code uses the $\gamma - Re_\theta$ transition model.

In order to determine the flutter behaviour of the airfoil two degrees of freedom are assigned to the airfoil; the airfoil is allowed to pitch and to plunge. The flutter behaviour is determined using the k-method, where the results from the unsteady CFD simulations are used as input. In order to compare the flutter behaviour of a laminar airfoil with free boundary layer transition to "convential" flutter behaviour of the same airfoil with a completely turbulent boundary layer, simulations with a fully turbulent boundary layer as well as with free boundary layer transition have been performed.

1.3 Thesis outline

The second chapter of this thesis gives an overview of the physical aspects of boundary layer transition as well as the transition models that are used in this thesis. After that, chapter 3 addresses aeroelastic aspects, where special attention is paid to flutter and the transonic dip. In the same chapter the equations of motion used for the classical flutter problem, as well as the method used to solve them are discussed. The last chapter of the fundamentals deals with the theory behind both CFD codes, i.e. mesh issues, the RANS equations and their discretisation as well as turbulence and transition modelling issues are discussed in this chapter. After the fundamentals, the results of the steady flow validation simulations with a deformed CAST-10 airfoil are shown and discussed in chapter 5. The results of these simulations are compared with experimental data. Chapter 6 discusses the settings used for the steady flow simulations with the original CAST-10 airfoil, as well as the results of these simulations. Both fully turbulent simulations as well as simulations with free transition are shown and comparisons are made. The settings and results of the unsteady flow simulations with fixed as well as free boundary layer transition are shown and discussed next. In chapter 8 the flutter boundary as well as the damping characteristics of the CAST-10 airfoil, with both a fully turbulent boundary layer as well as with free boundary layer transition are addressed. Finally, conclusions are drawn and recommendations for future work are given.

Chapter 2

Boundary Layers

In 1904, Ludwig Prandtl introduced the concept of a boundary layer. Boundary layer transition has been observed for the first time more than a century ago, by Osborne Reynolds (Reynolds [1883]). A lot of investigations into its nature and into methods to predict it have been performed since, but today it still remains an engineering challenge to predict boundary layer transition. In this chapter an overview will be given of some general boundary layer theory. Then the physical mechanisms of boundary layer transition will be discussed, after which the transition models used in this thesis will be presented. Finally, some aspects of turbulent boundary layers are discussed.

2.1 General aspects of boundary layers

In a fluid flow around an object at high Reynolds number (i.e. when the ratio between inertial and viscous forces is large), the flow close to the wall is most affected by the viscosity of the fluid. The flow further away from the object is strictly speaking also influenced by the viscosity of the flow. This effect is however very small, therefore it is assumed that the effect of viscosity is confined to a layer close to the wall; the boundary layer. This layer can be either laminar or turbulent. In a laminar boundary layer the flow is well organised, whereas in a turbulent boundary layer the flow is chaotic. The differences between the two types of boundary layers can be seen more clearly from the velocity profiles in the boundary layer, which are depicted in figure 2.1. The velocity at the wall should be zero, such that the flow does not slip at the wall. The velocity increases in vertical direction to the velocity of the outer flow.

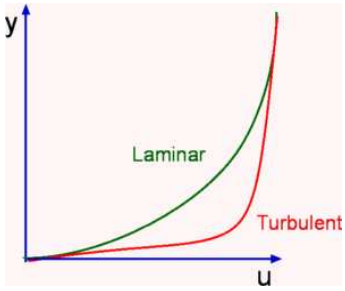

Figure 2.1: Comparison of the velocity profiles in a laminar and in a turbulent boundary layer (Laminar and Turbulent Boundary Layers [2005])

As can be seen from this figure the velocity in streamwise direction (u) increases faster in wall-normal direction for a turbulent boundary. Therefore, it is said that the velocity profile of the turbulent boundary layer is fuller. Because of this fuller velocity profile, a turbulent boundary layer is less prone to separation than a laminar boundary layer. Furthermore, a turbulent boundary layer is much thicker than a laminar boundary layer. The state of the boundary layer is governed by the so-called Reynolds number, which is defined as:

$$Re = \frac{\rho U_\infty L}{\mu}, \tag{2.1}$$

where ρ is the density, U_∞ is the freestream velocity, L is a characteristic length of the object considered and μ is the dynamic viscosity of the fluid. When the Reynolds number is small, the laminar boundary layer extends over a large part of the object's surface. At higher Reynolds numbers the laminar extent of the boundary layer is typically small.

In order to understand the quantitative differences between a laminar and turbulent boundary layer, some boundary layer parameters have to be introduced. Next to the boundary layer thickness δ two other parameters thickness parameters are the displacement thickness and the momentum thickness. In case of a compressible boundary layer they are defined as (White [2006]):

$$\delta^* = \int_0^\infty \left(1 - \frac{\rho}{\rho_e}\frac{u}{U_e}\right) dy, \tag{2.2}$$

$$\theta = \int_0^\infty \frac{\rho}{\rho_e}\frac{u}{U_e}\left(1 - \frac{u}{U_e}\right) dy, \tag{2.3}$$

where the subscript e indicates that the value of the flow parameter is evaluated at the boundary layer edge. Physically, the displacement thickness is the distance over which the streamlines outside the boundary layer are shifted due to the presence of the boundary layer (Schlichting [1979]). The momentum thickness is the loss of momentum, compared to a potential flow, inside the boundary layer (Schlichting [1979]). It is directly related to the drag of the object observed (Veldhuis [2010]). From these two parameters a new parameter can be defined; the shape factor H:

$$H = \frac{\delta^*}{\theta}. \tag{2.4}$$

The shape factor indicates the shape of the velocity profile. It has a large value in a laminar boundary layer (2 to 3 typically) and a smaller value in a turbulent boundary layer (1.5 to 2 typically) (see figure 2.2). Near separation the shape factor typically has a value of 3.7, when separation has occurred the value of the shape factor is of the order of 10 (Veldhuis [2010]). The momentum thickness increases during boundary layer transition. The displacement thickness distribution through the transition region is more complicated, as is shown in figure 2.2.

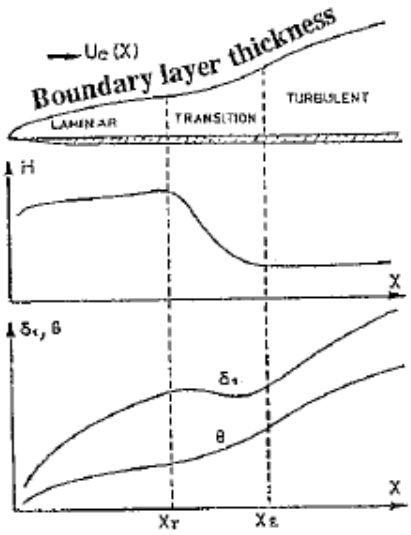

Figure 2.2: Shape factor, displacement and momentum thickness distribution through the transition region (Arnal [1990])

The displacement thickness increases in streamwise direction in a laminar boundary layer, entering the transition region this increase goes less fast and a local maximum is reached. Then the displacement thickness decreases and reaches a local minimum, after which it increases again. It keeps on increasing throughout the whole turbulent part of the boundary layer (Arnal [1990]), as can be seen from figure 2.2.

Two Reynolds numbers that are useful in relation to transition prediction, that is the transition Reynolds number Re_{x_t} and the Reynolds number based on the momentum thickness Re_{θ_t} (White [2006]):

$$Re_{x_t} = \frac{\rho U_\infty x_t}{\mu}, \tag{2.5}$$

$$Re_{\theta_t} = \frac{\rho U_\infty \theta}{\mu}. \tag{2.6}$$

Two other important parameters are the wall shear stress τ_w and the skin friction coefficient c_f (White [2006]), they are connected via:

$$c_f = \frac{\tau_w}{\frac{1}{2}\rho U_\infty^2}. \tag{2.7}$$

During transition the skin friction coefficient increases, because a turbulent boundary layer is much thicker than a laminar one. The skin friction coefficient can be an order of magnitude larger in a turbulent boundary layer in comparison to a laminar boundary layer (Arnal [1990]).

2.2 Physical aspects of boundary layer transition

This section discusses the physical process that occur during boundary layer transition. First for a flat plate, then the influence of pressure gradient is taken into account, as well as the influence of some other parameters. Finally, unsteady boundary layers are discussed.

2.2.1 Boundary layer transition on a flat plate

In this section boundary layer transition on a flat plate with zero pressure gradient is considered. Furthermore, the flow is assumed to be incompressible. Qualitatively, the processes that occur during boundary layer transition of a non-zero pressure gradient flow are the same as those that occur in a zero-pressure gradient flow (Tani [1969]).

Figure 2.3 shows the boundary layer along a flat plate. From this figure it can be seen that it starts in a laminar state from the leading edge, then at some point boundary layer transition starts, i.e. turbulent structures appear. This does not occur at one point, as is often assumed, but it takes some time and space for the turbulent structures to develop into a fully turbulent flow.

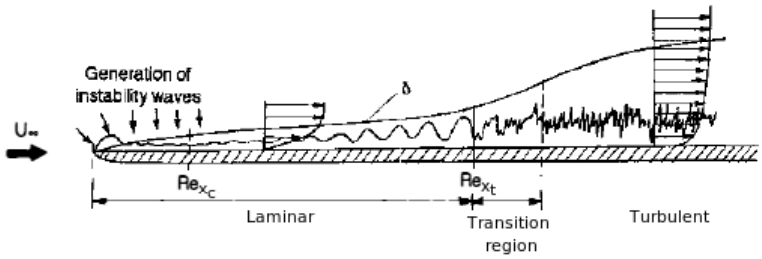

Figure 2.3: Development of a boundary layer along a flat plate (adapted from Kachanov [1994])

Transition is caused by disturbances, these disturbances cause the development of turbulent structures. Two sources of disturbance are: disturbances on the object itself, for example roughness and disturbances in the freestream flow, such as turbulence or noise. Two different types of transition can occur depending on the kind of disturbance; natural (when the amplitude of the disturbance is small) or bypass transition (when the amplitude of the disturbances is large). During natural transition two-dimensional waves develop, these waves are amplified linearly. Then nonlinear and three-dimensional phenomena will arise, which will cause secondary instabilities and boundary layer transition. During bypass transition the linear amplification of the disturbance waves is "bypassed"

and the nonlinear and three-dimensional phenomena occur directly. The transition region is located more upstream for bypass transition in comparison to natural transition (Arnal [1990]). The whole transition process is shown in figure 2.4.

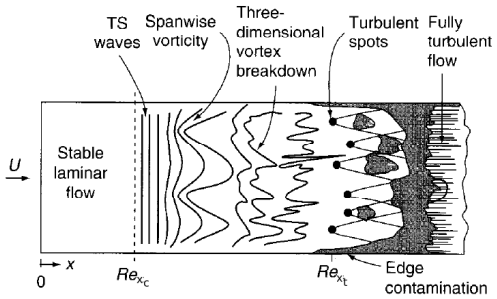

Figure 2.4: Transition process (adapted from White [2006])

The processes of nonlinear growth and the breakdown of disturbances takes a short distance in comparison to the linear growth phase (this phase takes 75-80% of the distance to transition onset) in case of natural transition (Arnal [1990]). The critical Reynolds number Re_{x_c} indicates the point at which the linear waves start to grow. The flow is however still laminar in the region in front of the transition onset location, which is indicated by Re_{x_t}. At this location boundary layer transition starts, i.e. the first turbulent spots occur at this location. Boundary layer transition ends when the boundary layer is completely turbulent. The transition region is then the region between the point of transition onset and the most upstream location at which the boundary layer is fully turbulent.

Tollmien-Schlichting waves

The linear two-dimensional growth of waves in case of natural transition has been observed from experiments (performed by Schubauer & Skramstad [1948]). These waves are called "Tollmien-Schlichting" waves (Schlichting [1951]). The linear theory describing the growth of these disturbances is based on the idea that a disturbance is added to a flow solution, this "new" solution is then inserted into the equations describing the flow, after which the governing equations are subtracted from these equations. This results in a set of disturbance equations, which can be linearised (Schlichting [1951]). Then the solution to these equations is assumed to be of complex exponential form, i.e.:

$$(u,v,w,p) = (\hat{u}(y),\hat{v}(y),\hat{w}(y),\hat{p}(y))\, e^{\beta_i t} e^{i(\alpha x - \beta_r t)}, \tag{2.8}$$

where the hat indicates the initial amplitude of the disturbance, α is the wave number, $\beta_r = 2\pi f$, where f is the frequency and β_i is the amplification or damping coefficient. The wave number α is related to the wavelength λ via: $\alpha = 2\pi/\lambda$.

When the solution of equation 2.8 is inserted into the disturbance equations, for an incompressible laminar flow, the Orr-Sommerfeld equation is obtained. This equation was developed by Orr [1907] and Sommerfeld [1908] independently of each other. An eigenvalue problem now arises since the boundary conditions are homogeneous (the disturbances vanish at the wall and in the freestream). From the eigenvalues it can be

determined whether and under which conditions the flow is stable. Stability diagrams can be drawn with neutral curves ($\alpha_i = 0$ for spatial stability and $\beta_i = 0$ for temporal stability). Figure 2.5 shows such a diagram for temporal stability. The line separating the stable and unstable regions is the neutral curve. Note that this a solution to the dimensionless Orr-Sommerfeld equations, that is, they have been made non-dimensional by the boundary layer thickness, such that the Reynolds number based on the boundary layer thickness arises in the equation. The so-called critical Reynolds number, below which none of the initial disturbances is amplified (Schlichting [1951]), is shown in figure 2.3 for a flat plate boundary layer.

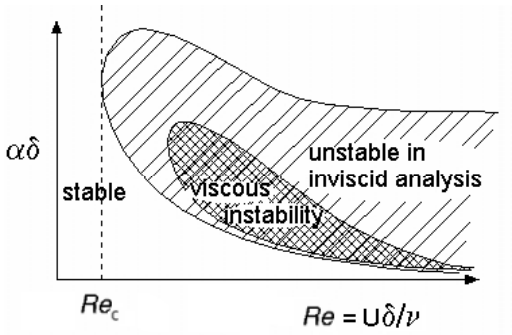

Figure 2.5: Stability diagram (FLOW CONTROL)

In the inviscid limit of the Orr-Sommerfeld equations the form of the velocity profile in the boundary layer shows whether the flow is stable (when it does not have an inflection point) or possibly unstable (when it has an inflection point and satisfies the theorem of Fjørtoft [1950]). Boundary layer velocity profiles which satisfy the conditions to be possibly unstable resemble those which have an adverse pressure gradient in reality (in viscous flow) (White [2006]). Figure 2.5 also shows the stability region in the viscous limit of the Orr-Sommerfeld equations, in that case the flow can become unstable even when the velocity profile does not have an inflection point.

Nonlinear wave growth, wave breakdown and turbulent spot formation

When the amplitude of the disturbances has reached a certain value, the amplification of these waves is no longer linear. The waves tend to become three dimensional, in spanwise direction along the flat plate the disturbance gets a nearly periodical behaviour with so-called "peaks" and "valleys", which are regions of maximum amplitude and regions of minimum amplitude, respectively. Figure 2.6 shows these peaks and valleys, which have been observed from experiments by Klebanoff et al. [1962].

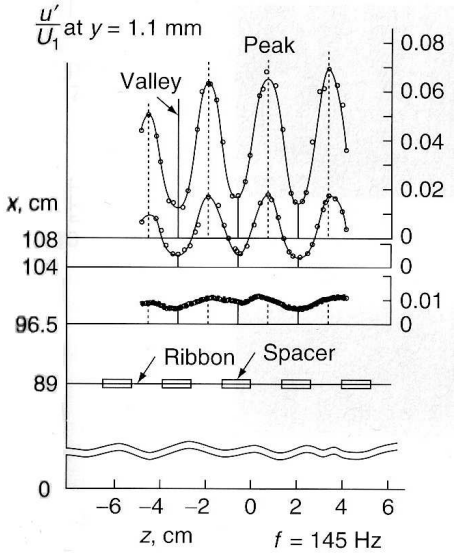

Figure 2.6: Spanwise variation of the streamwise velocity fluctuations (White [2006])

The amplitudes of the peaks and valleys become larger as the waves moves downstream, as can be observed from figure 2.6. Furthermore, there is a mean velocity defect at the peaks and an excess at the valleys. This will cause the boundary layer to get thicker at the peaks and thinner at the valleys, since the mass flow through the boundary layer should stay the same. When the wave grows and moves downstream, the vortices become more pronounced and they move more towards the peaks. Near the valleys weak vortices will develop with an opposite direction of rotation. The nonlinear theory of Benney & Lin [1960] describes the formation of these vortices.

When the wave amplitude has reached a certain amplitude (1-2 % of U_∞), the waves start to breakdown (White [2006]). The vortices that are formed then, break down again, this process continues and a cascade is formed. At first the vortices still fluctuate periodically, but as the vortices get smaller, their periodicy reduces and eventually only random fluctuations will exist, i.e. locally turbulent regions are formed. These regions are called "turbulent spots". These spots were first observed by Emmons [1951]. They grow larger as they move downstream, at some point they will overlap each other and finally they will merge to form a fully turbulent boundary layer.

Receptivity

The way in which the external disturbances lead to the existence of waves in the before undisturbed flow is described by the concept of receptivity. According to Goldstein [1983] and Kerschen [1989] the reciptivity is high in those parts of the boundary layer where the mean flow gradient in streamwise direction is large. This is near the leading edge and in regions where the local curvature is high, i.e. when the boundary layer has to adjust itself in a short distance. This concept only takes into account the birth of two-dimensional Tollmien-Schlichting waves. For three-dimensional disturbances, there is only experimental data available that shows the relation between the initial amplitude of the disturbance and the transition onset location (Arnal [1990]).

2.2.2 Parameters that effect transition

There are quite some parameters that influence the onset of boundary layer transition. Some examples are: the pressure gradient in the boundary layer, the turbulence intensity level, the roughness of the wall and the Mach number.

Pressure gradient

When transition on an airfoil is considered, a pressure gradient will be present in the boundary layer. The effect of a favourable (negative) pressure gradient is to shift the neutral curves obtained from the Orr-Sommerfeld equation towards higher Reynolds number, that is, to increase the critical Reynolds number (White [2006]). Furthermore, a positive (adverse) pressure gradient makes the transition region shorter and a favourable pressure gradient makes it longer (Tani [1969]).

When an adverse pressure gradient is present in a laminar flow, the laminar flow separates from the surface and reattaches as a turbulent boundary layer. Boundary layer transition has then occurred inside this separation bubble. Turbulent spots do not occur during this type of transition as the boundary layer is already fully turbulent when it reattaches (Tani [1969]).

Freestream turbulence

The freestream turbulence intensity is defined as:

$$Tu = \frac{\sqrt{\frac{1}{3}\left(\overline{u'^2} + \overline{v'^2} + \overline{w'^2}\right)}}{U_\infty}, \tag{2.9}$$

where u', v' and w' are the velocity fluctuations of the freestream in x-, y- and z-direction, respectively and U_∞ is the mean freestream velocity. The influence of the freestream turbulence level on transition is relatively small for small to moderate turbulence levels, that is, the same processes take place. The extent of the linear amplification phase decreases however with increasing freestream level (Tani [1969]).

Compressibility and shocks

From computations performed by Lees and Lin (Tani [1969]) it was found that the critical Reynolds number at which instability of the boundary layer occurs decreases when the Mach number is increased. These computations did however consider a boundary layer without a pressure gradient and without heat transfer (Tani [1969]).

When a shock is present a laminar boundary layer can be triggered to become turbulent. Transition then mostly happens inside a separation bubble. This separation bubble causes an effective change in the curvature of the airfoil, hence a shock wave will develop, when the freestream flow has a transonic speed. In case of a laminar shock/boundary layer interaction a λ-type shock occurs (Becker et al. [2007]). This means that two shocks are

present near the airfoil surface and they melt into one shock further away from the airfoil. Two differences between laminar shock/boundary layer and turbulent shock/boundary layer interactions are that the pressure increase takes place over a much longer distance and the position of the shock is further aft in case of a laminar shock/boundary layer interaction.

2.2.3 Unsteady boundary layers

In case of forced sinusoidal oscillations of the freestream flow, the transition in the boundary layer is characterised by an "unsteady Reynolds number" which is defined as $(U/\nu) \cdot (\Delta U/\omega)$, where U is the mean freestream velocity, ΔU is the amplitude of the velocity and ω is the angular frequency. From experiments performed by Obremski & Fejer [1967] it was found that above a certain critical value of the unsteady Reynolds number (27000 for a zero-pressure gradient flow) instability waves which look like Tollmien-Schlichting waves develop. Then turbulent bursts occur at the frequency of the oscillation, a turbulent burst is the time that a certain place in streamwise direction is turbulent (Obremski & Fejer [1967]). In this case the transition Reynolds number is independent of the frequency of the oscillation, it decreases however when the relative amplitude $\Delta U/U$ is increased. When the critical value of the unsteady Reynolds number is not reached, the location of transition seems to be fixed and independent of the amplitude and frequency of the oscillation (Tani [1969]). Miller & Fejer [1964] found that the dimensionless transition length $((Re_T - Re_t)/Re_t = (x_T - x_t)/x_t)$ depends on the oscillation frequency, but is independent of the amplitude of oscillation (for turbulent Reynolds numbers between $2.33 \cdot 10^5$ and $16.4 \cdot 10^5$). Furthermore, they observed that turbulent bursts occur periodically, instead of randomly as in case of transition of a steady boundary layer.

Obremski & Fejer [1967] observed that there are basically two phases that occur when a turbulent burst occurs periodically: a "creative" phase and a "convective phase". In the creative phase, instability waves are present in the surroundings of the turbulent spots, these spots initially grow both in upstream and downstream direction, then the growth is only in downstream direction. This leads to a turbulent spot growth rate that is much higher than that in a steady boundary layer. In the second phase, the convective phase, the growth rates of the leading edge (that is the downstream edge of the turbulent spot) and of the trailing edge of the turbulent spots are constant and no instability waves of large amplitude are present near the turbulent spots.

2.3 Transition modelling

This section describes the two methods that are used in this thesis to predict transition. First, a method based on linear stability theory is discussed, the so-called e^N-method. Then the concept of intermittency is discussed, after which the second model used, the Menter-Langty transition model which is based on transport equations is described.

2.3.1 e^N-method

This method was developed independently by van Ingen [1956] and Smith & Gamberoni [1956]. The e^N-method uses linear stability theory to investigate the stability of a flow and to predict when the flow becomes unstable, i.e. when a disturbance grows in time or space. Therefore, the e^N-method can only predict the growth of Tollmien-Schlichting waves (which takes 75-80% of the distance to transition onset, see section 2.2.1). Based on the stability of the linearly growing waves, the transition onset location and the point at which the disturbances are no longer amplified are determined. In order to do so the Orr-Sommerfeld equations (for incompressible flows) are used. The solution to these differential equations is assumed to be of exponential form, the stream function ψ for example is assumed to be of the following form (in two dimensions) (van Ingen [1956]):

$$\psi = \phi(y)\, e^{i(\alpha x - \beta t)}, \tag{2.10}$$

where $\phi(y)$ is the initial amplitude of the disturbance and $\beta = \beta_r + i\beta_i$, where $\beta_r = 2\pi f$. Here $\phi(y)$ is the eigenfunction and the corresponding eigenvalue is β. Using this decomposition of β equation 2.10 becomes (van Ingen [1956]):

$$\psi = \phi(y)\, e^{\beta_i t} e^{i(\alpha x - \beta_r t)}. \tag{2.11}$$

An additional parameter is the wave speed, it is defined as: $c_r = \beta_r/\alpha$. Now, in order to predict when the flow becomes unstable, either spatial or temporal stability theory can be used. In this thesis the spatial stability theory is used. The ratio between the amplitude a of the disturbance at a location x and the amplitude a_0 at the location x_i is given by (White [2006]):

$$\frac{a}{a_0} = e^{\left(\int_{x_i}^{x} -\alpha_i dx\right)} = e^N, \tag{2.12}$$

where x_i is the "most downstream location where the spatially growing wave becomes unstable" (Krumbein et al. [2011]) and $N = \int_{x_i}^{x} -\alpha_i dx$ is the so-called amplification factor. In terms of the Reynolds number the amplification factor can be written as:

$$N = \int_{Re_{x_i}}^{Re_x} -\alpha_i dRe_x. \tag{2.13}$$

When the amplification factor N is plotted versus the Reynolds number Re_x for different reduced frequencies $\beta_r \nu/U^2$, it can be seen that at a certain frequency a wave is first amplified, after which the amplitude reaches a maximum, then the wave becomes stable again (van Ingen [1956]). Transition onset is predicted at the point of maximum amplification. Therefore, the transition onset location can be found by connecting the maximum amplification factors at different reduced frequencies. Figure 2.7 shows a diagram with amplification factor curves and the curve connecting the maximum amplification factors.

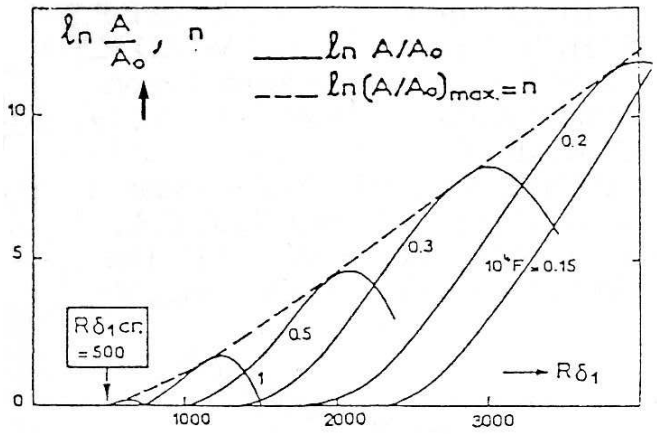

Figure 2.7: Amplification factor versus Reynols number (Arnal [1990])

In order to find the curve connecting the maximum amplification factors, a number of amplification factor curves are needed at certain frequencies. The frequency range that has to be used here is determined by finding the frequency of the most amplified disturbance at a certain location. Then this frequency is fixed and the location of the disturbance is varied, the locations (one upstream and one downstream of the chosen location) at which this disturbance is no longer amplified (neutral) are used in order to investigate the effect of a variation in frequency. At the location found upstream of the chosen location the frequency of the disturbance is increased until the reaction of the disturbance becomes neutral. This frequency is then used as the upper limit of the frequency range. At the location found downstream of the chosen (initial) location the frequency of the disturbance is decreased until it is no longer amplified. The frequency at which this happens is then used as the lower bound of the frequency range (Krumbein et al. [2011]).

Now the location of transition onset can be predicted by selecting a critical amplification factor N. The maximum amplification curve is then used to relate this critical N-factor to the transition Reynolds number and hence to the transition onset location.

The amplification factor is a function of the freestream turbulence level. This function was defined by Mack [1977] as follows:

$$N \approx -8.43 - 2.4 \ln (Tu) \,. \tag{2.14}$$

This equation is valid for $0.0007 \leq Tu \leq 0.0298$.

2.3.2 Intermittency

The concept of the intermittency factor γ can be used in the transition region, to indicate whether the flow is laminar, then $\gamma = 0$, or turbulent, when the intermittency factor becomes equal to one. In the transition region the intermittency factor has a value between zero and one. Formally, the intermittency factor is defined as: “the fraction

of the time the flow over any point $(x,\, z)$ is turbulent due to the growth/convection of the spots produced at $(x_0,\, z_0,\, t_0)$" (Sveningsson [2006]). The spots mentioned in this definition are the turbulent spots that arise when transition has started. The expression for the intermittency factor derived by Emmons [1951] is given by:

$$\gamma\,(x,\, z) = 1 - e^{-\int\int\int_R g(x_0,\, z_0,\, t_0) dx_0 dz_0 dt_0}, \tag{2.15}$$

where $g\,(x_0,\, z_0,\, t_o)$ is the spot production rate per unit area and R is the dependence volume, i.e. the volume in which a turbulent spot may be produced that influences the point $(x,\, z,\, t)$ (Emmons [1951]). In this intermittency function only the streamwise variation of the intermittency is taken into account. There is however a wall-normal variation as well. Furthermore it is assumed that the turbulent spots grow a at constant rate and that they grow independently of each other. Both of these assumptions have been confirmed by experiments performed by Elder [1960] (at least for the streamwise growth). When the freestream turbulence level is small γ is close to one near the wall and decreases towards the edge of the boundary layer. When the freestream turbulence level is high then γ is also approximately one at the boundary layer edge. Hence, when predicting bypass transition it is important to take this into account (Sveningsson [2006]).

2.3.3 Local Correlation-based Transition Model

A Local Correlation-based Transition Model (LCTM) is a transition model that uses local variables only. Transport equations for these local variables are developed, which are linked to experimental correlations. In order to predict transition the momentum thickness Reynolds number Re_θ has to be coupled to some local parameter. The LCTM of Menter et al. [2006] uses the strain-rate Reynolds number Re_v, which was first defined by van Driest & Blumer [1963]:

$$Re_v = \frac{\rho y^2 S}{\mu}, \tag{2.16}$$

where y is the distance from the nearest wall and S is the absolute value of the strain rate. Re_v is based on local properties only. It can be scaled and plotted against the non-dimensional distance from the wall. The momentum thickness Reynolds number can then be obtained from the maximum value of the strain-rate Reynolds number:

$$Re_\theta = \frac{\max(Re_v)}{2.193}. \tag{2.17}$$

This relation is actually dependent on the shape of the boundary layer profile (and hence on the pressure gradient parameter $\lambda_\theta = \left(\frac{\theta}{\delta}\right)^2 \Lambda = \frac{\theta^2 \frac{dU}{dx}}{\nu}$), but for favourable pressure gradients the constant in equation 2.17 is approximately constant. For strong adverse pressure gradients, the ratio of the maximum value of Re_v to Re_θ is different from one, hence the constant in equation 2.17 needs to be adjusted or the effect of pressure gradient has to be included into the experimental correlations (which is done in the model of Menter et al. [2006]).

Transport equations

Menter et al. [2006] developed the so-called $\gamma - Re_\theta$ transition model. This model is based on two transport equations. The first equation is a transport equation for the intermittency γ. In this case the intermittency is used to trigger the flow to become turbulent locally. Normally it is however used to modify the eddy viscosity (as in the transition model of Abu-Ghanam Shaw). The intermittency is connected to the Menter SST $k-\omega$ turbulence model, but another model could have been used as well (then some constants need to be recalibrated). γ is used to switch on the production of Turbulent Kinetic Energy (TKE) in the turbulent part of the boundary layer.

The second transport equation is for the transition onset momentum-thickness Reynolds number $\overline{Re}_{\theta_t}$. This equation takes the nonlocal effect of freestream turbulence intensity and pressure gradient at the boundary layer edge into account. Some modifications to the model are made in case of separated flow transition (Menter et al. [2006]).

The transport equation for the intermittency γ and the transition momentum thickness Reynolds number $\overline{Re}_{\theta_t}$ are given by:

$$\frac{\partial(\rho\gamma)}{\partial t} + \frac{\partial(\rho U_j \gamma)}{\partial x_j} = P_{\gamma_1} - E_\gamma + \frac{\partial}{\partial x_j}\left(\left(\mu + \frac{\mu_T}{\sigma_f}\right)\frac{\partial \gamma}{\partial x_j}\right), \tag{2.18}$$

$$\frac{\partial\left(\rho\overline{Re}_{\theta_t}\right)}{\partial t} + \frac{\partial\left(\rho U_j \overline{Re}_{\theta_t}\right)}{\partial x_j} = P_{\theta_t} + \frac{\partial}{\partial x_j}\left(\sigma_{\theta_t}\left(\mu + \mu_T\right)\frac{\partial \overline{Re}_{\theta_t}}{\partial x_j}\right), \tag{2.19}$$

where P_{γ_1} is the transition source term, E_γ is the destruction or relaminarisation source and P_{θ_t} is the source term of the momentum thickness Reynolds number. P_{γ_1} is zero in the laminar part of the boundary layer and it equal to one when the transition starts, this is controled by an onset function. Furthermore, another function (F_{length}) that is part of this production term controls the length of the transition region. The onset function depends on the critical Reynolds number Re_{θ_c}, which is connected to Re_{θ_t} via an empirical correlation (obtained from numerical experiments on a flat plate). The correlation between the transition Reynolds number and the F_{length} function is obtained from experiments. E_γ is a destruction term when the intermittency increases from zero to one and a relaminarisation term when the intermittency decreases from one towards zero.

The idea behind equation 2.19 is that Re_{θ_t} is seen as a transported scalar quantity. Via empirical correlations this Reynolds number can be computed in the freestream and in the boundary layer ($Re_{\theta_t} = f\,(\text{Tu}, dp/ds)$). Equation 2.19 changes the nonlocal empirical correlations into a local parameter, the transported scalar $\overline{Re}_{\theta_t}$.

Separation induced transition

If transition occurs when the boundary layer has separated, the agreement of the $Re_\theta - \gamma$ transition model with experiments decreases, especially when the freestream turbulence decreases. This might be caused by the fact that the TKE is lower at lower turbulence intensities. Therefore it takes some time before the TKE has a value such that the

boundary layer is able to reattach. This has to be corrected. In order to do so the intermittency is allowed to be larger than one locally, when separation occurs. This leads to a large production of TKE, which causes the boundary to reattach earlier.

Coupling to the turbulence model

The transition model presented in this section has to be coupled to a turbulence model. Menter et al. [2006] shows the coupling to the modified shear-stress transport SST model. The turbulent Prandtl number Pr_T was chosen to be 0.9. The original Menter SST model is described in section 4.3. Two modifications in the transport equations of the turbulence model are necessary for coupling with the transition model; a modification in the TKE production term and a modified TKE destruction term, i.e.:

$$\tilde{P}_k = \gamma_{\text{eff}} P_k, \tag{2.20}$$

$$\tilde{D}_k = \min\left(\max\left(\gamma_{\text{eff}},0.1\right),1.0\right) \cdot D_k, \text{ where } D_k = \beta_k \bar{\rho} k \omega. \tag{2.21}$$

Hence, the only modification to the original SST model is that the effective intermittency γ_{eff}, which is the maximum of γ and the modified intermittency due to separation, is used instead of the normal intermittency γ. This enables the model to predict the increase in laminar shear stress and heat transfer in buffeted laminar layers (which also occurred in experiments).

2.4 Turbulent boundary layer

A turbulent boundary layer can be divided into a number of layers and regions. The effect of the viscous forces in each layer changes depending on the distance from the wall. Figure 2.8 shows a basic sketch of the layers inside the boundary layer for a channel flow.

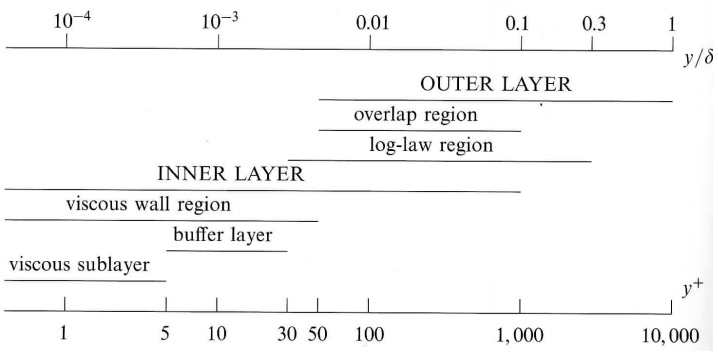

Figure 2.8: Overview of various wall layers and regions for a turbulent channel flow ($Re_\tau = 10^4$) (Pope [2009])

In this sketch y^+ is the non-dimensional wall distance: $y^+ = u_\tau y/\nu$, where u_τ is the so-called friction velocity defined as: $u_\tau = \sqrt{\tau_w/\rho}$. As can be seen from figure 2.8, the

boundary consist of two basic layers, an inner layer in which viscous shear effects are dominant and an outer layer in which turbulent shear effects are dominant and viscous shear effects are negligible. In a certain region these layers overlap each other forming another region, the so-called overlap region. In this region, both viscous and turbulent shear are equally important (White [2006]).

The log-law region is situated partly in the inner layer and partly in the outer layer as well (between $y^+ > 30$ and $y/\delta < 0.1$ for a channel flow). In this region the (non-dimensional) velocity profile can be described with logarithmic functions. This so-called "log law" is given by:

$$u^+ = \frac{1}{\kappa} \ln y^+ + B, \tag{2.22}$$

where u^+ is the non-dimensional velocity defined as: $u^+ = \bar{u}/u_\tau$ and B is a constant equal to 5.2.

Inside the inner layer, a further distinction can be made, into a viscous sublayer ($y^+ < 5$) where viscous shear effects are really dominant, and a buffer layer, which lays between $y^+ = 5$ and $y^+ = 30$. Inside the viscous sublayer the "law of the wall" is valid, which is a linear relationship between the non-dimensional velocity and the non-dimensional wall-distance:

$$u^+ = y^+. \tag{2.23}$$

The buffer layer is a transition layer in which the velocity profile transitions from linear to logarithmic. The whole inner layer can be described by the following formula of Spalding (White [2006]):

$$y^+ = u^+ + e^{-\kappa B} \left(e^{\kappa u^+} - 1 - \kappa u^+ - \frac{(\kappa u^+)^2}{2} - \frac{(\kappa u^+)^3}{6} \right), \tag{2.24}$$

where κ is the von Kármán constant, which is equal to 0.41. In the outer layer the so-called velocity defect law is valid, which is given by;

$$\frac{U_e - \bar{u}}{u_\tau} = f\left(\frac{y}{\delta}, \xi\right), \tag{2.25}$$

where U_e is the boundary layer edge velocity and ξ is the local pressure gradient: $\xi = \delta/\tau_w \cdot dp_e/dx$, where p_e is the pressure at the boundary layer edge. In this equation $U_e - \bar{u}$ is the velocity defect of the boundary layer. The logarithmic law can also be written in terms of outer layer parameter, then it looks as follows:

$$\frac{U_e - \bar{u}}{u_\tau} = -\frac{1}{\kappa} \ln\left(\frac{y}{\delta}\right) + A, \tag{2.26}$$

where A is constant that varies with pressure gradient ξ.

Chapter 3

Aeroelastic Aspects

Aeroelasticity is a very important topic in aircraft design nowadays. It deals with the interaction between aerodynamics and elastic structures. As aircraft tend to become more flexible due to the light weight designs and the slender structures, the interaction between the aerodynamics and the structure becomes more important in aircraft design.

This chapter first shows the kinds of aeroelastic problems that can occur. After that some aspects of the transonic flutter boundary are addressed. Then the basic principles of airfoil flutter are discussed. Next, the equation of motions of the classical flutter problem considered in this thesis are shown as well as the concepts necessary to solve these equations. Finally, it is outlined how to solve the equations of motions.

3.1 Aeroelastic problems

When a fluid-structure interaction is stable, the deformation of the structure as a result of the aerodynamic loads will become smaller in comparison to the initial deformation. When the interaction is unstable however, the deformation of the structure will increase the aerodynamic loading, which in turn increases the deflection. That is, the deformation of the structure grows, it diverges. This can lead to the destruction of the structure and hence needs to be prevented.

A distinction can be made based on the behaviour of the interaction between the fluid and the structure in time. That is, there can be static and dynamic aeroelastic problems. When an aeroelastic problem is static, it is not time dependent, whereas in a dynamic problem it is. Furthermore, in case of static problems the aerodynamic and elastic forces interact with each other. Whereas in dynamics problems an additional type of forces plays a role, the inertia forces. (Bisplinghoff et al. [1996])

Another way to classify aeroelastic problems is based on how they are tackled, i.e. a distinction is made between: “instability boundary problems” and the “response problems” (Hulshoff [2010]). In an instability boundary problem, an instability boundary is sought,

which separates stable and unstable aeroelastic motions. This boundary can be static or dynamic. When a static instability boundary is considered, one speaks of divergence, which is defined as: "a static instability of a lifting surface of an aircraft in flight, at a speed called the divergence speed, where the elasticity of the lifting surface plays an essential role in the instability" (Bisplinghoff et al. [1996]). In other words, it can happen that at some flight velocity, the divergence speed, the aerodynamics loads on the structure are such that they will lead to a diverging deformation of the structure. This means that over time, the deformation of the structure increases aperiodically due to the aerodynamic loading applied to it.

The dynamic instability that is part of the instability boundary problems is called flutter, which is defined by Bisplinghoff et al. [1996] as: "a dynamic instability occurring in an aircraft in flight, at a speed called the flutter speed, where the elasticity of the structure plays an essential part in the instability". In a dynamic instability problem the interaction between the deformation of the structure and the fluid is of harmonic nature, i.e. the aerodynamic flow around the structure causes deformation of the structure, which causes a change in the aerodynamic loading on the structure, which results again into a deformation of the structure. This process repeats itself, such that the aerodynamic loads on the structure oscillate. When the flight speed of the aircraft is below the flutter speed, then the oscillatory motion of the structure will be damped, i.e. the problem is stable. However, when the flight speed exceeds the flutter speed, then there will be an amplification of the oscillatory deformation, i.e. the motion of the structure becomes unstable. This can eventually lead to a destruction of the structure. At the flutter velocity, the motion of the structure is neither stable nor unstable, i.e. the amplitude of the motion is constant.

In the class "response problems" the response of a structure to a certain input is calculated. This input can be static or dynamic. An example of a static response problem is the elevator angle that would be needed to trim the aircraft to take into account the deflection of a flexible fuselage. A dynamic input could be a gust for example, but a pilot input is also a dynamic input (Hulshoff [2010]).

Hulshoff [2010] mentions that both classes of aeroelastic problems can be used to find the instability boundary of a structure. The first group mentioned here is however more efficient as it is a direct approach. This approach is used in this thesis in order to find the flutter boundary.

3.2 Transonic flutter

In transonic flow non-linearities come into play. Mixed subsonic and supersonic regions are present as well as shock waves, which interact with the boundary layer. Hence, transonic flow is inherently non-linear. Figure 3.1a shows a typical flutter boundary in the transonic regime.

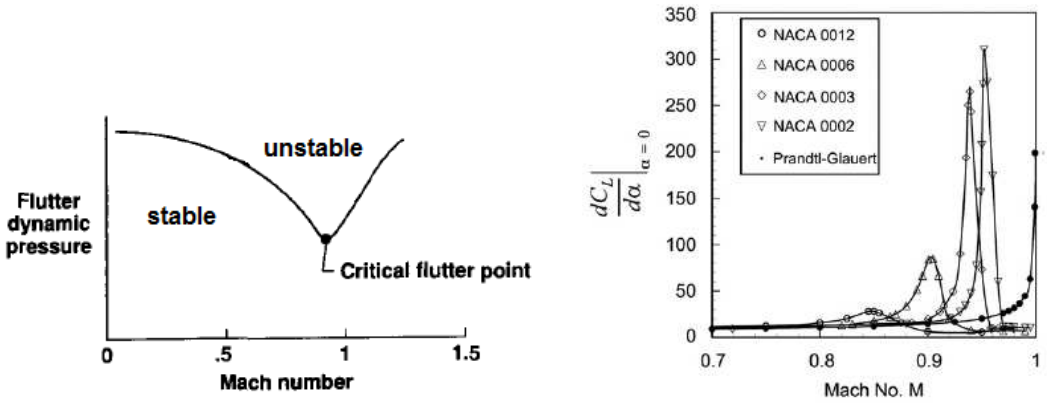

(a) Flutter boundary (adapted from Edwards & Malone [1992])

(b) Lift curve slope versus Mach number obtained from Euler calculations for NACA airfoils with varying thickness (O. Bendiksen [2011])

Figure 3.1: Examples of the flutter boundary and the lift curve slope as a function of Mach number in the transonic regime

From figure 3.1a the well-known "transonic dip" is observed, i.e. the flutter speed or the dynamic pressure at which flutter occurs is lower for transonic Mach numbers than for subsonic and supersonic Mach numbers. It has been found from (quasi-steady) simulations (O. Bendiksen [2011]) that the lift curve slope at $\alpha = 0°$ has a peak at the same Mach number as at which the transonic dip in the flutter boundary occurs. O. Bendiksen [2011] computed the lift curve slope for a NACA family with varying thickness with an Euler code (see figure 3.1b). This peak is seen to move to lower Mach numbers and to decrease in magnitude when the thickness of the airfoil increases (O. Bendiksen [2011]). The peak in lift curve slope is caused by shock dynamics rather than by shock/boundary layer interactions, since it is already observed from Euler calculations. There is however an effect of the boundary layer, since the peak reduces and the drop in lift curve slope after the peak is smaller when a boundary layer is present (O. Bendiksen [2011]). According to O. Bendiksen [2011] the peak in the lift curve slope corresponds to that shock wave position on the airfoil, where a small change in angle of attack leads to a large shift in shock position, such that the difference in lift coefficient is maximum. For frequencies larger than zero, the peak in lift coefficient is still present, it becomes however less pronounced when the frequency is increased. Furthermore, it shifts to lower Mach numbers. This is caused by unsteady effects, which lead to an effective lift curve slope. Flutter mostly occurs at low reduced frequencies (a non-dimensional frequency smaller than 1) however (in wind tunnel tests even lower, at a reduced frequency of approximately 0.2), hence it may be expected that the transonic dip occurs at approximately the same Mach number as the peak in (effective) lift curve slope. The rapid decrease in lift curve slope is caused by the fact that for Mach numbers larger than that where the maximum lift curve slope occurs, the shock moves forward when the angle of attack is increased (this is called inversed shock motion). This occurs as soon as the boundary layer separates behind the shock on the upper surface when the flow is viscous (O. O. Bendiksen [2011]). O. O. Bendiksen

[2011] shows that amplitude and phase of the unsteady lift and moment coefficients (see next section) reverse direction near the transonic dip and hence cause the occurrence of the transonic dip. Since the lift curve slope is essentially the magnitude of the lift coefficient, a quasi-steady approach can be used to find the location of the transonic dip as a first approximation. This is also true in three dimensions as shown by R. Voss et al. [2011].

3.3 Classical flutter problem for an airfoil

In this thesis the classical approach is used to find the flutter boundary of a two degrees of freedom (DOF) airfoil model. Normally, trimming is needed in order to obtain the desired lift coefficient at each flight condition. A simplification has however been made in this thesis by assuming a fixed angle of attack for all Mach numbers. This section shows the basic principle of flutter of airfoils, the equations of motion of this problem, as well as the method used to solve these equations.

3.3.1 Flutter of airfoil sections

Flutter is a self-sustained phenomenum, i.e. no external source is present that influences it. The harmonic oscillations of the structure are a pure result of the flow around the aircraft. Therefore, the energy that is needed to make the oscillations of the structure grow in time must come from the air that surrounds the aircraft. The transfer of energy to the structure occurs when the lift force and the vertical velocity vector have the same direction (in the absence of drag), since then work is done on the structure, that is, energy is extracted from the air flow and used to feed the motion of the structure. This motion is then unstable. However, when the lift force and the vertical velocity vector are in opposite directions, energy is extracted from the structure, which means that the motion is stable.

Fung [2002] performs a mathematical analysis in order to determine the work done by an airfoil in inviscid incompressible flow. When this airfoil is considered to have only one degree of freedom, plunge, the vertical harmonic motion $h(t)$ of this airfoil can be described by:

$$h(t) = h_0 e^{i\omega t}, \tag{3.1}$$

where h_0 is the amplitude of the motion and ω is the angular frequency of the motion. Assume that the vertical motion of the airfoil is positive in downward direction. The speed of this motion, can be determined from equation 3.1 by taking the time derivative of this expression. Here it is denoted with a dot, i.e. $\dot{h}$ is given by:

$$\dot{h} = i\omega h_0 e^{i\omega t}. \tag{3.2}$$

The instantaneous lift force on the airfoil can be determined from the quasi-steady lift, which is the lift that would exist on the airfoil when its motion is infinitesimally slow,

that is, when $\dot{h}$ is constant. This quasi-steady lift L_0 is defined as:

$$L_0 = \frac{1}{2}\rho U_\infty^2 S \frac{dC_L}{d\alpha}\frac{\dot{h}}{U_\infty}, \tag{3.3}$$

where the angle of attack is approximated by the last term of this equation ($\frac{\dot{h}}{U_\infty}$). The positive direction of the lift force is upwards. The instantaneous lift L is then given by:

$$L = L_0 m e^{i\phi} = |L|\, i e^{i\omega t} e^{i\phi}, \tag{3.4}$$

where m is the magnitude of the lift, i.e. $m = |L| / |L_0|$ and ϕ is the phase angle, that is, this angle indicates how much the instantaneous lift leads the quasi-steady lift, i.e. the motion of the airfoil (see section 3.3.3 for more details). The work done by the lift dW when the airfoil moves over a vertical distance dh can now be determined from:

$$dW = -\Re\{L\}\Re\{dh\} = -\Re\{L\}\Re\{\dot{h}\}dt, \tag{3.5}$$

where it should be noted that in order to determine the work, the real parts of the instantaneous lift and the vertical velocity of the airfoil are needed. Inserting equations 3.2, 3.3 and 3.4 into equation 3.5 and integrating this equation over one oscillation cycle, gives:

$$\begin{aligned}
W &= -\int_0^{2\pi/\omega} \Re\{L\}\Re\{\dot{h}\}dt && (3.6)\\
&= -\frac{1}{2}\rho U_\infty S \frac{dC_L}{d\alpha} m h_0 \omega \int_0^{2\pi/\omega} \Re\{\dot{h}e^{i\phi}\}\cdot\Re\{ie^{i\omega t}\}dt = && (3.7)\\
&= -\frac{1}{2}\rho U_\infty S \frac{dC_L}{d\alpha} m h_0^2 \omega^2 \int_0^{2\pi/\omega} \sin(\omega t+\phi)\sin(\omega t)dt && (3.8)\\
&= -\frac{\pi}{2}\rho U_\infty S \frac{dC_L}{d\alpha} m h_0^2 \omega \cos\phi = -\pi h_0 |L| \cos\phi. && (3.9)
\end{aligned}$$

From this equation it follows that when the phase angle ϕ is between $-90°$ and $90°$ then the work done by the lift is negative, i.e. energy is subtracted from the structure and the motion is stable. Hence, in an incompressible fluid the plunge motion is always stable. This does however not mean that flutter can only occur when there are multiple degrees of freedom. A single degree of freedom pitching motion can for example become unstable at very low speeds (Hulshoff [2010]).

When the airfoil is now allowed to both plunge and pitch (see left part of figure 3.2) the motion will become unstable. This can be seen from the graph in the right part of figure 3.2, which shows the motion of the airfoil ($\dot{h}(t)$) and the instantaneous lift ($L(t)$).

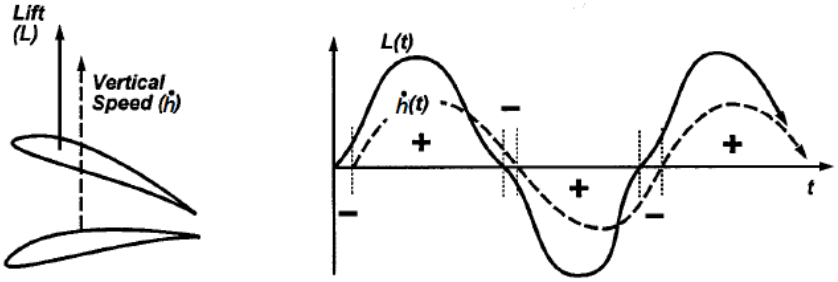

Figure 3.2: Sketch of the vertical motion of the airfoil and the response of the lift in time (Hulshoff [2010])

The (+)- and (−)-signs in this figure indicate whether the work done is positive or negative, respectively. Overall it can be seen that over an oscillation period the work is positive, hence the motion is unstable.

3.3.2 Equations of motion

In order to determine the flutter boundary of an airfoil via the instability boundary approach, the equations of motion of the airfoil need to be solved. In this thesis it is assumed that the airfoil has two uncoupled degrees of freedom. The airfoil is free to move vertically (plunge) and it is allowed to pitch around its elastic axis. It is assumed that the elastic axis (EA) is located at the quarter chord point of the airfoil. In such a way no additional moment due to the lift force is generated, since the moment reference point is located at the quarter chord point and the aerodynamic forces have their point of application at the quarter-chord point. In order to model the DOF of the airfoil, springs are used. Figure 3.3 shows the model used to derive the equations of motion.

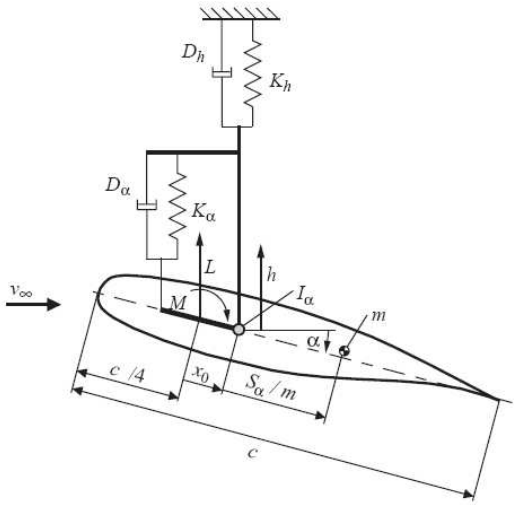

Figure 3.3: Sketch of the model with two degrees of freedom (adapted from Dietz et al. [2004])

The equations of motion can be derived from Newton's second law. The stiffnesses of the

vertical spring and that of the torsional spring are denoted with K_h and K_α, respectively. The first degree of freedom, plunge, is denoted with h, whereas the pitch angle of the airfoil is indicated with α. Furthermore, the airfoil has a mass m, a mass moment of inertia around the elastic axis I_α and a static moment due to gravity around the elastic axis S_α. It should be noted that the distance between the elastic axis and the quarter chord point is zero, that is x_0 is zero and the elastic axis is located at the quarter chord point. The distance between the center of gravity and the elastic axis is denoted with $x_\alpha = S_\alpha/m$ in figure 3.3, which is non-zero, i.e. there is a static mass moment S_α related to the elastic axis, such that there is inertial coupling. The equations of motion of this two degree of freedom system then become (Försching [1974]):

$$m\ddot{h} + S_\alpha \ddot{\alpha} + K_h h + L = 0, \tag{3.10}$$

$$S_\alpha \ddot{h} + I_\alpha \ddot{\alpha} + K_\alpha \alpha - M_{EA} = 0, \tag{3.11}$$

where the lift L and the moment about the elastic axis M_{EA} in these equations are dependent on time, equations 3.12 and 3.13 give explicit expressions for L and M_{EA}.

$$L(t) = qSc_{l_\alpha}\alpha(t) + qSc_{l_h}h(t), \tag{3.12}$$

$$M_{EA}(t) = qSc_{m_{y_\alpha}}\alpha(t)\,c + qSc_{m_{y_h}}h(t)\,c. \tag{3.13}$$

In order to arrive at these equations it is assumed that the pitch angle of the airfoil is small and that the angle between the heave displacement and the horizontal is small as well. The equations of motion can now be written in matrix form, with the degree-of-freedom vector $\vec{x} = [h,\ \alpha]^T$. Equation 3.14 shows this matrix form, together with the definition of the matrices used.

$$M\ddot{\vec{x}} + (K - qSA_0)\,\vec{x} = \vec{0}, \tag{3.14}$$

where

$$M = \begin{bmatrix} m & S_\alpha \\ S_\alpha & I_\alpha \end{bmatrix}, \qquad K = \begin{bmatrix} K_h & 0 \\ 0 & K_\alpha \end{bmatrix} \qquad \text{and} \qquad A_0 = \begin{bmatrix} -c_{l_h} & -c_{l_\alpha} \\ c_{m_{y_h}}c & c_{m_{y_\alpha}}c \end{bmatrix}.$$

3.3.3 Forced motions

The aerodynamic derivatives present in the aerodynamic force matrix A_0 can be determined by forcing the airfoil to undergo a certain motion, i.e. the aircraft is forced to oscillate in the elastic mode shapes, in two dimensions the airfoil is usually assigned two degrees of freedom, pitch and plunge. In order to describe the response of the airfoil caused by the sinusoidal oscillations of the airfoil a theory was developed in which the fluctuating response signal is decomposed into a steady part, which is constant in time, and a fluctuating part, with a certain magnitude (that is amplitude) and a certain phase

angle, which is the angle with which the response is lagging behind the motion of the airfoil. The response can also be represented in terms of real and imaginary parts. The real part physically represents the actual lift coefficient when the airfoil is at its maximum positive deflection, whereas the imaginary part represents the lift coefficient at the moment that the airfoil moves upwards and passes the equilibrium position, similarly for the moment coefficient. It should be noted that this description of the airfoil response is only valid if the response fluctuates sinusoidally as well, i.e. if the response is linear. This might not be the case when the flow has separated or in the neighbourhood of moving shock waves, then higher harmonics come into play. The general equation for a rotation is given by:

$$\alpha(t) = \alpha_0 + \sum_{n=1}^{N} \left(a_n \cos\left(n\omega t\right) + b_n \sin\left(n\omega t\right) \right), \tag{3.15}$$

where α is the angle of attack, α_0 is the mean angle of attack, N is the degree of the Fourier series, ω is the angular velocity which equals $2\pi/T$, where T is the period of the motion. a_n and b_n are the Fourier coefficients which represent the amplitude of the rotational motion. The angular velocity ω is connected to the reduced frequency k via:

$$k = \frac{\omega c}{U_\infty}, \tag{3.16}$$

where c is the chord length and U_∞ is the freestream velocity. When only the first harmonic is taken into account N should be one. Furthermore, when a pure sine airfoil motion is desired, the Fourier coefficient a_n should be zero, such that: $\alpha(t) = \alpha_0 + b_1 \sin\left(\omega t\right)$, where b_1 is the amplitude of the motion.

The resulting lift coefficient c_l as a function of time is then given by (Bisplinghoff et al. [1996]):

$$c_l\left(t\right) = c_{l_0} + \sum_{n=1}^{N} \left(c_n \sin\left(n\omega t\right) + d_n \cos\left(n\omega t\right) \right), \tag{3.17}$$

where c_{l_0} is the mean value of the lift coefficient and c_n and d_n are the Fourier coefficients, i.e. the real and the imaginary parts of the lift coefficient in the frequency domain. In this case N should be infinity in order to represent the temporal variation of the lift coefficient correctly. Often a finite number of terms is however enough. In case of a pure sine airfoil motion the discrete forms of c_{l_0}, c_n and d_n are given by (Bisplinghoff et al. [1996]):

$$c_{l_0} = \frac{1}{N_T} \sum_{i=0}^{N_T-1} c_l\left(t_i\right), \tag{3.18}$$

$$c_n = \frac{2}{N_T} \sum_{i=0}^{N_T-1} c_l(t_i) \cos(n\omega t_i) = c_l', \tag{3.19}$$

$$d_n = \frac{2}{N_T} \sum_{i=0}^{N_T-1} c_l(t_i) \sin(n\omega t_i) = c_l'', \tag{3.20}$$

where N_T is the number of timesteps per period, $c_l(t_i)$ is the lift coefficient at a certain timestep and c_l' and c_l'' indicate the real and imaginary parts of the lift coefficient in the frequency domain, respectively. When it is assumed that the response is linear, that is, only the first harmonic can be used to reconstruct the response signal, then the response of the lift coefficient can be written as:

$$c_l(t) = c_{l_0} + |c_l| \sin(\omega t + \phi), \tag{3.21}$$

where the magnitude $|c_l|$ and phase angle ϕ of the unsteady lift coefficient can be computed from:

$$|c_l| = \sqrt{c_n^2 + d_n^2} = \sqrt{c_l'^2 + c_l''^2}, \tag{3.22}$$

$$\phi = \arctan\left(\frac{d_n}{c_n}\right) = \arctan\left(\frac{c_l''}{c_l'}\right). \tag{3.23}$$

Similar expressions can be obtained for the pitching moment coefficient. If it is assumed that the angle of attack is small then the magnitude of the derivative of the lift coefficient with respect to the angle of attack $|c_{l_\alpha}|$ can be computed in the frequency domain by dividing the magnitude of the lift coefficient $|c_l|$ by the magnitude of the angle of attack $|\alpha|$, i.e.:

$$|c_{l_\alpha}| = \frac{|c_l|}{|\alpha|}. \tag{3.24}$$

Similarly for the real and imaginary parts of c_{l_α} and for the moment coefficient.

This decomposition of the motion and the response of an airfoil can also be used for plunging airfoils. Then the angle of attack in equations 3.15 and 3.24 needs to be replaced by the vertical displacement h.

3.3.4 Solving the equations of motion

The so-called k-method will be used to solve the equations of motion. This method assumes that the response of the airfoil is purely harmonic, i.e. it is assumed that the solution to the equations of motion (3.14) has the following harmonic form:

$$\vec{x} = \hat{\vec{x}} e^{pt}, \text{ where } p = i\omega, \tag{3.25}$$

where the hat indicates the amplitude of the response of the airfoil and ω is the frequency of the response. Substituting this solution into equation 3.14 leads to:

$$\left(-\omega^2 M + (K - qSA_0)\right) \hat{\vec{x}} = \vec{0}, \tag{3.26}$$

or in full form:

$$\left(-\omega^2 \begin{bmatrix} m & S_\alpha \\ S_\alpha & I_\alpha \end{bmatrix} + \begin{bmatrix} K_h & 0 \\ 0 & K_\alpha \end{bmatrix} - qS \begin{bmatrix} -c_{l_h} & -c_{l_\alpha} \\ c_{m_{y_h}} c & c_{m_{y_\alpha}} c \end{bmatrix}\right) \begin{bmatrix} \hat{h} \\ \hat{\alpha} \end{bmatrix} = \begin{bmatrix} 0 \\ 0 \end{bmatrix}. \tag{3.27}$$

The aerodynamic coefficients in these equations (c_{l_h}, c_{l_α}, $c_{m_{y_h}}$ and $c_{m_{y_\alpha}}$) are complex-valued. They are obtained by transferring the time signals of the lift and moment coefficients obtained from the CFD code to the frequency domain (see section 3.3.3). The aerodynamic coefficients are the derivatives of the lift and moment coefficients with respect to the angle of attack or the vertical displacement, such that when multiplied by the angle of attack or the vertical displacement, the lift or moment coefficient is obtained (see equations 3.12 and 3.13).

It is common to non-dimensionalise the system of equations 3.27. This can be done by dividing the first equation by mc and the second by mc^2. Then, the following system of equations is obtained (Dietz et al. [2004]):

$$\left(-\omega^2 \begin{bmatrix} 1 & \frac{S_\alpha}{mc} \\ \frac{S_\alpha}{mc} & \frac{I_\alpha}{mc^2} \end{bmatrix} + \begin{bmatrix} \frac{K_h}{m} & 0 \\ 0 & \frac{K_\alpha}{mc^2} \end{bmatrix} - \frac{qS}{m} \begin{bmatrix} -c_{l_h} & -\frac{c_{l_\alpha}}{c} \\ c_{m_{y_h}} & \frac{c_{m_{y_\alpha}}}{c} \end{bmatrix}\right) \begin{bmatrix} \frac{\hat{h}}{c} \\ \hat{\alpha} \end{bmatrix} = \begin{bmatrix} 0 \\ 0 \end{bmatrix}. \tag{3.28}$$

Simplifying this equation, dividing it by ω^2 and inserting $S = c$, where it is assumed that the airfoil has unit depth, gives (Dietz et al. [2004]):

$$\left(\begin{bmatrix} 1 & x_\alpha \\ x_\alpha & r_\alpha \end{bmatrix} + \begin{bmatrix} \xi^2\eta^2 & 0 \\ 0 & r_\alpha^2\eta^2 \end{bmatrix} + \frac{2}{\mu\pi k^2} \begin{bmatrix} -c_{l_h} c & -c_{l_\alpha} \\ c_{m_{y_h}} c & c_{m_{y_\alpha}} \end{bmatrix}\right) \begin{bmatrix} \frac{\hat{h}}{c} \\ \hat{\alpha} \end{bmatrix} = \begin{bmatrix} 0 \\ 0 \end{bmatrix}, \tag{3.29}$$

with:

$$\text{Non-dimensional distance between EA and center of mass:} \quad x_\alpha = \frac{S_\alpha}{mc}, \tag{3.30}$$

$$\text{Radius of gyration about EA:} \quad r_\alpha = \sqrt{\frac{I_\alpha}{mc^2}}, \tag{3.31}$$

$$\text{Mass ratio:} \quad \mu = \frac{m}{\frac{1}{4}\pi\rho_\infty c^2}, \tag{3.32}$$

$$\text{Uncoupled natural bending frequency:} \quad \omega_h = \sqrt{\frac{K_h}{m}}, \tag{3.33}$$

$$\text{Uncoupled natural torsional frequency:} \quad \omega_\alpha = \sqrt{\frac{K_\alpha}{I_\alpha}}, \tag{3.34}$$

$$\text{Uncoupled frequency ratio:} \quad \xi = \frac{\omega_h}{\omega_\alpha}, \tag{3.35}$$

$$\text{Frequency parameter:} \quad \eta^2 = \frac{\omega_\alpha}{\omega^2}. \tag{3.36}$$

(3.37)

A fictitious structural damping is now assumed, which is proportional to the spring stiffnesses. The damping matrix is given by:

$$D = 2i \begin{bmatrix} \xi^2 \delta_h & 0 \\ 0 & r_\alpha^2 \delta_\alpha \end{bmatrix} = 2i \begin{bmatrix} \delta_h & 0 \\ 0 & \delta_\alpha \end{bmatrix} \cdot K. \tag{3.38}$$

The complete system of equations then becomes:

$$\left(\begin{bmatrix} 1 & x_\alpha \\ x_\alpha & r_\alpha \end{bmatrix} - \left(1 + 2i \begin{bmatrix} \delta_h & 0 \\ 0 & \delta_\alpha \end{bmatrix} \right) \cdot \begin{bmatrix} \xi^2 \eta^2 & 0 \\ 0 & r_\alpha^2 \eta^2 \end{bmatrix} + \frac{2}{\mu \pi k^2} \begin{bmatrix} -c_{l_h} c & -c_{l_\alpha} \\ c_{m_{y_h}} c & c_{m_{y_\alpha}} \end{bmatrix} \right) \begin{bmatrix} \hat{\frac{h}{c}} \\ \hat{\alpha} \end{bmatrix} = \begin{bmatrix} 0 \\ 0 \end{bmatrix}. \tag{3.39}$$

Rewriting this system of equations leads to:

$$\underbrace{\left(\left(1 + 2i \begin{bmatrix} \delta_h & 0 \\ 0 & \delta_\alpha \end{bmatrix} \right) \cdot \begin{bmatrix} \xi^2 & 0 \\ 0 & r_\alpha^2 \end{bmatrix} \right)^{-1} \left(\begin{bmatrix} 1 & x_\alpha \\ x_\alpha & r_\alpha \end{bmatrix} + \frac{2}{\mu \pi k^2} \begin{bmatrix} -c_{l_h} c & -c_{l_\alpha} \\ c_{m_{y_h}} c & c_{m_{y_\alpha}} \end{bmatrix} \right)}_{B(k)} \begin{bmatrix} \hat{\frac{h}{c}} \\ \hat{\alpha} \end{bmatrix} = \lambda \begin{bmatrix} \hat{\frac{h}{c}} \\ \hat{\alpha} \end{bmatrix}, \tag{3.40}$$

where $\lambda = \frac{\omega_\alpha^2}{\omega^2}$. This system of equations represents an eigenvalue problem: $B(k)\vec{x} = \lambda \vec{x}$, with the eigenvalue λ. Hence, in order to obtain a non-trivial solution the determinant of the matrix $B(k)$ should be zero. The eigenvalues obtained from this eigenvalue problem are complex. The frequency and damping can be obtained from the real and imaginary parts of λ:

$$\text{Frequency (rad/s):} \qquad \omega = \frac{\omega_\alpha}{\Re\{\sqrt{\lambda}\}}, \tag{3.41}$$

$$\text{Damping:} \qquad \delta = \frac{\Im\{\sqrt{\lambda}\}}{\Re\{\sqrt{\lambda}\}}. \tag{3.42}$$

The so-called logarithmic decrement is also often used to indicate the damping of a system, it is connected to the damping ratio δ via: $d = 2\pi\delta$, when δ is small. Since the matrix $B(k)$ depends on the reduced frequency k these frequency and damping coefficients can only be found iteratively. More specifically, the aerodynamic coefficients depend on the reduced frequency, hence the frequency used to compute them needs to match the frequency obtained from the solution, i.e. eigenvalue, of the system.

Now, the mathematical solution is known, first the non-physical solutions need to be found and eliminated. Non-physical solutions are in this case solutions with a negative imaginary part, i.e. with a negative frequency. The remaining solutions can be plotted in a so-called flutter diagram, which shows the frequency and damping as a function of the dynamic pressure (or airspeed). Both, of these curves are necessary in order to determine whether flutter occurs, since for flutter to occur the solution to the equations of motion should be harmonic and it should grow in time. This happens when both the damping, in this case actually the growth rate, is positive and the imaginary part, the frequency, is

non-zero. An example of the frequency and damping curves for a 2 DOF airfoil is shown in figure 3.4.

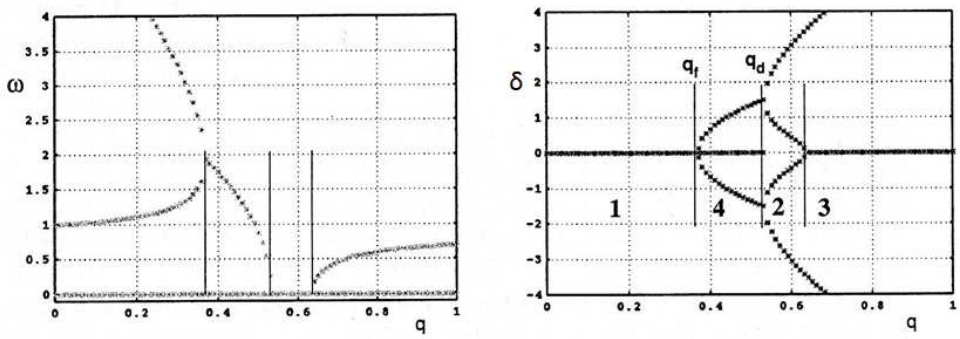

Figure 3.4: Example of the frequency (left) and damping (right) curves of a 2 DOF airfoil (adapted from Hulshoff [2010])

In this figure flutter occurs when $q > q_f$, that is, in the area marked with 4 and divergence occurs in area 2 at a dynamic pressure of q_d.

Instead of the dynamic pressure, the so-called flutter index Fi is often used on the abscissa by aeroelasticians. The flutter index is a non-dimensional parameter defined by:

$$Fi = \frac{2U_\infty}{\sqrt{\mu c \omega_\alpha}}. \tag{3.43}$$

This parameter is proportional to the product of the freestream velocity U_∞ and the square-root of the density ρ_∞ and the mass ratio μ, which is the ratio the structural to inertial forces to the aerodynamic forces. Hence, effects of flight altitude, airspeed and structural density are taken into account when the flutter index is used.

3.3.5 Approach used to determine the flutter boundary

The flutter program written by C. Hippe has been used to compute the frequencies and damping as a function of the flutter index for both DOF at each Mach number. In order to generate the input for this program, the time signals of the lift and moment coefficient obtained from the CFD code are converted to the frequency domain by a Fourier transform. The output of the program can be used to compute the flutter boundary. A schematic of this procedure can be found in figure B.1 of Appendix B.

As can be seen from figure B.1, first the structural eigenvalues are solved for. They serve as input to the eigenvalue calculation including the aerodynamic forces. Then the density, mass ratio and flutter index are computed for the current Mach number and flutter index. The aerodynamic coefficients obtained from the Fourier transform of the CFD code results are then used in order to obtain the aerodynamic coefficients at all reduced frequencies (in the specified range) by interpolation. Then the solution to the eigenvalue problem is computed and the new reduced frequency obtained from these eigenvalues is compared to the reduced frequency at which the aerodynamic coefficients have been computed (Wright & Cooper [2007]). Iterations are performed until the difference between these reduced

frequencies is smaller than the tolerance set or when the maximum number of iterations is reached. Then the frequency and the logarithmic decrement are computed from the eigenvalues. This procedure is repeated for all the flutter indices in the range at both DOF and at all Mach numbers.

The Matlab codes used to transform the time signals to the frequency domain and to generate the correct input format for the flutter program are shown in sections B.2 and B.3 of Appendix B. The flutter program, which computes the frequency and damping at all Mach numbers, can be found in section B.4 of Appendix B. The matlab program used to compute the flutter boundary from these frequency and damping curves is shown in section B.5 of Appendix B.

Chapter 4

Computational Fluid Dynamics Codes

In this chapter the two Computational Fluid Dynamics (CFD) codes that have been used in this thesis will be discussed. The first code is the DLR TAU code, which is developed by the German Aerospace Center (DLR). The second CFD code that has been used is the commercial code CFX, distributed by ANSYS.

First some fundamentals about the meshes that have been used for simulations with both CFD codes will be discussed. Then the governing equations are discussed as well as the boundary conditions, the spatial and temporal discretisation schemes used and the solver strategy. Finally, the turbulence models used are described and issues concerning the transition model are discussed.

4.1 Computational meshes

For a RANS type of simulation a mesh with a structured boundary layer part is needed. Outside the boundary layer the mesh can be structured or unstructured. When the mesh is unstructured outside of the boundary layer, it is of the hybrid type. The DLR TAU code can deal with unstructured and hybrid meshes only, whereas the ANSYS CFX code can also deal with structured meshes. The advantage of an unstructured grid is that it is easier to generate a mesh for complex geometries, a drawback is however that the solution procedure to solve the governing equations is more difficult (surface normal, area and fluxes are more difficult to define). Furthermore unstructured meshes also require more memory. An advantage is however that one can adapt an unstructured grid easily (Cebeci et al. [2005]). A hybrid mesh in two dimensions consist of hexahedra directly around the airfoil, whereas the unstructured outer flow part consists of prisms. The meshes used in this thesis are quasi-two-dimensional, since they have a very small depth consisting of only one cell. This means that the surface of the airfoil actually consists of cells.

The meshes used in this thesis have been generated with the unstructured mesh generator CENTAUR. This program can generate unstructured meshes fully automatically. There are however some important settings that can be changed in order to minimise the discretisation errors. First of all, the height of the first cell above the airfoil and the total height of the structured part of the grid are important parameters, as well as the stretching factor (the factor by which cells grow in wall-normal direction) and the number of cells in the structured part of the mesh. All of these settings are important for turbulence modelling. Furthermore, the number of cells on the surface in streamwise direction is also important. It needs to be such that the curvature of the geometry is preserved.

Some properties of meshes that are important for obtaining a good convergence of the solution are: mesh orthogonality, expansion ratio (which is equivalent to the stretching factor) and aspect ratio. The mesh orthogonality basically indicates how close the angles of the elements in the mesh are compared to some specified angle (90° in case of quadrilateral elements and 60° for triangular elements). The mesh expansion factor is the "ratio of the maximum to minimum distance between the control volume node and the control volume boundaries" (*ANSYS CFX-Solver Modeling Guide* [2010]). It takes however too much time and memory to calculate this, therefore the ratio between the maximum and the minimum sector volumes is used, see figure 4.1a. In two dimensions this becomes the ratio between the maximum and minimum sector areas.

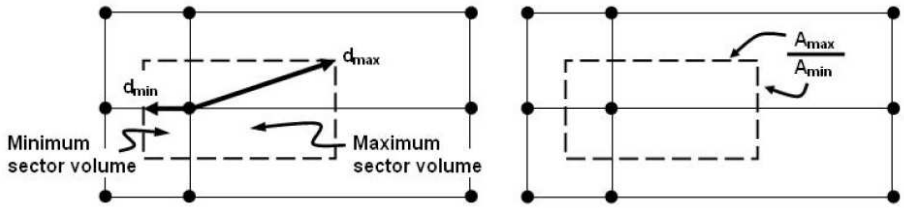

(a) Schematic of calculation of mesh expansion factor

(b) Schematic of calculation of mesh aspect ratio

Figure 4.1: Schematic overview of calculation of mesh expansion factor and mesh aspect ratio (*ANSYS CFX-Solver Modeling Guide* [2010])

The mesh expansion factor has to be below 20 in order to have a mesh of an acceptable quality.

The mesh aspect ratio is a measure of the amount of stretching of a mesh element. It is calculated by taking "the ratio of the maximum to minimum surface integration point surface areas in all elements" (ANSYS CFX-Solver Modeling Guide [2010]), see figure 4.1b. The aspect ratio should be below 100 for a mesh of acceptable quality (ANSYS CFX-Solver Modeling Guide [2010]). In two dimensions this area ratio is just a length ratio.

4.1.1 Mesh motion

In the DLR TAU code there is no movement of the grid in case of unsteady simulations, since the motion applied is a rigid-body motion. Hence, the whole grid is moved if a motion is applied to the airfoil. However, in the ANSYS CFX code the movement of

the airfoil is accomplished by a mesh deformation. That is, the motion of the airfoil is specified and the nodes of the mesh in the rest of the simulation domain are moved according to a mesh motion model. The mesh motion model used in CFX is the called "Diffusion Displacement". In this model the motion of the airfoil is diffused to other mesh points according to the following relation:

$$\nabla \cdot (\Gamma_{\text{disp}} \nabla \delta) = 0, \qquad \text{where } \Gamma_{\text{disp}} = \left(\frac{1}{d}\right)^{C_{\text{stiff}}} \tag{4.1}$$

and δ is the displacement with respect to the previous mesh location, Γ_{disp} is the mesh stiffness, which indicates how stiff the mesh is, d is the distance from the nearest boundary and C_{stiff} is the mesh stiffness exponent. The mesh stiffness is not the same everywhere in the simulation domain. It varies with the distance from the boundaries (i.e. farfield boundaries and the airfoil walls). The stiffness near the boundaries is very high, such that mesh quality is preserved near these boundaries. The mesh interior will deform the most. The mesh stiffness exponent indicates C_{stiff} how fast the mesh stiffness decreases with increasing d. In this thesis a mesh stiffness exponent of 5 has been used. Smaller values lead to negative volumes. The geometric conservation law must be satisfied for all grid cells.

The airfoil motion is specified by specifying the location of the airfoil at each timestep. The farfield boundaries are kept stationary, whereas the motion of the symmetry planes is not specified. The motion of these planes depends on the motion of the other nodes in the mesh.

4.2 Governing equations

4.2.1 Reynolds/Favre-Averaged Navier-Stokes equations

Both CFD codes used in this thesis are based on the Reynolds-Averaged Navier-Stokes (RANS) equations. These RANS equations are derived from the Navier-Stokes equations. The conservative form of these equations is:

$$\frac{\partial \rho}{\partial t} + \nabla \cdot (\rho \vec{u}) = 0, \tag{4.2}$$

$$\rho \frac{\partial \vec{u}}{\partial t} + \rho \vec{u} \cdot \nabla \vec{u} = -\nabla p + \nabla \cdot \bar{\bar{\tau}}, \tag{4.3}$$

$$\rho \frac{\partial E}{\partial t} + \rho \vec{u} \cdot \nabla E = -\nabla \cdot (p \vec{u}) + \nabla \cdot (\vec{u} \cdot \bar{\bar{\tau}}) + \nabla \cdot \vec{q}, \tag{4.4}$$

where in ρ is the density, $\vec{u} = [u,v,w]^T$ is the velocity vector, p is the pressure, T the temperature, $E = e + \frac{1}{2}\left(u^2 + v^2 + w^2\right)$ is the total specific energy (here e is the internal energy) and $\vec{q} = -k \nabla T$ is the heat flux vector, wher k is the thermal conductivity. $\bar{\bar{\tau}}$ is the stress tensor, whose components are given by:

$$\tau_{ij} = \mu \left(\frac{\partial u_i}{\partial x_j} + \frac{\partial u_j}{\partial x_i} \right) + \lambda \delta_{ij} \frac{\partial u_k}{\partial x_k}, \tag{4.5}$$

where μ and λ are the viscosity and the Lamé coefficients, respectively. The Lamé coefficient is usually taken as: $\lambda = -\frac{2\mu}{3}$ (Anderson [2007]).

In order to have the same number of equations as there are unknowns, the equation of state is used to complete the system. Equation 4.6 shows this equation in terms of the internal energy.

$$p = (\gamma - 1)\,\rho e = (\gamma - 1)\,\rho\left(E - \frac{1}{2}\left(u^2 + v^2 + w^2\right)\right), \tag{4.6}$$

where γ is the ratio of specific heats. Since directly solving the Navier-Stokes equations for turbulent flows is not yet possible for the Reynolds numbers considered, a method that partly models the flow is needed. From experiments it was observed that turbulence consists of small and large scale structures. These structures are called "eddies", actually they are like small vortices. There is a transfer of kinetic energy between these length scales. This transfer is presented by the Richardson energy cascade. In this cascade the kinetic energy from the large scale structures is transferred to the small scale structures, since the large scales are unstable. This process continues to smaller and smaller scales and finally the kinetic energy is dissipated by the (molecular) viscosity, the rate at which this dissipation takes place is the so-called dissipation rate ϵ (Pope [2009]).

In the Reynolds-Averaged Navier-Stokes approach all eddies are modelled. It is assumed that the flow quantities can decomposed into an average and a certain fluctuation around this average. For incompressible flows the decomposition used is the Reynolds' average. In equation form this decomposition looks as follows (Breugem [2010]):

$$\phi\,(x,t) = \bar{\phi}\,(x,t) + \phi'\,(x,t)\,, \tag{4.7}$$

where ϕ can be a velocity component, the pressure or the temperature. The mean is indicated by an (over)bar and the fluctuation of the flow quantity is indicated by an accent.

In compressible flows density fluctuations occur, the Reynolds' decomposition can also be used for these density fluctuations. This is however unpractical, as extra unknowns will then result. Therefore the Favre average is used for compressible flows. It is defined as follows (Chung [2002]):

$$\phi = \frac{\overline{\rho\phi}}{\bar{\rho}} + \phi'' = \tilde{\phi} + \phi'', \tag{4.8}$$

where the fluctuation of a flow quantity is now indicated by a double accent and the Favre average is indicated by a tilde. In case of compressible flow the Reynolds' average is used for the pressure and the density, whereas the Favre average is used for the other flow quantities (such as the velocity components). When these decompositions are substituted in equations 4.2, 4.3 and 4.4 and when the average is taken of the resulting equations, the following so-called Favre-Averaged Navier-Stokes equations result (Chung [2002]):

$$\frac{\partial \bar{\rho}}{\partial t} + \frac{\partial \left(\bar{\rho}\tilde{u}_j\right)}{\partial x_j} = 0, \tag{4.9}$$

$$\frac{\partial \left(\bar{\rho}\tilde{u}_i\right)}{\partial t} + \frac{\left(\bar{\rho}\tilde{u}_i\tilde{u}_j\right)}{\partial x_j} = -\frac{\partial \bar{p}}{\partial x_i} + \frac{\partial}{\partial x_j}\left(\overline{\tau_{ij}} - \overline{\rho u_i'' u_j''}\right), \tag{4.10}$$

$$\begin{aligned}\frac{\partial}{\partial t}\left(\bar{\rho}\tilde{E}\right) + \frac{\partial}{\partial x_j}\left(\bar{\rho}\tilde{u}_j\tilde{H}\right) = -\frac{\partial}{\partial x_j}\left(\overline{q_j} - \overline{\rho u_j'' H''} - \overline{\tau_{ij}u_i''} + \frac{1}{2}\overline{\rho u_j'' u_i'' u_i''}\right) \\ + \frac{\partial}{\partial x_j}\left(\left(\overline{\tau_{ij}} - \overline{\rho u_i'' u_j''}\right)\tilde{u}_i\right),\end{aligned} \tag{4.11}$$

where in the momentum equation $\overline{\tau_{ij}}$ is given by:

$$\overline{\tau_{ij}} = -\frac{2}{3}\mu\frac{\partial \bar{u}_k}{\partial x_k}\delta_{ij} + \mu\left(\frac{\partial \bar{u}_i}{\partial x_j} + \frac{\partial \bar{u}_j}{\partial x_i}\right) \tag{4.12}$$

and H is the total enthalpy, defined as $H = h + \frac{1}{2}\left(u^2 + v^2 + w^2\right)$, with h the enthalpy. As can be seen from equations 4.10 and 4.11 there are three terms in these equations that are unknown, these need to be modelled, i.e. the system of equations that needs to be solved is not closed. Therefore the modelling of the additional terms is called the "closure problem". The first of these, $\overline{\rho u_i'' u_j''}$, is called the Favre-averaged turbulent stress tensor it can be modelled by (Chung [2002]):

$$\overline{\rho u_i'' u_j''} = -\frac{2}{3}\mu_T\frac{\partial \bar{u}_k}{\partial x_k}\delta_{ij} + \mu_T\left(\frac{\partial \bar{u}_i}{\partial x_j} + \frac{\partial \bar{u}_j}{\partial x_i}\right) - \frac{2}{3}\bar{\rho}k\delta_{ij}, \tag{4.13}$$

where k is the turbulent kinetic energy (TKE), which is defined as: $k = 1/2 \cdot \overline{u_i'' u_i''}$. The second unknown that needs to be modelled is the Favre-averaged turbulent heat flux vector $\overline{\rho u_i'' H''}$. It can be modelled as follows (Chung [2002]):

$$\overline{\rho u_j'' H''} = -\frac{\mu_T c_p}{Pr_T}\frac{\partial \tilde{T}}{\partial x_j} = -\frac{\mu_T}{Pr_T}\frac{\partial \tilde{H}}{\partial x_j}, \tag{4.14}$$

where μ_T is the turbulent dynamic viscosity, c_p is the specific heat at constant pressure and Pr_T is the turbulent Prandtl number ($Pr_T = \mu_T c_p/k$, where k is the thermal conductivity).

The last term that needs to be modelled is the Favre-averaged turbulent molecular diffusion and turbulent transport term $\overline{\tau_{ij}u_j''} + \frac{1}{2}\overline{\rho u_j'' u_i'' u_i''}$ (Chung [2002]):

$$\overline{\tau_{ij}u_i''} + \frac{1}{2}\overline{\rho u_j'' u_i'' u_i''} = \left(\mu + \frac{\mu_T}{\sigma_k}\right)\frac{\partial k}{\partial x_j}, \tag{4.15}$$

where σ_k is a constant equal to 1.

In the following, the term "RANS equations" will refer to equations 4.9 until 4.11, i.e. to the Favre-Averaged Navier-Stokes equations

4.2.2 Boundary conditions

In order to solve the RANS equations boundary conditions are needed. At the airfoil surface the no-slip condition is applied, i.e. the velocity vector is zero there ($\vec{u} = \vec{0}$). At the boundaries of the simulation domain a farfield boundary condition is used in TAU, whereas in CFX inlet and outlet boundary condition have to specified. TAU automatically assigns either the freestream conditions or the conditions of the flow approaching or leaving the boundary to the boundary. In CFX the Cartesian velocity components are specified at the inlet, as well as the static temperature, the turbulence intensity and eddy viscosity ratio (μ_T/μ, see also section 4.3.3). Whereas at the outlet the averaged static pressure is specified, i.e. the average of the difference between the atmospheric pressure and the absolute pressure, hence the local static pressure is allowed to vary (ANSYS CFX-Solver Theory Guide [2010]). For the unsteady simulations the inlet and outlet boundary conditions have been set as non-reflective (a beta-feature in CFX), such that no reflections at the farfield boundary can occur. In order to assure two-dimensional flow symmetry boundary conditions are used at the symmetry planes, i.e. the velocity in y-direction is set to zero and the gradients of scalars in y-direction are set to zero here.

4.2.3 Spatial discretisation

For spatially discretising the RANS equations finite volumes are used. On these finite volumes a number of first order as well as second-order accurate spatial discretisation schemes are available in both CFD codes. Both CFD codes are vertex-based, i.e. the flow variables and fluid properties are stored at the corners of the finite volumes. The DLR TAU code uses the flux-splitting approach when an upwind discretisation scheme is selected. A number of upwind flux vector types can be used to determine the upwind flux vector (TAU Technical Documentation [2010]). A couple of examples of second-order upwind flux vector types are: Advection Upstream Splitting Method (AUSM), van Leer and Roe. The ANSYS CFX code uses a so-called high resolution scheme, which is as close to second order accurate as possible without generating oscillations in regions where steep gradients occur (ANSYS CFX-Solver Theory Guide [2010]).

In both CFD codes the transport equations of the turbulence model are also solved with the second order accurate upwind scheme. The same holds for the additional transport equations of the $\gamma - Re_\theta$ transitional model in ANSYS CFX.

4.2.4 Temporal discretisation

Steady-state problems

In order to obtain a steady-state solution to the governing equations a so-called pseudo time stepping is used in both CFD codes. That is a pseudo time derivative is added to the governing equations in order to reach a steady state. The advantage of this method over explicit time integration is that local time stepping can be used, that is the time step is locally adjusted such that it is the maximum allowed time step locally. This leads to a faster convergence to the steady state solution (TAU Technical Documentation [2010]).

In both CFD codes the implicit first order Backward Euler scheme has been used for this pseudo time stepping.

Unsteady problems

For unsteady problems the so-called dual time stepping approach is used, in which a pseudo time derivative is added to the governing equations in order to obtain convergence at each timestep and the integration in physical time is applied via a temporal discretisation scheme. Hence, two temporal integration schemes are needed. Since local time stepping cannot be used in physical time (because this would lead to an incorrect solution in time), the time step used is limited by smallest cell of the grid. Hence, there is no way to improve the efficiency of the explicit time integration schemes in physical time (in pseudo time local timestepping could be used to improve efficiency) and therefore an implicit time integration scheme should be used for the integration in physical time (van Zuijlen [2010]). In this thesis the first order Backward Euler scheme was again selected for the pseudo time stepping in both CFD codes, whereas the physical time stepping has been performed with the second order accurate backward differencing scheme.

4.2.5 Solver strategy

In this thesis the DLR TAU code has been used, more specifically TAU release 2010.1.0 has been used. Release 13.0 (Beta) of the ANSYS CFX code has been used.

A major difference between the DLR TAU code and the ANSYS CFX code is that the ANSYS CFX code is an implicit pressure-based solver, which solves the hydrodynamic equations (for u, v, w and p) at once (ANSYS CFX-Solver Theory Guide [2010]), after which the density is obtained from the equation of state (Menter et al. [2004]). The DLR TAU code is however a density-based solver, in which the momentum equations are solved first for the velocity field. Then the density is obtained from the continuity equation, after which the pressure is obtained from the equation of state (TAU Technical Documentation [2010]). The advantages of a coupled method, such as CFX, is that less iterations are needed to reach a steady state. Each iteration takes however longer than in case of a non-coupled method.

In both CFD codes a dual grid is used to solve the equations and a multigrid procedure is applied in order to accelerate convergence.

4.3 Turbulence and transition models

4.3.1 Turbulence models

There are a number of different types of turbulence models that can be used to close the "closure problem". The simplest are algebraic models. Current state-of-the art are one- and two-equation models, which solve one or two additional transport equations, respectively. Finally, the most complicated models are the so-called Reynolds-stress models in which 7 additional transport equations are solved. The one- and two- equation turbulence models used in this thesis are presented in this section.

One-equation turbulence model of Spalart and Allmaras

In the one-equation turbulence model of Spalart and Allmaras one additional transport equation is used to close the closure problem. This is a transport equation for the eddy viscosity given by (TAU Technical Documentation [2010]):

$$\frac{\partial\left(\bar{\rho}\hat{\nu}\right)}{\partial t}+\frac{\partial\left(\bar{\rho}\tilde{u}_i\hat{\nu}\right)}{\partial x_i}=c_{b_1}\rho\hat{S}\hat{\nu}+\left(\frac{\partial}{\partial x_i}\left(\frac{\mu_l+\hat{\mu}}{\sigma}\frac{\partial\hat{\nu}}{\partial x_i}\right)+\bar{\rho}\frac{c_{b_2}}{\sigma}\left(\frac{\partial\hat{\nu}}{\partial x_i}\right)^2\right)-c_{w_1}f_w\bar{\rho}\left(\frac{\hat{\nu}}{d}\right)^2, \quad (4.16)$$

where $\hat{v}$ is the modified turbulent kinematic viscosity, μ_l is the dynamic laminar viscosity, $\hat{\mu}$ is the modified turbulent dynamic viscosity and d is the wall distance. The modified turbulent kinematic viscosity is connected to the turbulent kinematic viscosity via:

$$\mu_T=\bar{\rho}\nu_T, \qquad \nu_T=f_{v_1}\hat{\nu}, \qquad f_{v_1}=\frac{\chi^3}{\chi^3+c_{v_1}^3}, \qquad \chi=\frac{\hat{\nu}}{\nu_l}. \quad (4.17)$$

f_w in equation 4.16 is a function of $\hat{v}$. More information about this function and about the constants used in this model can be found in Spalart & Allmaras [1992].

Wilcox k-ω two-equation turbulence model

The Wilcox k-ω model is a turbulence model that consists of two additional transport equations, one for the turbulent kinetic energy k and another one for the specific dissipation rate ω, which is defined as: $\omega=\epsilon/k$. In order to couple the transport equations to an expression for μ_t, the following equation is used (TAU Technical Documentation [2010]):

$$\mu_T=\rho\frac{k}{\omega}. \quad (4.18)$$

The transport equations for k and ω are:

$$\frac{\partial\left(\bar{\rho}k\right)}{\partial t}+\frac{\partial}{\partial x_j}\left(\tilde{u}_j\bar{\rho}k\right)-\frac{\partial}{\partial x_j}\left(\left(\mu+\sigma_k\mu_T\right)\frac{\partial k}{\partial x_j}\right)=P_k-\beta_k\bar{\rho}k\omega, \quad (4.19)$$

$$\frac{\partial\left(\bar{\rho}\omega\right)}{\partial t}+\frac{\partial}{\partial x_j}\left(\tilde{u}_j\bar{\rho}\omega\right)-\frac{\partial}{\partial x_j}\left(\left(\mu+\sigma_\omega\mu_T\right)\frac{\partial\omega}{\partial x_j}\right)=\gamma\frac{\bar{\rho}}{\mu_T}P_\omega-\beta_\omega\bar{\rho}\omega^2. \quad (4.20)$$

where γ is a constant and $\hat{P}$ and P are the production terms. The details of this model can be found in Wilcox [1988].

Menter SST two-equation turbulence model

The Menter Shear-Stress Transport (SST) is an extension to the Menter baseline model. This baseline model is actually a combination of the Wilcox k-ω model and the k-ϵ model. The Wilcox k-ω is accurate in the near-wall region, whereas the k-ϵ model is independent of the freestream in the outer layer (Menter [1994]). The transport equation for the turbulent kinetic energy k is the same as for that of the Wilcox k-ω model (see equation 4.19). The transport equation for ω has been changed a little bit, such that extra cross-diffusion terms appear and the modelling constants are variable (Menter [1994]). This adapted transport equation for ω is given by (TAU Technical Documentation [2010]):

$$\frac{\partial\left(\bar{\rho}\omega\right)}{\partial t}+\frac{\partial}{\partial x_j}\left(\tilde{u}_j\bar{\rho}\omega\right)-\frac{\partial}{\partial x_j}\left(\left(\mu+\sigma_\omega\mu_T\right)\frac{\partial\omega}{\partial x_j}\right)=\frac{\gamma\bar{\rho}}{\mu_T}P_\omega-\beta_\omega\bar{\rho}\omega^2 +2\sigma_{\omega_2}\left(1-F_1\right)\frac{\bar{\rho}}{\omega}\frac{\partial k}{\partial x_j}\frac{\partial\omega}{\partial x_j}. \quad (4.21)$$

where γ is a constant and F_1 is a blending function. Further details can be found in Menter [1994].

4.3.2 Near-wall treatment

Most turbulence models are not suited for regions near the wall. Hence, extra care needs to be taken in these regions. There are two options to do this:

1. Use so-called "wall functions"
2. Add viscosity and damping terms to the turbulence model

In the first approach the turbulence model is only applied until in the overlap region (see section 2.4). Then so-called "wall functions" are used from the overlap region till the wall. These wall functions are derived from the log-law and adapted to the turbulence model. The advantage of this method is that the first grid cell above the wall can have a height such that it reaches the overlap layer of the boundary layer. Hence, no fine grid up to the wall is needed.

In the second approach viscosity and damping functions for near wall behaviour are added to the turbulence model, this requires a very fine mesh up to the wall. The first grid cell above the wall should have a height such that it resides in the viscous sublayer, i.e. $y^+ < 1$ for the first grid cell above the wall (White [2006]). This approach is also called the low Reynolds number approach. The Reynolds number referred to here is however not the common Reynolds number (based on a characteristic length of the object in the flow), but to the turbulent Reynolds number $Re_T = U_0 l/\nu_T$, where U_0 is the characteristic velocity of the mean flow and l is the characteristic length scale of the mean flow (Pope [2009]). This Reynolds number is very low in the viscous sublayer, hence the name "low Reynolds number approach" (ANSYS CFX-Solver Modeling Guide [2010]).

Since in this thesis fine meshes were used up to the wall, the low turbulent Reynolds number approach has been used in both CFD codes.

4.3.3 Transition Modelling

Some implementation and usage aspects of the transition models implemented in both CFD codes will be shown in this section.

DLR TAU code

The transition model that is implemented into the DLR TAU code and that has been validated, is the based on the e^N-method of van Ingen [1956]. This method was described in section 2.3.1. In order to do so an external linear stability code called LILO is used. This code performs the stability analysis and computes the amplification rates. The laminar boundary layer parameters that are needed in order to perform this stability analysis can be obtained from the TAU code or from an external boundary layer code called COCO. In three dimensions there are in principle two lines along which transition can be predicted; inviscid streamlines derived from the boundary layer edge velocities or along so-called line-in-flight cuts (cuts parallel to the xz-plane). In two dimensions these two coincide (Krimmelbein [2009]).

The coupling between the DLR TAU code and the transition module is quite complicated. It is schematically shown in figure 4.2. From this figure it can be seen that during the iterations that the RANS solver of TAU performs, the flow solution is taken from the RANS solver and used by the transition prediction module to predict transition. The transition location obtained from the transition prediction module is not directly used by the RANS solver, that is, underrelaxation is applied. Then the RANS solver continues its iterations with the new transition location. A schematic of the transition module itself is shown in figure 4.3.

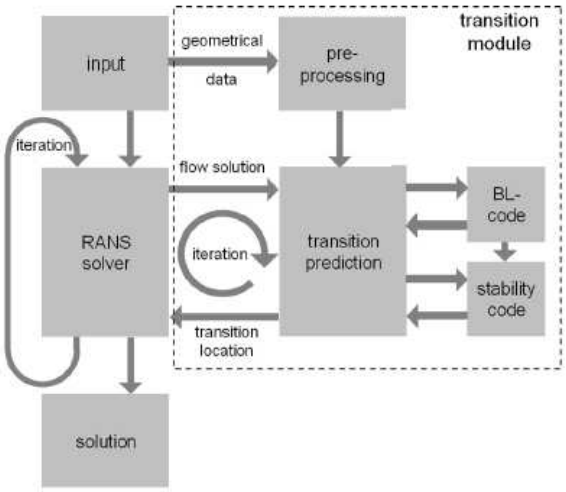

Figure 4.2: Schematic of the coupling between TAU and the transition module (Krimmelbein [2009])

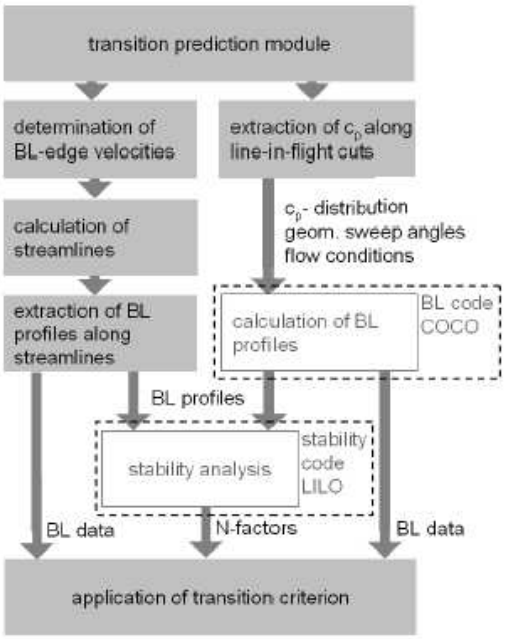

Figure 4.3: Schematic of the transition module (Krimmelbein [2009])

As can be seen from figure 4.3, inside the transition module there are basically two options for prediction. If the boundary layer data is extracted from the DLR code, then the boundary layer edge velocities are determined first, after that the streamlines are calculated and finally the boundary layer profiles along these streamlines are computed. These serve as an input for the stability code LILO. When the boundary layer code COCO is used for determination of the velocity profiles then the pressure distributions along line-in-flight cuts are extracted from the RANS code, after which COCO computes the velocity profiles. Finally, the N-factors that are obtained from the stability of analysis of LILO are used together with the boundary layer data to predict the transition location. The boundary layer code is useful when one does not want to use a very fine grid up to the wall. It is however limited to quasi-2D boundary layer flows and to flows without a laminar separation bubble. Furthermore it is only first order accurate. In this thesis the boundary layer data has always been subtracted from the TAU code, as the meshes used are very fine up to the wall.

During the transition prediction, first a pre-prediction phase can be performed. During this phase a simple criterium (the point of laminar separation) is used to predict transition after which the estimated transition location is used and is communicated with the RANS solver. After a certain number of iterations by the RANS solver, the pre-predication phase is ended and the actual transition prediction with the e^N-method is applied.

In the e^N method the amplification factors are obtained by integration (see section 2.3.1). The boundary layer edge streamline is used as the integration path. This is an approximation to the direction of the group velocity, which is "a representation of the velocity and direction of the energy transport of a wave" (Krimmelbein [2009]).

The output of the stability analysis code LILO are N-factor curves (see section 2.3.1). The transition prediction module uses these curves together with the critical N-factor

specified to predict the transition location.

ANSYS CFX code

The most important transition model implemented into the ANSYS CFX code is the so-called Gamma-Theta model (see section 2.3.3). In order to use this model the turbulence intensity has to be specified at the inlet in CFX. A certain intensity is however needed at the leading edge of the airfoil. Therefore, Langtry [2006] describes a method to determine the amount of decrease in turbulence intensity from the inlet to the leading edge of the airfoil. The turbulence kinetic energy decreases according to:

$$k = k_{\text{inlet}} \left(1 + \omega_{\text{inlet}} \beta t\right)^{\frac{-\beta^*}{\beta}} , \tag{4.22}$$

where β and β^* are constants equal to 0.09 and 0.0828, respectively and t is a timescale given by: $t = x/U_\infty$, where x is the distance from the inlet. When using the definition of Tu (see equation 2.9), the definition of the turbulent kinetic energy (see section 4.2.1) and when noting that the eddy viscosity is given by: $\mu_T = \rho k/\omega$, then the turbulence intensity at the airfoil's leading edge can be computed from the turbulence intensity at the inlet and the eddy viscosity ratio at the inlet by using equation 4.23.

$$Tu = \left(Tu_{\text{inlet}}^2 \left(1 + \frac{3\rho U_\infty x \beta Tu_{\text{inlet}}^2}{2\mu \left(\mu_T/\mu\right)_{\text{inlet}}} \right)^{\frac{-\beta^*}{\beta}} \right)^{1/2} . \tag{4.23}$$

The eddy viscosity ratio at the inlet, influences how fast Tu decays. When $\left(\mu_T/\mu\right)_{\text{inlet}}$ is large, then the decay rate will be small.

Chapter 5

Steady Flow Simulations with Deformed Airfoil Geometries

At the German Aerospace Center (DLR) wind tunnel measurements with the CAST-10 airfoil have been performed. During the latest measurement campaign in April/May 2011 it turned out that the CAST-10 airfoil (made of CFRP without ribs) undergoes deformation during the measurements. Therefore, an in-house developed measurement technique called PiColor has been used to measure the deformation of the airfoil. Furthermore, pressure sensors were used to measure the pressure at the surface of the airfoil. Transition strips were placed near the nose at the upper and lower surface of the airfoil in order to have an (almost) completely turbulent boundary layer. At the upper surface the transition strips were at $x/c = 3\%$ and had a height of 0.183 mm and at the lower surface the transition strips were at $x/c = 7.5\%$ and had a height of 0.0787 mm.

5.1 Dealing with the airfoil deformation

In order to be able to compare the results from CFD simulations with the wind tunnel measurements the deformation of the airfoil has to be taken into account. Therefore a Matlab code, which can be found in Appendix C, was written. This code extracts the differences between the "tunnel off" and "tunnel on" contour of the airfoil. These differences, called Δz, are then added to the original airfoil contour (actually the contour as produced). The deformation was however only measured at 20 points on the upper surface and 20 points on the lower surface of the airfoil. When the line connecting Δz at these 20 locations would be added to the undeformed airfoil contour a sharp-edged airfoil would be obtained, which obviously leads to phenomena which are not present on the deformed airfoil. Therefore two approaches can be used to add the measured Δz to the undeformed airfoil contour:

1. Make a spline through the z-coordinates of the deformed airfoil, such that the variation between the points is smooth.

2. Draw a trendline through the Δz points in such a way that the measured points are being captured as good as possible. Then add this trendline to the coordinates of the undeformed airfoil.

The second approach has the advantage that the equation of the trendline (a polynomial) can be determined and this equation can be used for determining the deformation of the airfoil at other angles of attack as well. The deformation is namely different for each load case (Mach number and angle of attack). That is, the same equation can be used for another angle of attack, only the coefficients have to be changed. So with one function one can generate a family of curves. Furthermore, more z-coordinates can be obtained from this method, since the established equation can be used for all points between the first and the last measurement location. The equations of the polynomials used can be found in Appendix C as well as the coefficients used for each load case and a graphical example of the polynomial approximation.

The deformation of the contour could not be measured near the leading and trailing edge of the airfoil (the measurement range was approximately 2-28 cm of the 30 cm chord). Therefore, the deformation of the front and the rear part of airfoil was assumed to be the same as that at 2 cm and at 28 cm, respectively. In the end this only changes the thickness of the airfoil. The thickness increase was only 0.3% of the chord for all the angles of attack at $M = 0.765$. Another way to deal with the missing measurements is to connect the original coordinate of the leading edge to that of the deformed airfoil at 2 cm, similarly for the trailing edge. The pressure distributions obtained from both approaches have been compared, for $\alpha = 0.6°$ the difference in thickness was clearly visible, but the same difference could have been obtained by a slight change in angle of attack. Therefore, the initial, more releastic, approach has been used. There are two ways in which the deformation of the airfoil can be obtained:

1. Subtract the z-coordinates of the "tunnel off" measurement at zero angle of attack from all other measurements (at all angles of attack). In this way the deformation can be seen to consist of a deformation and a rotation.

2. Subtract the z-coordinates of the "tunnel off" measurement at a certain angle of attack from the "tunnel on" measurements at the same angle of attack, i.e. when the angle of attack is 0.2° then the "tunnel off" measurement at $\alpha = 0.2°$ is subtracted from the "tunnel on" measurement at $\alpha = 0.2°$. In this way the deformation is a pure deformation.

Either of these methods can be used. In this thesis the first method is used however since less uncertainties are present for this method. The angles of attack and Mach numbers of the "tunnel off" measurements corresponding to the "tunnel on" measurements are namely not exactly the same. Hence, errors will be made when using this approach. Since the deformation of the airfoil is measured separately on the upper and on the lower surface of the airfoil, some uncertainties are already present in both methods. Therefore, the first method is preferred, such that no additional uncertainties are introduced.

For the first method, the Δz obtained is added to the undeformed airfoil at zero angle of attack. Then the deformed and "rotated" airfoil at the undeformed angle of attack is

obtained. When the rotation of the deformation is subtracted from Δz, a pure deformation is obtained, as for the second method. This deformation can be added to the undeformed airfoil at zero angle of attack, this gives the deformed airfoil at a reduced angle of attack, i.e. if the rotation of the airfoil is denoted with θ then this reduced angle of attack $\alpha_{corrected}$ is given by:

$$\alpha_{corrected} = \alpha - \theta \tag{5.1}$$

This correction will be called the "angle of attack correction" throughout this chapter. In the wind tunnel however, the airfoil has been rotated upwards to obtain a certain angle of attack and the wind direction is fixed. Therefore the deformation coordinates already take into account the original angle of attack and hence when performing a numerical simulation α should be zero. This means that the angle of attack under which the flow has to enter the domain in the numerical simulations is equal to $-\theta$. This method is schematically demonstrated in figure 5.1. Note that the angles have been enlarged here for clarity.

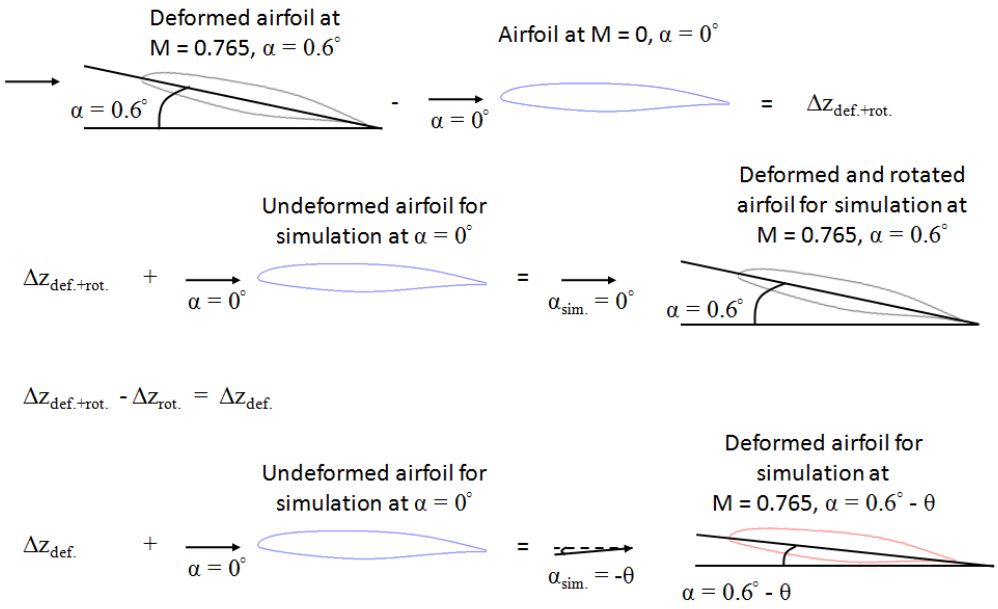

Figure 5.1: Schematic demonstrate of the first method to introduce the deformation from the wind tunnel experiments into the numerical simulation

In this figure the $\Delta z_{\text{def.}}$ is the difference in z-coordinates of the airfoil which contains a deformation only, $\Delta z_{\text{def.+rot.}}$ is the difference in z-coordinates of the airfoil which contains a deformation and a rotation and $\Delta z_{\text{rot.}}$ is the difference in z-coordinates of the airfoil which contains a rotation θ only. The angle of attack that needs to be used in the numerical simulations is indicated with $\alpha_{\text{sim.}}$.

For the second approach the Δz obtained from this procedure is added to the undeformed airfoil at the original angle of attack, then the deformed airfoil at the original angle of

attack is obtained. Hence, when numerical simulations are performed the angle of attack at which the flow has to enter the domain has to be zero.

When the coordinates of the new airfoil are known, this new airfoil can be drawn compared to the undeformed airfoil. Figure 5.2 shows the undeformed airfoil (in blue) and the deformed airfoil after angle of attack correction (in red) at $M = 0.765$ and $\alpha = 0.0°$.

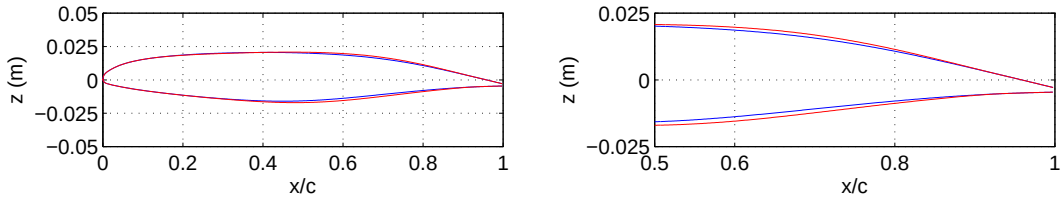

(a) Complete airfoil (b) Zoom at rear of the airfoil

Figure 5.2: Comparison of the undeformed (blue) and deformed (red) CAST-10 airfoil at $M = 0.765$ and $\alpha = 0.0°$

As can be seen from this figure, the deformation is significant. The airfoil has been stretched in z-direction. The same picture can be drawn for $M = 0.5$ and $\alpha = 0.0°$. It is shown in figure 5.3.

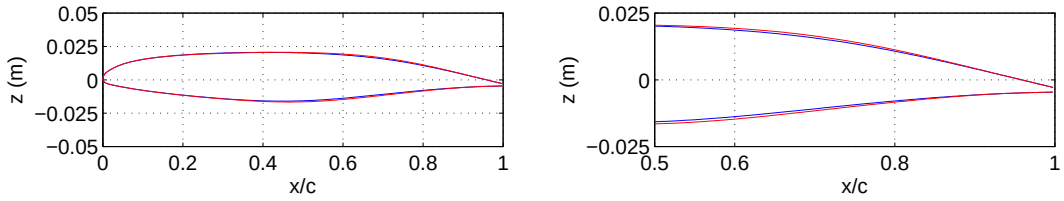

(a) Complete airfoil (b) Zoom at rear of the airfoil

Figure 5.3: Comparison of the undeformed (blue) and deformed (red) CAST-10 airfoil at $M = 0.5$ and $\alpha = 0.0°$

From this figure it can be seen that the deformation is less severe than for the higher Mach number, but still the profile is stretched in z-direction. Section 5.3 compares the results obtained with the undeformed and deformed airfoils.

5.2 General set-up

This section shows the general set-up of the steady simulations with the deformed airfoils. The mesh that has been used for these simulations is shown in figure 5.4. This is the mesh used for the simulation of the flow around the deformed CAST-10 airfoil at $M = 0.765$ and $\alpha = 0.0°$. The simulations at the other Mach numbers and angle of attacks have

been performed with similar meshes, that is, meshes with the same settings, but with a different (deformed) airfoil geometry. The mesh used is a hybrid mesh, with a structured layer consisting of 70 hexahedra cells in wall-normal direction in order to capture the boundary layer. Outside of this layer the mesh consists of prisms. The mesh density at the leading and trailing edges has been refined.

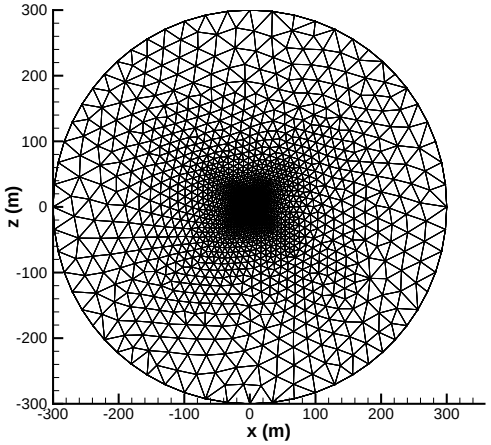

(a) Complete airfoil

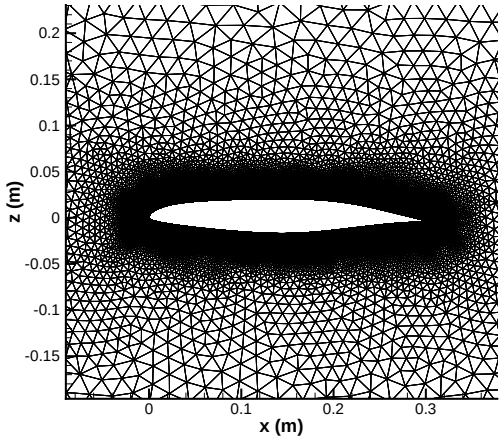

(b) Zoom of the complete airfoil

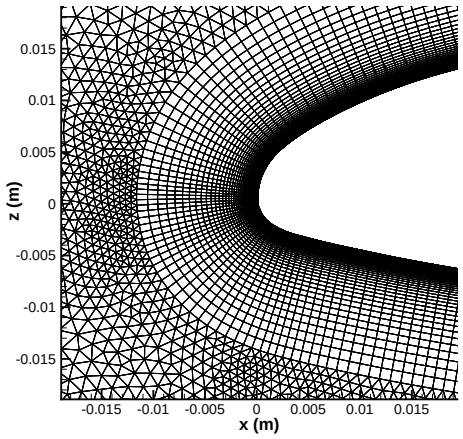

(c) Zoom at nose of the airfoil

Figure 5.4: Computational mesh for the deformed CAST-10 airfoil at $M = 0.765$ and $\alpha = 0.0°$

The mesh consists of 63957 mesh points on both symmetry planes, i.e. the total number of mesh points is 127914. There is only one cell in spanwise (y) direction, this is needed in order to perform CFD simulations. The spanwise thickness of the mesh is 0.001 m. The farfield has been modelled by a circle, which has a radius of 1000 times the chord length away from the airfoil (300 m). Some properties of the mesh used are shown in table 5.1. These settings have been determined based on a grid independency study; which showed that the results obtained with the current mesh settings are grid independent (the deviations in force and moment coefficients are smaller than 10%). Details of this

study can be found in Appendix D.

First cell height	0.00150196 mm ($y^+ = 4/9$)
Number of structured layers	70
Stretching factor of structured part	1.100538
Length of cells on airfoil surface	1 mm
Length of cells at leading/trailing edge	0.1 mm
Stretching ratio of unstructered part	1.9

Table 5.1: Mesh properties of deformed airfoil meshes

The steady simulations discussed in this chapter have been performed with the DLR TAU code. The boundary conditions at the farfield boundary have been set to farfield boundary conditions. Symmetry boundary conditions on the sides of the simulation domain (parallel to the $x - z$-plane) have been used to ensure two-dimensional flow.

The temporal discretisation scheme used for all steady simulations is the implicit Backward Euler scheme in combination with local time stepping. An investigation into the spatial discretisation scheme and the turbulence model that fits best to the experimental results has been performed (see section 5.2.1).

The Reynolds number has been set to $2 \cdot 10^6$ in all simulations, the Mach number and angle of attack have been varied. Furthermore, the static pressure has been set equal to that of the corresponding wind tunnel experiment. When the Mach number was equal to 0.765 the static pressure as measured in the windtunnel is approximately equal to 35200 Pa. In the $M = 0.5$ case the static pressure was approximately 59000 Pa. The static temperature is computed by TAU, for $M = 0.765$ it is 272 K and for $M = 0.5$ it is approximately 292 K.

5.2.1 Turbulence models

Since the solution to the RANS equations can be very sensitive to the chosen turbulence model, first the differences in results between the turbulence models available in the DLR TAU code have been investigated. Figure 5.5a shows the pressure distributions obtained with three different turbulence models: the Spalart-Allmaras original version one-equation model, the two-equation Wilcox k-ω model and the Menter SST model. Furthermore the effects of a change in spatial discretisation scheme were investigated as well, the central discretisation scheme as well as the second-order upwind scheme (with the upwind flux obtained from the AUSMDV method) have been used. Figure 5.5b shows the skin friction coefficient distribution for the same turbulence models and spatial discretisation schemes. It should be noted that this investigation has been performed with a slightly different mesh than the mesh with the properties shown in table 5.1. Since, the results where found to be mesh independent (see section D.1) this should not affect the current investigation.

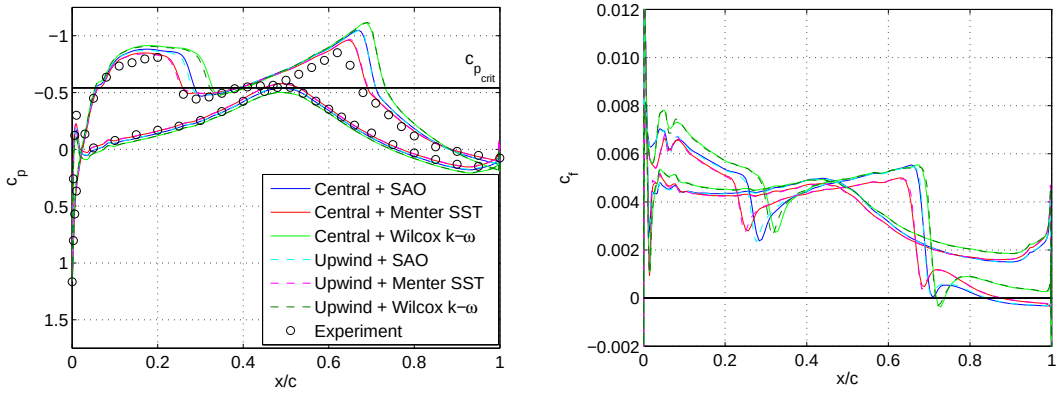

(a) Pressure distribution

(b) Skin friction distribution

Figure 5.5: Comparison of the surface pressure and skin friction distributions of the CAST-10 airfoil for different turbulence models

From these figures it can be seen that the differences between using a second order upwind or a central discretisation scheme are very small as they should be, since both schemes are second order accurate. It was however observed that results converge faster when the central scheme is used. Furthermore it can be observed from figure 5.5a that the Menter SST turbulence model fits the best to the experimental results. The other two turbulence models predict the shock at locations further away from the experimental shock locations. Hence, the Menter SST turbulence model has been used for further simulations with the deformed airfoil and the central discretisation scheme was selected for spatial discretisation.

5.3 Fully turbulent simulations

In this section the results of the steady simulations with fixed boundary layer transition, i.e. a fully turbulent boundary layer are shown. They are compared to the available experimental results. First, the angle of attack that fits best to the experimental results is determined. Then comparisons with the results obtained when using the undeformed airfoil are shown.

5.3.1 Angle of attack variation

The angle of attack that has been set in the experiments in the transonic wind tunnel Göttingen (TWG) can in general not be used one to one in the simulations with the DLR TAU code. There is an offset between the angle of attack at which the same results are obtained. Therefore an investigation has been performed into this deviation. Figure 5.6 shows the pressure distributions of the deformed airfoils at $M = 0.765$ and $\alpha = 0.0°$ and $\alpha = 0.8°$, here both the results obtained at the original angle of attack (the angle of attack in the wind tunnel) as well as and the results from the TAU simulations of the angle of attack that compared the best to the experimental values, are shown.

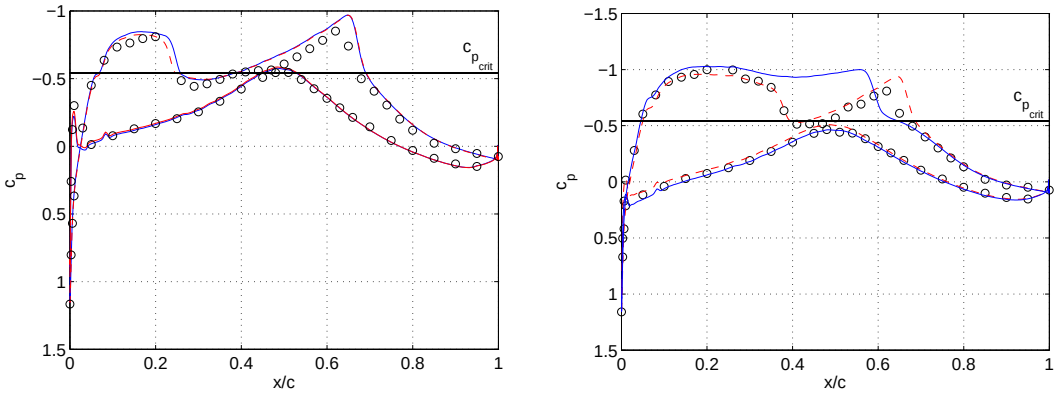

(a) $\alpha = 0.0°$ (b) $\alpha = 0.8°$

Figure 5.6: Comparison of the surface pressure distribution of the deformed CAST-10 airfoil at $M = 0.765$ from TAU at the original angle of attack (blue) and at angle of attack that compares best to the experiments (red) with experiments (symbols)

From these figures it can be seen that the agreement with the wind tunnel results is well (for the corrected angle of attack). The pressure jump at the second shock is however overpredicted by the DLR TAU code in comparison to the experiments. Furthermore, its location is also further off than that of the first shock. It has been found that the location of the first shock is far more sensitive to the angle of attack than that of the second shock.

In the wind tunnel the CAST-10 airfoil was also measured at $\alpha = 1.0°$, simulations with the deformed airfoil corresponding to this angle of attack have been performed as well. In the wind tunnel only one shock was present at this angle of attack. Figure 5.7 shows however that the results of the simulations at various angles of attack either give two shocks or a single shock at a completely wrong location. This might be caused by the fact that although the airfoil was not moving in the wind tunnel, the deformation was such that the flow itself was unsteady.

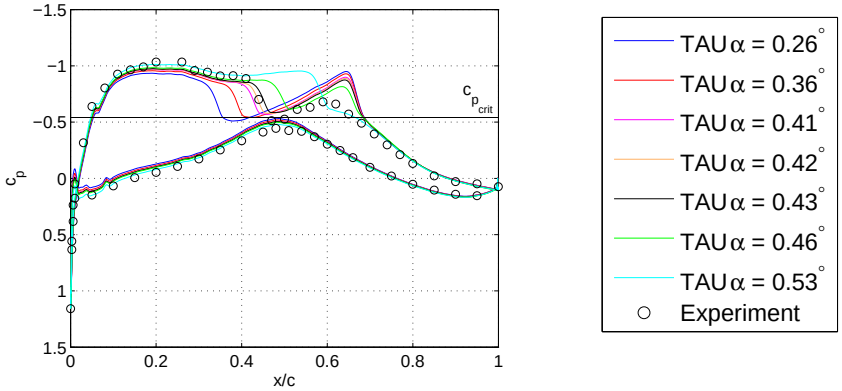

Figure 5.7: Comparison of the surface pressure distribution of the deformed CAST-10 airfoil at number of angles of attack at $M = 0.765$ from TAU with experiments (symbols)

This angle of attack investigation has been performed by trial and error for three angles of attack and then a polynomial was fitted through these points, such that it was easier to estimate which angle of attack should be used in TAU in order to get results that compare well to the experimental values. Figure 5.8 shows the difference between the angle of attack in the simulation and that in the wind tunnel versus the angle of attack in the wind tunnel. Two polynomial which have been fit through the data points are shown as well.

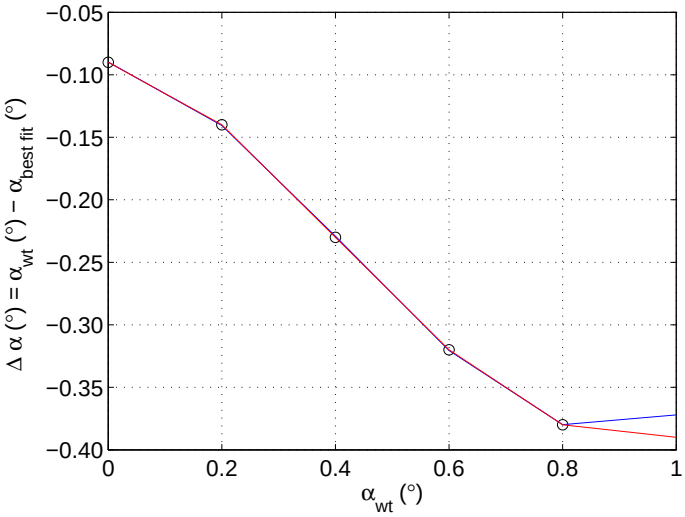

Figure 5.8: Angle of attack correction between wind tunnel and TAU versus angle of attack in the wind tunnel (blue = polynomial of order 3, red = polynomial of order 4 and symbols = angles that show agreement)

Tables 5.2 shows the force and moment coefficients for the different testcases, the experimental values are shown as well. It should be noted that the force and moment coefficients obtained from the TAU simulations shown here those are taken of which the pressure distribution fits the best to the experimental one. The experimental value of the lift coefficient is obtained from the integrated lift via:

$$c_l = \frac{L}{\frac{1}{2}\rho_\infty U_\infty^2 c} \tag{5.2}$$

	$\alpha = 0.0°$		$\alpha = 0.2°$		$\alpha = 0.4°$	
Coefficient	TAU	Experiment	TAU	Experiment	TAU	Experiment
c_l	0.2918	0.2536	0.3190	0.2762	0.3398	0.3276
c_d	0.0157	-	0.0160461467758	-	0.0161	-
c_{m_y}	-0.0536	-	-0.0526	-	-0.0515	-

Table 5.2

	$\alpha = 0.6°$		$\alpha = 0.8°$	
Coefficient	TAU	Experiment	TAU	Experiment
c_l	0.3701	0.3686	0.4086	0.4059
c_d	0.0163	-	0.0162	-
c_{m_y}	-0.0512	-	-0.0513	-

Table 5.2: Force and moment coefficient obtained from TAU and from experiments

From this table it can be seen that the lift coefficients are close to the experimental values, especially for $\alpha = 0.6°$ and $\alpha = 0.8°$ the difference is less than 1%. The results for $\alpha = 1.0°$ are not shown in table 5.2, because the pressure distributions as obtained from the TAU simulations did not fit to the experimental results.

5.3.2 Deformed and undeformed airfoil

The pressure and skin friction distributions obtained with the DLR TAU code for the deformed profile at $M = 0.765$ and $\alpha = 0.0°$ are shown in figure 5.9. Furthermore, this figure also shows the pressure and skin friction distributions of the undeformed airfoil at $M = 0.765$ and $\alpha = 0.0°$ obtained with TAU and the experimental values (of the deformed airfoil).

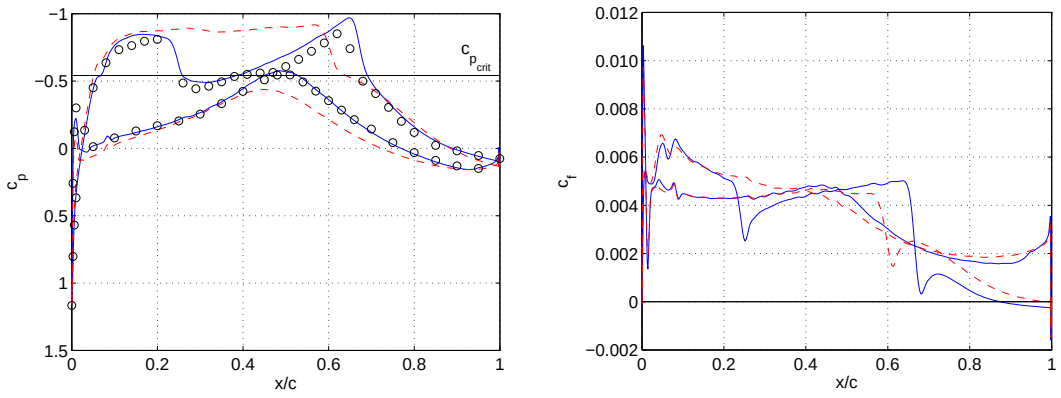

(a) Pressure distribution

(b) Skin friction distribution

Figure 5.9: Surface pressure and skin friction distributions at $M = 0.765$ and $\alpha = 0.0°$ (blue = deformed airfoil TAU, red = undeformed airfoil TAU, symbols = experiment)

From figure 5.9a it can clearly be seen that the deformation of the airfoil, although small in absolute value, has an enormous impact on the flow pattern on the airfoil. For the undeformed airfoil one strong shock is present on the airfoil (indicated by one stark pressure increase) whereas for the deformed airfoil two shock waves (indicated by two strong increases in pressure) are present. This can be explained by comparing the undeformed airfoil and the deformed airfoil without angle of attack correction. This comparison is shown in figure 5.10. From this figure it can be observed that the curvature of the deformed airfoil decreases in the region from $x = 0.2$ m until $x = 0.25$ m (the red and blue

line get closer to each other there). This is exactly the region in which the first shock is present. Then the curvature increases again and the flow accelerates, until just downstream of the flat part of the upper surface of airfoil, where the second shock is present. This part extends further downstream for the deformed airfoil and hence the expansion on this airfoil extends further downstream, causing a more downstream second shock. The skin friction coefficient distribution is shown in figure 5.9b. As can be seen from this figure, there is a bit of separation at the rear of the upper surface for the deformed airfoil, this is not the case for the undeformed airfoil. Furthermore, the skin friction coefficient shows two drops at the upper surface of the deformed airfoil, these drops are located at the shocks. Downstream of the first shock the skin friction increases again and drops down at the second shock, after which it increases a bit and near the trailing edge separation occurs. For the undeformed airfoil the skin friction also drops at the shock, reaches a local maximum downstream of it and decreases towards the trailing edge, but only a very little trailing edge separation occurs. When looking at the pressure distributions it can be seen at the shock the pressure gradient is adverse and hence the skin friction coefficient drops at the shock. Downstream of the shocks the pressure decreases, hence a favourable pressure gradient is present, which leads to an increase of the skin friction coefficient again (the velocity profile becomes fuller again).

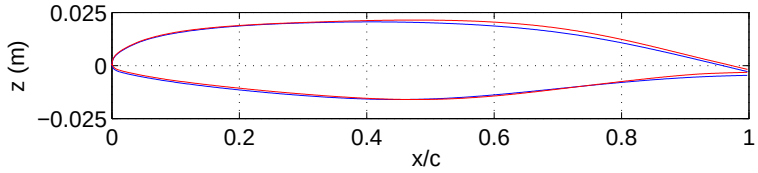

(a) Complete airfoil

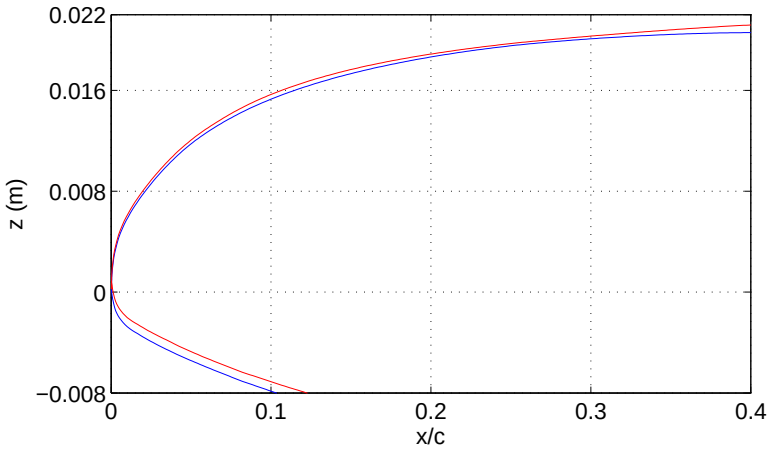

(b) Zoom at front of the airfoil

Figure 5.10: Comparison of the undeformed (blue) and deformed (red) CAST-10 airfoil without angle of attack correction at $M = 0.765$ and $\alpha = 0.0°$

The pressure and skin friction distribution of the other angles of attack at $M = 0.765$ show similar behaviour, except for that at $\alpha = 1.0°$. As an example the pressure and skin friction distributions at $\alpha = 0.8°$ are shown here. Figure 5.11 shows these distributions for the deformed and undeformed airfoil. The pressure distribution looks indeed similar to that at $\alpha = 0.0°$, except for the fact that both the undeformed and the deformed airfoil produce a single shock and during the experiment two shocks were observed. The shock at the undeformed airfoil is however stronger, as the pressure increase is larger for this airfoil. By applying an angle of attack offset between the angle of attack in the wind tunnel and that in the experiment, two shocks exist on the deformed airfoil as well (see figure 5.6b). The skin friction distribution for $\alpha = 0.8°$ is shown in figure 5.11b. From figure 5.11b it can be seen that the shock at the undeformed airfoil is clearly stronger, since it causes local separation of the flow from the surface, i.e. the skin friction coefficient becomes negative, that is backflow occurs, after which the flow reattaches again.

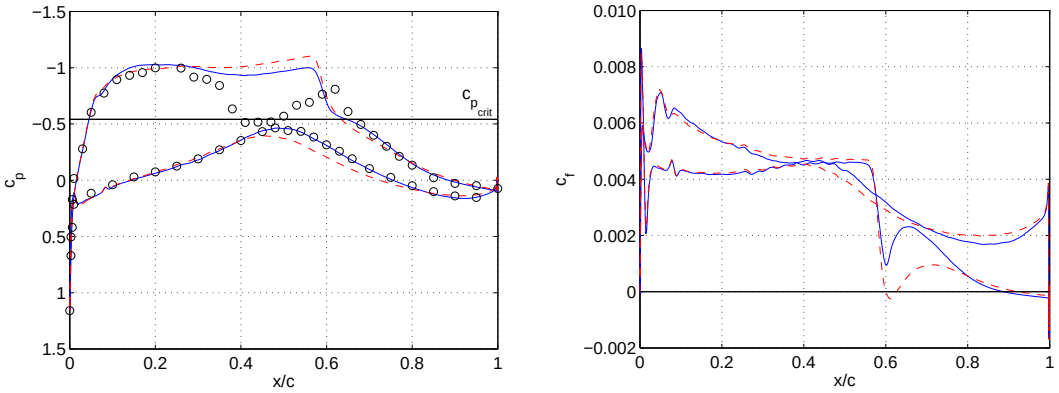

(a) Pressure distribution (b) Skin friction distribution

Figure 5.11: Surface pressure and skin friction distributions at $M = 0.765$ and $\alpha = 0.8°$ (blue = deformed airfoil TAU, red = undeformed airfoil TAU, symbols = experiment)

Figure 5.12 shows the pressure and skin friction distributions as obtained from the DLR TAU code for the deformed and the undeformed airfoil at $M = 0.5$ and $\alpha = 0.0°$. For comparison, the experimental values are shown as well.

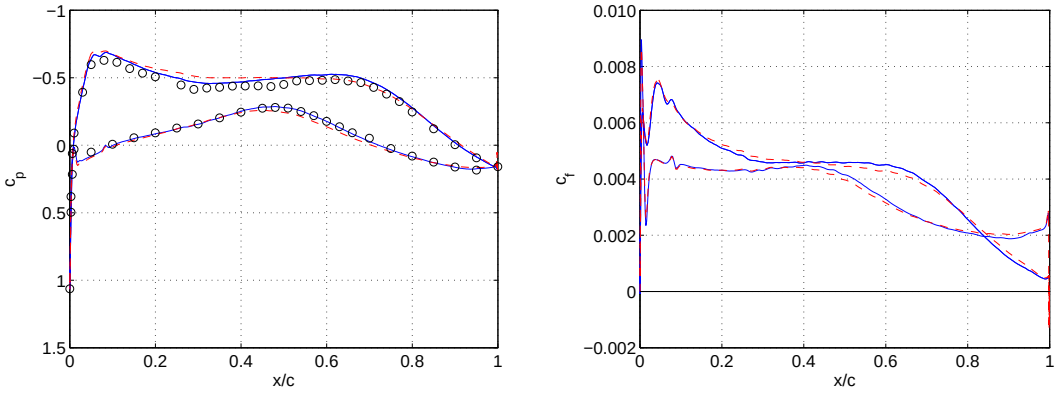

(a) Pressure distribution (b) Skin friction distribution

Figure 5.12: Surface pressure and skin friction distributions at $M = 0.5$ and $\alpha = 0.0°$ (blue = deformed airfoil TAU, red = undeformed airfoil TAU, symbols = experiment)

From this figure it can be seen that the influence of the deformation of the airfoil is small, i.e. the pressure distributions of the undeformed and the deformed airfoil look similar. They compare quite well with the experimental values. Figure 5.12b shows the skin friction coefficient distribution obtained with the DLR TAU code at $M = 0.5$ and $\alpha = 0.0°$ for the deformed and the undeformed airfoil. From figure 5.12b it is also observed that the differences, in terms of the skin friction coefficient, between the deformed and the undeformed airfoil are small. No separation occurs at this Mach number and angle of attack.

Chapter 6

Steady Flow Simulations with the Original CAST-10 Airfoil

In this chapter the results obtained from steady flow simulations with fixed and free boundary layer transition will be shown and discussed. The simulations that have been performed vary in freestream conditions, that is, Mach number and angle of attack. The original CAST-10 airfoil has been used for these simulations. First, the general set-up of the CFD simulations is described, after which results obtained from simulations with both CFD codes are shown. Next, some peculiarities in the lift and moment coefficient polars are discussed. Finally, the results of quasi-steady flow simulations that have been performed in order to find the Mach number at which the lift curve slope has a maximum, are displayed and discussed.

6.1 General set-up

This section shows the general set-up of the steady flow simulations. The mesh that has been used for these simulations is shown in figure 6.1. This mesh is very similar to the mesh used in the deformation study, except that now the original CAST-10 airfoil has been used. Furthermore, now 100 hexahedra layers are present and the y^+-value has been changed as well as the stretching factor. The mesh properties of the mesh used can be seen from table 6.1. A mesh independency study that has been performed has confirmed that this mesh gives mesh independent results. Appendix D can be consulted for more details.

First cell height	0.00168970722 mm ($y^+ = 1/2$)
Number of structured layers	100
Stretching factor of structured part	1.063156
Length of cells on airfoil surface	1 mm
Length of cells at leading/trailing edge	0.1 mm
Stretching ratio of unstructered part	1.78

Table 6.1: Default grid settings

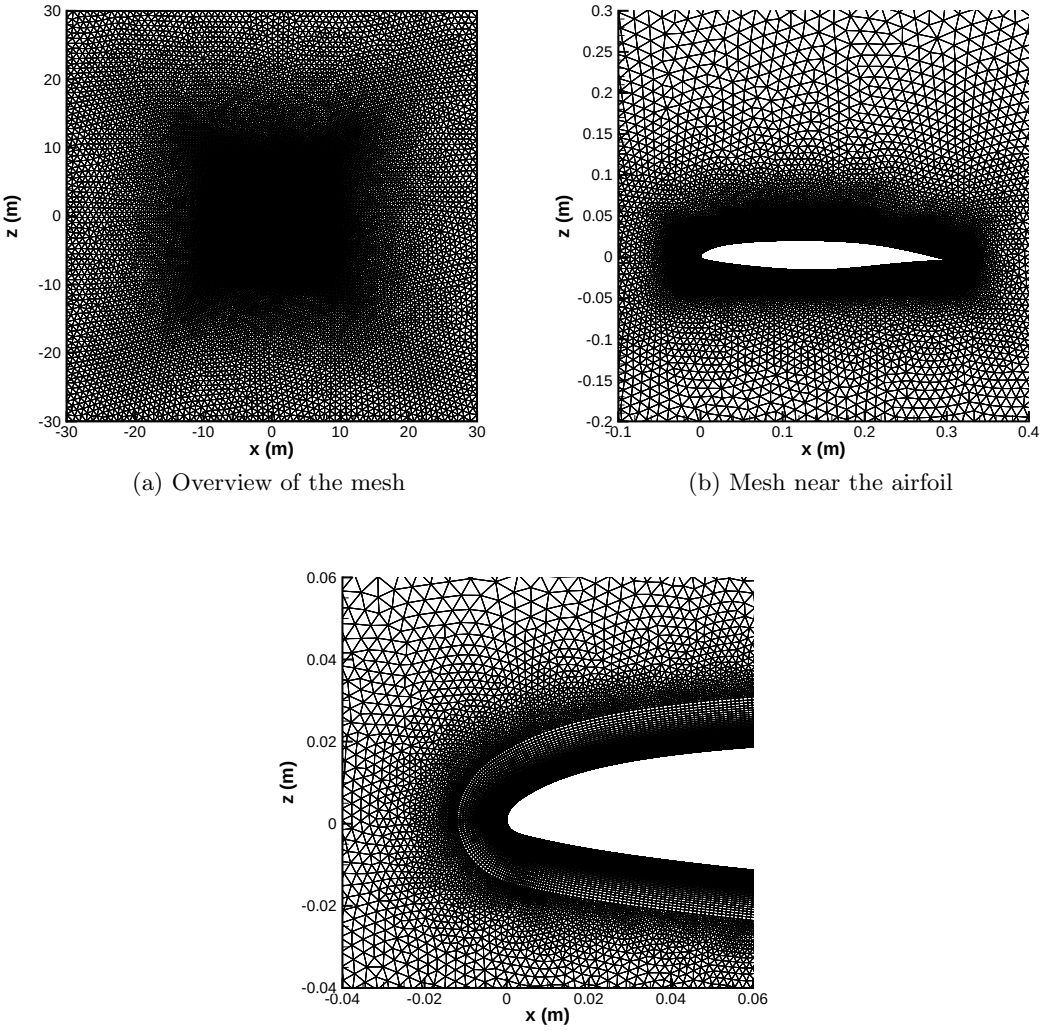

(a) Overview of the mesh

(b) Mesh near the airfoil

(c) Details of hexahedra layer near the leading edge

Figure 6.1: Computational mesh used for the CFD simulations with the original CAST-10 airfoil

The total number of mesh points is 220388 for the current mesh. As can be seen from figure 5.4a the farfield boundary is modelled by a box with dimensions 30 m times 30 m

(100 times the chord length away from the airfoil). In CFX the mesh is 0.6 m in spanwise (y) direction. It consists however of only one cell in spanwise direction as in TAU.

The boundary conditions at the farfield boundary have been set to farfield boundary conditions in the TAU, whereas inlet and outlet boundary conditions were used in CFX. If the angle of attack was equal to zero, only the left face was set as inlet and the right face as outlet, then the top and bottom boundaries of the simulation domain were set as freeslip walls. In case of a positive angle of attack, the bottom boundary also needs to be an inlet, whereas the top boundary has to be an outlet. For negative angles of attack the inlet and outlet boundary conditions at the top and bottom of the farfield boundary should be set the other way around (i.e. the bottom is an outlet and the top boundary is an inlet). Symmetry boundary conditions have been applied at the sides of the simulation domain in both codes.

The turbulence model that has been used in all simulations is the Menter SST model. For spatial discretisation, the second order upwind scheme has been used, which is accomplished by a flux vector of the type AUSDMV in TAU and the high-resolution scheme in CFX. The DLR TAU code used the local timestepping method, whereas in ANSYS CFX global timestepping is used. The temporal discretisation scheme that has been used to integrate in pseudo-time is the first order Backward Euler scheme.

For the transitional simulations the e^N-method was used in TAU, whereas the $Re_\theta - \gamma$-model was used in CFX. The critical N-factor has been set to 10. This value is based on validation work performed by G. Voss [2011]. In CFX the turbulence intensity together with the eddy viscosity ratio μ_t/μ_l have to be specified at the inlet. Using $Tu_{\text{inlet}} = 0.079\%$ and $(\mu_t/\mu)_{\text{inlet}} = 10$ in equation 4.23 leads to a turbulence intensity level of 0.05% at the airfoil's leading edge, which is equivalent to an N-factor of 10 (see equation 2.14). The value turbulence intensity at the leading edge of the airfoil has been checked a-posteriori in CFX. It was indeed observed to be 0.05%.

The Reynolds number has been set to $2 \cdot 10^6$ in all simulations. The temperature is 273.15 K.

6.2 Fully turbulent simulations

6.2.1 Pressure and skin friction distributions

Figure 6.2 shows the pressure distributions and skin friction coefficient distributions on the CAST-10 airfoil for $M = 0.5$ at an angle of attack of zero degree. Distributions obtained with both CFD codes are shown, the blue (continous) lines show the results obtained with the DLR TAU code, whereas the red (dashed) lines show the results from ANSYS CFX.

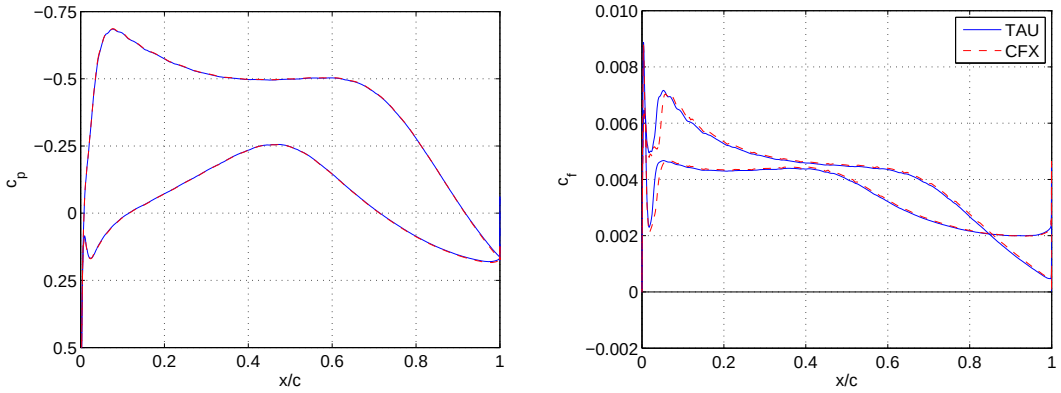

(a) Pressure distribution, $M = 0.5$

(b) Skin friction distribution, $M = 0.5$

Figure 6.2: Pressure and skin friction distributions on the CAST-10 airfoil with a fully turbulent boundary layer at $M = 0.5$ and $\alpha = 0°$

From these figures it can be seen that the agreement between the pressure distributions of both CFD codes is excellent. For the skin friction distribution the agreement between both CFD codes is also good, except near the leading edge. Although the flow should be fully turbulent, the turbulence model predicts some laminar flow near the leading edge, with very early transition. This can be seen from the increase in c_f near the leading edge. The location of this increase is however slightly different for both CFD codes. The prediction of an transition point located near the leading edge is common feature of low Reynolds number turbulence models. After the early transition of the boundary layer, the agreement of c_f between both CFD codes is however excellent. The skin friction distribution contains some very small oscillations, these are however present for both CFD codes and might be caused by the mesh.

Figure 6.3 shows the pressure and skin friction distributions of the CAST-10 airfoil at two transonic Mach numbers ($M = 0.755$ and $M = 0.765$) and zero degree angle of attack. From these figures it can be seen that the flow over the airfoil becomes transonic, that is, one or more shock waves are present on the airfoil. TAU predicts a double shock system when $M = 0.755$, whereas CFX predicts only one shock. The locations of these shocks are of course different for both codes. The skin friction coefficient distribution is also clearly different for both codes at $M = 0.755$, both codes predict however a local minimum in skin friction at the position of the shock. This minimum is more pronounced for the DLR TAU code. For the higher Mach number ($M = 0.765$) only one shock wave is present, the location of this shock differs by about 3% between the CFD codes. This difference is however small (approximately 3% of the chord length). Furthermore, the pressure distributions at both Mach numbers are identical on the lower surface of the airfoil and also in the region in front and behind of the shock on the upper surface. The same holds for the skin friction distribution (except near the leading edge). For $M = 0.765$ a very small separated region is present at the upper surface of the airfoil near the trailing edge.

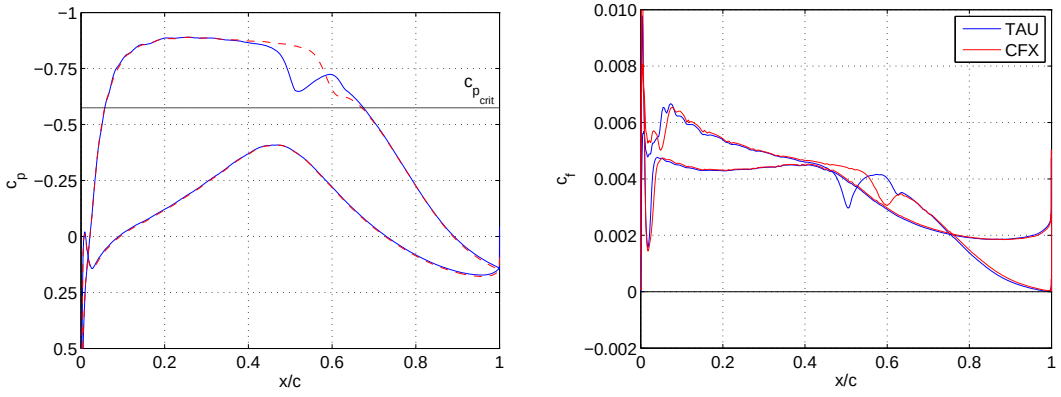

(a) Pressure distribution, $M = 0.755$

(b) Skin friction distribution, $M = 0.755$

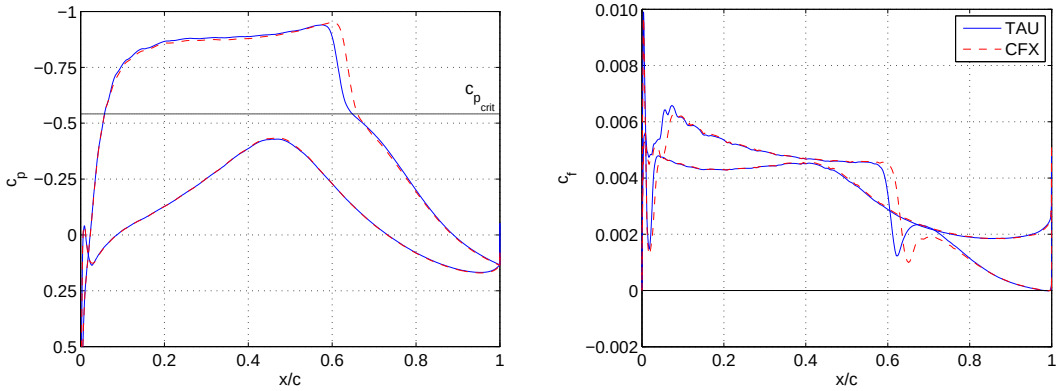

(c) Pressure distribution, $M = 0.765$

(d) Skin friction distribution, $M = 0.765$

Figure 6.3: Pressure and skin friction distributions on the CAST-10 airfoil with a fully turbulent boundary layer at $M = 0.755$ and $M = 0.765$ and $\alpha = 0°$

At $M = 0.8$ the flow starts to separate from the upper surface of the airfoil. Figure 6.4 shows the pressure and skin friction distributions at this Mach number and at $\alpha = 0°$. Figure 6.4a shows that at $M = 0.8$ there is a shock on both upper and lower surface of the airfoil. The position of the shock waves is slightly different for both CFD codes (less than 1% of the chord length). Both in front of and behind the shock waves the agreement in pressure distribution is however excellent. The skin friction distribution shows that the flow at the upper surface separates at the location of the shock wave. The separation area extends towards the trailing edge. In the skin friction distribution the same small difference can be seen between the results of both CFD codes.

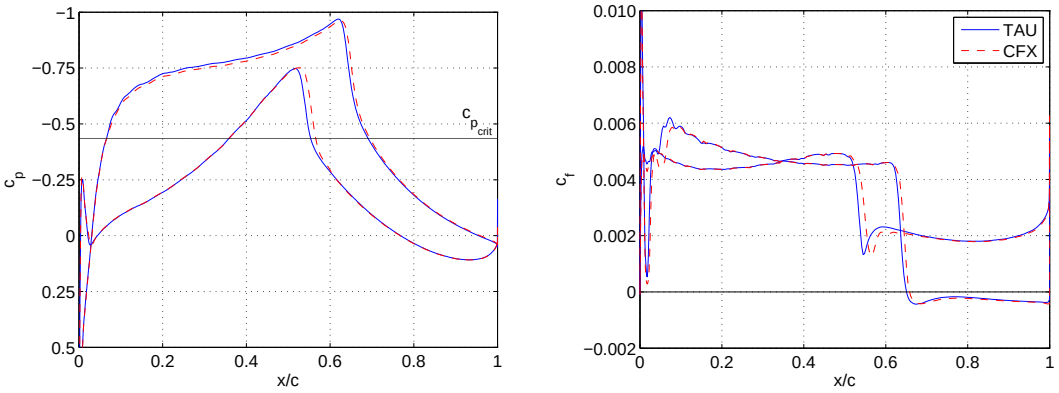

(a) Pressure distribution, $M = 0.8$

(b) Skin friction distribution, $M = 0.8$

Figure 6.4: Pressure and skin friction distributions on the CAST-10 airfoil with a fully turbulent boundary layer at $M = 0.8$ and $\alpha = 0°$

6.2.2 Force and moment coefficients

The force and moment coefficients corresponding to the pressure and skin friction distributions shown above are shown in table 6.2 for both CFD codes. It can be observed from this table that the coefficients, obtained from both CFD codes, are very close to each other. However, they are not identical, not even for $M = 0.5$, where the pressure distributions were identical (the skin friction distributions showed however some deviations, see figure 6.2b). At this Mach number the lift and moment coefficient show a difference of approximately 0.5%, whereas the drag coefficient shows a difference of 3%. The largest differences are present between the moment coefficients (up to 47% at $M = 0.755$). This can be explained by the fact that there is small difference in shock locations between both CFD codes. This small change causes however a large change in moment coefficient, because the moment arm to the quarter-chord point is large.

	TAU			CFX		
M	c_l	c_d	c_{m_y}	c_l	c_d	c_{m_y}
0.5	0.36555	0.010817	-0.060691	0.367418	0.0105493	-0.0610151
0.755	0.448536	0.013211	-0.067994	0.462884	0.013172	-0.071178
0.765	0.45576	0.014378	-0.071673	0.459375	0.0149961	-0.0743592
0.8	0.31377	0.023841	-0.062909	0.305904	0.0249254	-0.0632672

Table 6.2: Force and moment coefficients for the CAST-10 airfoil at different Mach numbers and $\alpha = 0°$ (fully turbulent)

The pressure and skin friction distributions as well as the force and moment coefficients at $M = 0.745$, $M = 0.75$ and $M = 0.76$ can be found in Appendix F.

6.3 Free transition simulations

6.3.1 Pressure and skin friction distributions

Figure 6.5 shows the pressure distributions and skin friction coefficient distributions on the CAST-10 airfoil at $M = 0.65$ at an angle of attack of zero degree with a fully turbulent boundary layer as well as with free boundary layer transition. Distributions obtained with both CFD codes are shown, the blue lines show the results obtained with the DLR TAU code, the dark blue line shows a fully turbulent boundary layer, whereas the lighter blue line shows free boundary layer transition. The red and orange lines show the results from ANSYS CFX with a fully turbulent boundary layer and with free boundary layer transition, respectively. In the c_f-distribution, the continuous lines indicate the upper surface and the dashed lines indicate the lower surface.

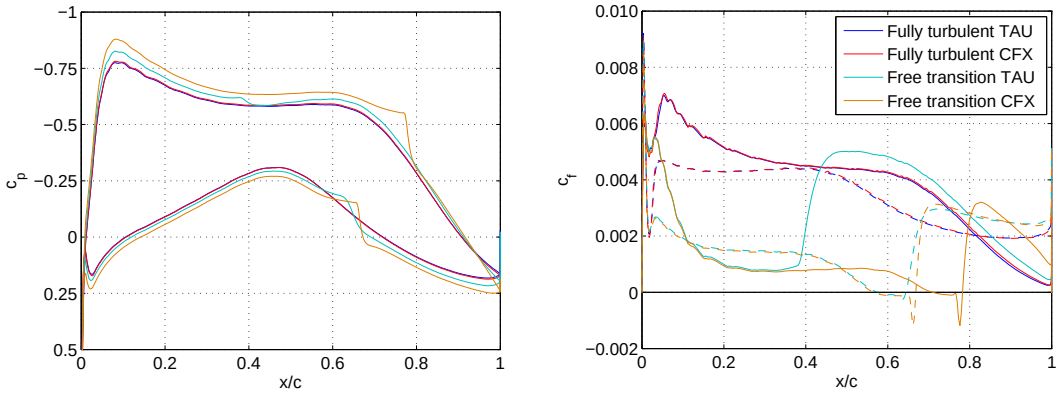

(a) Pressure distribution, $M = 0.65$

(b) Skin friction distribution, $M = 0.65$

Figure 6.5: Pressure and skin friction distributions on the CAST-10 airfoil with a fully turbulent boundary layer transition and with free boundary layer transition at $M = 0.65$ and $\alpha = 0°$

From these figures it can be seen that the agreement between the pressure and skin friction distributions obtained from both CFD codes is excellent when the boundary layer is fully turbulent. No separation is observed from the skin friction coefficient distribution of the fully turbulent boundary layer and no shock is present on the airfoil for both Mach numbers.

In case of free boundary layer transition there are some clear differences between both CFD codes. From the pressure distribution it can be seen that the pressure is lower on the upper surface and higher on the lower surface for the ANSYS CFX code. Hence, the lift obtained from the ANSYS CFX code will be higher. Upon comparing to the fully turbulent pressure distributions, one observes the same phenomenum. Apart from this higher lift, the deviations are small. There are some small increases in pressure indicating the transition locations, these can be seen more clearly from the skin friction distribution. From figure 6.5b it can be seen that on the upper surface, transition is predicted much further upstream by the DLR TAU code in comparison to the ANSYS CFX code (for TAU at approximately 38% and for CFX at about 78%). Furthermore, CFX predicts

a separation bubble and TAU does not. A possible explanation for these deviations in transition locations is that for the $Re_\theta - \gamma$-model used in the CFX code empirical correlations are necessary (see section 2.3.3). The empirical correlations implemented in CFX are however calibrated for a turbomachinery flow and might therefore not lead to correct results when applied to case of external flows. On the lower surface, the transition locations obtained with both codes are however very close and both codes predict transition through a separation bubble. Before transition occurs the skin friction distributions obtained from both CFD codes show however excellent agreement.

Figure 6.6 shows the pressure and skin friction distributions of the CAST-10 airfoil obtained with a fully turbulent boundary as well as with free boundary layer transition at two transonic Mach numbers ($M = 0.74$ and $M = 0.745$) and zero degree angle of attack.

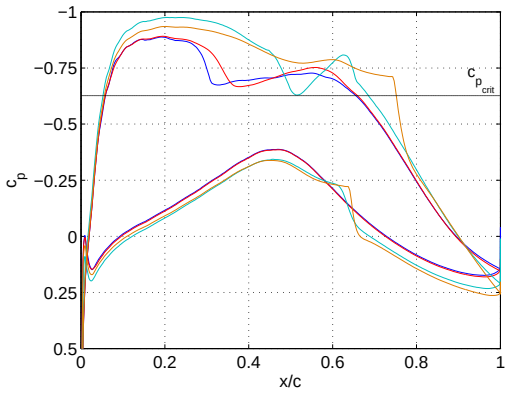

(a) Pressure distribution, $M = 0.74$

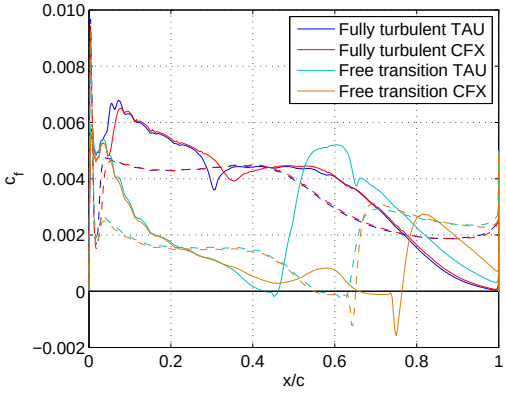

(b) Skin friction distribution, $M = 0.74$

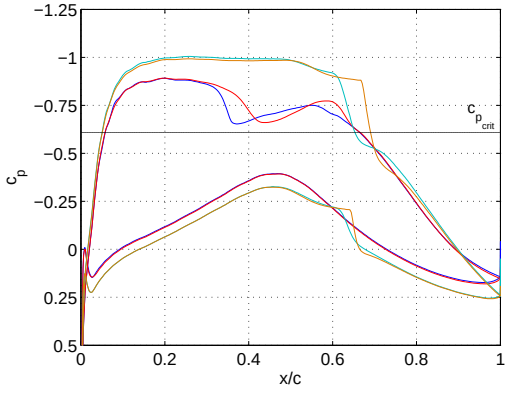

(c) Pressure distribution, $M = 0.745$

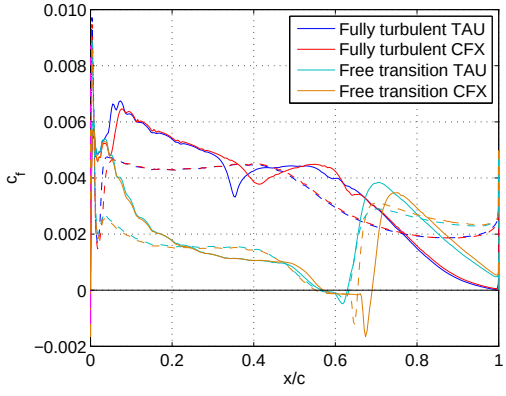

(d) Skin friction distribution, $M = 0.745$

Figure 6.6: Pressure and skin friction distributions on the CAST-10 airfoil with a fully turbulent boundary layer and with free boundary layer transition at $M = 0.74$ and $M = 0.745$ and $\alpha = 0°$

From these figures it can be seen that the flow over the airfoil is transonic, that is, the pressure on the upper surface is lower than the critical pressure. Hence, in order to recompress the air, one or more shock waves are present on the airfoil. When the flow is

fully turbulent both CFD codes predict a large low pressure region on the upper surface of the airfoil. In all cases there is a first shock between $x/c = 0.25$ and $x/c = 0.4$. This shock is however not strong enough to recompress the air completely, hence the flow stays supersonic and expands, after which it is recompressed by a very weak shock or no shock at all. The locations of the shock(s) is different for both codes. Therefore, the skin friction coefficient distribution is also clearly different for both codes.

In case of free boundary layer transition it can be seen that at $M = 0.74$ two weak shocks are predicted by TAU, whereas CFX predicts a pressure increase with a very small gradient after which the flow expands and then recompresses through a strong shock wave around $x/c = 0.75$. When looking at the skin friction distribution it is again observed, as in the subsonic case, that the transition location on the upper surface predicted by TAU is at approximately 45% of the chord length, whereas that predicted by CFX is at 75% of the chord length. Furthermore, TAU predicts a very small separation bubble, whereas CFX shows a much larger separation bubble, which can be explained by the fact that CFX predicts a stronger shock wave. However, at the lower surface the transition locations obtained with both CFD codes are closer to each other.

For the larger Mach number, both TAU and CFX predict a strong shock wave in case of free boundary layer transition. The position of the shock is however slightly different (5% of the chord length). On the lower surface excellent agreement is obtained between the results from both codes. As can be seen from figure 6.6c the transition location obtained with both codes shows good agreement, when the deviation in shock location is taken into account. This shows that, in this case, the location of transition onset is fixed by the shock wave. Therefore, when the shock wave locations obtained with both CFD codes match, then the transition locations will match as well.

It can be seen that the location of the shock(s) is more downstream in case of free boundary layer transition, as was found in literature (see section 2.2.2). Furthermore, in case of free boundary layer transition the skin friction coefficient distribution has a much lower level than in case of a fully turbulent boundary layer (the difference is more than 50% from $x/c > 0.1$ until transition onset). After transition, the differences in skin friction coefficient between the fixed and free transition results become less, as expected. Another difference is that the boundary layer separates on both upper and lower surface in case of free boundary layer transition, this does not happen in case of a fully turbulent boundary layer, not even at $M = 0.8$ (see figure 6.4b).

6.3.2 Force and moment coefficients

The force and moment coefficients at the three Mach numbers shown here are depicted in table 6.3.

	TAU			CFX		
	Fully turbulent					
M	c_l	c_d	c_{m_y}	c_l	c_d	c_{m_y}
0.65	0.399890	0.011436	-0.064621	0.404711	0.011228	-0.065491
0.74	0.433617	0.012740	-0.066644	0.445638	0.012562	-0.068711
0.745	0.437437	0.012891	-0.066857	0.449799	0.012757	-0.069065
	Free transition					
M	c_l	c_d	c_{m_y}	c_l	c_d	c_{m_y}
0.65	0.443157	0.0075175	-0.073493	0.499917	0.0056254	-0.095619
0.74	0.545471	0.007997	-0.085340	0.5554	0.009603	-0.10944
0.745	0.611251	0.007235	-0.097169	0.616856	0.007790	-0.110397

Table 6.3: Force and moment coefficients for the CAST-10 airfoil at different Mach numbers and $\alpha = 0°$

From this table it can be observed that when the results of the fully turbulent simulations are compared to those with free boundary layer transition, the lift coefficient is higher (typical between 11-28%), the drag coefficient is lower (between 24-50%) and the moment coefficient is lower as well for the free transition case (approximately 12-37%). This holds for both CFD codes. This is consistent with the pressure and skin friction distributions. The differences between the results obtained with both codes are of course also visible as pointed out earlier.

The pressure and skin friction distributions as well as the force and moment coefficients obtained from simulations with free boundary layer transition at $M = 0.74125$, $M = 0.741875$ and $M = 0.75$ and $\alpha = 0°$ can be found in Appendix F.

6.3.3 Peculiarities in lift and moment coefficient polars

In case of free boundary layer transition some peculiarities were observed in the lift coefficient versus angle of attack graphs for almost all Mach numbers. Figure 6.7 shows an example of a lift and moment coefficient versus angle of attack graph at several of Mach numbers obtained with TAU and with CFX. It should be noted that for some Mach number and angle of attack combinations the transition prediction module of the DLR TAU code failed to convergence. The results of these simulations have therefore not been included. In addition to this, for some Mach number-angle of attack combinations the transition location kept on oscillating between two cells of the grid, that is, over 1 mm. Simulations exhibiting this behaviour have been treated as converged. The mean values of the transition location as well as the mean values of the force and moment coefficient have been used in that case. The convergence of simulations with free transition in CFX was also bad, the results shown here are however converged.

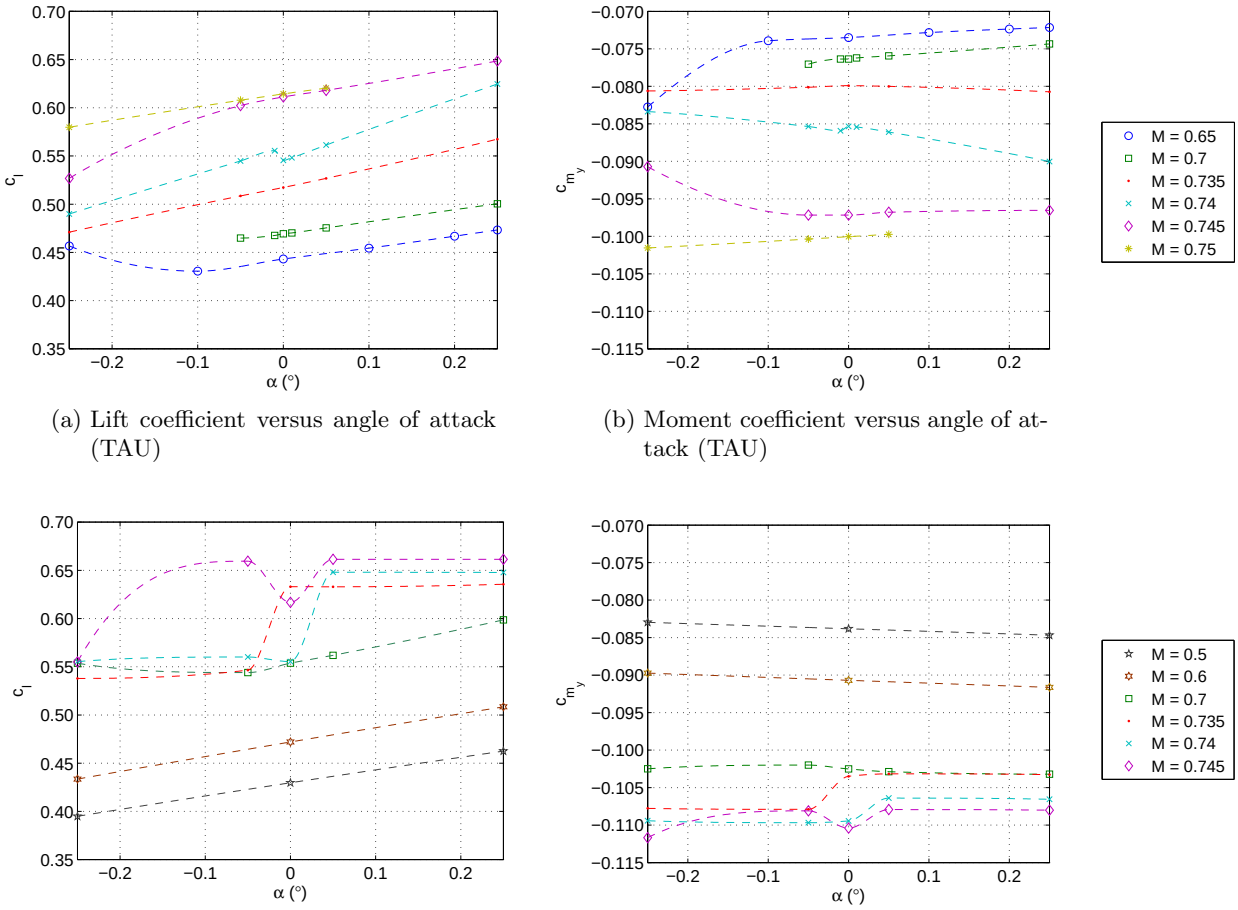

(a) Lift coefficient versus angle of attack (TAU)

(b) Moment coefficient versus angle of attack (TAU)

(c) Lift coefficient versus angle of attack (CFX)

(d) Moment coefficient versus angle of attack (CFX)

Figure 6.7: Lift and moment coefficient versus angle of attack for several Mach numbers obtained from TAU and CFX (free boundary layer transition)

As can be seen from these figures the behaviour of the lift coefficient is highly non-linear for $M = 0.65$, $M = 0.74$ and $M = 0.745$ for TAU. For $M = 0.65$ and $M = 0.745$ this non-linear behaviour is present for angles of attack smaller than zero degree, whereas for $M = 0.74$ it is present around zero angle of attack. From the simulations with CFX it can be observed that this non-linear behaviour is also present around zero angle of attack at all transonic Mach numbers. At $M = 0.7$ the non-linear behaviour is present for lower angles of attack. From figure 6.7b it is observed that all Mach numbers show a strongly non-linear behaviour and therefore no $dc_{m_y}/d\alpha\big|_{\alpha=0°}$ at $\alpha = 0°$ can be determined by finite differences. Figure 6.7d shows however a linear behaviour for $M = 0.5$ and $M = 0.6$. From the fully turbulent simulations performed with both codes it was observed that the behaviour of both lift and moment coefficient is linear for the range of angles of attack considered here ($\alpha = -0.25°$ till $\alpha = 0.25°$). The non-linear behaviour of the lift coefficient as well as the differences between TAU and CFX can be explained from the transition locations on the airfoil. Figure 6.8 shows these transition locations as function of the angle of attack for the same Mach numbers as the lift and moment coefficients. It should

be noted that the transition onset location depicted here is determined automatically by TAU, upon observing the skin friction distribution it was found that this location is inside the separation bubble. When no separation bubble is present, then it is taken to be just in front of the c_f increase. The transition onset location is not automatically determined in CFX, therefore the location at which the skin friction coefficient is minimum has been plotted in figures 6.8b and 6.8c, since CFX predicts a separation bubble for all the testcases used in this thesis, this transition onset location is always located inside the separation bubble.

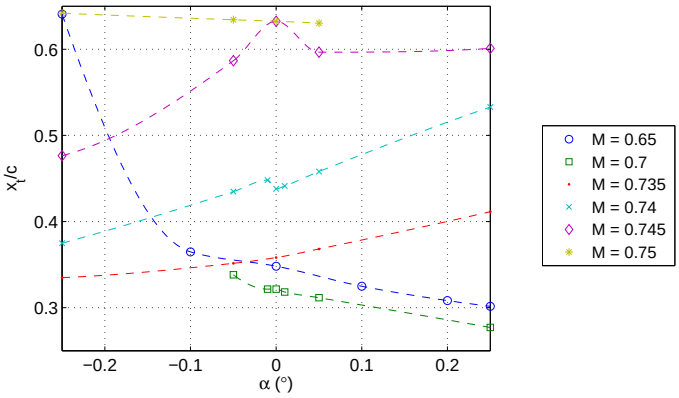

(a) Upper surface (TAU)

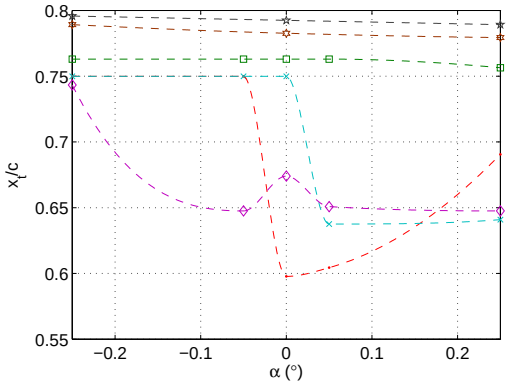

(b) Upper surface (CFX)

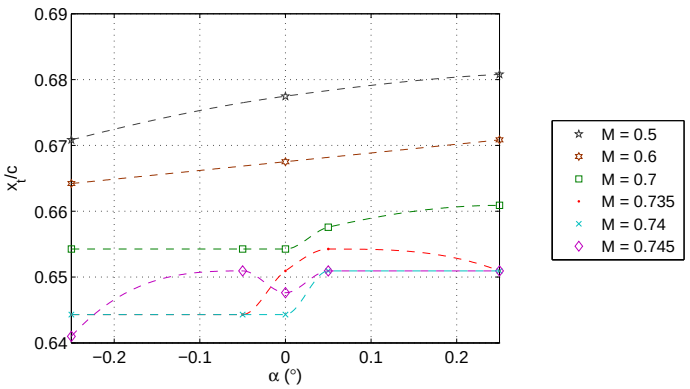

(c) Lower surface (CFX)

Figure 6.8: Transition locations on the CAST-10 airfoil versus angle of attack for several Mach numbers obtained

From figure 6.8a it can be seen that at $M = 0.65$, $M = 0.74$ and $M = 0.745$ the transition location on the upper surface obtained from TAU shifts over a large distance, especially for $M = 0.65$ it moves from $x/c = 0.64$ to $x/c = 0.36$ approximately. The transition location at the lower surface obtained from TAU was found to have almost no influence on the lift coefficient, since it was relatively constant for the angle of attack range considered here. This is probably caused by the double curvature at the lower surface. From CFX, the variations in transition location as a function of the angle of attack are more severe, as CFX predicts a much further aft transition location on the upper surface

and the transition location on the lower surface is not fixed with angle of attack and Mach number (its variation is however small, up to approximately 5% of the chord length). When looking at the transition locations at $M = 0.74$ obtained from CFX for example, it is observed that at $\alpha = -0.05°$ and $0°$ the transition location on the upper surface is located behind that of the lower surface, whereas at $\alpha = 0.05°$ the transition location at the lower surface is further downstream than that of the upper surface. This is reflected in the lift coefficient versus angle of attack curve, figure 6.7c, as the lift coefficient increases from $\alpha = 0°$ to $\alpha = 0.05°$. An explanation for the differences in the behaviour of the transition location(s) obtained from both CFD codes might be the empirical correlations used in the ANSYS CFX code, as noted earlier. Further investigations need to clarify this aspect.

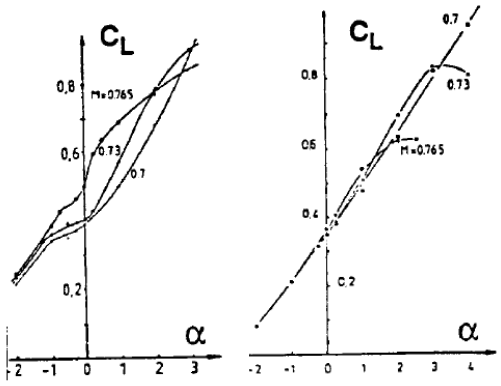

(a) Free transition (b) Fixed transition

Figure 6.9: Lift coefficient versus angle of attack at free and fixed transition for several Mach numbers (Blanchard & J.F. Breil [1989])

The non-linear behaviour of the lift and moment coefficient in case of free boundary layer transition has also been observed from experiments performed with the CAST-10 airfoil (Blanchard & J.F. Breil [1989]). Figure 6.9 shows the lift coefficient versus angle of attack at three Mach numbers: $M = 0.7$, $M = 0.73$ and $M = 0.765$ both with natural transition as well as with fixed transition (transition strips at $x/c = 0.05$). The Reynolds number was $4 \cdot 10^6$ and the turbulence level was 0.1%. The behaviour of the lift coefficient is clearly non-linear. The same effect was also observed by Stanewsky [1974] for the CAST-10 and the CAST-12 airfoil.

6.4 Quasi-steady determination of the transonic dip

As was noted in section 3.2 trends in the flutter boundary can already be observed from quasi-steady flow simulations. Therefore, the lift-curve slope at an angle of attack of $0°$ has been determined by the use of finite differences. In order to do so simulations at two angles of attack ($\alpha = 0.25°$ and $\alpha = -0.25°$) have been performed. This has been done

for several Mach numbers. Results of this approach are depicted in figure 6.10, which shows the lift-curve slope $dc_l/d\alpha$ at $\alpha = 0°$ versus the Mach number. Inside this figure some pressure distributions at $\alpha = 0°$ are shown as well. The blue (continuous) curves are results from TAU, whereas the red (dashed) curves are results from CFX. The dashed curves connecting the lift-curve slope points have been obtained by interpolation. The Prandtl-Glauert compressibility correction to the incompressible lift-curve slope of 0.11 per degree has also been included for reference.

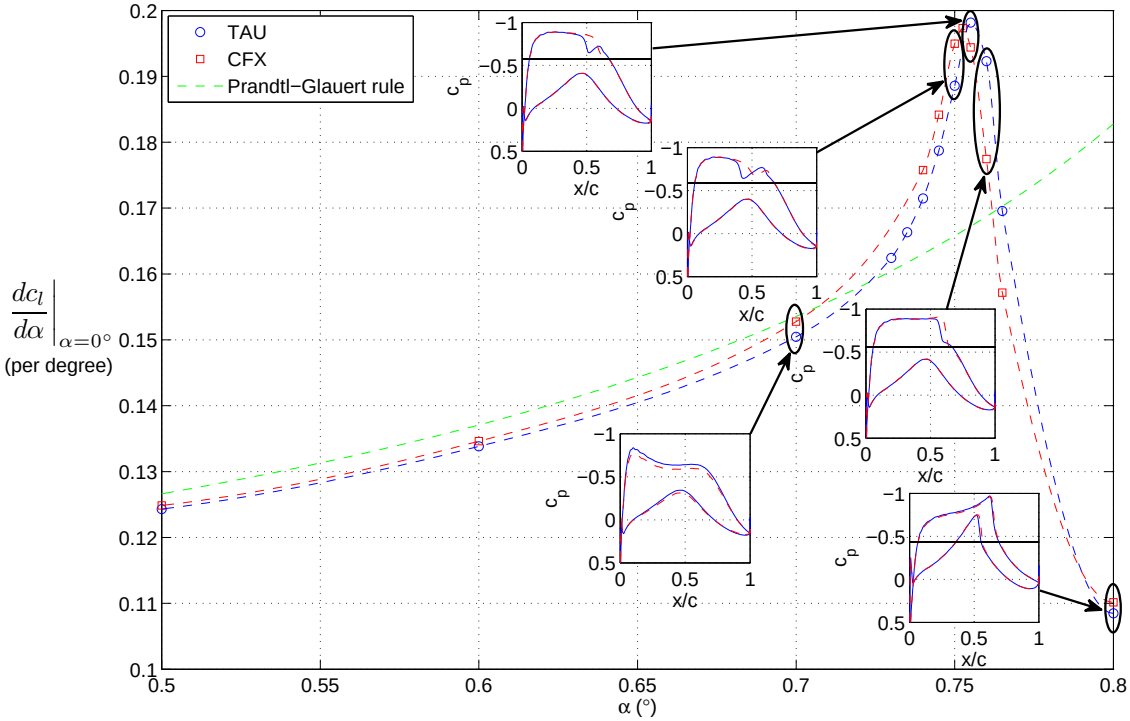

Figure 6.10: Quasi-steady lift curve slope versus Mach number (fully turbulent)

Figure 6.10 shows that there is a maximum in lift-curve slope at a Mach number of 0.755 for the DLR TAU code and at $M = 0.7525$ for the ANSYS CFX code. The curves obtained with both CFD codes are really close to each other. However, the curve obtained with CFX is shifted to the left a bit. The pressure distributions near the maximum lift-curve slope show a clear difference between TAU and CFX. However, for both codes there no strong shock is present at the maximum at $\alpha = 0°$. At $\alpha = 0.25°$ there is however a strong shock wave as can be seen from figure 6.11, which shows the pressure distributions at $\alpha = 0.25°$ and $\alpha = -0.25°$ at $M = 0.755$ obtained with TAU and at $M = 0.7525$ obtained with CFX.

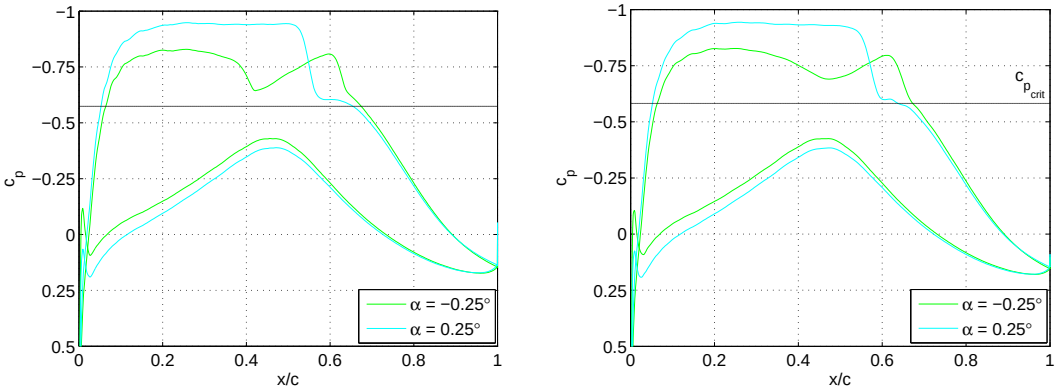

(a) $M = 0.755$ (TAU) (b) $M = 0.7525$ (CFX)

Figure 6.11: Pressure distribution at $\alpha = 0.25°$ and $\alpha = -0.25°$

The pressure distributions obtained from both CFD codes show that there are two weak shocks at $\alpha = -0.25°$. Hence, the area enclosed by the pressure distribution at $\alpha = -0.25°$ is much smaller than at $\alpha = 0.25°$, causing a large difference in lift and therefore a large lift-curve slope at the peak Mach number. At Mach numbers larger than the peak Mach number, a strong shock is present on the airfoil. Boundary layer separation only occurs for $M > 0.765$. It should furthermore be noted that the results of both CFD codes are below the Prandlt-Glauert compressibility correction for subsonic Mach numbers. Normally, the effect of compressibility is to increase the lift-curve slope. The trend towards the incompressible lift-curve slope of 2π per radian (= 0.11 per degree) is however present. At higher Mach numbers the lift-curve slope becomes however larger than the Prandtl-Glauert compressibility correction. For $M = 0.8$ the lift-curve slope becomes again less than that predicted by the Prandtl-Glauert correction. This is explained by the fact that shock-induced separation occurs behind the shock at this Mach number and the Prandtl-Glauert correction is for inviscid flow.

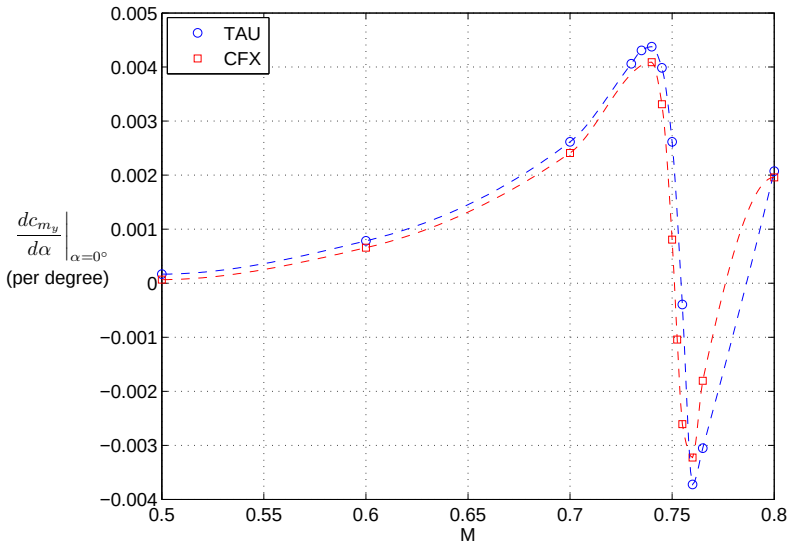

Figure 6.12: Quasi-steady moment curve slope versus Mach number (fully turbulent)

In the same way the derivative of the pitching moment coefficient with respect to the angle of attack $dc_{m_y}/d\alpha$ at $\alpha = 0°$ can be computed using finite differences. Figure 6.12 shows $dc_{m_y}/d\alpha\big|_{\alpha=0°}$ as a function of the Mach number. The dashed curves have been obtained by interpolation. The pitching moment slope curves shows a local maximum around $M = 0.74$ and then a local minimum at $M = 0.76$ for the results obtained with both CFD codes.

Quasi-steady flow simulations have also been performed with free boundary layer transition with both CFD codes. For these simulations the angles of attack $\alpha = 0.05°$ and $\alpha = -0.05°$ have been used, since the lift curve slope is very non-linear (see section 6.3.3). Figure 6.13 shows the lift curve slope at $\alpha = 0°$ versus Mach number for simulations with both a fully turbulent boundary layer as well as with free boundary layer transition for both CFD codes. The dark blue and red symbols are the results of the fully turbulent simulations with TAU and CFX, respectively. The light blue and the orange symbols show the results of the simulations with free boundary layer transition from TAU and CFX, respectively. The Prandtl-Glauert compressibility correction to the incompressible lift-curve slope of 0.11 per degree has also been included for reference. The dashed curves connecting the lift curve slope points have been obtained by interpolation. The pressure distribution at $\alpha = 0°$ of the simulations with free transition have also been included.

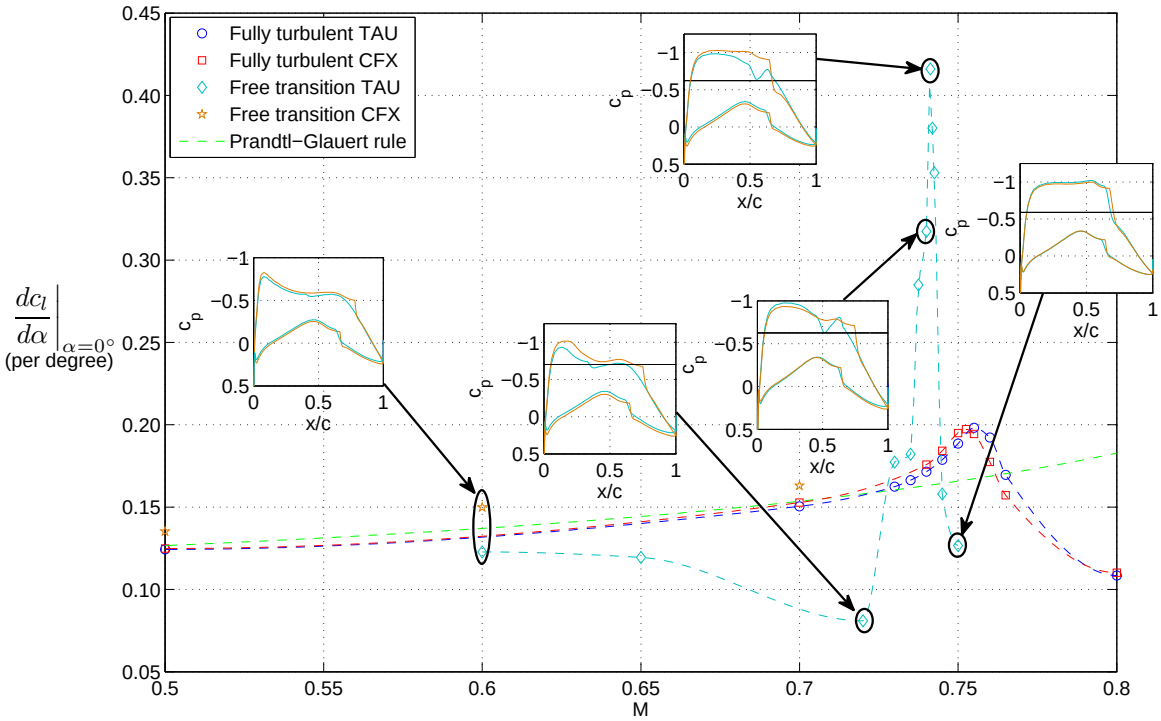

Figure 6.13: Quasi-steady lift curve slope versus Mach number

It should be noted that for some Mach numbers ($M = 0.6$, $M = 0.7375$, $M = 0.74$ and $M = 0.74125$) the lift-curve slope was obtained by taking the forward difference instead of a finite difference. Furthermore, only the results at subsonic Mach numbers of the CFX code have been included, since it was not possible to use finite differences to obtain

the lift-curve slope at higher Mach numbers. From figure 6.13 it is observed that the peak in lift-curve slope is much higher in case of free boundary layer transition (more than twice as high). Furthermore, it is located at $M = 0.74125$, whereas the peak in the fully turbulent curve is located at $M = 0.755$ (for TAU). From figure 6.6 it could be seen that in case of free transition, a strong shock is present at lower Mach numbers than when the transition is fixed at the leading edge. In addition to this it was observed from figure 6.11 that at the Mach number at which the peak in lift-curve slope occurs, there is a strong shock wave at the higher angle of attack and a weak shock wave at the lower angle of attack. This explains the behaviour of the lift-curve slope in case of free boundary layer transition, since a stronger shock occurs earlier in that case. The pressure- and skin friction distributions at $\alpha = 0.05°$ and $\alpha = -0.05°$ at the peak Mach number ($M = 0.74125$) are compared in figure 6.14.

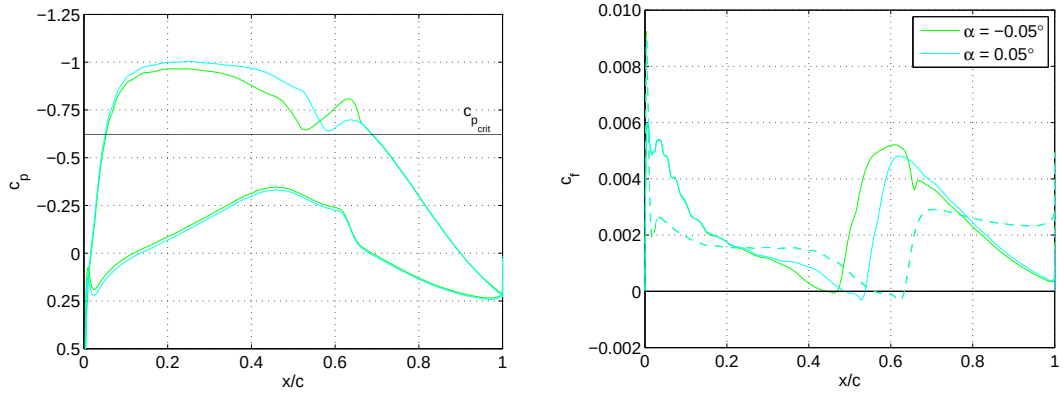

(a) Pressure distribution

(b) Skin friction distribution

Figure 6.14: Pressure and skin friction distributions at $M = 0.74125$ and $\alpha = -0.05°$ and $\alpha = 0.05°$ obtained with TAU

From figure 6.14a it can be seen that in this case there is no single strong shock pressure at the larger angle of attack, this is because now the angle of attack is only 0.05° and not 0.25°. At 0.25° a single strong shock is present at this Mach number. The difference in the pressure distributions at this Mach number is however the largest compared to that at other Mach numbers. From the skin friction distribution it is observed that the transition location is at the first shock for both angles of attack. Furthermore, for the smallest angle of attack there is a very small separation bubble at the upper surface, whereas for $\alpha = 0.05°$ this separation bubble is much larger.

The lift-curve slope versus Mach number with free boundary layer transition obtained with CFX shows a clearly different behaviour than that obtained with TAU. This can be explained by the fact that there are large differences in the transition location at the upper surface obtained with each of the CFD codes (see section 6.3).

Chapter 7

Unsteady Flow Simulations with the Original CAST-10 Airfoil

The aerodynamic coefficients needed to solve the equations of motion have been determined from unsteady flow simulations at several Mach numbers and reduced frequencies. In these simulations the airfoil was allowed to either pitch or plunge. This chapter shows the results obtained from the unsteady flow simulations. Since many simulations were performed in order to determine the flutter boundary, only a selection will be shown here. Unless otherwise indicated the results shown have been obtained with TAU. The remaining figures can be found in Appendix G. First, the general settings used for the unsteady flow simulations will be described. Then, results of the response of the airfoil in time are shown for one example as well as the lift and moment coefficient loops. An amplitude investigation has been performed, the results of this investigation are shown next. After that, the results are shown in the time and in the frequency domain. Finally, a comparison is made to results obtained with ANSYS CFX for some selected cases.

7.1 General set-up

For the unsteady flow simulations the same grid as for the steady flow simulations has been used. A grid independency study has been carried out as well, from which it was found that the differences between the grids were typically less than 10%, except for one particular grid. Appendix D shows gives more details about this grid independency study. The motion of airfoil has been implied via a rigid body motion in the DLR TAU code, that is, the whole grid is moved. In CFX mesh deformation is used to apply a motion to the airfoil. The boundary conditions are the same as in the steady case for the TAU code. For the CFX code, all inlet/outlet boundaries have been set as non-reflective boundary conditions in CFX, such that disturbances are not reflected at these boundaries.

The turbulence model, transition models and the spatial discretisation scheme that have been used are the same as for the steady flow simulations. For the discretisation in time

the second order backward differencing scheme has been used for the physical timestepping in both TAU and CFX, whereas the first order Backward Euler scheme has been used for the pseudo timestepping in both codes. The timestep that has been used for the physical timestepping is $\Delta t = 2.4792 \cdot 10^{-4}$. It has been determined based on a timestep independency study, which is shown in Appendix E. Actually, the number of timesteps per period has been determined, the timestep can then be obtained by dividing the time that one period lasts by the number of timesteps, i.e. $\Delta t = T/\text{NOTPP}$. The period T can however be computed from the angular velocity ω via: $T = 2\pi/\omega$, where the angular velocity is coupled to the reduced frequency k via $k = \frac{\omega c}{U_\infty}$. Rewriting leads to the following equation for the timestep Δt:

$$\Delta t = \frac{2\pi}{\text{NOTPP}} \frac{c}{kU_\infty} \tag{7.1}$$

This timestep size has been kept constant for all Mach numbers and reduced frequencies, such that for each testcase all physical effects are captured. In order to do so, the number of timesteps per period needs to be varied depending on Mach number and reduced frequency. Tables 7.1 and 7.2 give an overview of the number of timesteps used at each Mach number and reduced frequency for the fully turbulent and free transition flow simulations, respectively.

M	k					
	0.05	0.1	0.2	0.3	0.5	0.8
0.5	918	459	230	153	92	57
0.745	616	308	154	103	62	39
0.75	612	306	153	102	61	38
0.755	608	304	152	101	61	38
0.76	604	302	151	101	60	38
0.765	600	300	150	100	60	38
0.8	574	287	143	96	57	36

Table 7.1: Number of timesteps per period for each Mach number/reduced frequency combination (fully turbulent)

M	k				
	0.1	0.2	0.3	0.5	0.8
0.65	353	177	118	71	44
0.74	310	155	103	62	39
0.74125	310	155	103	62	39
0.741875	309	155	103	62	39
0.745	308	154	103	62	39
0.75	306	153	102	61	38

Table 7.2: Number of timesteps per period for each Mach number/reduced frequency combination (free transition)

Note that the numbers in this table have been rounded. For the integration in pseudo time a certain number of iterations is required as well. For all fully turbulent simulations 400 so-called inner iterations have been used, whereas for the simulations with free boundary layer transition 3200 inner iterations were used. These number have been determined based on the convergence of the lift and moment coefficient during each inner iteration (see Appendix E). Transition has been predicted once during each timestep, namely at the end of the timestep (when the number of inner iterations has reached 3200).

Two types of motion were applied to the airfoil, a pitching motion described by a sine wave and a plunging motion, in which the vertical movement of the airfoil is also described by a sine. The mean angle of attack is 0° and the amplitude of the pitching motion is 0.05°, whereas the mean value and the amplitude of the plunging motion are 0 m and $0.001c/k$,

respectively. The amplitude of the plunging motion varies with the reduced frequency, such that the effective angle of attack of the motion (which is given by kh_m/c, where h_m is the amplitude of the plunging motion) is constant and approximately equal to 0.06° and hence of the same order of magnitude as the amplitude of the pitching motion. Such small amplitudes have been selected in order to make sure that the airfoil's response is linear. These amplitudes have been determined from an amplitude investigation, which can be found in section 7.3.

The unsteady flow simulations have been performed for the Mach numbers as determined from the quasi-steady flow simulations (i.e. at $M = 0.5$, 0.745, 0.75, 0.755, 0.76, 0.765 and 0.8 for the fully turbulent simulations and at $M = 0.65$, 0.74, 0.74125, 0.741875, 0.745 and 0.75 in case of free boundary layer transition. The reduced frequencies have been chosen between 0.05 and 0.8, the spacing has however been increased near the frequency at which flutter is expected to occur. The reduced frequencies used are: $k =$ 0.05, 0.1, 0.2, 0.3, 0.5 and 0.8. For the simulations with free boundary layer transition the lowest reduced frequency ($k = 0.05$) has been left out, because the computational effort for this frequency was too large and it is furthermore expected that this reduced frequency is much smaller than that at which flutter occurs.

7.2 Unsteady lift and moment

First, the main characteristics of the unsteady forced motion induced aerodynamics are summarised. When the airfoil is pitching or plunging harmonically, the lift and moment coefficient will also show an harmonic response in time, when the amplitude of the motion is small enough. Figure 7.1 shows the lift and moment coefficient versus time (made non-dimensional by the period of the motion) for a pitching airfoil at $M = 0.765$ and $k = 0.20$ (for a fully turbulent boundary layer). The steady pressure distribution corresponding at $\alpha = 0°$ for this Mach number is shown in figure 6.3c.

From figure 7.1 it can be seen that both the lift and the moment coefficient show a harmonic behaviour. The maximum of the lift coefficient and that of the moment coefficient do however not occur at the maximum angle of attack. Hence, there is a phase shift between the motion of the airfoil and its response. In this case both the lift coefficient and the moment coefficient lag the motion of the airfoil behind.

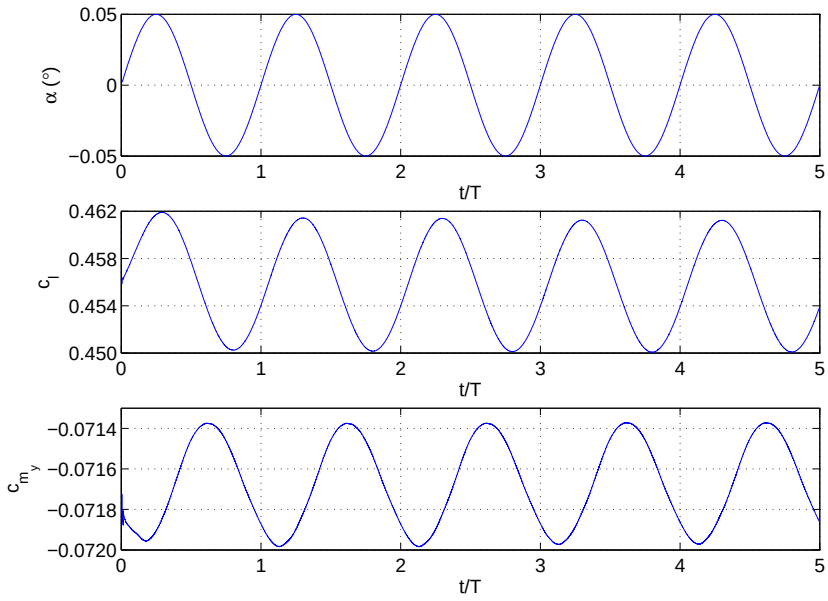

Figure 7.1: Angle of attack, lift coefficient and moment coefficient versus non-dimensional time (fully turbulent)

The lift and moment coefficient can also be plotted against the angle of attack as in case of non-moving airfoil (the so-called steady lift and moment polars). Figure 7.2 shows the lift and moment coefficients versus angle of attack for the pitching airfoil at $M = 0.765$ and $k = 0.20$. These curves are often referred to as "hysteresis loops". The arrows indicate in which direction the curves have to be followed.

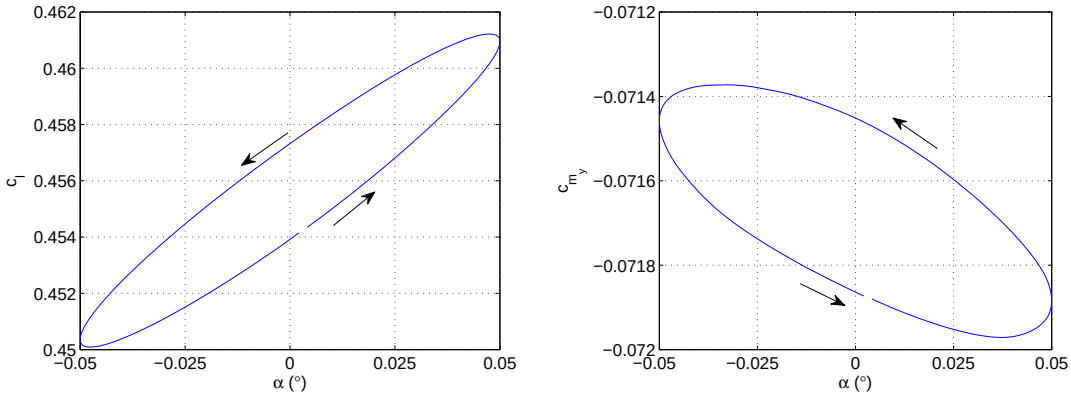

(a) Lift coefficient versus angle of attack

(b) Moment coefficient versus angle of attack

Figure 7.2: Lift and moment coefficient versus angle of attack for the pitching motion with $M = 0.765$ and $k = 0.20$ (fully turbulent)

From these figures it can be seen that the lift coefficient increases when the angle of attack increases and the moment coefficient decreases when α increases. When the angle

of attack has reached its maximum and decreases again, the lift coefficient first increases and then decreases and the moment coefficient increases again. The airfoil does not follow the same line as on its way up however. The lift coefficient at a certain angle of attack is higher when the airfoil is moving down, than when it is moving up. This is caused by the fact that the flow needs to adjust itself to a change in angle of attack, i.e. the when the airfoil is moving down the flow around it is such as if the airfoil was at a higher angle of attack in stationary flow. The moment coefficient is less negative when the airfoil is moving down.

7.2.1 Transition onset locations

When boundary layer transition is free, the location of transition onset is also expected to vary harmonically in time. Figure 7.3a shows the angle of attack of a pitching motion at $M = 0.74$, $k = 0.20$ and an amplitude of $0.05°$ versus the non-dimensional time. The transition locations on the upper and lower surface are also shown in time. The corresponding steady flow solution can be found in figure 6.6a. The transition location on the upper surface is seen to move harmonically in time, whereas the transition onset location on the lower surface does not change at all in time. Similar behaviour is observed at $M = 0.74125$, $M = 0.741875$ and $M = 0.745$, at the other reduced frequencies and for the plunging motion. This is probably caused by the fact that the amplitude of the pitching motion α_m is only $0.05°$ and hence this is not enough to change the transition location on the lower surface. For simulations with a higher amplitude ($0.25°$) it was observed that the transition location on the lower surface does change (see figure 7.3b). It varies stepwise however, an explanation for this behaviour is that the cells of the mesh used are 1 mm wide, i.e. that means in terms of the chord length the cells are $10\text{c}/3 \text{ mm} = 3.33 \cdot 10^{-3} \cdot \text{c m}$ wide. Hence, when the transition location movement is smaller than this width it will not be captured by the mesh.

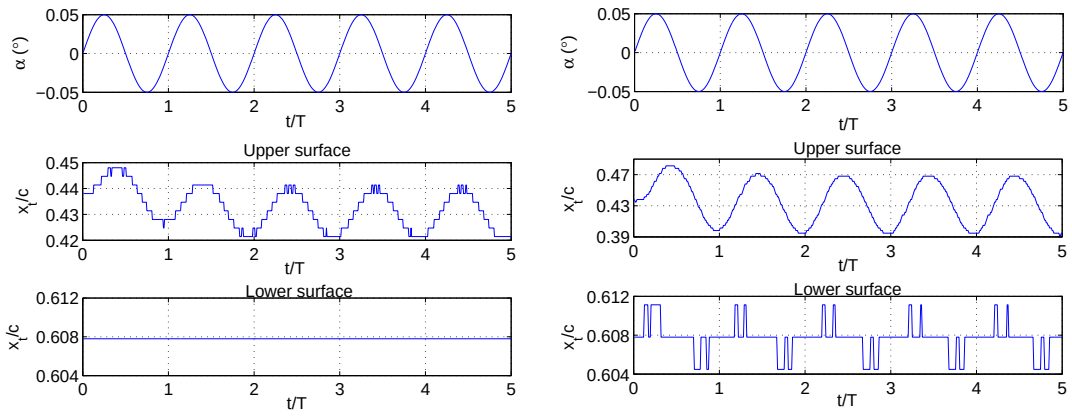

(a) $\alpha_m = 0.05°$ (b) $\alpha_m = 0.25°$

Figure 7.3: Angle of attack, transition onset locations on upper and lower surface versus non-dimensional time at $M = 0.74$ and $k = 0.20$ (free transition)

The harmonic variation of the transition location on the upper surface of the airfoil is coupled to the motion of the shock waves on the upper surface. At $M = 0.74$ two shocks

wave are present at the upper surface, transition occurs at the foot of the first shock. This can be observed from figure 7.4, which shows pressure distributions at different instants in time for the pitching motion with an amplitude of 0.05° at $M = 0.74$, $k = 0.20$.

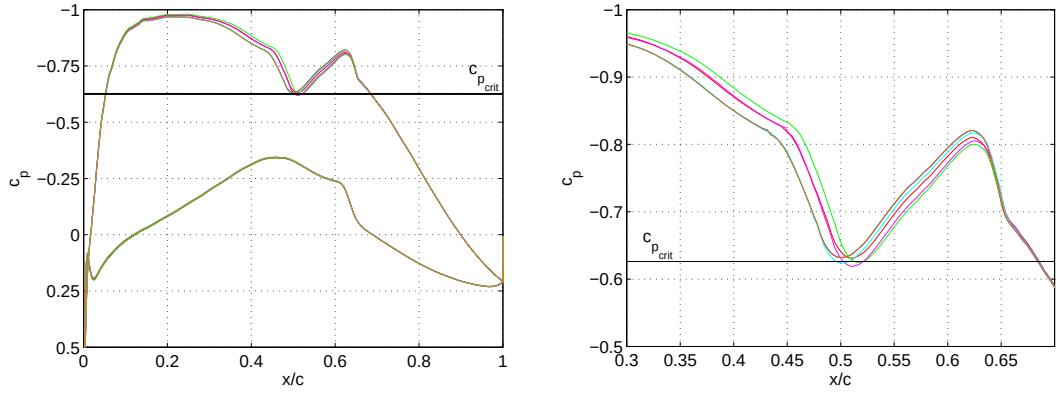

(a) Overview (b) Zoom

Figure 7.4: Pressure distributions at several time instants at $M = 0.74$, $k = 0.20$ and $\alpha_m = 0.05°$ (free transition)

Figure 7.5 shows the transition location history at $M = 0.65$ and $M = 0.75$. From these figures it can be observed that the transition location on the lower surface does change for both Mach numbers, not harmonically however, but stepwise. Similar behaviour is observed for other reduced frequencies and for the plunging motion. Furthermore, at $M = 0.75$ the transition location on the upper surface also varies stepwise. Hence, the change in transition location is too small to be completely captured by the mesh as for $M = 0.74$, $k = 0.20$ and $\alpha_m = 0.05°$. The transition location on the upper surface at $M = 0.75$ is observed to move over two cells (2 mm $\rightarrow x/c = 6.67 \cdot 10^{-3}$). The movement of the shock wave is therefore also limited to two cells.

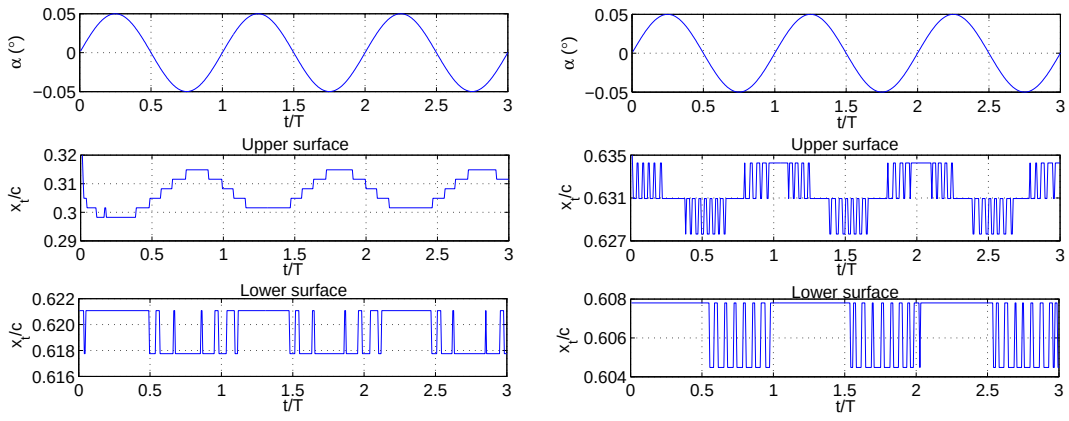

(a) $M = 0.65$ (b) $M = 0.75$

Figure 7.5: Angle of attack, transition onset locations on upper and lower surface versus non-dimensional time at two Mach numbers and $k = 0.20$ (free transition)

Since meshes with smaller cells along the airfoil contour did not show converged results (see Appendix D) it was not possible to check whether such a mesh would give a harmonic variation of the transition location. Therefore further investigations are necessary, maybe with a variation in the numerical parameters used (the multigrid scheme for example).

7.3 Amplitude investigation

Initially, a pitching amplitude of 0.25° was selected for the unsteady pitch simulations. For the plunging airfoil simulations, initially an amplitude of $0.005c/k$ was selected. After a few simulations at different Mach numbers at the smallest reduced frequency, it turned out that this amplitude leads to a non-linear response of the airfoil's moment coefficient, especially for Mach numbers around the quasi-steady maximum in lift curve slope. However, for the classical flutter approach used in this thesis, only the first harmonic components in the frequency domain are used and therefore it is necessary that the response of the airfoil is dominated by these first harmonics. That is, the higher order harmonic components should be small, such that the airfoil's response can be represented by its first harmonic components only. Hence, a linear response of both the airfoil's lift and moment coefficient is necessary. In the time domain, this means that the graphs of lift and moment coefficient versus angle of attack (or vertical displacement when the airfoil is plunging) should be of elliptical form. Therefore, an amplitude investigation has been performed.

7.3.1 Fully turbulent simulations

Pitching motion

The testcase used for the amplitude investigation is a pitching motion at $M = 0.755$ and $k = 0.05$. The initially selected amplitude has been decreased by a factor of 5 twice, i.e. the amplitudes used for the pitching airfoil simulations are: $\alpha_m = 0.25°$, $0.05°$ and $0.01°$. The resulting lift and moment coefficient response as a function of the angle of attack divided by the amplitude of the airfoil's motion, are shown in figure 7.6. From this figure it can be observed that response of the lift coefficient is almost independent of the amplitude of the motion. Furthermore, figure 7.6a shows curves with an almost elliptical form. This is clearly not the case for the moment coefficient. From figure 7.6b it follows that the moment coefficient strongly depends on the amplitude of the pitching motion. It should be noted however, that not all timesteps were fully converged. Therefore, some small oscillations occur in the moment coefficient versus angle of attack curves. Hence, the non-linear response of the moment coefficient might be a result of that. Further investigations (with converged results at each timestep) are needed to clarify this aspect.

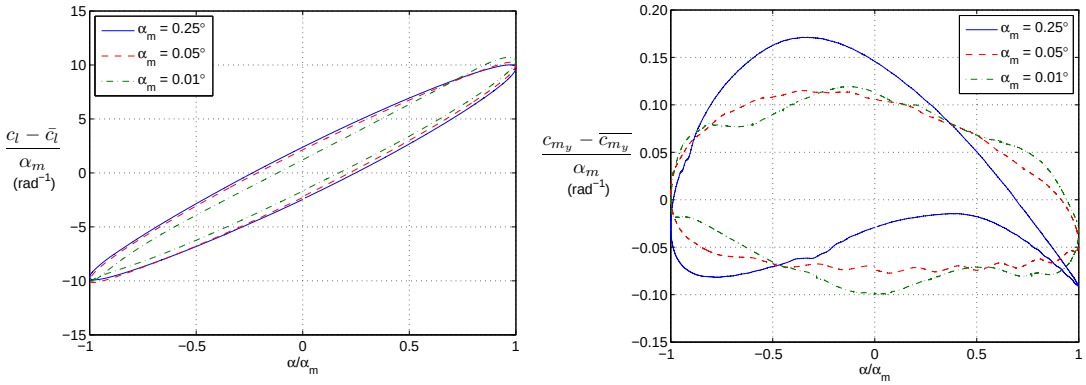

(a) Lift coefficient versus normalised angle of attack

(b) Moment coefficient versus normalised angle of attack

Figure 7.6: Lift and moment coefficient versus angle of attack at $M = 0.765$ and $k = 0.05$ for three different amplitudes of the pitching mode (fully turbulent)

The magnitude and phase angle of the airfoil's response are shown in table 7.3. Note that the magnitude shown here, has been normalised by the amplitude of the pitching motion, such that the results can be compared to each other. From this table it can be seen that especially from $\alpha_m = 0.25°$ to $\alpha_m = 0.05°$, the changes in phase and magnitude are large for both lift and moment coefficient, for the lift coefficient they are typically 15%, whereas for the moment coefficient differences of approximately 50% occur. From $\alpha_m = 0.05°$ to $\alpha_m = 0.01°$ the changes in phase and magnitude are much smaller (up to about 5%). An exception is the phase angle of the lift coefficient, which first gets smaller when the amplitude is reduced and then it gets larger again. From figure 7.6a, it can also be seen that for the smallest amplitude strange behaviour of the lift coefficient is present near the minimum angle of attack. This might be an explanation for the difference in phase angle of the lift coefficient.

	Magnitude (-)		Phase angle (°)	
α_m (°)	c_{l_α}	$c_{m_{y_\alpha}}$	c_{l_α}	$c_{m_{y_\alpha}}$
0.25	8.5837	$1.9155 \cdot 10^{-1}$	-11.19	-159.93
0.05	10.102	$9.4586 \cdot 10^{-2}$	-13.53	-105.18
0.01	10.164	$9.9182 \cdot 10^{-2}$	-8.94	-101.50

Table 7.3: Magnitude and phase angle of lift and pitching moment coefficient at $M = 0.765$ and $k = 0.05$ for three different amplitudes of the pitching mode (fully turbulent)

In the end an amplitude of 0.05° has been selected for the unsteady pitching simulations needed to calculate the flutter boundary. The non-linear behaviour, that is the deviation from the elliptical form of the lift and moment coefficient loops, at this Mach number and reduced frequency is caused by the fact that the lift and moment coefficient are not fully converged at each timestep. This behaviour might however disappear for other Mach numbers and reduced frequencies (see section 7.4.1).

Plunging motion

For the plunging mode a similar amplitude investigation has been performed. The testcase selected was the same as for the pitching motion, that is, a plunging airfoil at $M = 0.755$ and $k = 0.05$. The amplitudes investigated are: $h_m = 0.005c/k$, $0.001c/k$ and $0.0002c/k$. Figure 7.7 shows the response of the lift and moment coefficient as a function of the normalised amplitude (h/h_m).

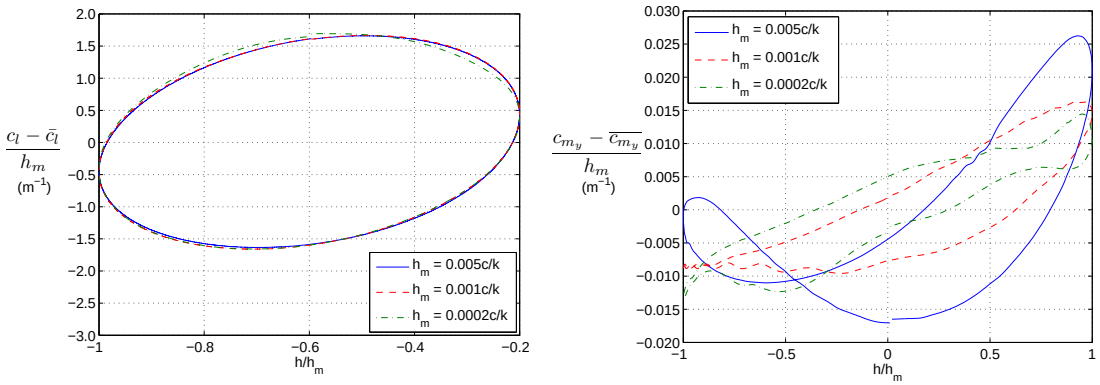

(a) Lift coefficient versus normalised vertical displacement

(b) Moment coefficient versus normalised vertical displacement

Figure 7.7: Lift and moment coefficient versus the normalised vertical displacement at $M = 0.765$ and $k = 0.05$ for three different amplitudes of the plunging mode (fully turbulent)

From figure 7.7a it is observed that the lift coefficient follows an elliptic curve for all amplitudes and these curves are almost identical. For the moment coefficient however, a strong non-linear behaviour can be seen. This behaviour seems to become a little bit more linear when the amplitude is reduced. However, it should be noted again that the moment coefficient was not fully converged at every timestep. Hence, in order to judge the variation in the airfoil's response with amplitude, further investigations are necessary in which the number of inner iterations has to be increased, such that the moment coefficient will converge at every timestep.

The magnitude and phase angle of the airfoil's response are shown in table 7.4. Here, the magnitude has been normalised again by the amplitude of the plunging motion. From this table it can be seen that differences in magnitude are not that large, typically about 2% or less. For the phase angle of the moment coefficient they are however more than 10% and hence significant.

	Magnitude (-)		Phase angle (°)	
h_m (°)	c_{l_h}	$c_{m_{y_h}}$	c_{l_h}	$c_{m_{y_h}}$
$0.005c/k$	1.6527	$1.2310 \cdot 10^{-2}$	74.76	-28.91
$0.001c/k$	1.6760	$1.2349 \cdot 10^{-2}$	74.15	-23.43
$0.0002c/k$	1.6384	$1.2108 \cdot 10^{-2}$	77.66	-20.76

Table 7.4: Magnitude and phase angle of lift and plunging moment coefficient at $M = 0.765$ and $k = 0.05$ for for three different amplitudes of the plunging mode (fully turbulent)

Hence, in the end the results of the flutter simulations will not be influenced much by the bad convergence behaviour. Furthermore, this testcase is a critical one, as at this Mach number the maximum lift curve slope occurs and the smallest reduced frequency corresponds to the slowest motion, in which the flow has more time to respond to the motion of the airfoil. Hence, for larger reduced frequencies a more linear response is expected and obtained (see sections 7.4 and 7.5). This also holds for the pitching motion. In order to be consistent with the pitching mode, an amplitude of $0.001c/k$, which corresponds to an effective angle of attack of approximately 0.06° has been used for all other unsteady flow simulations.

7.3.2 Free transition simulations

Pitching motion

An amplitude investigation has also been performed in case of free boundary layer transition. The testcase used for this investigation is an pitching motion at $M = 0.74$ and $k = 0.30$. The amplitudes that have been used are the same as in the fully turbulent case. Figure 7.8 shows the lift and moment hysteresis loops, which have been made non-dimensional by the amplitude of the motion.

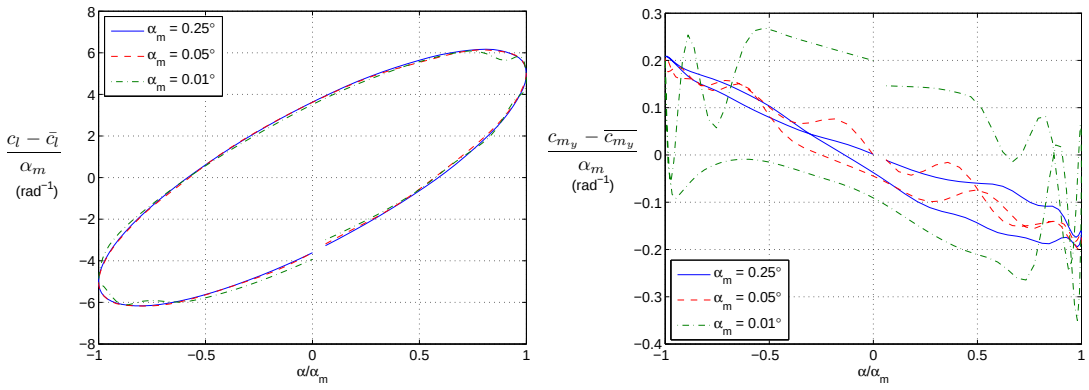

(a) Lift coefficient versus normalised angle of attack

(b) Moment coefficient versus normalised angle of attack

Figure 7.8: Lift and moment coefficient versus angle of attack at $M = 0.74$ and $k = 0.30$ for three different amplitudes of the pitching mode (free transition)

From these figures it can be observed that the lift coefficient is not really influenced by a change in amplitude. The influence on the moment coefficient is however large. At $\alpha_m = 0.01°$ very large oscillations are present, hence when this response is converted to the frequency domain only taking into account the first harmonic component will not be accurate. When the amplitude is increased, the oscillations become smaller and therefore the first harmonic will be a better approximation. The magnitude (scaled with the amplitude of the motion) and phase angle of the lift and moment coefficient are shown in table 7.5. From this table it becomes clear that the magnitude and phase angle are approximately the same at the largest two amplitudes, the largest difference is approximately 1%, whereas those of the smallest amplitude are clearly different, especially for the moment coefficient there is a difference of 27%. Therefore an amplitude of 0.05° has been selected for further computations.

	Magnitude (-)		Phase angle (°)	
α_m (°)	c_{l_α}	$c_{m_{y\alpha}}$	c_{l_α}	$c_{m_{y\alpha}}$
0.25	6.1650	$1.9104 \cdot 10^{-1}$	-35.91	-185.97
0.05	6.1906	$1.9225 \cdot 10^{-1}$	-35.42	-185.54
0.01	6.0402	$1.8039 \cdot 10^{-1}$	-36.19	-236.43

Table 7.5: Magnitude and phase angle of lift and moment coefficient at $M = 0.74$ and $k = 0.30$ for three different amplitudes of the pitching mode (free transition)

Plunging motion

The force and moment coefficients have been plotted against the non-dimensional vertical displacement for the testcase selected ($M = 0.74$ and $k = 0.30$) in figure 7.9.

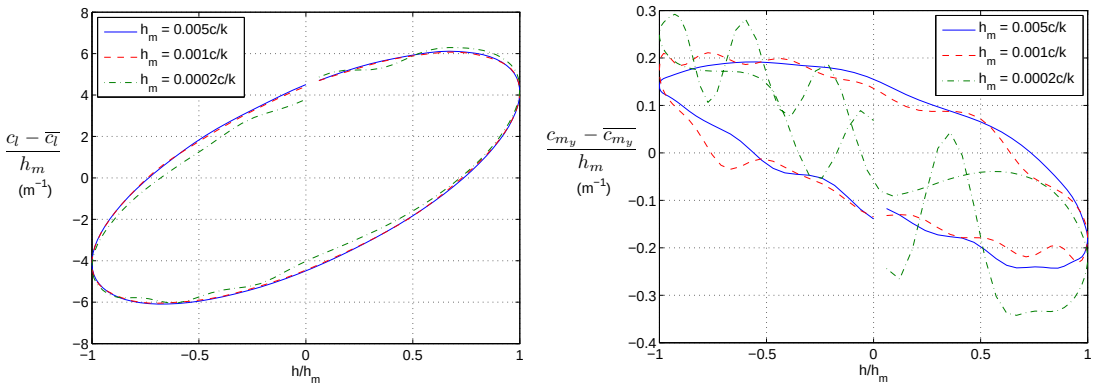

(a) Lift coefficient versus normalised vertical displacement

(b) Moment coefficient versus normalised vertical displacement

Figure 7.9: Lift and moment coefficient versus normalised vertical displacement at $M = 0.74$ and $k = 0.30$ for three different amplitudes of the pitching mode (free transition)

These figures show that the amplitude of the airfoil motion does not change the response of the lift coefficient. The response of the moment coefficient is however highly influenced

by the amplitude of the motion. At the two largest amplitudes the response looks similar, at $h_m = 0.0002c/k$ however, the contribution of the higher than first order harmonics is large. In order to see the influence in the frequency domain, the magnitude and phase angle of the first harmonic component are shown in table 7.6. From this table it can be seen that the magnitude and phase angle obtained by using the smallest amplitude are clearly different than those obtained with the other two amplitudes, especially for the moment coefficient, where the magnitude and phase angle show a difference of 21% and 14% compared to $h_m = 0.001c/k$, respectively. Hence, an amplitude of $h_m = 0.001c/k$ has been selected, as for the fully turbulent simulations.

	Magnitude (-)		Phase angle (°)	
h_m (°)	c_{l_h}	$c_{m_{y_h}}$	c_{l_h}	$c_{m_{y_h}}$
$0.005c/k$	6.0893	$2.1081 \cdot 10^{-1}$	47.41	-140.33
$0.001c/k$	6.0621	$2.0970 \cdot 10^{-1}$	47.12	-141.37
$0.0002c/k$	6.0382	$2.5457 \cdot 10^{-1}$	44.21	-165.30

Table 7.6: Magnitude and phase angle of lift and moment coefficient at $M = 0.74$ and $k = 0.30$ for three different amplitudes of the pitching mode (free transition)

7.4 Fully turbulent simulations

7.4.1 Pitching motion

In this subsection some unsteady flow results of the pitching mode will be shown in both time and frequency domain.

Time domain

Figure 7.10 shows the lift and moment coefficient versus the angle of attack for the pitching motion at $M = 0.5$, 0.755, 0.765 and 0.8. This figure depicts the complete response as obtained from the CFD simulations. The graphs of the remaining Mach numbers can be found in the Appendix G. The amplitude of the motion is 0.05°. The black arrows indicate the direction in which the curves have to be followed. When coloured arrows are present, then the direction of the corresponding curve deviates from that of the other curves.

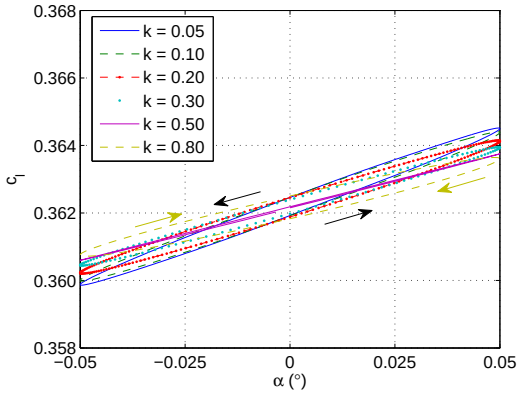

(a) Lift coefficient versus angle of attack $M = 0.5$

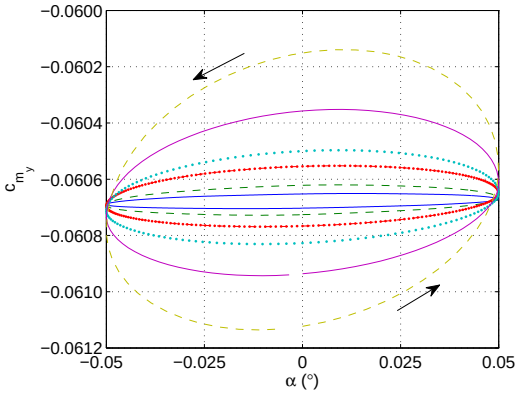

(b) Moment coefficient versus angle of attack $M = 0.5$

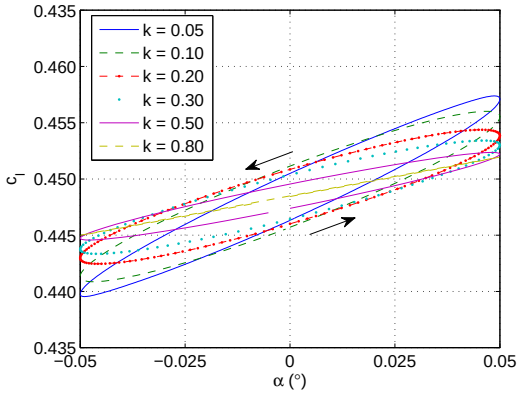

(c) Lift coefficient versus angle of attack $M = 0.755$

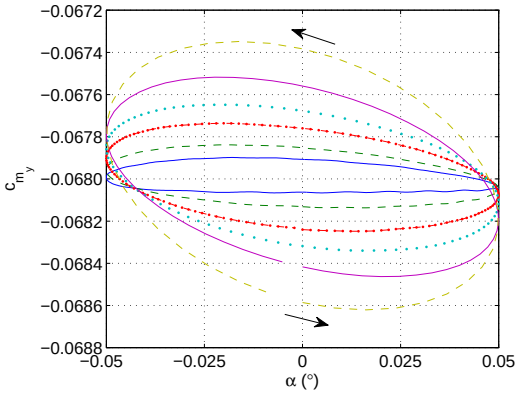

(d) Moment coefficient versus angle of attack $M = 0.755$

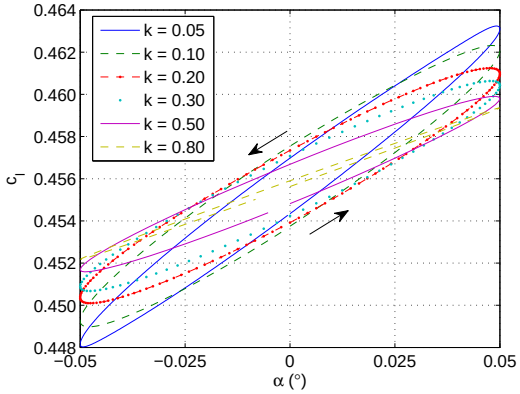

(e) Lift coefficient versus angle of attack $M = 0.765$

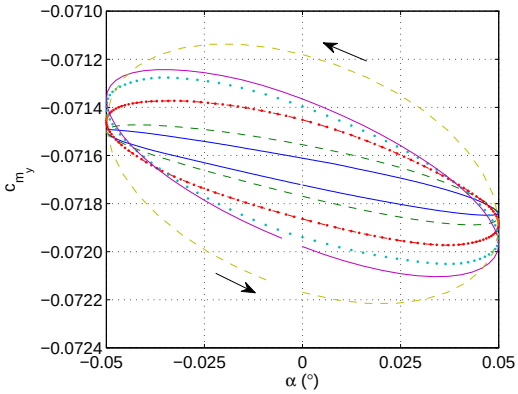

(f) Moment coefficient versus angle of attack $M = 0.765$

Figure 7.10

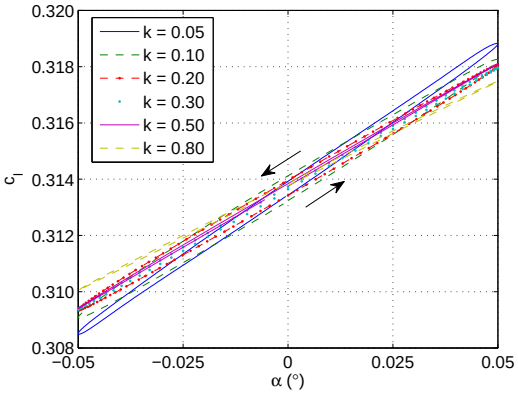

(g) Lift coefficient versus angle of attack $M = 0.8$

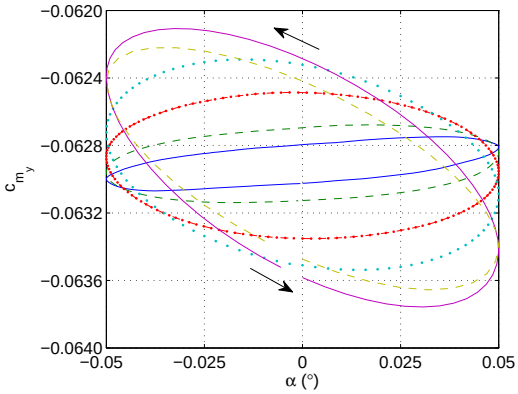

(h) Moment coefficient versus angle of attack $M = 0.8$

Figure 7.10: Lift and moment coefficient versus angle of attack for the pitching motion at $M = 0.5$, 0.755, 0.765 and 0.8 (fully turbulent)

From these figures it can be seen how the lift and moment coefficient change as a function of the angle of attack when the reduced frequency is changed. For the lift coefficient it can be seen that the inclination of the ellipses decreases when the reduced frequency is increased. Therefore, the range of lift coefficients achieved becomes smaller. For the moment coefficient the opposite is true, the inclination of the ellipses increases and hence the range of the moment coefficients achieved increases. The angle of attack at which the maximum moment coefficient occurs is clearly not the maximum amplitude of the motion, it occurs when the airfoil is pitching down again. The angle of attack at which this maximum occurs becomes smaller with increasing reduced frequency. For the lift coefficient there is a similar shift in maximum lift coefficient with reduced frequency, it is however much smaller than for the pitching moment coefficient. When the Mach number is increased from $M = 0.5$ to $M = 0.755$, the range of lift coefficients achieved increases. However, when the Mach number is increased further the difference between maximum and minimum lift coefficient decreases. The range of the moment coefficients achieved also increases when the Mach number is increased (compare figures 7.10b and 7.10d). When the Mach number is increased further to $M = 0.765$ the range of the moment coefficients achieved increases for small reduced frequencies, however for $k = 0.50$ and $k = 0.80$ this range decreases. When increasing the Mach number even further to $M = 0.8$, the range of moment coefficient achieved increases again for all reduced frequencies (except for the lowest one). When the Mach number is increased, the maximum moment coefficient is attained at a negative angle of attack (but still when the airfoil is moving down). For the smallest reduced frequencies at $M = 0.8$, the maximum moment coefficient occurs at a positive angle of attack again.

Frequency domain

The magnitude and phase angle of the pitching characterise this motion in the frequency domain. These quantities as well as the magnitude and phase angle obtained for the plunging motion, are needed in order to determine the flutter behaviour of the airfoil.

Figure 7.11 shows the magnitude and phase angle versus reduced frequency for all Mach numbers for the pitching motion. Note that the magnitude shown here has been divided by the magnitude of the angle of attack (i.e. the amplitude of the pitching motion). Then the absolute value of the lift curve slope or the moment curve slope is obtained, since the amplitude of the pitching motion is small.

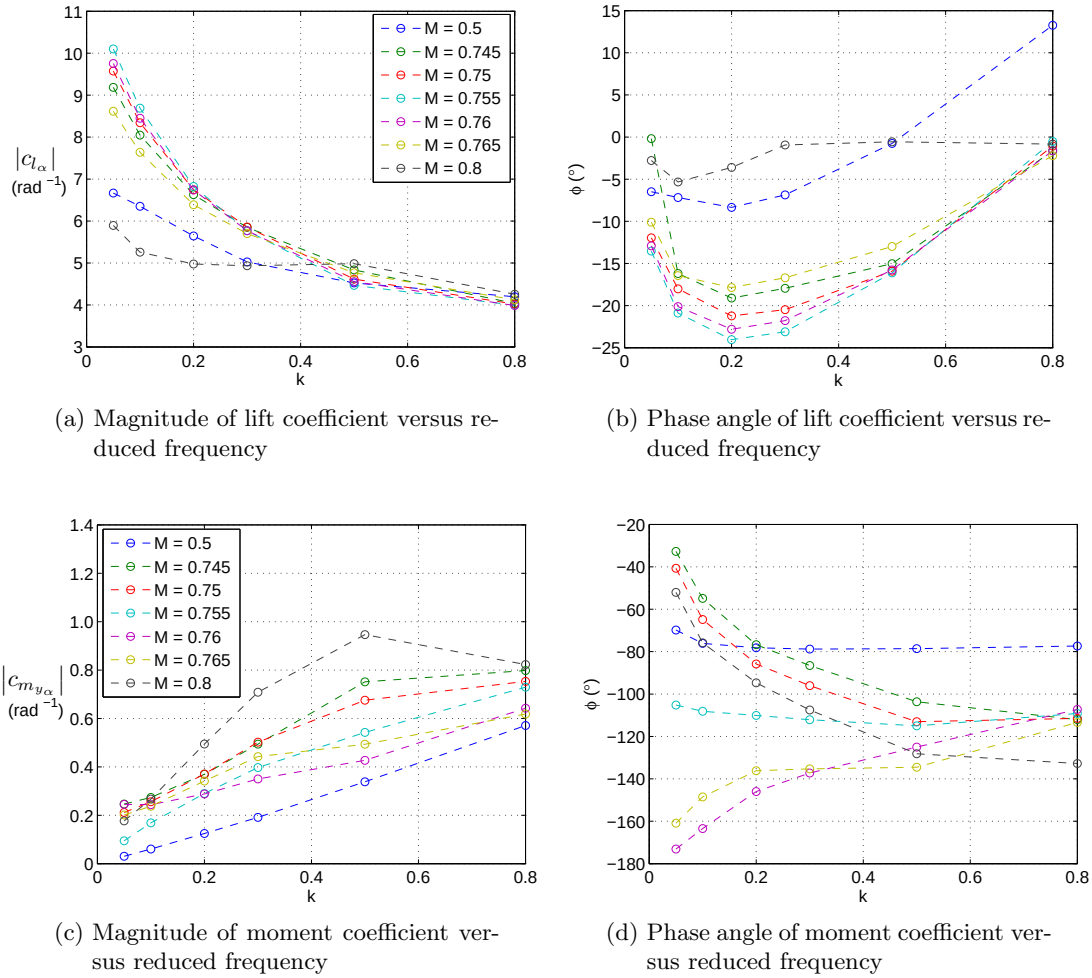

(a) Magnitude of lift coefficient versus reduced frequency

(b) Phase angle of lift coefficient versus reduced frequency

(c) Magnitude of moment coefficient versus reduced frequency

(d) Phase angle of moment coefficient versus reduced frequency

Figure 7.11: Magnitude and phase angle of lift and moment coefficient versus reduced frequency for all Mach numbers for the pitching motion (fully turbulent)

From these figures it can be seen that the magnitude of the lift coefficient made non-dimensional by the magnitude of the angle of attack, decreases with increasing reduced frequency for all Mach numbers. This can be explained from the fact that at small reduced frequencies, the pitching motion of the airfoil is very slow, hence the flow has time to adjust itself to its instantaneous angle of attack and the airfoil is therefore able to reach higher lift coefficients. On the contrary, when the motion of the airfoil is fast, then the flow has less time to adjust itself to the new angle of attack and hence the stationary lift coefficient at maximum amplitude might not be reached. This is connected to the phase angle, which indicates how much the lift coefficient lags the motion behind. From

figure 7.11b it is observed that the phase angle is negative for most Mach numbers and reduced frequencies, hence the lift coefficient lags the motion behind. The phase angle first decreases with increased reduced frequency, but after reaching a local minimum around $k = 0.20$ it increases again. This happens for all Mach numbers. Due to the phase lag, the maximum lift coefficient is not reached when the maximum angle of attack of the motion occurs, but a little bit later, when the angle of attack is decreasing again.

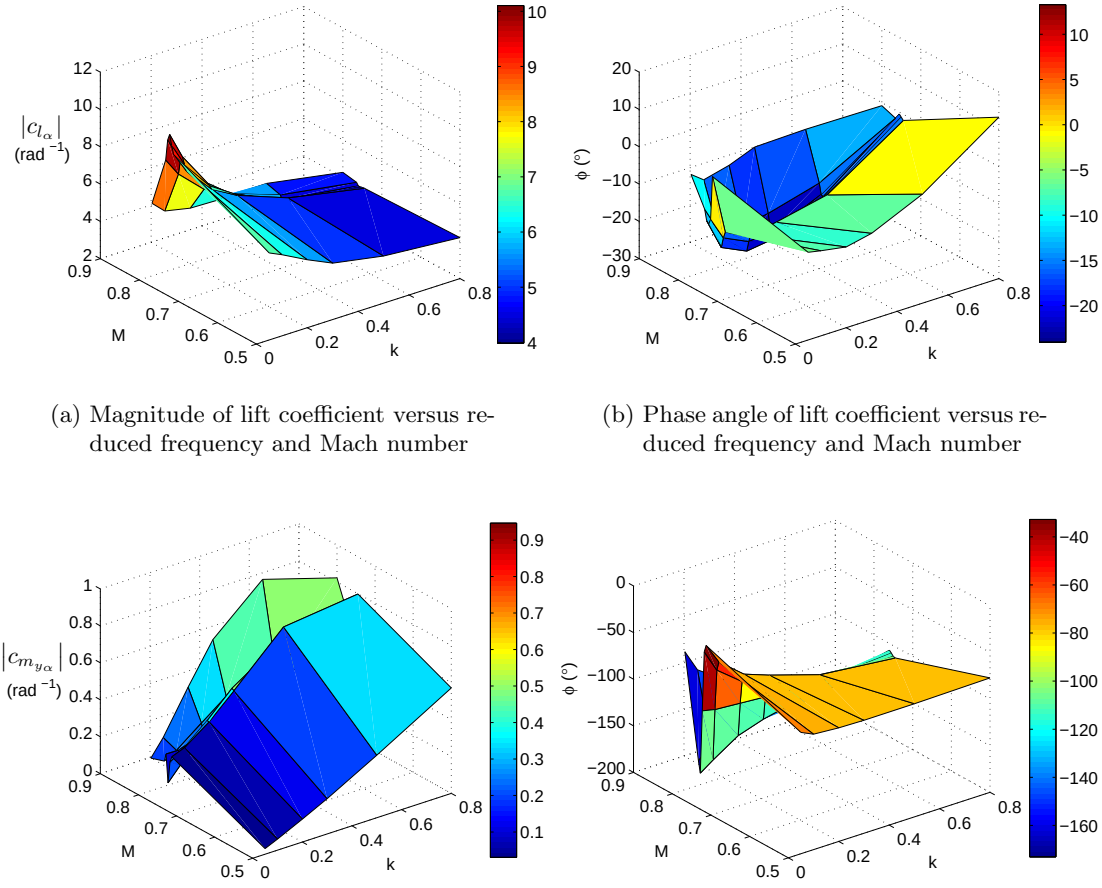

(a) Magnitude of lift coefficient versus reduced frequency and Mach number

(b) Phase angle of lift coefficient versus reduced frequency and Mach number

(c) Magnitude of moment coefficient versus reduced frequency and Mach number

(d) Phase angle of moment coefficient versus reduced frequency and Mach number

Figure 7.12: Magnitude and phase angle of lift and moment coefficient versus reduced frequency and Mach number for the pitching motion (fully turbulent)

From figure 7.11c it is seen that the magnitude of the moment coefficient with respect to the angle of attack increases with increasing reduced frequency. Apparently the decrease in magnitude of the lift coefficient causes a less negative moment. The phase lag of the moment coefficient is much larger (more than 10 times at the transonic dip) than that of the lift coefficient at the lowest reduced frequency. When the reduced frequency increases, the phase angle decreases for most Mach numbers, for $M = 0.76$ and $M = 0.765$ however, the phase angle increases with increasing reduced frequency. The phase angle is negative

for all reduced frequencies and Mach numbers, hence the moment coefficient is always lagging the motion behind.

The influence of Mach number and reduced frequency is seen more clearly in figures 7.12a till 7.12d. From figures 7.12a and 7.12b it can be observed that increasing the Mach number first increases the magnitude and decreases the phase angle of the lift coefficient, however when the Mach number has reached 0.755 this behaviour reverses, i.e. the magnitude decreases with increasing Mach number, whereas the phase angle increases with Mach number. It should be noted that behaviour of the magnitude of the lift coefficient as a function of Mach number resembles that of the lift-curve slope at zero frequency for small reduced frequencies (see section 6.4). The influence of the Mach number on the magnitude and the phase angle of the moment coefficient can be seen from figures 7.12c and 7.12d. At first the magnitude increases when the Mach number is increased, however when $M > 0.745$ the magnitude decreases when M is increased and when $M > 0.76$ the magnitude increases again. The phase angle shows the same behaviour with increasing Mach number.

7.4.2 Plunging motion

The results in both time and frequency domain obtained for the plunging motion are shown in this section.

Time domain

For the plunging motion the changes in lift and moment coefficient as a function of non-dimensional vertical displacement are shown in figure 7.13 for $M = 0.5$, 0.755, 0.765 and 0.8 and all reduced frequencies. The fully computed response is depicted here. The amplitude of the plunging motion is dependent on the reduced frequency, therefore the vertical displacement has been made non-dimensional by the amplitude h_m at each reduced frequency. The arrows again indicate in which direction the curves have to be followed. In case of a coloured arrow, the curve of that colour has to be followed in the direction of the corresponding arrow.

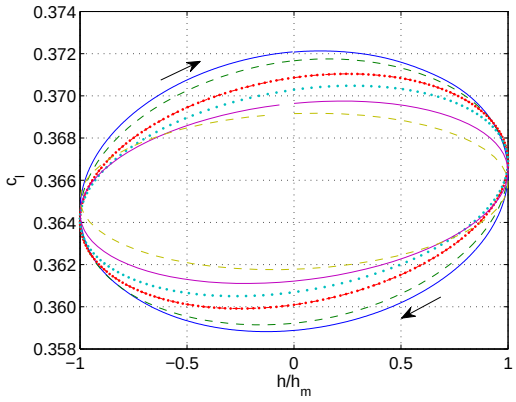

(a) Lift coefficient versus non-dimensional displacement $M = 0.5$

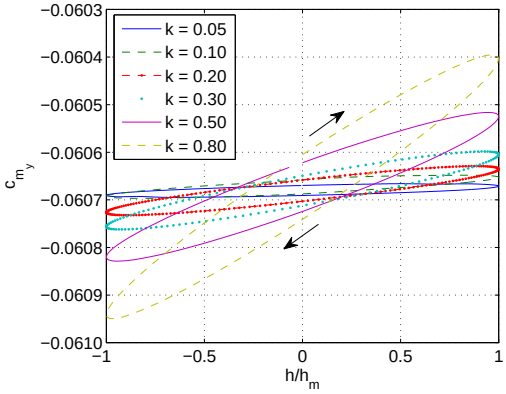

(b) Moment coefficient versus non-dimensional displacement $M = 0.5$

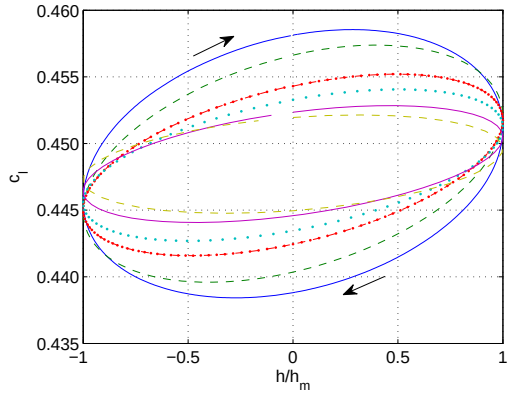

(c) Lift coefficient versus non-dimensional displacement $M = 0.755$

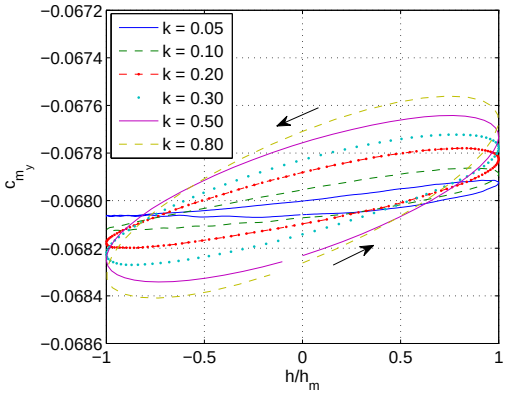

(d) Moment coefficient versus non-dimensional displacement $M = 0.755$

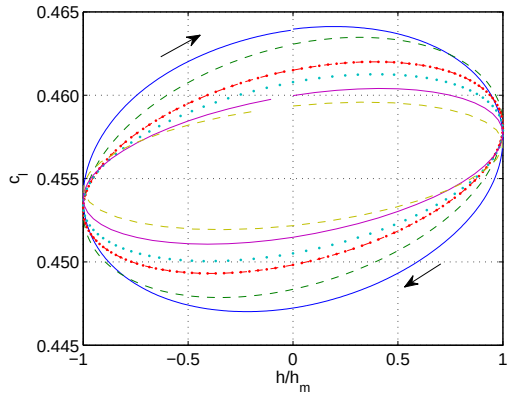

(e) Lift coefficient versus non-dimensional displacement $M = 0.765$

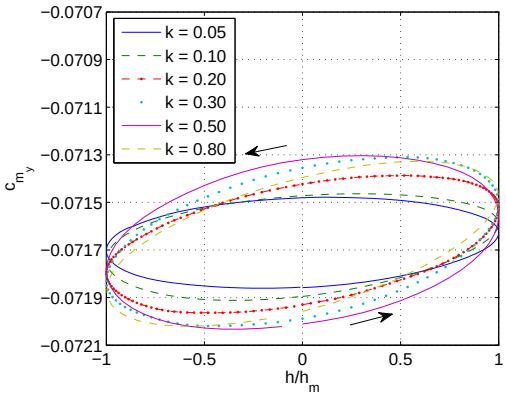

(f) Moment coefficient versus non-dimensional displacement $M = 0.765$

Figure 7.13

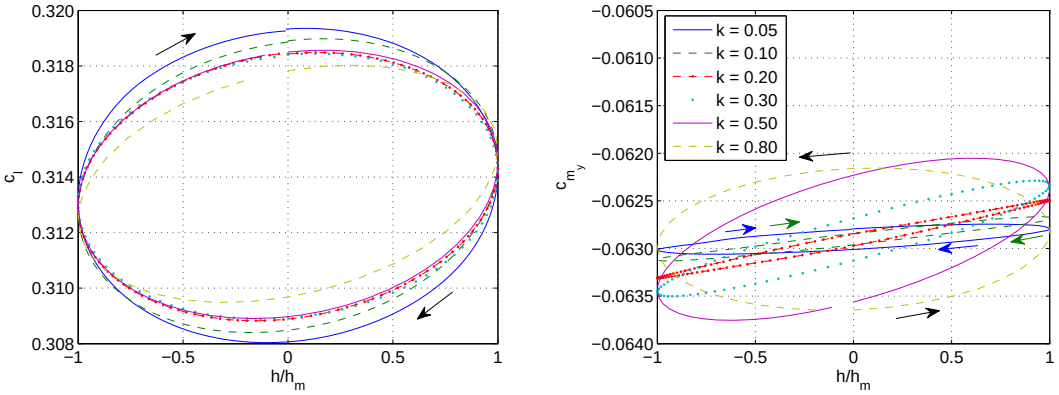

(g) Lift coefficient versus non-dimensional displacement $M = 0.8$

(h) Moment coefficient versus non-dimensional displacement $M = 0.8$

Figure 7.13: Lift and moment coefficient versus non-dimensional vertical displacement for the plunging motion at $M = 0.5$, 0.755, 0.765 and 0.8 (fully turbulent)

From these figures it is observed that the inclination and the range of the lift coefficients achieved decreases with increasing reduced frequency. It is expected that the maximum lift coefficient occurs when the effective angle of attack is maximum, that is, when the airfoil is passing the equilibrium position on its way down, this is however not the case as can be seen from the lift-coefficient-versus-vertical displacement graphs. Instead the maximum lift coefficient occurs when the airfoil is moving upwards and hence has a negative effective angle of attack w.r.t. to freestream flow. Increasing the reduced frequency shifts the maximum lift coefficient achieved towards larger vertical displacements. With increasing Mach number the difference between minimum and maximum lift coefficient increases, for $M > 0.755$ the range achieved by the lift coefficient decreases however. Furthermore, the maximum lift coefficient occurs at larger upward displacements when the Mach number increases, however when $M = 0.755$ is reached and the Mach number is increased even further, the upward displacement at which maximum lift occurs decreases again. This is the case for all reduced frequencies, except for the highest one. For the moment coefficient the inclination and range of the ellipses also increase with increasing reduced frequency. There is a large variation in the range of the moment coefficient ellipses with increasing Mach number. First, the range of the moment coefficients increases, then for $0.745 < M < 0.76$ it decreases with increasing Mach number and for $M > 0.76$ it increases again. The maximum moment coefficient occurs at an upward displacement smaller than the maximum upward displacement for the smallest reduced frequencies at Mach numbers smaller than $M = 0.755$ and at $M = 0.8$, i.e. when the airfoil is moving upwards. However, for $M = 0.755$, $M = 0.76$ and $M = 0.765$, the maximum moment coefficient occurs only when the airfoil is moving down again and it shifts towards the maximum upward deflection when the reduced frequency is increased.

Frequency domain

The same figures in the frequency domain can be made for the plunging motion. Figure 7.14 shows the variation of the magnitude and the phase angle with the reduced frequen-

cies for all Mach numbers. Here, the magnitude of the lift and moment coefficients has been divided by the magnitude of the vertical displacement (i.e. the amplitude of the plunging motion).

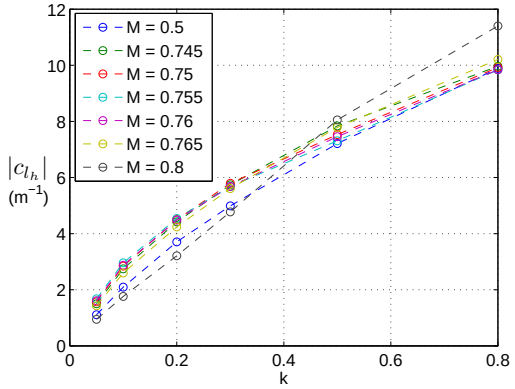

(a) Magnitude of lift coefficient versus reduced frequency

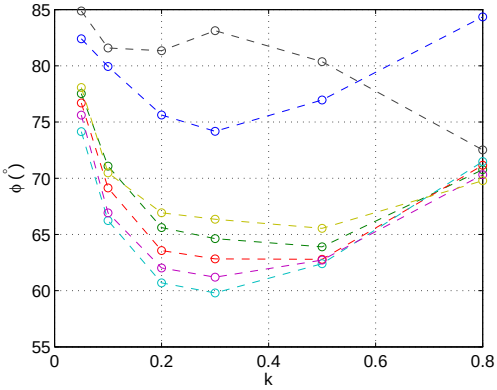

(b) Phase angle of lift coefficient versus reduced frequency

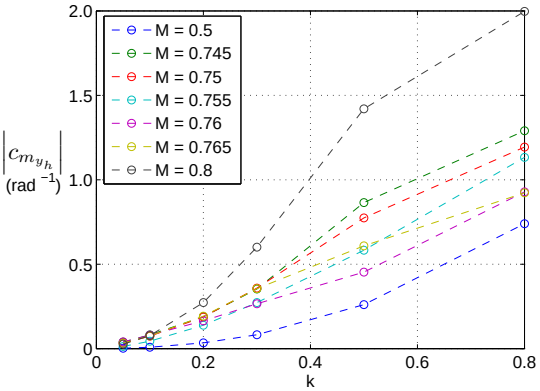

(c) Magnitude of moment coefficient versus reduced frequency

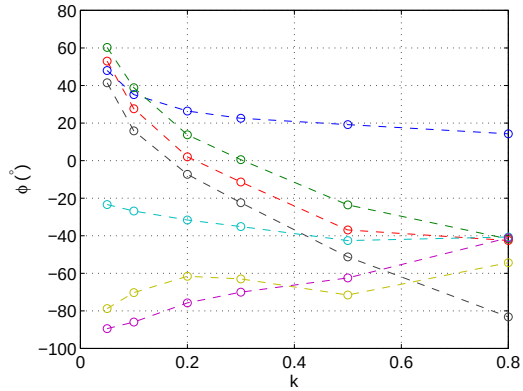

(d) Phase angle of moment coefficient versus reduced frequency

Figure 7.14: Magnitude and phase angle of lift and moment coefficient versus reduced frequency for all Mach numbers for the plunging motion (fully turbulent)

These figures show that the magnitude of both the lift and moment coefficient increases with increasing reduced frequency. This is in contrast to the magnitude of the lift coefficient of the pitching motion, which decreases with increasing reduced frequency. The phase angles of the lift coefficient are all positive, hence the lift coefficient leads the plunging motion of the airfoil. This lead becomes less when the reduced frequency is increased, after reaching a local minimum the phase angle with which the lift coefficient leads the motion becomes larger again. The phase angle of the moment coefficient is positive for $M = 0.745$, 0.75 and 0.8 at small reduced frequencies, it becomes however negative when the reduced frequency is increased. For $M = 0.755$, 0.76 and 0.765 the phase angle is negative and stays negative over the whole frequency range. This can also be observed from figures 7.15a till 7.15d, which show 3D plots with the Mach number on the third axis.

From these figures it is also seen that the magnitude of both lift and moment coefficient first increases with Mach number (until $M = 0.745$), then decreases and when $M > 0.765$ it increases again.

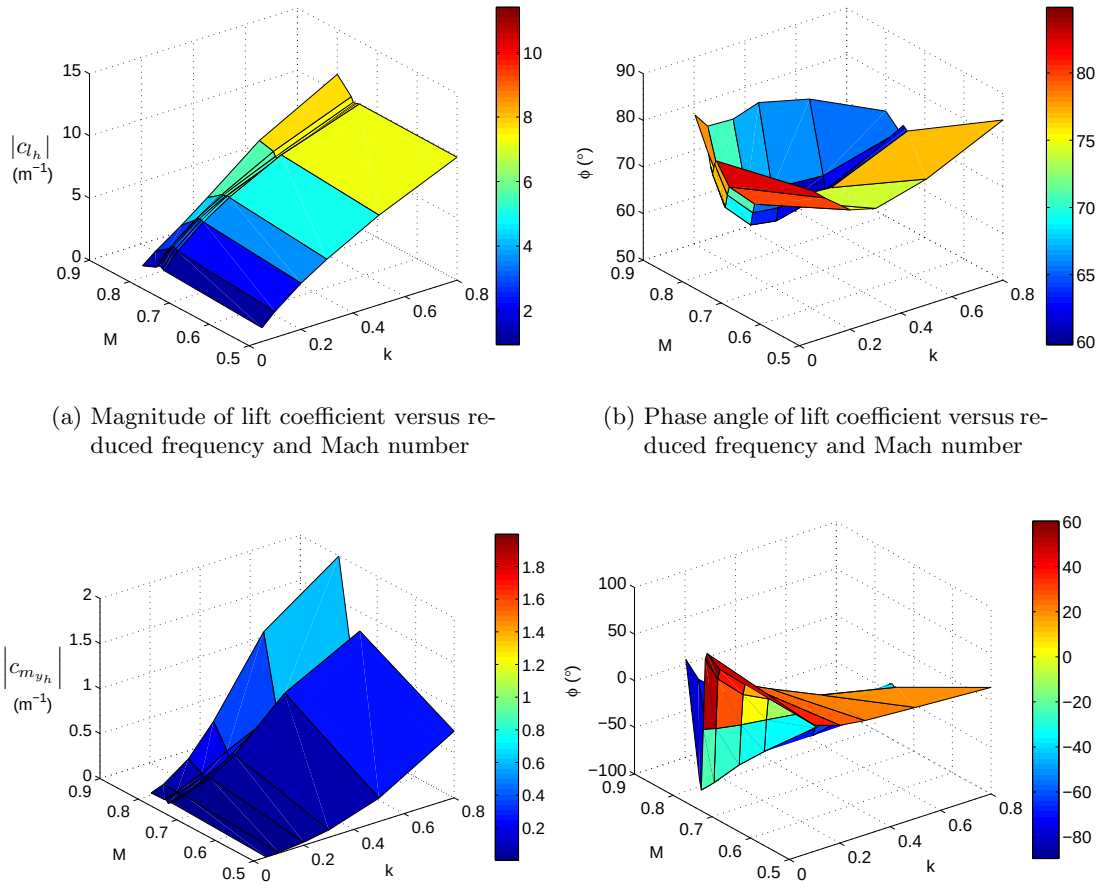

(a) Magnitude of lift coefficient versus reduced frequency and Mach number

(b) Phase angle of lift coefficient versus reduced frequency and Mach number

(c) Magnitude of moment coefficient versus reduced frequency and Mach number

(d) Phase angle of moment coefficient versus reduced frequency and Mach number

Figure 7.15: Magnitude and phase angle of lift and moment coefficient versus reduced frequency for all Mach numbers for the plunging motion (fully turbulent)

7.5 Free transition simulations

7.5.1 Pitching motion

The results of the unsteady flow simulations with free boundary layer transition will be shown and discussed in this section, both in time domain and in the frequency domain.

Time domain

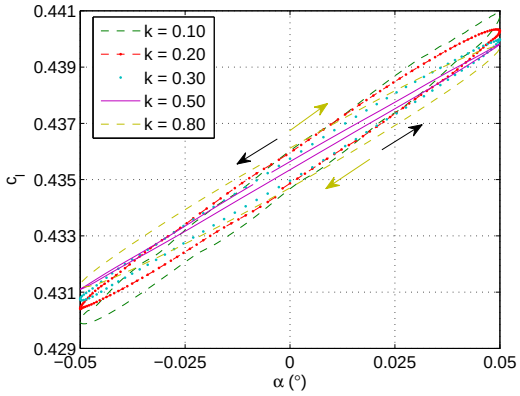

(a) Lift coefficient versus angle of attack $M = 0.65$

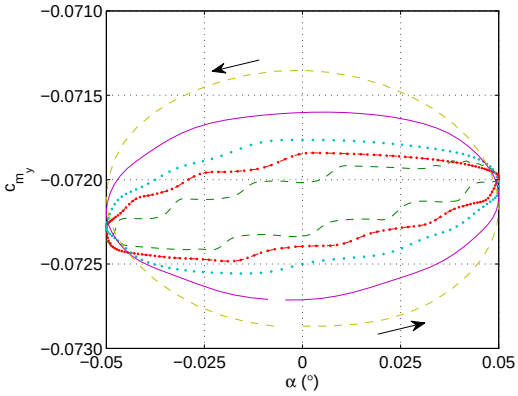

(b) Moment coefficient versus angle of attack $M = 0.65$

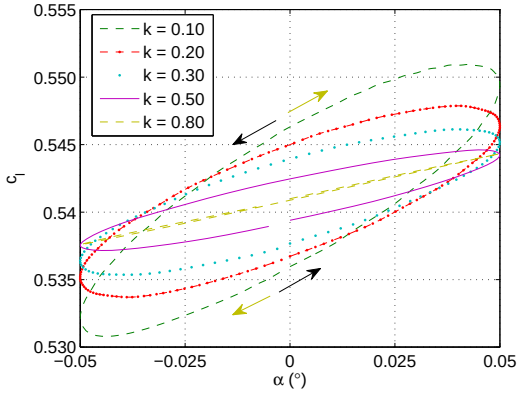

(c) Lift coefficient versus angle of attack $M = 0.74$

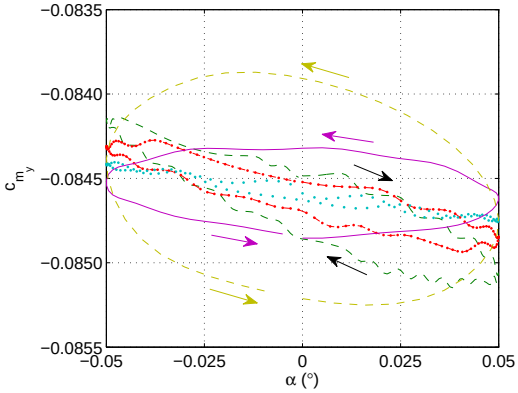

(d) Moment coefficient versus angle of attack $M = 0.74$

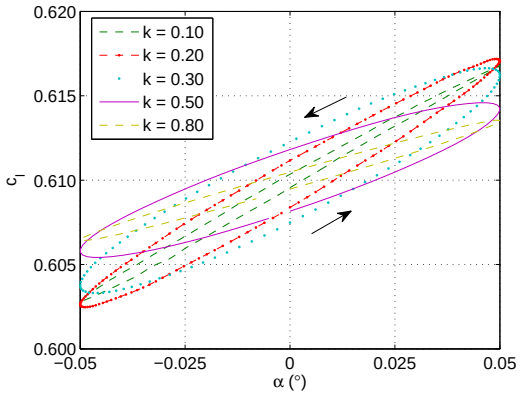

(e) Lift coefficient versus angle of attack $M = 0.745$

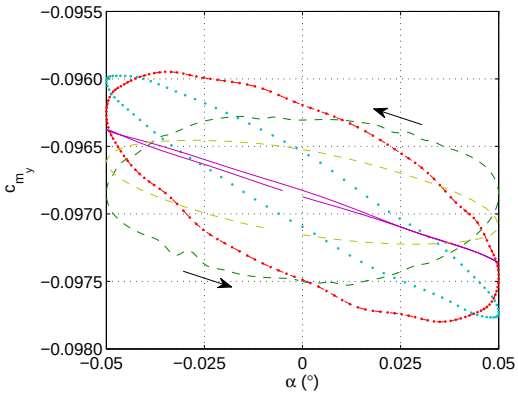

(f) Moment coefficient versus angle of attack $M = 0.745$

Figure 7.16: Lift and moment coefficient versus angle of attack for the pitching motion at $M = 0.65$, 0.74 and 0.745 (free transition)

Figure 7.16 shows the lift and moment coefficients versus the angle of attack of the pitching motion at $M = 0.65$, 0.74 and 0.745. The results of the remaining Mach numbers can be found in Appendix G. The direction of the curves is indicated by the arrows. From these figures it is immediately clear that when looking at the moment coefficient, higher harmonic components come into play. These higher harmonics components are present for all Mach numbers, although they disappear at higher reduced frequencies. At $M = 0.74$ these higher harmonics are most pronounced. From the lift coefficient-versus-angle of attack graphs it can be seen that the range of lift coefficient achieved (hence the magnitude) decreases with increasing reduced frequency. For the highest Mach numbers ($M = 0.745$ and $M = 0.75$) it first increases after which it decreases again. The lift coefficient is lagging the motion behind for almost all Mach numbers and reduced frequencies, except for $M = 0.65$ and 0.74 both at $k = 0.80$, for these cases the lift coefficient is leading the motion (see figure 7.17b). At $M = 0.74$ this lag first increases with reduced frequency, at reduced frequencies larger than 0.2 this lag becomes less however. At $M \geq 0.745$ the same behaviour is observed, however the lag increases again at $k = 0.50$ for this Mach number. The range of moment coefficients achieved increases with reduced frequency at the lowest Mach number. At $M = 0.74$ this range first decreases at higher reduced frequencies it increases however again. At $M = 0.745$ and higher the magnitude of the moment coefficient first increases, after which it decreases. The moment coefficient lags the motion behind for all Mach numbers and reduced frequencies. This lag increases with increasing reduced frequency at the lowest Mach number. At $M = 0.745$ a minimum is reached at a reduced frequency of 0.5, then the lag of the motion coefficient decreases again (the same holds for $M = 0.75$). At $M = 0.74$ the lag decreases with increasing reduced frequency. The lag is very large at the three lowest reduced frequencies at this Mach number (the curves of these reduced frequencies have to be followed counter-clockwise, hence the maximum occurs only in the last part of the motion, when the airfoil is moving up again). At $k > 0.50$ the lag increases.

As the Mach numbers used in case of free transition are located at approximately the same locations along the quasi-steady lift-curve slope curve as those used in case of a fully turbulent boundary layer (subsonic, near/at lift-curve slope peak and when the lift-curve slope is going down again, see also figure 6.13), a comparison is made here. Upon comparing figure 7.16 to figures 7.10a till 7.10f obtained from the fully turbulent simulations, it is clear that the behaviour at $M = 0.65$ resembles that at $M = 0.5$ (fully turbulent), the same hold for $M = 0.74$ and $M = 0.755$ (fully turbulent) and $M = 0.745$ and $M = 0.765$ (fully turbulent). At $M = 0.745$ and $k = 0.10$ (free transition) the range of lift coefficient achieved is however lower than that at $k = 0.20$ for the same Mach number. In case of the fully turbulent simulations at $M = 0.765$ this is not the case. For the moment coefficient, the behaviour is only the same for the lowest Mach number. The behaviour of the moment coefficient obtained from the fully turbulent simulations at $M = 0.755$ is not comparable to that of the moment coefficient obtained from the simulations with free transition at $M = 0.74$, as the range of moment coefficients achieved increases with reduced frequency for the fully turbulent simulations, whereas for the simulations with free transition it decreases and then increases. At $M = 0.745$ (free transition) the behaviour of the moment coefficient is not comparable to that at $M = 0.765$ either, since the range of moment coefficients does not increases with reduced frequency,

as at $M = 0.765$, but increases and then decreases.

Frequency domain

The time signals obtained in case of free transition can again be converted to the frequency domain. The resulting magnitude and phase angle are shown in this section for all Mach numbers and reduced frequencies and for both modes. Figure 7.17 shows the magnitude scaled by the amplitude of the pitching motion and the phase angle of both lift and moment coefficient as a function of the reduced frequency for all Mach numbers.

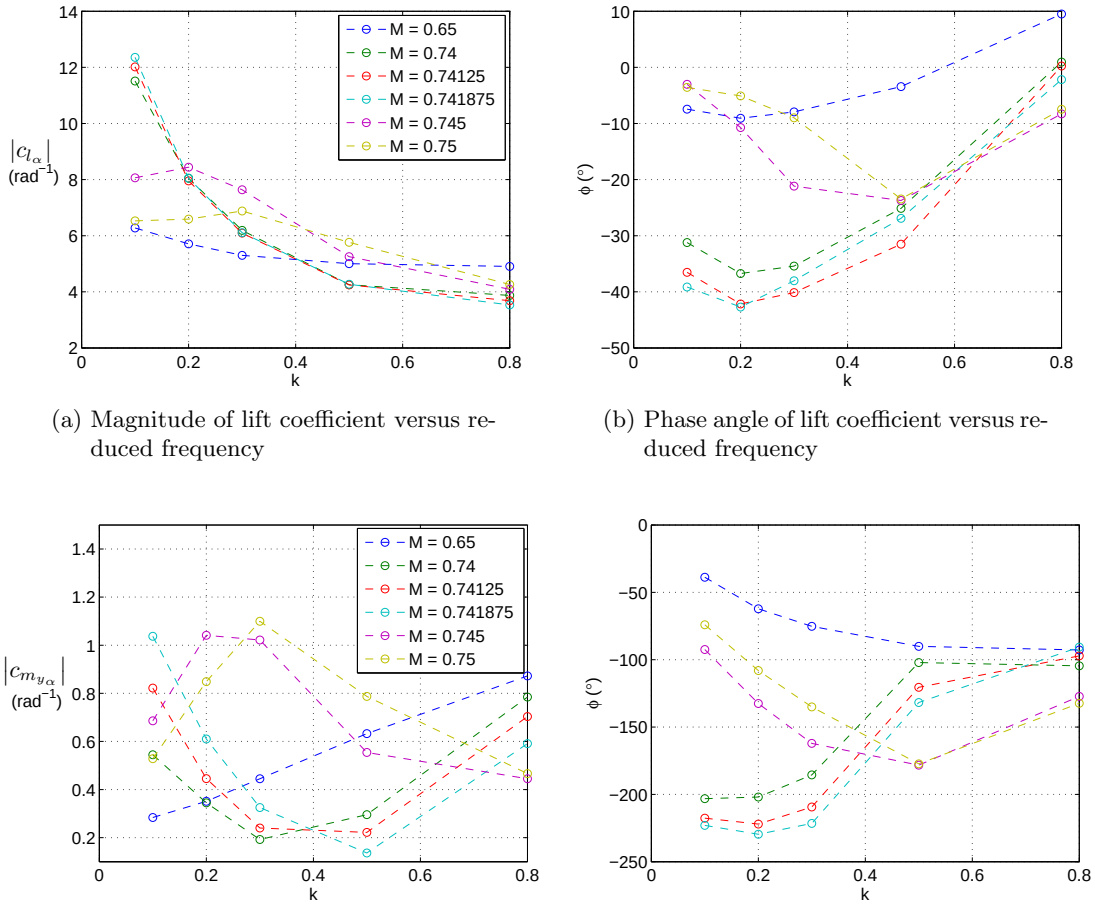

(a) Magnitude of lift coefficient versus reduced frequency

(b) Phase angle of lift coefficient versus reduced frequency

(c) Magnitude of moment coefficient versus reduced frequency

(d) Phase angle of moment coefficient versus reduced frequency

Figure 7.17: Magnitude and phase angle of lift and moment coefficient versus reduced frequency for all Mach numbers for the pitching motion (free transition)

From figure 7.17a it is observed that the magnitude of the lift coefficient decreases with increasing reduced frequency for the lowest Mach numbers. As in case of a fully turbulent boundary layer this can be explained by the fact that the speed of the motion increases with increasing reduced frequency and hence the maximum lift coefficient reached decreases. For $M \geq 0.745$ the magnitude first increases and then decreases. As already

pointed out above the lift coefficient is lagging the motion behind for all Mach numbers, except for the highest reduced frequencies at $M = 0.65$. The phase angle is therefore negative. As for the fully turbulent simulations, the phase angle decreases with increasing reduced frequency and reaches a minimum, after which it increases. The magnitude of the moment coefficient shows a completely different behaviour than in case of a fully turbulent boundary layer. Only for $M = 0.65$ the behaviour is similar to that of the fully turbulent subsonic case. When the Mach number is increased one first sees a minimum in the magnitude at a certain reduced frequency (at $k = 0.30$ or $k = 0.50$). At the two highest Mach numbers, a maximum is however present at $k = 0.20$ for $M = 0.745$ and $k = 0.30$ for $M = 0.75$. The phase angle shows the same behaviour as for the fully turbulent simulations, except that the order is exchanged.

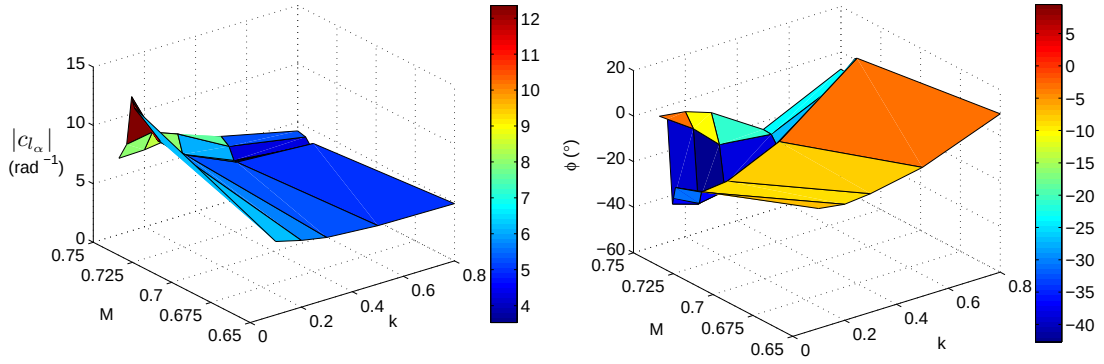

(a) Magnitude of lift coefficient versus reduced frequency and Mach number

(b) Phase angle of lift coefficient versus reduced frequency and Mach number

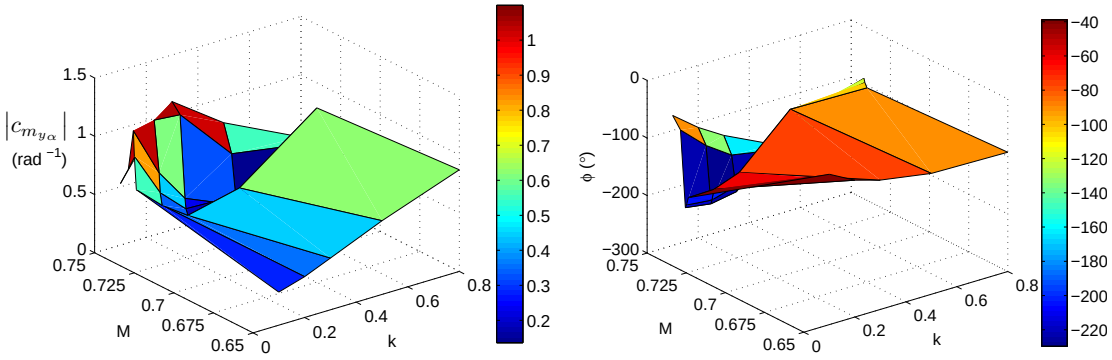

(c) Magnitude of moment coefficient versus reduced frequency and Mach number

(d) Phase angle of moment coefficient versus reduced frequency and Mach number

Figure 7.18: Magnitude and phase angle of lift and moment coefficient versus reduced frequency and Mach number for the pitching motion (free transition)

Figure 7.18 shows the magnitude and phase angle of the lift and moment coefficient versus reduced frequency and Mach number. Upon comparing this figure with figure 7.12 it can

be seen that for both figures the magnitude of the lift coefficient reaches a maximum for the lowest reduced frequencies as the reduced frequency increases however a minimum appears. The magnitude of the lift coefficient shows again a maximum near $M = 0.74$, as in the quasi-steady case (see section 6.4). When the Mach number is increased, the phase angle of the lift coefficient reaches a minimum for all reduced frequencies, when the reduced frequency is increased this minimum becomes less deep. The behaviour of the moment coefficient is as noted before completely different from that in the fully turbulent case. The magnitude has a maximum for the lowest reduced frequencies, whereas with increasing reduced frequency this maximum becomes a minimum. The phase angle reaches a minimum when the Mach number is increased, as in the fully turbulent case. The values attained at this minimum are however lower in case of free boundary layer transition. The global minimum is approximately 230 degree, whereas in case of fully turbulent boundary it is about 175°. The largest changes present in all curves now appear near $M = 0.74$, whereas in the fully turbulent case they occured at $M = 0.755$.

7.5.2 Plunging motion

In this section the results obtained for the plunging mode are shown. First, the results are shown in the time domain, after which the results are depicted in the frequency domain.

Time domain

Figure 7.19 shows the response of the lift and moment coefficient at $M = 0.65$, 0.74 and 0.745 versus the non-dimensional vertical distance. Curves for all reduced frequencies are shown. The arrows again indicate whether the curves have to be followed clockwise or counterclockwise. It is observed that the range of lift coefficients achieved decreases with increasing reduced frequency for all Mach numbers. The lift coefficient is leading the motion for all Mach numbers and reduced frequencies. For all Mach numbers this lead decreases with increasing reduced frequency, then a minimum is reached, after which the lead increases again. From the response of the moment coefficient it can be observed that again higher harmonic components are present. For the moment coefficient it can be seen that its range increases with reduced frequency at $M = 0.65$. For higher Mach numbers the range of moment coefficient first decreases and after a minimum at $k = 0.50$ it increases again. For even higher Mach numbers ($M > 0.745$), the magnitude increases and after reaching a maximum at $k = 0.30$ it decreases again. At the lowest Mach number the moment coefficient is leading the motion, this lead decreases with increasing reduced frequency. For the highest Mach numbers ($M \geq 0.745$) the phase angle decreases with increasing frequency (for $k > 0.5$ it increases again). The same holds for the other Mach number initially, then a minimum is reached however and the lag becomes less.

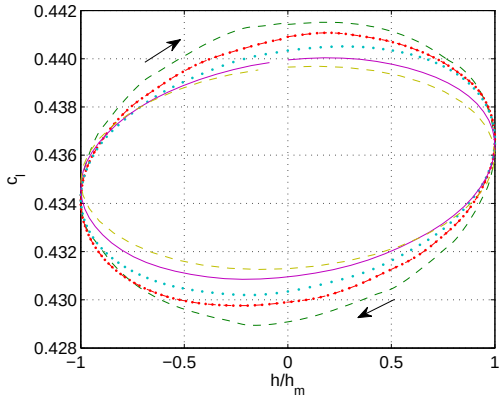

(a) Lift coefficient versus non-dimensional displacement $M = 0.65$

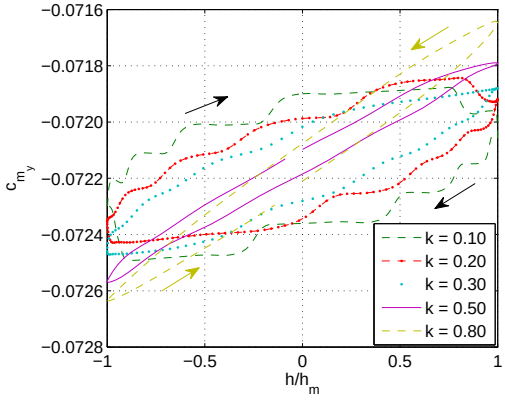

(b) Moment coefficient versus non-dimensional displacement $M = 0.65$

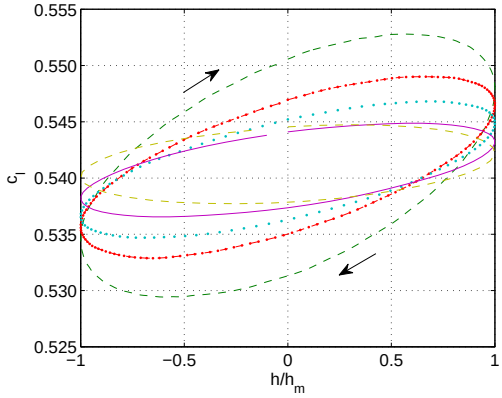

(c) Lift coefficient versus non-dimensional displacement $M = 0.74$

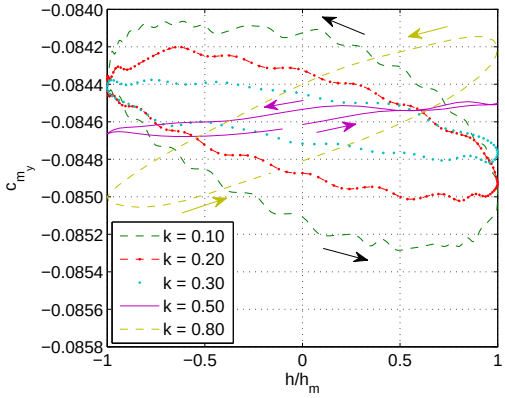

(d) Moment coefficient versus non-dimensional displacement $M = 0.74$

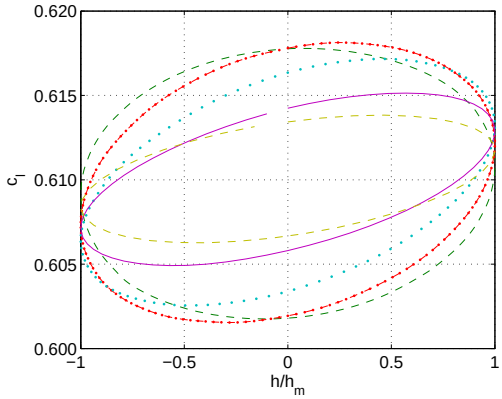

(e) Lift coefficient versus non-dimensional displacement $M = 0.745$

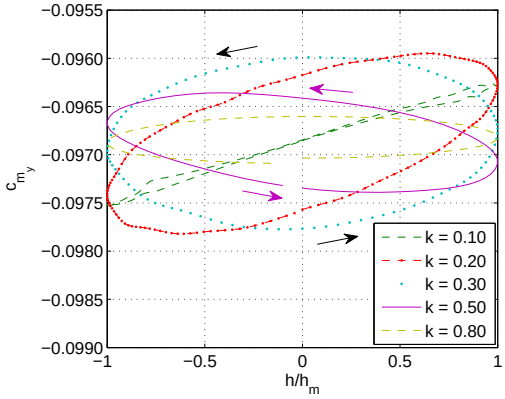

(f) Moment coefficient versus non-dimensional displacement $M = 0.745$

Figure 7.19: Lift and moment coefficient versus non-dimensional vertical displacement for the plunging motion at $M = 0.65$, 0.74 and 0.745 (free transition)

Upon comparing with the fully turbulent flow simulations (see figure 7.13) it can be seen

that the behaviour of the lift coefficient is the same (compare $M = 0.5$ vs. $M = 0.65$, $M = 0.755$ vs. $M = 0.74$ and $M = 0.765$ vs. $M = 0.745$). For the moment coefficient the behaviour is only the same at the lowest Mach number, as for the pitching motion. At $M = 0.74$ the behaviour is completely different as the range of moment coefficients achieved decreases and then increases, whereas for the fully turbulent flow simulations it increases with reduced frequency. Furthermore, the phase angle also behaves differently. At the highest Mach numbers, the range of moment coefficients increases for both fully turbulent and free transition simulations, then a maximum is however reached for the flow simulations with free transition, whereas in case of a fully turbulent boundary layer the magnitude keeps on increasing.

Frequency domain

The magnitude and phase angle for both lift and moment coefficient for all Mach numbers of the plunging motion are shown versus the reduced frequency in figure 7.20.

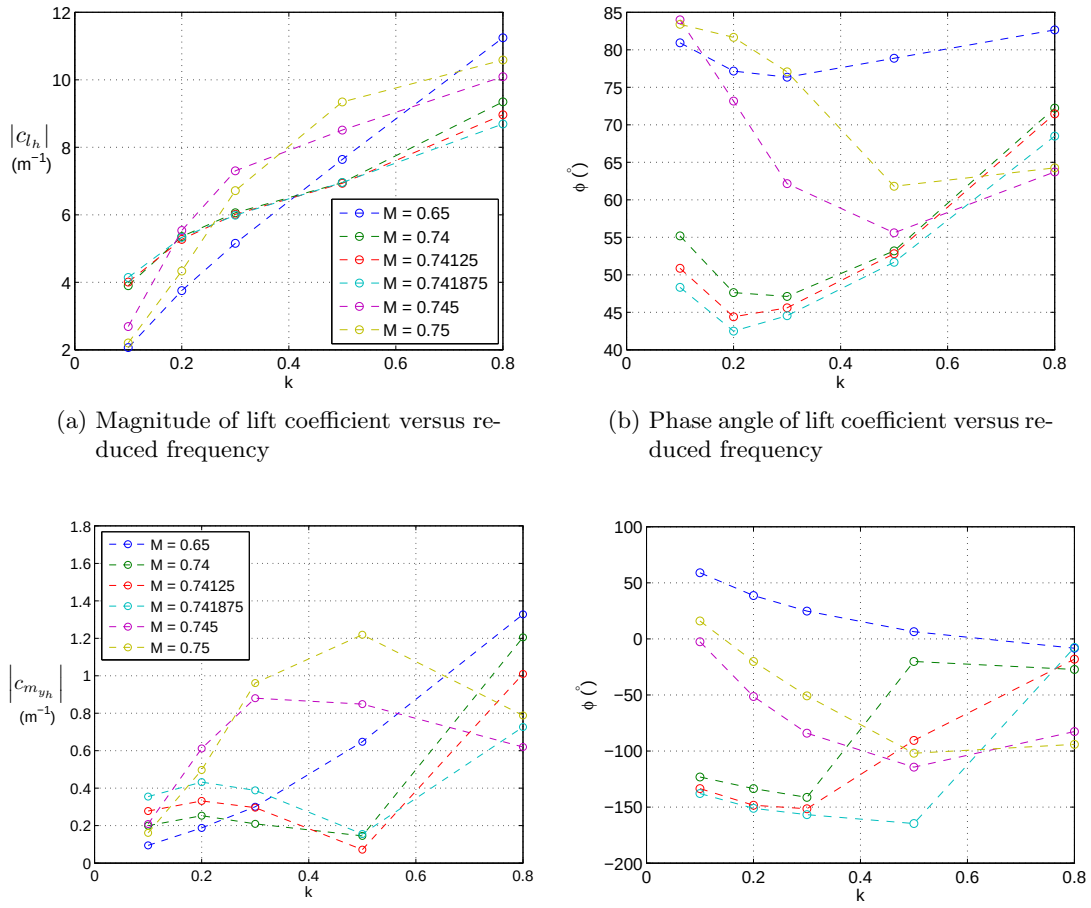

(a) Magnitude of lift coefficient versus reduced frequency

(b) Phase angle of lift coefficient versus reduced frequency

(c) Magnitude of moment coefficient versus reduced frequency

(d) Phase angle of moment coefficient versus reduced frequency

Figure 7.20: Magnitude and phase angle of lift and moment coefficient versus reduced frequency for all Mach numbers for the plunging motion (free transition)

Both magnitude and phase angle of the lift coefficient show the same trends as observed from figure 7.14 (fully turbulent flow simulations), i.e. the magnitude increases with increasing reduced frequency and the phase first decreases and then increases. The magnitude of the moment coefficient shows, as for the pitching motion, a different behaviour in comparison to the fully turbulent flow simulations, except at $M = 0.65$. As for the pitching motion a maximum is reached at the higher Mach numbers. At $M = 0.74$, $M = 0.74125$ and $M = 0.741875$ a minimum in magnitude appears at $k = 0.50$, after which the magnitude increases again. The phase angle decreases with increasing reduced frequency for the lowest and the highest Mach numbers. At the lowest Mach number this means that the moment coefficient goes from leading the motion to lagging the motion behind. This also holds for $M = 0.75$. At the remaining Mach numbers the phase angle first decreases and then increases for larger reduced frequencies.

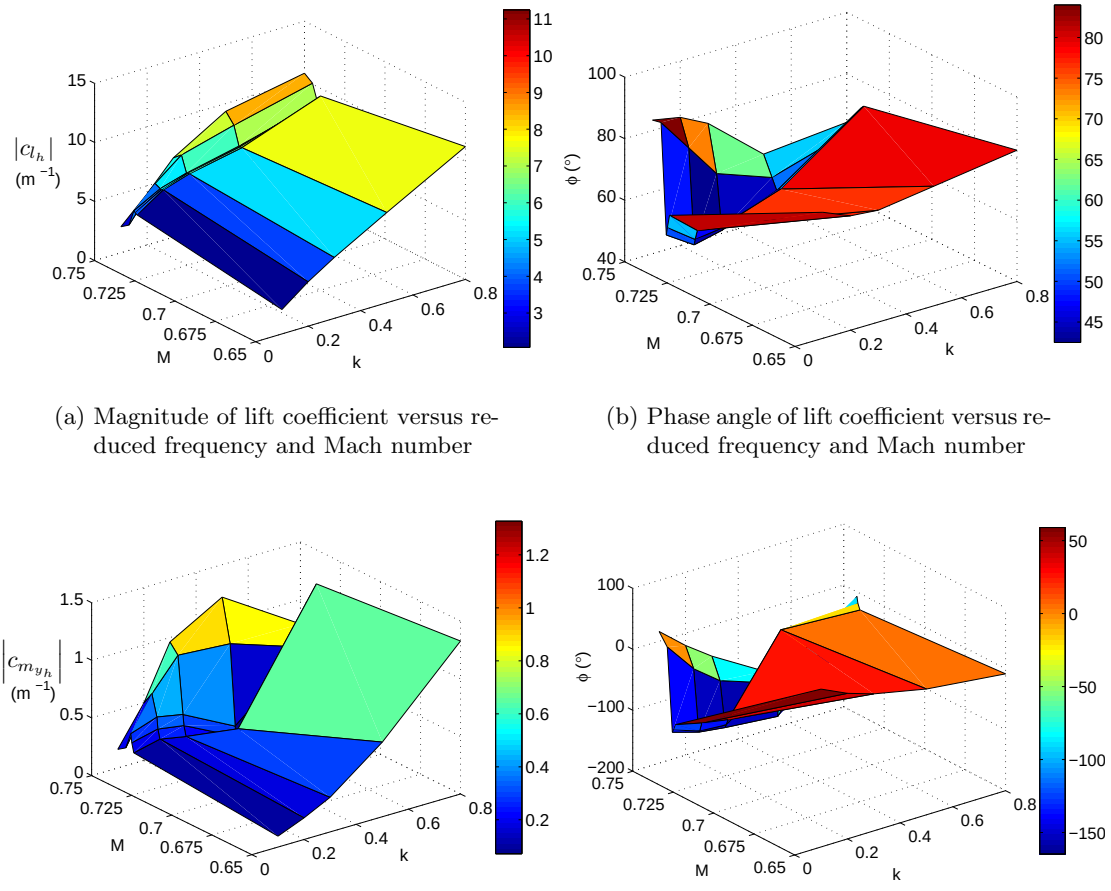

(a) Magnitude of lift coefficient versus reduced frequency and Mach number

(b) Phase angle of lift coefficient versus reduced frequency and Mach number

(c) Magnitude of moment coefficient versus reduced frequency and Mach number

(d) Phase angle of moment coefficient versus reduced frequency and Mach number

Figure 7.21: Magnitude and phase angle of lift and moment coefficient versus reduced frequency for all Mach numbers for the plunging motion (free transition)

Figures 7.21a and 7.21b depict the magnitude and phase angle of the lift coefficient as

a function of both Mach number and reduced frequency. Upon comparing these figures with figures 7.15a and 7.15b, it is noted that the trends observed are the same. That is, the magnitude tends to decrease with increasing Mach numbers after reaching a minimum it increases again. The same holds for the phase angle. The magnitude of the moment coefficient is highly irregular, for the lowest reduced frequencies a maximum is reached when the Mach numbers is increases, whereas at the higher reduced frequencies a minimum appears. The phase angle of the moment coefficient behaves only the same as the fully turbulent flow simulations for the highest reduced frequencies. The phase angle reaches much lower values in case of free boundary layer transition (-165° versus −90° for a fully turbulent boundary layer).

7.6 TAU-CFX comparison

This section shows a comparison between the results obtained with the DLR TAU code and those obtained with ANSYS CFX. Only the pitching mode is considered. Furthermore with CFX the unsteady flow simulations performed are limited to one Mach number ($M = 0.745$) and two reduced frequencies ($k = 0.20$ and $k = 0.30$). The amplitude of the pitching motion is 0.05° and the mean angle of attack is 0°.

7.6.1 Fully turbulent simulations

Figure 7.22 shows the lift and moment coefficient versus the angle of attack at $M = 0.745$ and both reduced frequencies for a fully turbulent boundary layer. It should be noted that based on a small investigation, the number of timesteps per period at $k = 0.20$ has been chosen to be 51, whereas 34 timesteps per period have been used at $k = 0.30$. The number of inner iterations used is 30. This number may seem small in comparison to the values used for TAU, but as CFX is an implicit solver, less iterations are needed to reach convergence. From these figures it is observed despite the difference in position the shape of the hysteresis loops of the lift coefficient are similar for both CFD codes. The difference in position can be explained by the fact that it is determined by the mean value of the lift coefficient (c_{l_0} in equation 3.17). This mean value is approximately equal to the corresponding steady lift coefficient, since the steady lift coefficients obtained from both CFD codes are already different by approximately 3% (see table F.1), the unsteady results can never be the same. From the moment coefficient-versus-angle of attack graphs it can be observed that, not only the position but also the shape of the moment coefficient loops is different for both CFD codes. The magnitude seems to be larger for the TAU code (by about 1% for $k = 0.20$ and by about 6% for $k = 0.30$), whereas the phase lag is 13% larger for the results obtained with CFX. This is probably caused by the fact that for the results from CFX, the moment coefficient is not fully converged at all timesteps, i.e. the value of the moment coefficient is not constant at the end of each timestep, especially near the minimum and maximum. This can be seen from figure 7.23. This figure should show a staircase-function, where the horizontal parts show the convergence at each timestep and the vertical parts are the jumps from one timestep to the next. This is however not the case near the maximum as shown in the zoom. Further investigations are needed to clarify this aspect.

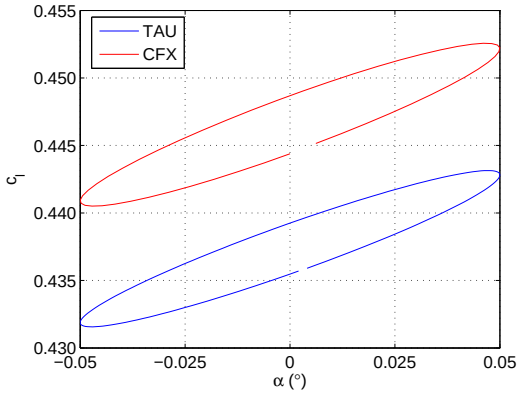

(a) Lift coefficient versus angle of attack $M = 0.745$, $k = 0.20$

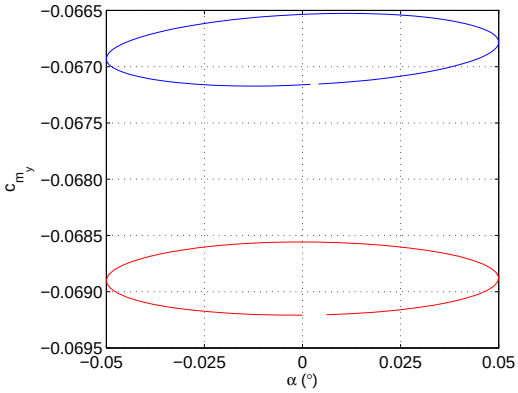

(b) Moment coefficient versus angle of attack $M = 0.745$, $k = 0.20$

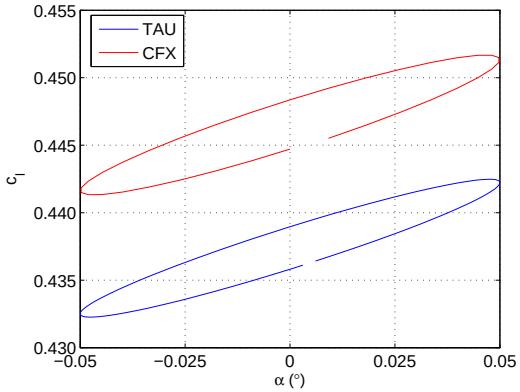

(c) Lift coefficient versus angle of attack $M = 0.745$, $k = 0.30$

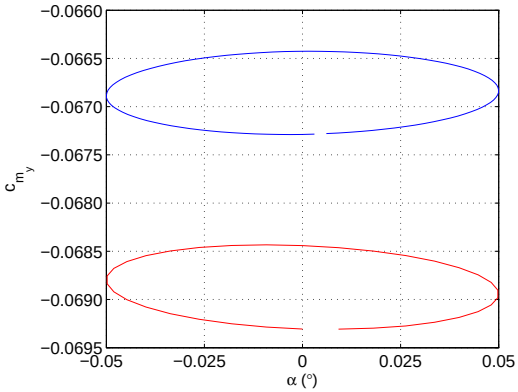

(d) Moment coefficient versus angle of attack $M = 0.745$, $k = 0.30$

Figure 7.22: Lift and moment coefficient versus angle of attack for the pitching motion at $M = 0.745$ and $k = 0.2$ and $k = 0.30$ (TAU = blue, CFX = red, fully turbulent)

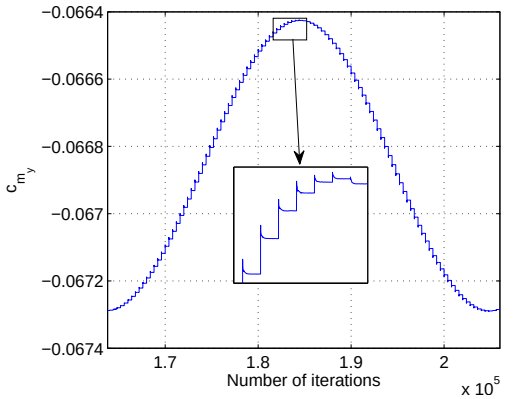

(a) TAU

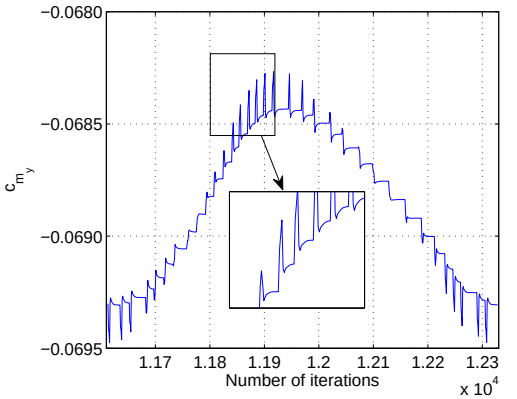

(b) CFX

Figure 7.23: Convergence of the pitching moment coefficient at each timestep (moment coefficient versus total number of (inner) iterations) at $M = 0.745$ and $k = 0.30$ (fully turbulent)

7.6.2 Free transition simulations

Simulations with free boundary layer transition have been performed at $M = 0.745$ as well. The reduced frequencies used are again 0.2 and 0.3. The results of these simulations are shown in figure 7.24. Initially, the same number of timesteps was used as in the fully turbulent case. This did however not lead to a fully converged lift and moment coefficient. Therefore the number of timesteps per period has been increased to 100 for both reduced frequencies, the number of inner iterations has been increased to 100 as well.

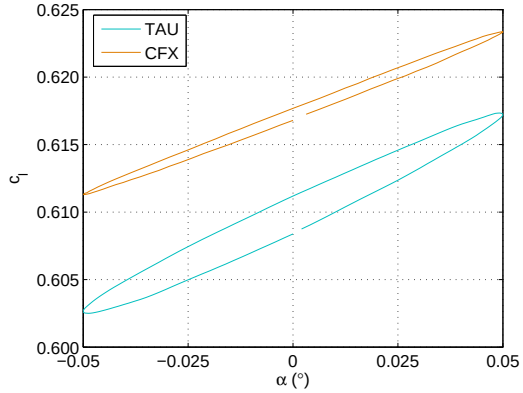

(a) Lift coefficient versus angle of attack $M = 0.745$, $k = 0.20$

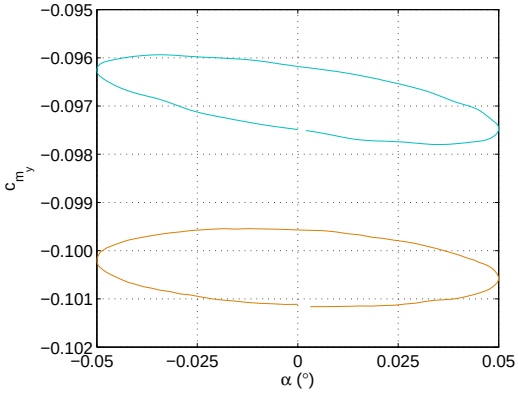

(b) Moment coefficient versus angle of attack $M = 0.745$, $k = 0.20$

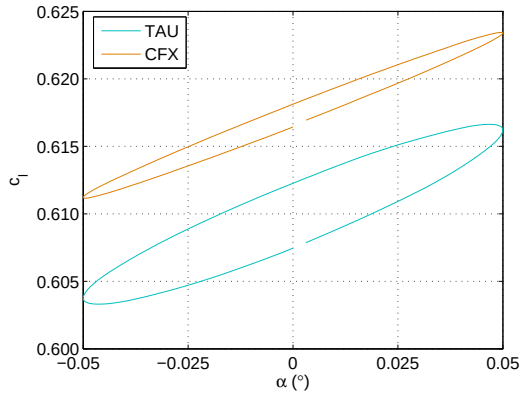

(c) Lift coefficient versus angle of attack $M = 0.745$, $k = 0.30$

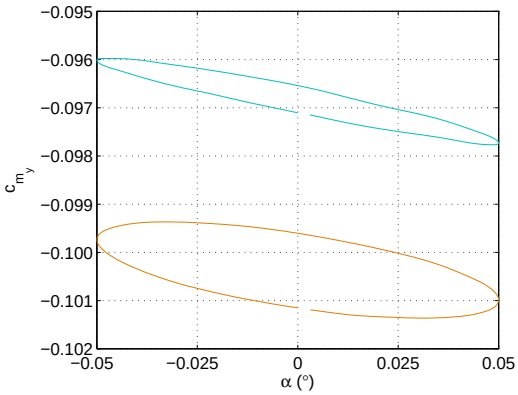

(d) Moment coefficient versus angle of attack $M = 0.745$, $k = 0.30$

Figure 7.24: Lift and moment coefficient versus angle of attack for the pitching motion at $M = 0.745$ and $k = 0.2$ and $k = 0.30$ (TAU = blue, CFX = red, free transition)

From these figures it is observed that apart from the position, the shape of the hysteresis loops is now also clearly different. For the lift coefficient, the magnitude is much larger (18% for $k = 0.20$ and about 8% for $k = 0.30$) for the results obtained from TAU, whereas the difference in phase angle is approximately 60%. The magnitude of the moment coefficient is larger for CFX, at least for the highest reduced frequency it is about 11%

larger, whereas the phase lag is larger for the moment coefficient obtained from TAU (about 22% and 52% for $k = 0.20$ and $k = 0.30$, respectively). This behaviour of the moment coefficient is opposite of that obtained in case of a fully turbulent boundary layer. From the steady pressure and skin friction distributions at $M = 0.745$ (see figures 6.6c and 6.6d) it can be seen that the transition location is clearly different for both CFD codes, explaining the different positions of the lift and moment coefficient loops. The differences in magnitude and phase angle are thought to be caused by the different transition locations as well as by the bad convergence of both lift and moment coefficient at each timestep. When looking at the convergence history of the results obtained from the CFX code, it is seen that the lift and moment coefficient are not fully converged at each timestep and hence wrong results might be obtained since each timestep is started from the solution of the previous timestep. Therefore, a temporal convergence study has to be performed with CFX as well as an investigation into the differences in transition locations obtained from both CFD codes.

Chapter 8

Flutter Behaviour of the Original CAST-10 Airfoil

The aerodynamic coefficients obtained from the unsteady simulations with the DLR TAU code have been used as input for the calculation of the flutter boundary. This chapter first shows the structural parameters used. Next the frequency and damping curves are displayed, after which the flutter boundary is shown. Finally, the aerodynamic forces at flutter are shown and discussed.

8.1 General set-up

In order to compute the frequency and damping curves as well as the flutter boundary from the results of unsteady CFD simulations, the procedure as outlined in section 3.3.5 has been used. The structural parameters used are those of a wind tunnel model used by Dietz et al. [2004] in their wind tunnel experiments. These parameters are depicted in table 8.1.

Structural parameter	Value
Mass m	26.268 kg
Mass moment of inertia I_α	0.079 kg/m^2
Torsional spring constant K_α	$6.646 \cdot 10^3$ Nm/rad
Vertical spring constant K_h	$1.078 \cdot 10^6$ N/m
Static moment related to EA S_α	0.331 kgm
Pitch-damping coefficient δ_α	0.15%
Plunge-damping coefficient δ_h	0.43%
Radius of gyration about EA	0.1828

Table 8.1: Structural parameters used calculation of the flutter boundary

The range of the flutter indices has been set from 0.05 to 0.4 (in 50 steps), as flutter is expected in this range. For the fully turbulent flow simulations the real and imaginary parts of the aerodynamic coefficients at 7 Mach numbers ($M = 0.5$, 0.745, 0.75, 0.755, 0.76, 0.765 and 0.8) and 6 reduced frequencies ($k = 0.05$, 0.10, 0.20, 0.30, 0.50 and 0.80) have been used as input to the flutter program, whereas 6 Mach numbers ($M = 0.65$, 0.74, 0.74125, 0.741875, 0.745 and 0.75) and 5 reduced frequencies ($k = 0.10$, 0.20, 0.30, 0.50 and 0.80) have been used in case of free boundary layer transition.

8.2 Frequency and damping curves

Figure 8.1 shows the frequency and damping curves versus the flutter index for both degrees of freedom for both the fully turbulent as well as the simulations with free boundary layer transition. The continuous lines represent the pitching mode and the dashed lines represent the plunging mode. Positive damping indicates an unstable motion.

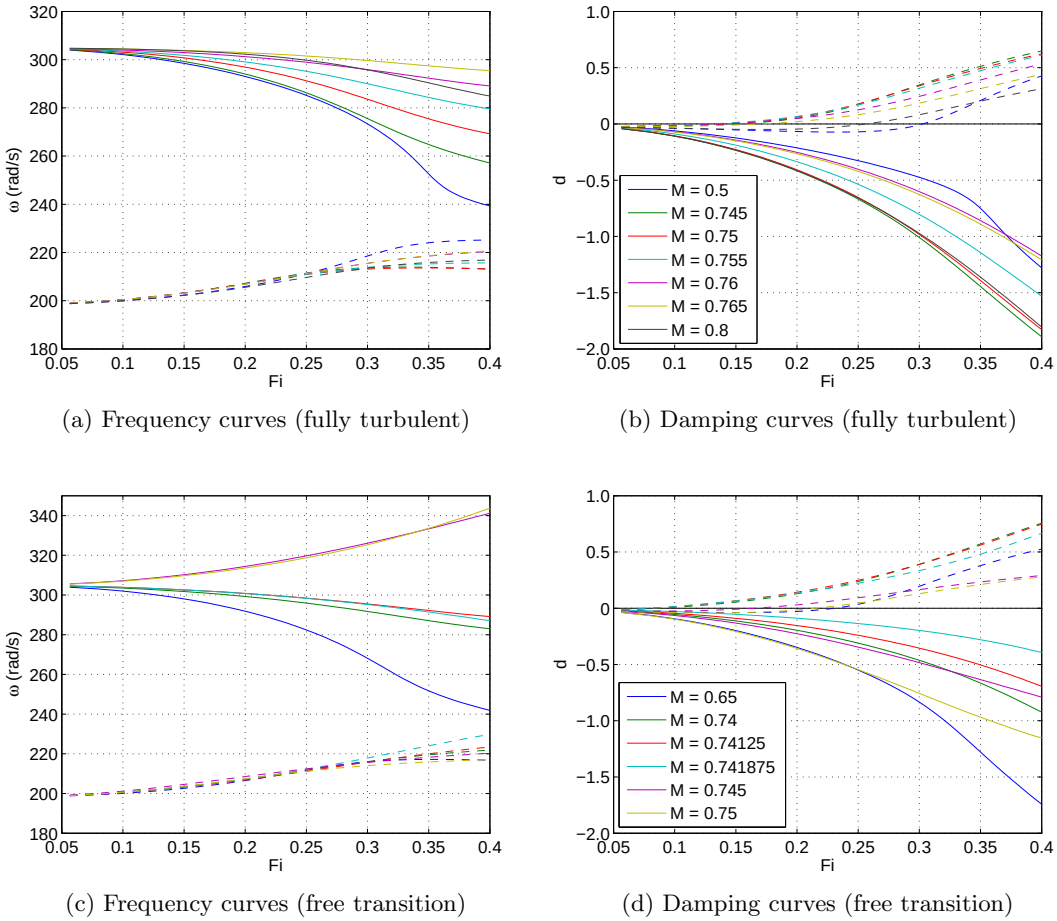

(a) Frequency curves (fully turbulent)

(b) Damping curves (fully turbulent)

(c) Frequency curves (free transition)

(d) Damping curves (free transition)

Figure 8.1: Frequency and damping curves versus flutter index for both the pitching (continuous) and plunging mode (dashed)

From the frequency curves it can be observed that the frequency of the plunging mode

increases with increasing flutter index. When boundary layer transition is free the frequency of the pitching mode at the two highest Mach numbers grows, whereas at all other Mach numbers and when the boundary layer is fully turbulent, the frequency of the pitching mode decreases. When the damping curves are analysed one observes that the damping is always negative for the pitching mode, that is, the pitching mode is never amplified and hence always stable. For the plunging mode the damping is first negative, then it becomes positive between $Fi = 0.10$ and $Fi = 0.35$ for all Mach numbers when the boundary layer is fully turbulent. In case of free boundary layer transition, the damping becomes positive between $Fi = 0.05$ and $Fi = 0.25$. Hence, the plunging mode clearly becomes unstable at lower flutter indices in case of free boundary layer transition.

8.3 Flutter boundary

The point at which the damping curves cross the horizontal axis marks the boundary between stable and unstable motions. The corresponding flutter index has been computed and is plotted versus the Mach number in figure 8.2. For comparison the flutter boundary obtained from unsteady CFD simulations (with the TAU code) using the two-equation k-ω Linear Explicit Algebraic (LEA) with the NLR 7301 airfoil as performed by Verdon [2004] is included in this graph. Furthermore, the flutter boundary obtained from experiments with the NLR 7301 airfoil performed by Dietz et al. [2004] has been included. They performed wind tunnel tests with a pitching and a plunging airfoil and used the time signals of the lift and moment coefficient to determine the flutter boundary (same procedure as outlined in section 3.3.5). These aerodynamic loads were determined in two ways: by integrating the pressure distribution as obtained from pressure transducers (denoted with measured pressure in figure 8.2) and by using the integral forces and moment obtained from a balance measurement (denoted by measured balance). It should be noted that the structural model that has been used is the same in all cases (see table 8.1).

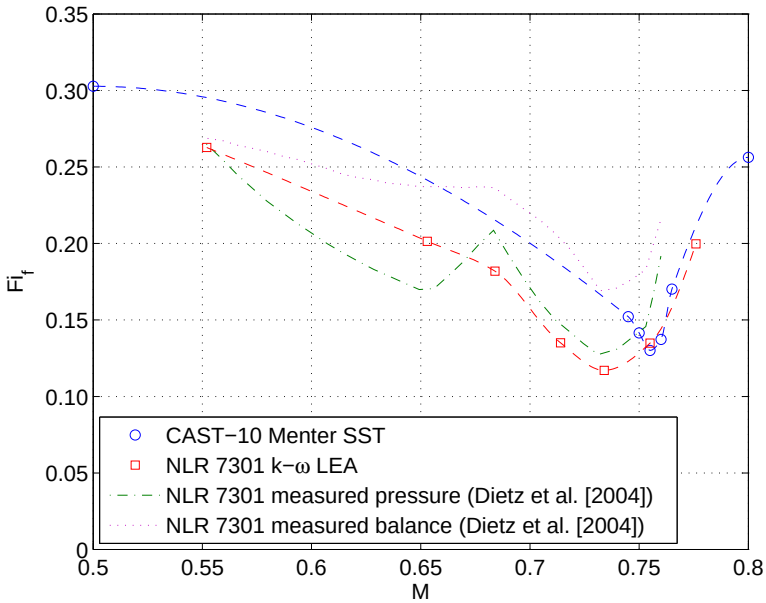

Figure 8.2: Flutter index at flutter versus Mach number

From figure 8.2 it can be seen that the flutter index at which flutter occurs decreases with increasing Mach number. At $M = 0.755$ the flutter index at which flutter occurs is minimum (for the CAST-10 airfoil), when the Mach number increases further the flutter index at flutter increases again. Hence, there is a so-called "transonic dip" in the flutter boundary. From the flutter boundaries of the NLR 7301 airfoil it can be seen that the range of flutter indices at which flutter occurs is approximately the same, indicating that the DLR TAU code is in principle able to predict the correct flutter indices range. Furthermore, it can be seen that the location of the transonic dip is at a higher Mach number for the CAST-10 airfoil than for the NLR 7301 airfoil (for which the transonic dip obtained from unsteady simulations with TAU, the red points in figure 8.2, is located at $M = 0.734$). The transonic dip is also less deep for the CAST-10 airfoil. When the TAU results are compared the flutter index at flutter at the transonic dip is 0.13 for the CAST-10 airfoil and approximately 0.12 for the NLR 7301 airfoil. These differences can only be caused by different aerodynamics, since the structural parameters are the same. It should be noted that there are also some differences between the two flutter boundaries obtained from unsteady measurements and the computed flutter boundary for the NLR 7301 airfoil, according to Dietz et al. [2004] these might be explained by the fact that there was a small torsion of the model during the experiments (see Dietz et al. [2004] for more details). The reduced frequency at which flutter occurs is approximately 0.24 for all Mach numbers, except for the lowest Mach number, at $M = 0.5$ the reduced frequency at flutter is around 0.4.

The flutter boundary obtained in case of free boundary layer transition is shown in figure 8.3, where for reference the flutter boundary obtained from the fully turbulent flow simulations is also shown.

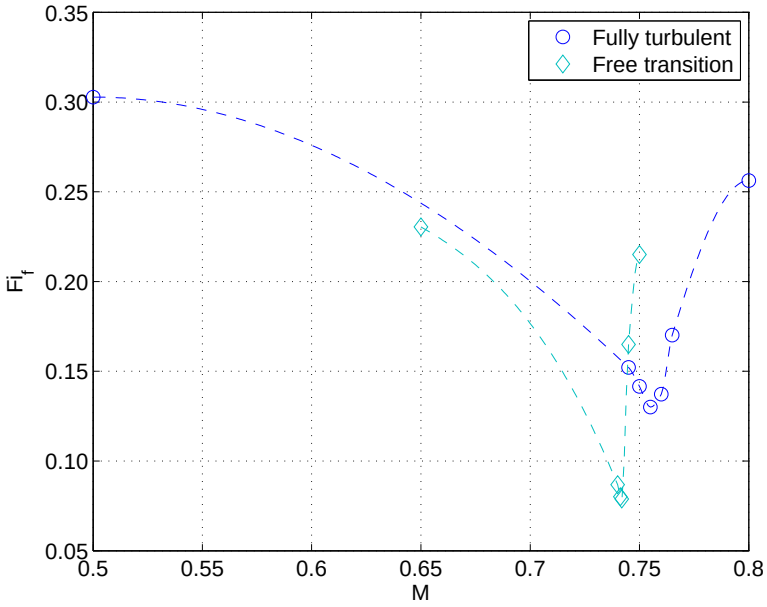

Figure 8.3: Flutter index at flutter versus Mach number

This figure shows that the influence of free boundary layer transition is large. The tran-

sonic dip occurs at $M = 0.741875$ in case of free boundary layer transition. Not only the location of the transonic dip is shifted towards lower Mach numbers, it is also much deeper ($Fi_f = 0.08$ versus $Fi_f = 0.13$). This indicates that, near the transonic dip, the motion of the airfoil becomes unstable at a lower speed or dynamic pressure in case of free boundary layer transition. Furthermore, the width of the dip is much smaller, hence small changes in Mach number will have a great influence on the stability of the airfoil, when at flying speeds near the transonic dip. The reduced frequencies at which flutter occurs are approximately equal to those obtained for a fully turbulent boundary layer, that is between approximately 0.24 and 0.25 for all Mach numbers, except at $M = 0.65$, at which the reduced frequency at flutter is approximately 0.29.

It should be noted that in this thesis the influence of boundary layer transition has been investigated on one airfoil only. Hence, further investigations (numerical as well as experimental) are necessary, these have to show if the flutter behaviour as that observed in this thesis also occurs for other airfoils or other mean angles of attack.

8.4 Comparison to the quasi-steady results

In order to compare the flutter boundary with the quasi-steady curve shown in section 6.4, they have been plotted in one graph in figure 8.4.

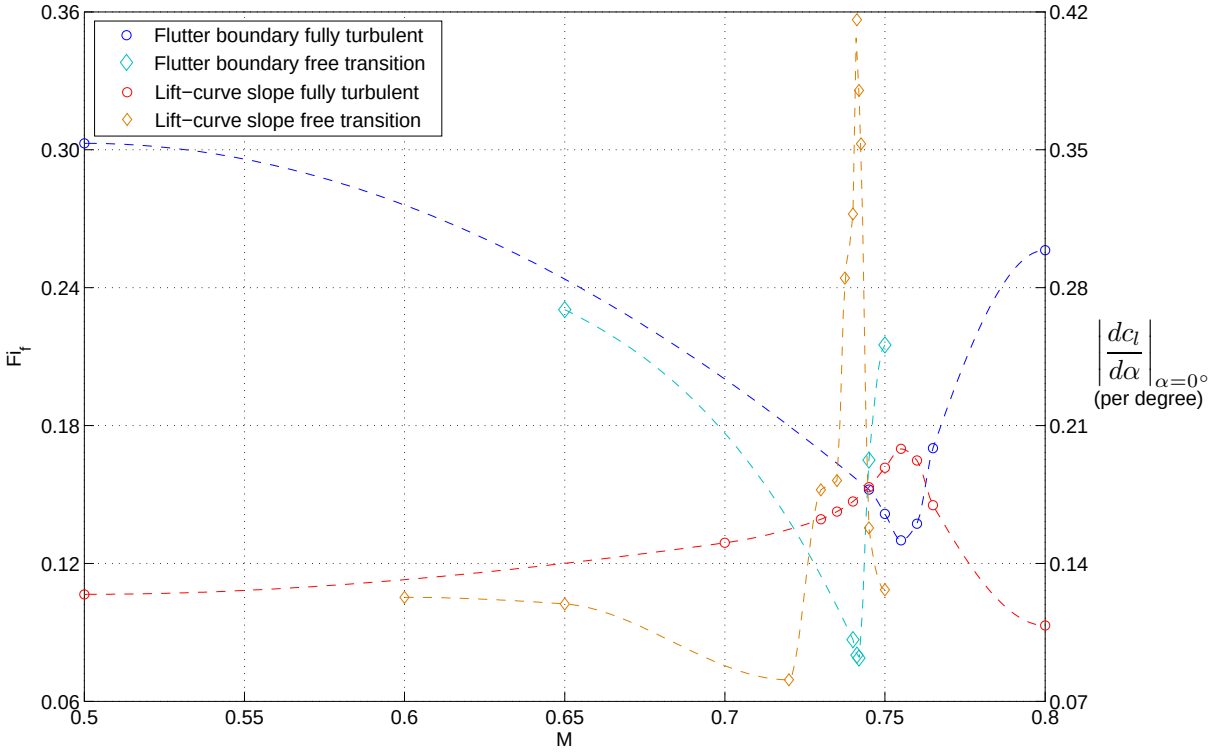

Figure 8.4: Flutter boundary and quasi-steady lift curve slope versus Mach number

In this figure, the blue symbols are the flutter boundaries (the left vertical axis corre-

sponds to these symbols) and the red and orange symbols are the quasi-steady lift curve slopes (the right vertical axis corresponds to these symbols). The dashed lines have been obtained by spline interpolation.

From figure 8.4 it can be observed that, in case of a fully turbulent boundary layer, the transonic dip occurs at the same Mach number as the maximum of the quasi-steady lift-curve slope, namely at $M = 0.755$. In case of free transition, the dip is shifted slightly with respect to the quasi-steady lift-curve slope (the dip is located at $M = 0.741875$ and the peak at $M = 0.74125$). It should however be noted that the lift-curve slope at the maximum was obtained from forward differences and hence might not be correct. Furthermore, it can be seen that the width of the transonic dip is also equal to the width of the peak in quasi-steady lift curve slope. In the case of free boundary layer transition it can be seen that the quasi-steady lift-curve slope is lower than in case of a fully turbulent boundary layer for subsonic Mach numbers. This is however not reflected in the flutter boundary, as the flutter index at $M = 0.65$ is with 0.23 smaller than in case of a fully turbulent boundary layer where $Fi_f = 0.24$ (predicted by spline interpolation). Furthermore, there is a minimum at $M = 0.72$ in the quasi-steady lift-curve slope, which is however not reflected in the flutter boundary. From the unsteady flow simulations performed at this Mach number, no converged results could however be obtained, since the time history of the transition location showed random (non-physical) oscillations. Hence, in order to check whether the flutter boundary shows a maximum at $M = 0.72$, further investigations need to be performed.

This section has shown that the location and the width of the transonic dip can already be determined from the quasi-steady lift curve slope. The depth of the dip, that is the minimum value of the flutter index at which flutter occurs, can however not be obtained from the quasi-steady lift curve slope plot.

8.5 Aerodynamic forces at flutter

8.5.1 Fully turbulent

Figures 8.5 and 8.6 show the magnitude and phase angle of the aerodynamic loads at the flutter frequency. These have been obtained by linear interpolation between the reduced frequencies around the flutter reduced frequency. The dashed lines have been obtained by linear interpolation between the values obtained for the aerodynamic loads at the flutter frequency. The reduced flutter frequency is approximately 0.24 for all Mach numbers, except for $M = 0.5$ for which the reduced frequency at which flutter occurs is approximately 0.4.

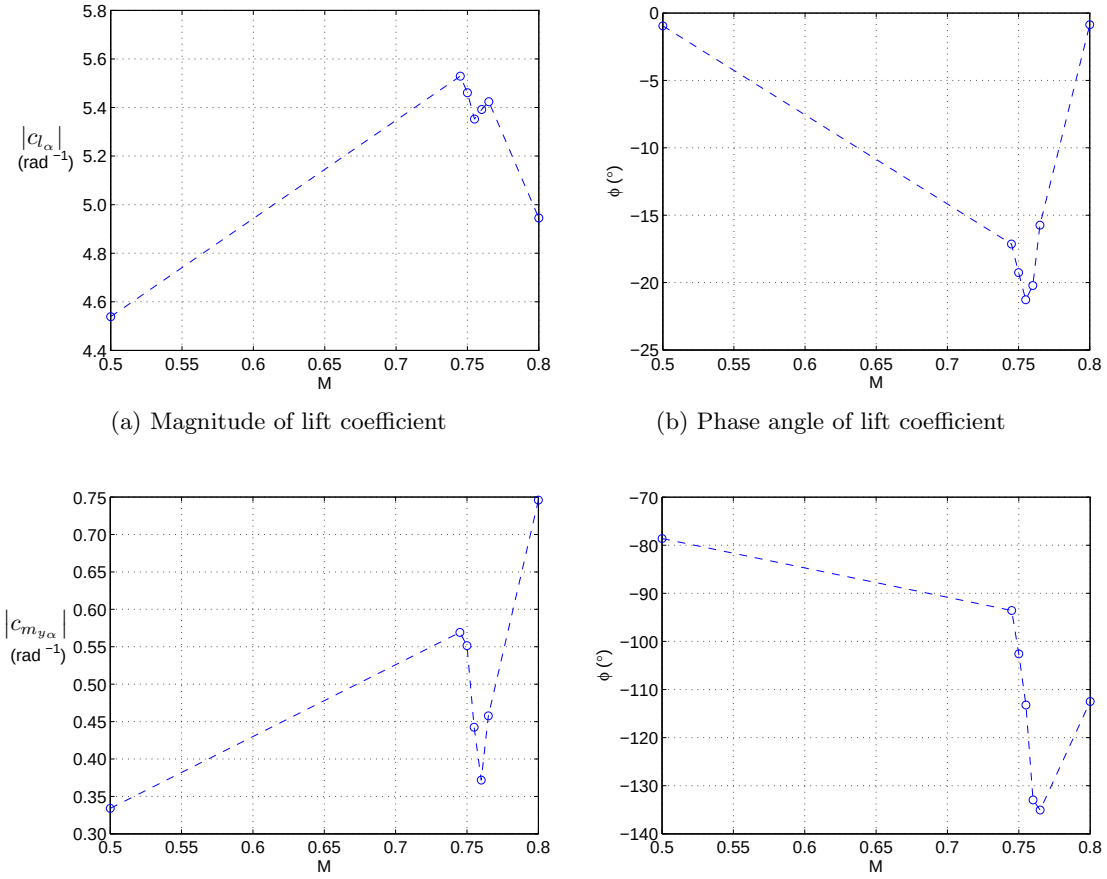

(a) Magnitude of lift coefficient

(b) Phase angle of lift coefficient

(c) Magnitude of moment coefficient

(d) Phase angle of moment coefficient

Figure 8.5: Magnitude and phase of the generalised airloads of the pitching mode versus Mach number at flutter (fully turbulent)

From figures 8.5 and 8.6 it is clear that large changes occur around $M = 0.755$, that is, at the location of the transonic dip. For the pitching mode, both the magnitude and phase angle of the lift coefficient, as well as the magnitude of the moment coefficient exhibit a minimum at this Mach number. The phase angle of the moment coefficient shows a minimum at a higher Mach number. The plunging mode shows the same behaviour except for the magnitude of the lift coefficient. These large changes are thought to be caused by shock dynamics. As explained in section 3.2, the shock wave on the airfoil moves aft when the Mach number increases, however at a certain Mach number its motion reverses.

Figures 8.5a till 8.6d have been compared to the measurements of Dietz et al. [2004]. It was found that only the magnitude of the plunge mode behaves slightly different. From figure 7.14a it can however be seen that the magnitude of the lift coefficient for the plunging mode is approximately 6 near $k = 0.4$ (the reduced frequency at which flutter occur is $k = 0.39$ at $M = 0.5$). The remaining coefficients show the same behaviour as that observed by Dietz et al. [2004]. Dietz et al. [2004] compare their results to those of the theoretical case of a flat plate. They found that when using the theoretical values of the magnitude and phase angle of all aerodynamics coefficients and only replacing

the phase angle of the lift coefficient for the pitching mode by that found from their experiments, the qualitative behaviour of the flutter boundary resembles that obtained from the measurements. Therefore Dietz et al. [2004] suggest that this phase lag causes the appearance of the transonic dip, as claimed earlier by O. Bendiksen [1992]. Furthermore, Dietz et al. [2004] note that the response of the lift coefficient (for the pitching motion) tends to get in phase with the plunge motion (that is, the trend of the phase angle is to decrease to $-90°$), causing the lift to do work on the airfoil, i.e. energy is added to the motion of the structure.

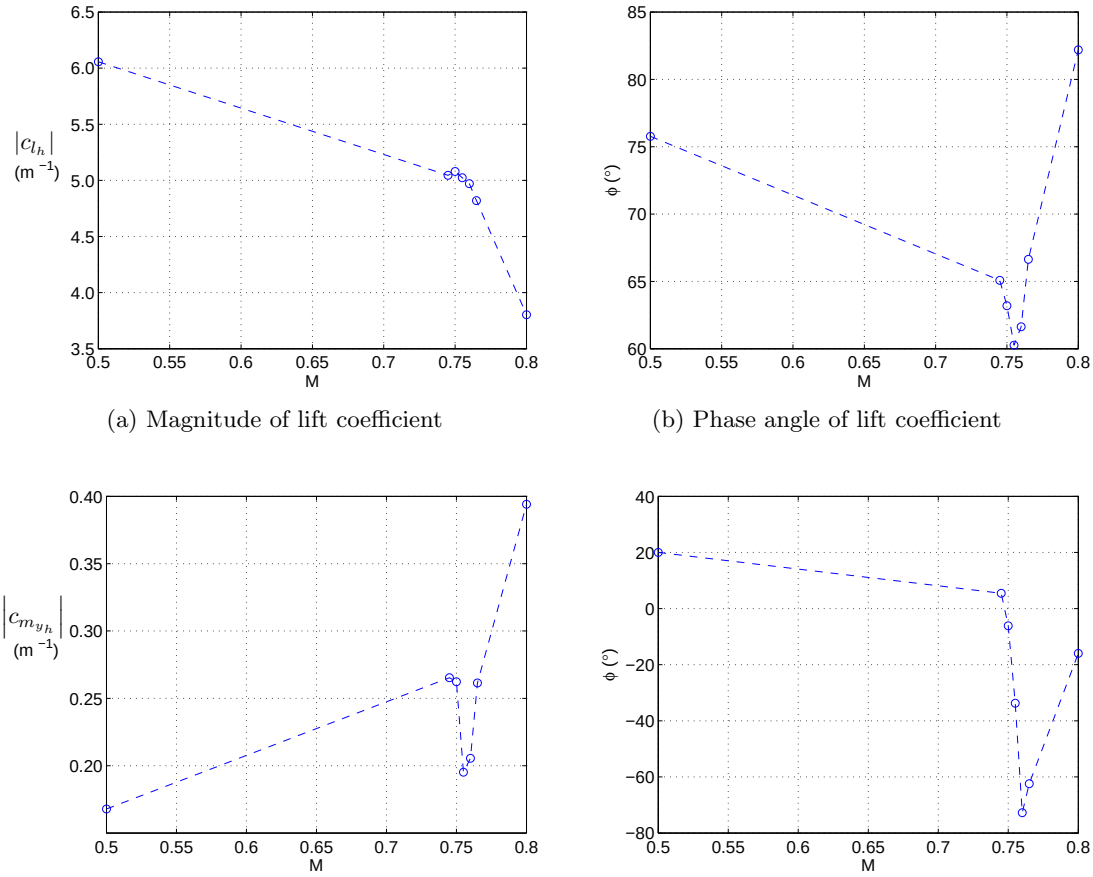

(a) Magnitude of lift coefficient

(b) Phase angle of lift coefficient

(c) Magnitude of moment coefficient

(d) Phase angle of moment coefficient

Figure 8.6: Magnitude and phase of the generalised airloads of the plunging mode versus Mach number at flutter (fully turbulent)

8.5.2 Free transition

Figures 8.7 and 8.8 show the magnitude and phase angle of the aerodynamic loads at the flutter frequency in case of free boundary layer transition. At $M = 0.65$ the reduced flutter frequency is 0.29, for the remaining Mach numbers it is between 0.24 and 0.25.

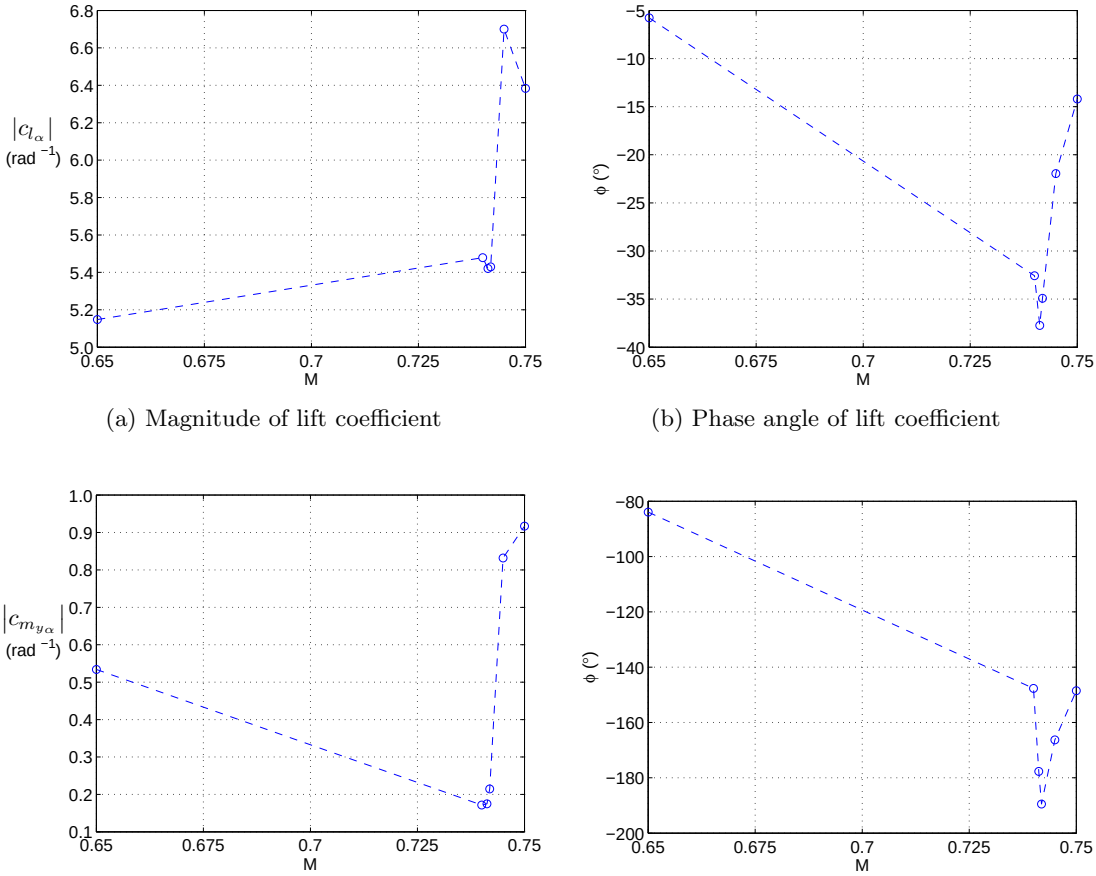

(a) Magnitude of lift coefficient

(b) Phase angle of lift coefficient

(c) Magnitude of moment coefficient

(d) Phase angle of moment coefficient

Figure 8.7: Magnitude and phase of the generalised airloads of the pitching mode versus Mach number at flutter (free transition)

From figures 8.7 and 8.8 it can be seen that the magnitude and phase angle of the lift and moment coefficient for pitching mode resemble those obtained in case of a fully turbulent boundary layer. Except for the magnitude of the moment coefficient, which does not show a maximum in case of free transition. The minima present in all curves are obtained near $M = 0.741875$. For the plunging mode the phase angle and the magnitude of the lift coefficient resemble those obtained for the fully turbulent simulations. The magnitude of the moment coefficient attains a minimum as for the fully turbulent simulations, but no real dip is present. From the magnitude of lift and moment coefficient of both modes, it is observed that in case of free boundary layer transition larger values are reached in comparison to the fully turbulent case. The range of phase angles achieved is also larger in case of free boundary layer transition. When the transonic dip is caused by the phase lag of the lift coefficient of the pitching mode, this might be an explanation for the deeper transonic dip in case of free boundary layer transition, as the phase angle of the lift coefficient of the pitching mode is closer to $-90°$ in case of free boundary layer transition.

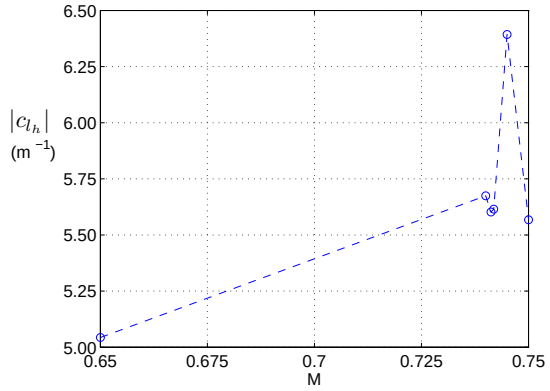

(a) Magnitude of lift coefficient

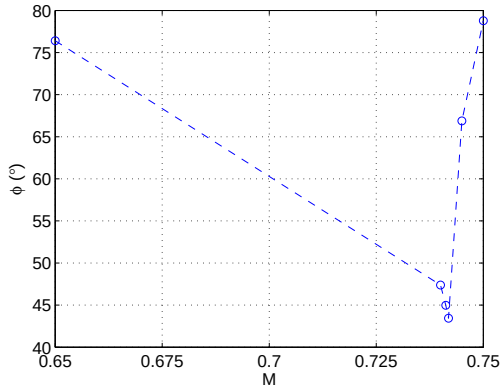

(b) Phase angle of lift coefficient

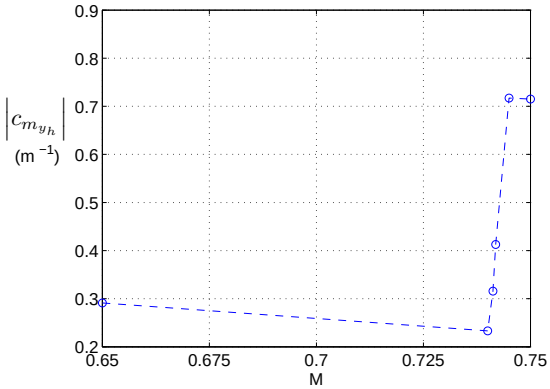

(c) Magnitude of moment coefficient

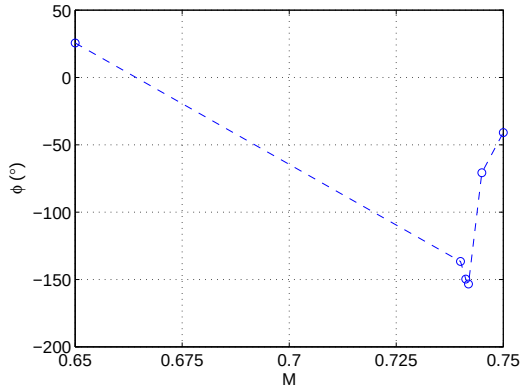

(d) Phase angle of moment coefficient

Figure 8.8: Magnitude and phase of the generalised airloads of the plunging mode versus Mach number at flutter (free transition)

Chapter 9

Conclusions

The influence of laminar to turbulent boundary layer transition on the flutter behaviour of a laminar supercritical airfoil has been investigated in this thesis. In order to do so numerical simulations, both steady and unsteady, were performed. The unsteady flow simulations were used to determine the flutter behaviour of the CAST-10 airfoil.

The steady flow simulations with the deformed airfoil geometries have shown that, when the airfoil has deformed itself during wind tunnel experiments, this deformation needs to be taken into account during CFD simulations as well. Doing this leads to results comparable to those obtained in wind tunnel experiments. Furthermore, the effect of deformation reduces with Mach number. At $M = 0.5$ the difference in pressure distribution between the deformed and undeformed airfoil is small.

From the steady flow simulations with free and fixed boundary layer transition (fixed at the airfoil's leading edge), it can be concluded that the difference in pressure and skin friction distributions is large when the flow is transonic. In the subsonic cases the pressure distributions are almost identical. It was observed that the shock wave that is formed above the airfoil is much stronger when boundary layer transition is free, if the freestream Mach number is the same. In case of a transonic freestream flow, the shock wave seems to fix the transition onset location of the boundary layer. Quasi-steady flow simulations were performed to estimate the location of the transonic dip. The lift curve slope turned out to be highly non-linear in case of free boundary layer transition. From the lift-curve slope versus Mach number graphs it can be concluded that the location of the peak is shifted to a lower Mach number in case of free boundary layer transition, since the peak is located at $M = 0.74125$ when boundary layer transition is free and at $M = 0.755$ (for TAU) when the flow is fully turbulent. Therefore it is expected that the transonic dip in the flutter boundary is located at a lower Mach number when boundary layer transition is free. Furthermore, the quasi-steady lift-curve slope graph has also shown that the transonic dip is expected to be much deeper in case of free boundary layer transition, since, in that case, the peak in lift-curve slope is more than twice as high as in case of a fully turbulent boundary layer. From the comparison between the results of both CFD codes it can be concluded that the agreement is excellent when the flow is fully turbulent

(except for the position of the shock). The pressure and skin friction distributions show however less agreement when boundary layer transition is free, at least not in subsonic cases, which might be explained by the empirical correlations of the γ-Re_θ transition model implemented in ANSYS CFX.

The results of the unsteady flow simulations performed with TAU show that in case of free boundary layer transition, the transition onset location varies harmonically for some Mach numbers, whereas for others it varies stepwise, this is caused by the mesh. Furthermore, the hysteresis loops show that higher harmonical components come into play in case of free transition, that is, the response of the airfoil to a sine change in angle of attack (or vertical displacement) is not a pure sine or cosine. Upon comparing the response of the airfoil in case of free and fixed transition, it is clear that the behaviour of both magnitude and phase angle of the lift coefficient is approximately the same for both free and fixed transition, at Mach numbers that show comparable steady pressure distributions. From the response of the moment coefficient of both modes, it was however observed that the behaviour of the magnitude as a function of reduced frequency is very different. The phase angle shows the same behaviour, the phase lag is however much larger in case of free boundary layer transition for both pitching and plunging mode. This also holds for the phase angle of the lift coefficient of the pitching motion. From a comparison of the results obtained with TAU and CFX, it can be concluded that the fully turbulent results show good agreement, taking into account the differences in steady lift and moment coefficient. The differences in the moment coefficient versus angle of attack graphs, as well as the hysteresis loops of the lift and moment coefficient in case of free boundary layer transition, are larger. This is most likely caused by the fact that the results obtained with CFX are not fully converged at each timestep and in the case of free transition by the differences in the predicted transition locations.

The frequency and damping curves obtained from the CFD results (of TAU) with both free and fixed transition show slightly different behaviour. The plunging mode is however unstable in both cases. The flutter index, a non-dimensional parameter that includes the effects of velocity, altitude and structural density on flutter, at which the damping becomes positive (i.e. at which the motion becomes unstable) is however much lower in case of free boundary layer transition. At the transonic dip the flutter index at which flutter occurs is 0.08 in case of free boundary layer transition and 0.13 in case of a fully turbulent boundary layer. Hence, the transonic dip is much deeper when boundary layer transition is free. Furthermore, its location is shifted to a lower Mach number ($M = 0.741875$) than when the boundary layer is completely turbulent (in which case the transonic dip is located at $M = 0.755$). However, since this is only a first investigation these conclusions are drawn with caution. The flutter boundary obtained from CFD simulations compares well (in terms of flutter indices achieved) to experimental values obtained from wind tunnel experiments with the NLR 7301 airfoil. Upon comparing with the quasi-steady lift-curve slope graph it can be concluded that the location and the width of the transonic dip can already be estimated from the quasi-steady flow simulations. From the values of the magnitude and phase angle of the lift and moment coefficient at flutter, it can be concluded that the phase lag of the lift coefficient during the pitching motion might be responsible for the differences in flutter boundary, as this phase lag is much larger in case of free transition.

Chapter 10

Recommendations

Although this thesis has given a very satisfactory answer to the main question, it is only a first step. Future investigations into the influence of boundary layer transition on the flutter behaviour of an airfoil are necessary.

For comparison between TAU and CFX it is clear that investigations into the deviations in case of free boundary layer transition are necessary. Furthermore, more simulations with both TAU and CFX need to be performed in order to investigate the non-linearities in the force and moment coefficient curves with free boundary layer transition. Furthermore, some research is needed into the variation of the transition location in the unsteady case. Finer meshes should be tried and a larger amplitude variation should be performed. For better comparison of the unsteady results obtained from both CFD codes, a temporal independency study needs to be performed with CFX, such that the results of unsteady flow simulations with both CFD codes can be compared. More unsteady flow simulations need to be performed with the TAU code as well, such that the flutter boundary has more base points to rely on. Especially in case of free boundary layer transition. Further investigations are also needed to prove the hypothesis about the differences in location and depth of the transonic dip between fixed and free boundary layer transition. Finally, the influence of aerodynamic (such as the turbulence model) and structural parameters of the airfoil needs some attention.

Recommendations for future research are, to perform the same research with another supercritical laminar airfoil, perhaps one that is more often used in the aviation industry. To make the investigation more realistic, an airfoil with the same thickness as the laminar airfoil can be used for comparison with the fully turbulent case. Furthermore, experiments are also needed to check the results obtained from the CFD simulations. Finally, in order to be able to apply the results to real aircraft, investigations with a three-dimensional wing or even a half-aircraft model are needed (in which the effect of cross-flow instabilities on the transition onset behaviour are also taken into account).

References

4th aiaa cfd drag prediction workshop. (2008, November). http://aaac.larc.nasa.gov/tsab/cfdlarc/aiaa-dpw/Workshop4/gridding_4.html. (Gridding Guidelines)

Anderson, J. D. (2007). *Fundamentals of aerodynamics* (Fourth ed.). McGraw-Hill.

Ansys cfx-solver modeling guide. (2010, November). (Release 13.0)

Ansys cfx-solver theory guide. (2010, November). (Release 13.0)

Arnal, D. (1990). Transition description and prediction. In *Numerical simulation of unsteady flows and transition to turbulence* (p. 304-316).

Becker, B., Reyer, M., & Swoboda, M. (2007). Steady and unsteady numerical investigation of transitional shock-boundary-layer-interactions on a fan blade. *Aerospace Science and Technology*, *11*, 507-517.

Bendiksen, O. (1992). *Role of shock dynamics in transonic flutter.*

Bendiksen, O. (2011, February). Review of unsteady transonic aerodynamics: Theory and applications. *Progress in Aerospace Sciences*, *47*(2), 135-167.

Bendiksen, O. O. (2011). *Unsteady aerodynamics and flutter near mach 1: Aerodynamic and stability reversal phenomena.* (International Forum of Aeroelasticity and Structural Dynamics (IFASD) 2011)

Benney, D., & Lin, C. (1960). On the secondary motion induced by oscillations in a shear flow. *Physics of Fluids*, *3*, 656-657.

Bisplinghoff, R., Ashley, H., & Halfman, R. (1996). *Aeroelasticity.* Courier Dover Publications.

Blanchard, A., & J.F. Breil, A. S. adn. (1989). *Main results of cast-10 airfoil tested in t2 cryogenic wind tunnel* (Tech. Rep. No. N90-17652). Toulouse, France: ONERA/CERT, DERAT. (In: CAST-10-2/DOA 2 Airfoil Studies Workshop Results)

Breugem, W.-P. (2010). *Turbulence a, wb1424atu.* (Mechanical Engineering, Delft University of Technology)

Cebeci, T., Shao, J. P., Kafyeke, F., & Laurendeau, E. (2005). *Computational fluid dynamics for engineers.* Springer.

Chung, T. (2002). *Computational fluid dynamics* (First ed.). Cambridge University Press.

Dietz, G., Schewe, G., & Mai, H. (2004). Experiments on heave/pitch limit-cycle oscillations of a supercritical airfoil close to the transonic dip. *Journal of Fluids and Structures*, *19*, 1-16. (Institut für Aeroelastik des DLR)

Driest, E. van, & Blumer, C. (1963). Boundary layer transition: Freestream turbulence and pressure gradient effects. *AIAA Journal*, *1*(6), 1303-1306.

Edwards, J., & Malone, J. (1992). Current status of computational methods for transonic unsteady aerodynamics and aeroelastic applications. *Computing Systems in Engineering*, *3*(5), 545-569.

Elder, J. (1960). An experimental investigation of turbulent spots and breakdown to turbulence. *Journal of Fluid Mechanics*, *9*, 235-246.

Emmons, H. (1951). The laminar-turbulent transition in a boundary layer - part i. *Journal of Aeronautical Sciences*, *18*(7), pages = 490-498,).

Fjørtoft, R. (1950). Application of integral theorems in deriving criteria of stability for laminar flows and for the baroclinic circular vortex. *Geofys. Pub. Oslo*, *17*(6), 1-52.

Flow control. (n.d.). http://www.adl.gatech.edu/classes/flocon/flocon1/ch1and2.html.

Försching, H. (1974). *Grundlagen der aeroelastik.* Springer-Verlag.

Fung, Y. (2002). *An introduction to the theory of aeroelasticity.* Dover Publications.

Goldstein, M. (1983). The evolution of tollmien-sclichting waves near a leading edge. *Journal of Fluid Mechanics*, *127*, 59-81.

Hippe, C., & Verdon, N. (n.d.). *Flutter program.*

Hulshoff, S. (2010). *Ae4-930 aeroelasticity.* (Lecture Notes Aeroelasticity (AE4-930))

Ingen, J. van. (1956). *A suggested semi-emprical method for the calculation of the boundary layer transition region* (Tech. Rep. No. V.T.H.-74). Delft University of Technology, Aerospace Engineering.

Kachanov, Y. (1994). Physical mechanisms of laminar-boundary-layer transition. *Annual Review of Fluid Mechanics*, *26*, 411-482.

Kerschen, E. (1989). *Boundary layer receptivity* (Tech. Rep. No. 89-1109). AIAA.

Klebanoff, P., Tidstrom, K., & Sargent, L. (1962). The three-dimensional nature of boundary-layer instability. *Journal of Fluid Mechanics*, *12*, 1-34.

Krimmelbein, N. (2009). Tau transition module (v9.28) user guide (v1.04) [Computer software manual]. Lilienthalplatz 7, 38018 Braunschweig.

Krumbein, A., Krimmelbein, N., & Seyfert, C. (2011). *Automatic transition prediction in unsteady airfoil flows using an unstructured cfd code.* (29th AIAA Applied Aerodynamics Conference)

Kühl, P., & Zimmer, H. (1974). *The design of airfoil profiles for commercial aircraft with improved high speed flight characteristics* (Tech. Rep. No. 74/16 B). Dornier GmbH.

Laminar and turbulent boundary layers. (2005). http://www-mdp.eng.cam.ac.uk/web/library/enginfo/aerothermal_dvd_only/aero/fprops/introvisc/node8.html. (University of Sydney)

Langtry, R. B. (2006). *A correlation-based transition model using local variables for unstructured parallelized cfd codes.* Unpublished doctoral dissertation, University of Stuttgart. (Faculty of Mechanical Engineering, Institut fuer Thermische Stroemungsmaschinen und Maschinenlaboratorium)

Mack, L. (1977). *Transition prediction and linear stability theory* (Tech. Rep. No. CP 224). AGARD.

Menter, F. (1994, August). Two-equation eddy-viscosity turbulence models for engineering applications. *AIAA Journal*, *32*(8), 1598-1605.

Menter, F., Galpin, P., Esch, T., Kuntz, M., & Berner, C. (2004). *Cfd simulations of aerodynamic flows with a pressure-based method.* (24th International Congress of the Aeronautical Sciences)

Menter, F., Langtry, R., & Voelker, S. (2006). Transition modelling for general purpose cfd codes. *Flow Turbulence Combustion*, *77*, 277-303.

Miller, J., & Fejer, A. (1964). Transition phenomena in oscillating boundary-layer flows. *Journal of Fluid Mechanics*, *18*, 438-448.

Mineck, R. E. (1987). *Wall interference tests of a cast 10-2/doa 2 airfoil in an adaptive-wall test section* (Tech. Rep.). NASA Langley Research Center. (NASA Technical Memorandum 4015)

Obert, E. (2009). *Aerodynamic design of transport aircraft.* IOS Press. (under the imprint of Delft University Press)

Obremski, H., & Fejer, A. (1967). Transition in oscillating boundary layer flows. *Journal of Fluid Mechanics*, *29*, 93-111.

Orr, W. (1907). The stabillity or instability of the steady motions of a perfect liquid and of a viscous liquid. *Proc. Roy. Irish Acad. Sect. A*, *27*, 9-68; 69-138.

Pope, S. B. (2009). *Turbulent flows.* Cambridge University Press.

Ray, E., & Hill, A. (Eds.). (1988, September). *Cast-10-2/doa 2 airfoil studies workshop results.*

Reynolds, O. (1883). On the experimental investigation of the circumstances which determine whether the motion of water shall be direct or sinuous, and the law of resistance in parallel channels. *Phil. Trans. Roy. Soc.*, *174*, 935-982.

Salas, M. D. (2006). Some observations on grid convergence. *Computers & Fluids*, *35*, 688-692.

Schlichting, H. (1951). *Grenzschichttheorie* (First ed.; G. Braun, Ed.). Verlag Braun.

Schlichting, H. (1979). *Boundary-layer theory* (Seventh ed.). McGraw-Hill. (Translation of Grenzschicht-Theorie)

Schubauer, G., & Skramstad, H. (1948). *Laminar boundary-layer oscillations and stability of laminar flow* (Tech. Rep. No. 909). National Advisory Committee on Aeronautics.

Smith, A., & Gamberoni, N. (1956). *Transition, pressure gradient and stability theory* (Tech. Rep. No. ES-26388). Douglas Aircraft.

Sommerfeld, A. (1908). Ein beitrag zur hydrodynamischen erklärung der turbulenten flussigkeitsbewegungen. *Proc. Fourth Int. Cong. Math.*, *III*, 116-124.

Spalart, P., & Allmaras, S. (1992). *A one-equation turbulence model for aerodynamic flows* (Tech. Rep. No. AIAA-92-0439). Boeing Commercial Airplane Group.

Stanewsky, E. (1974). *Windkanalerprobung von drei ueberkritschen profilen: Ergebnisse fuer die profile cast-10-2 und cast 12-1* (Tech. Rep. No. 251 74 C 14). DFVLR Aerodynamische Versuchsanstalt Goettingen.

Stanewsky, E., Demurie, F., Ray, E., & Johnson, C. (1988, September). High reynolds number tests of the cast-10-2/doa 2 transonic airfoil at ambient and cryogenic temperature conditions. In E. Ray & A. Hill (Eds.), *Cast-10-2/doa 2 airfoil studies workshop results* (p. 47-60).

Sveningsson, A. (2006, October). *Transition modelling - a review.* (Department of Thermo and Fluid Dynamics, Chalmers University of Technology)

Tani, I. (1969). Boundary-layer transition. *Annual Review of Fluid Mechanics*, *1*, 169-196.

Technical documentation of the dlr tau-code release 2010.1.0 [Computer software manual]. (2010). Braunschweig.

Tijdeman, H. (1977). *Investigation of the transonic flow around oscillating airfoils.* Unpublished doctoral dissertation, TU Delft. (Nationaal Lucht- en Ruimtevaartlaboratorium (National Aerospace Laboratory NLR))

Veldhuis, L. (2010). *Aircraft aerodynamics primer.* (Lecture Notes Aircraft Aerodynamics (AE4-130))

Verdon, N. (2004). *Computation of the flutter boundary of a transonic airfoil* (Tech. Rep.). German Aerospace Center (DLR).

Voss, G. (2011, October). *Untersuchungen am laminarprofil cast10 im dlr-projekt igreen.* (iGreen Project Meeting, Deutsches Zentrum für Luft- und Raumfahrt, Insitut für Aeroelastik)

Voss, R., Tichy, L., & Thormann, R. (2011). *A rom based flutter prediction process and its validation with a new reference model.* (International Forum of Aeroelasticity and Structural Dynamics (IFASD) 2011)

White, F. M. (2006). *Viscous fluid flow* (Third ed.). McGraw-Hill.

Wilcox, D. (1988). Reassessment of the scale-determining equation for advanced turbulence models. *AIAA Journal*, *26*(11), 1299-1310.

Wright, J. R., & Cooper, J. E. (2007). *Introduction to aircraft aeroelasticity and loads.* John Wiley & Sons.

Zuijlen, S. van. (2010). *Computational fluid dynamics ii: Time marching algorithms.* (Faculty of Aerospace Engineering)

Appendix A

CAST-10 Airfoil

In this thesis CFD simulations have been performed with the CAST-10 airfoil designed by Dornier. This is a supercritical airfoil, hence at its design conditions there is no shock wave or only a weak shock wave on the airfoil, which leads to a lower wave drag than a conventional airfoil (with a strong shock wave at its design condition) would have. In order to achieve this the maximum thickness point is located far aft in comparison to a conventional airfoil. Characteristic of the CAST-10 airfoil is furthermore that the flow stays laminar on a large part of the chord for both the upper and the lower surface. Hence it can be used to lower the skin friction drag as well. The maximum thickness point ($(t/c)_{\max} = 12\%$) of the airfoil is located at 45 % of the chord. The airfoil has a blunt trailing edge with a thickness of $(t/c)_{\text{te}} = 0.005$ (Stanewsky et al. [1988]).

The CAST-10 airfoil has been subject of a lot of investigations already (see Ray & Hill [1988]). Its theoretical design point is: $M = 0.76$, $C_L = 0.595$ and $\alpha = 0.3°$. The coordinates of the original CAST-10 airfoil are given in table A.1.

Upper surface		Lower surface	
$\frac{x}{c}$	$\frac{z}{c}$	$\frac{x}{c}$	$\frac{z}{c}$
0.0000	0.0034	0.0000	0.0034
0.0003	0.0062	0.0004	0.0004
0.0015	0.0094	0.0014	-0.0021
0.0033	0.0124	0.0031	-0.0043
0.0063	0.0159	0.0061	-0.0066
0.0140	0.0217	0.0096	-0.0081
0.0195	0.0250	0.0153	-0.0099
0.0247	0.0279	0.0273	-0.0127
0.0356	0.0331	0.0339	-0.0141
0.0470	0.0376	0.0470	-0.0169
0.0654	0.0432	0.0673	-0.0205
0.0846	0.0478	0.0874	-0.0238
0.1179	0.0536	0.1148	-0.0277
0.1519	0.0580	0.1562	-0.0328
0.2139	0.0633	0.2741	-0.0446
0.2764	0.0665	0.3366	-0.0492
0.3321	0.0681	0.3919	-0.0520
0.3949	0.0689	0.4539	-0.0532
0.4576	0.0686	0.5161	-0.520
0.5132	0.0673	0.5714	-0.0489
0.5757	0.0645	0.6340	-0.0436
0.6376	0.0601	0.6967	-0.0373
0.6925	0.0542	0.7525	-0.0316
0.7539	0.0453	0.8149	-0.0255
0.8152	0.0338	0.8775	-0.0204
0.8763	0.0203	0.9189	-0.0177
0.9172	0.0106	0.9468	-0.0162
0.9511	0.0024	0.9743	-0.0151
0.9782	-0.0042	1.0000	-0.0145
1.0000	-0.0095		

Table A.1: CAST-10 coordinates (Mineck [1987])

Appendix B

Programs Used for Determination of the Flutter Boundary

B.1 Approach

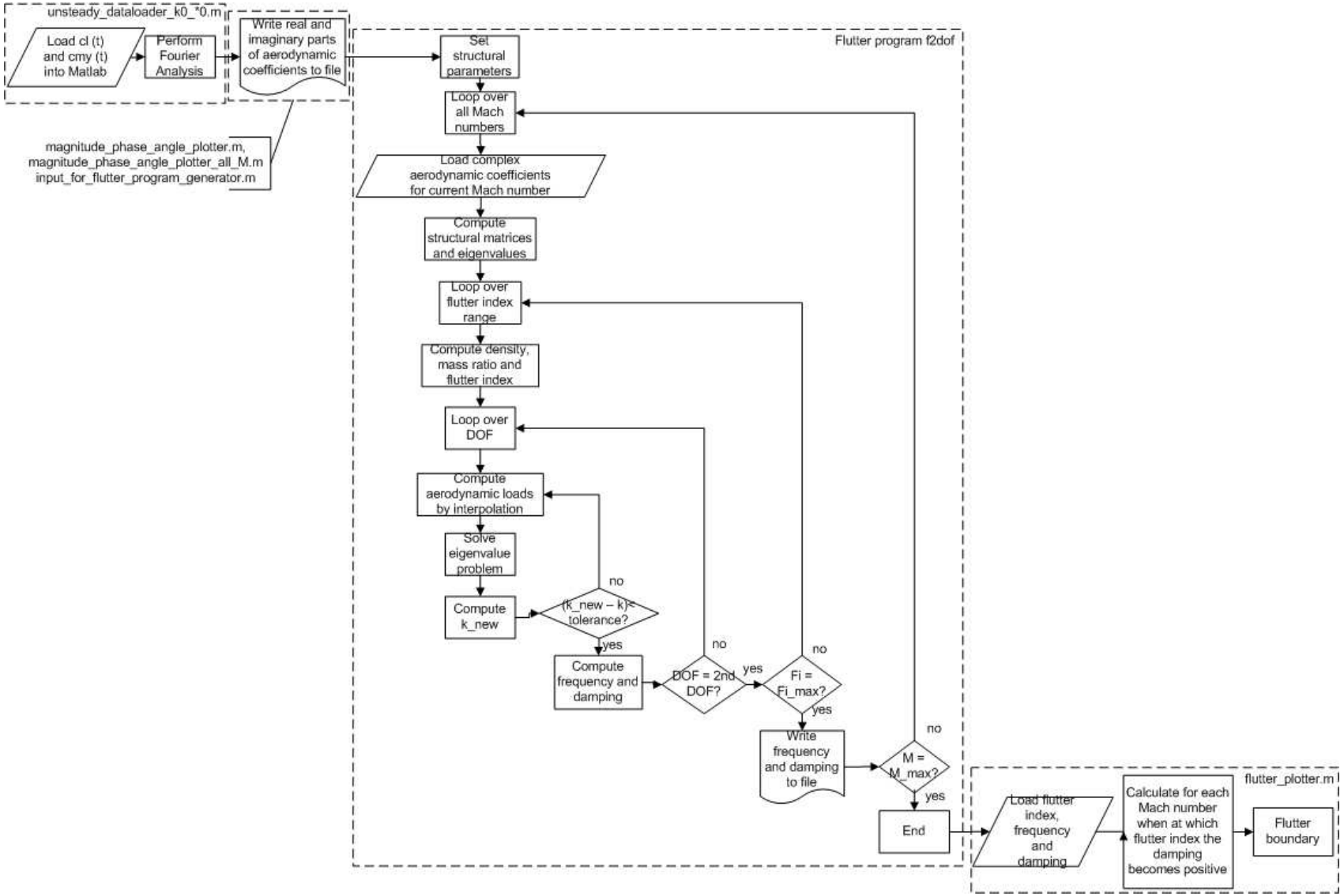

Figure B.1: Schematic overview of the procedure used to compute the frequency and damping curves and the flutter boundary

B.2 Fourier transform

```
function [scaled_mag_cl, phase_cl_sine, real_cl, im_cl, scaled_mag_cmy,...
 phase_cmy_sine, real_cmy, im_cmy,D] = unsteady_dataloader_k0_20

% Specify input data
datfile1=...
'CAST-10_original_unsteady_M0_745_pitch_amplitude_0_05_k0_20.monitor.tmp.dat';
datfile2=...
'CAST-10_original_unsteady_M0_745_pitch_amplitude_0_05_k0_20_2.monitor.tmp.dat';
datfile3=...
'CAST-10_original_unsteady_M0_745_pitch_amplitude_0_05_k0_20_3.monitor.tmp.dat';
datfile4=...
'CAST-10_original_unsteady_M0_745_pitch_amplitude_0_05_k0_20_4.monitor.pval.unsteady.dat'

% Set parameters
NOTPP=154;              % number of timesteps per period
NOII=400;               % number of inner iterations
M=0.745;                % Mach number
k=0.2;                  % Reduced frequency
a=sqrt(1.4*287*273.15);
V=M*a;
omega=k*V/0.3;
T=2*pi/omega;
delta_t=T/NOTPP;
lines=NOTPP*NOII;
amp=0.05;               % Amplitude in degrees
amplitude=amp*pi/180;
NOP = 5;                % Number of periods in input data

% Create strings for data storage
Mach=num2str(M);
RedFreq=num2str(k);
Ampl=num2str(amp);

% Load input data files and assemble data
A=load(datfile1);
C=load(datfile2);
E=load(datfile3);
G=load(datfile4);
C(:,2)=C(:,2)+251*NOII;
E(:,2)=E(:,2)+462*NOII;
G(:,2)=G(:,2)+616*NOII;
B=[A(1:251*NOII,:); C(1:(462-251)*NOII,:); E(1:(616-462)*NOII,:); G];
F=B(end-lines-2*NOII:end-2*NOII,:);

% Remove inner iterations from matrix
```

```
for i=NOII:NOII:lines
    D(i/NOII,:)=F(i,:);
end
for i=NOII:NOII:lines*NOP
    E(i/NOII,:)=B(i,:);
end

% Compute magnitude and phase of last period of cl
y1=D(1:end,7);
N=length(y1);
Y1 = fft(y1);
cl_mean=abs(Y1(1))/N;
mag_cl=abs(Y1(2:end))/N*2;
phase_cl=angle(Y1(2:end));
im_cl=imag(Y1(2:end))/N*2;
real_cl=real(Y1(2:end))/N*2;

% Change phase into shift w.r.t. to sine
phase_cl_sine=phase_cl+pi/2;

% Reconstruct time signal of cl
cl_time=cl_mean+mag_cl(1)*real(exp(1i*(omega*D(:,1)+phase_cl(1))));

% Compute convergence of magnitude and phase of cl
for j=1:(NOP-1)*NOTPP
    y3=E(j:j+NOTPP-1,7);
    y5=E(j:j+NOTPP-1,16);
    Y3(:,j)=fft(y3);
    Y5(:,j)=fft(y5);
    mean_cl_2(j)=abs(Y3(1,j))/N;
    mean_alpha(j)=abs(Y5(1,j))/N;
    mag_cl_2(j)=abs(Y3(2,j))/N*2;
    mag_alpha(j)=abs(Y5(2,j))/N*2/amplitude;
    phase_alpha(j)=angle(Y5(2,j));
    phase_cl_2(j)=angle(Y3(2,j))-phase_alpha(j);
    im_cl_2(j)=imag(Y3(2,j))/N*2;
    im_alpha(j)=imag(Y5(2,j))/N*2;
    real_cl_2(j)=real(Y3(2,j))/N*2;
    real_alpha(j)=real(Y5(2,j))/N*2;
end

% Convert phase to degree
phase_cl=phase_cl*180/pi;
phase_cl_sine=phase_cl_sine*180/pi;

% Save magntiude and phase angle
filemagcl=['mag_cl_M' Mach '_k' RedFreq '_a' Ampl];
```

```
save(filemagcl, 'mag_cl', '-ascii', '-double');
filephasecl=['phase_cl_M' Mach '_k' RedFreq '_a' Ampl];
save(filephasecl, 'phase_cl', '-ascii', '-double');
filephaseclsine=['phase_cl_sine_M' Mach '_k' RedFreq '_a' Ampl];
save(filephaseclsine, 'phase_cl_sine', '-ascii', '-double');

% Save magnitude and phase with respect to alpha
scaled_mag_cl=mag_cl/amplitude;
fraction_mag_cl=mag_cl(1:end-1)./mag_cl(2:end);
filescaledmagcl=['scaled_mag_cl_M' Mach '_k' RedFreq '_a' Ampl];
save(filescaledmagcl, 'scaled_mag_cl', '-ascii', '-double');
filefractionmagcl=['fraction_mag_cl_M' Mach '_k' RedFreq '_a' Ampl];
save(filefractionmagcl, 'fraction_mag_cl', '-ascii', '-double');

% Compute magnitude and phase of the last period of cmy
y2=D(1:end,11);
N=length(y2);
Y2 = fft(y2);
cmy_mean=-abs(Y2(1))/N;
mag_cmy=abs(Y2(2:end))/N*2;
phase_cmy=angle(Y2(2:end));
im_cmy=imag(Y2(2:end))/N*2;
real_cmy=real(Y2(2:end))/N*2;

% Reconstruct time signal
cmy_time=cmy_mean+mag_cmy(1)*real(exp(1i*(omega*D(:,1)+phase_cmy(1))));

% Compute convergence of magnitude and phase of cmy
for j=1:(NOP-1)*NOTPP
    y4=E(j:j+NOTPP-1,11);
    Y4(:,j)=fft(y4);
    mean_cmy_2(j)=abs(Y4(1,j))/N;
    mag_cmy_2(j)=abs(Y4(2,j))/N*2/amplitude;
    phase_cmy_2(j)=angle(Y4(2,j))-phase_alpha(j);
    im_cmy_2(j)=imag(Y4(2,j))/N*2;
    real_cmy_2(j)=real(Y4(2,j))/N*2;
end

% Bound phase_cmy_2 to -pi .. pi
if (phase_cmy(1)+pi/2)>pi
    phase_cmy_sine(1)=phase_cmy(1)+pi/2-2*pi;
else
    phase_cmy_sine(1)=phase_cmy(1)+pi/2;
end

% Convert phase to degree
phase_cmy=phase_cmy*180/pi;
```

```
phase_cmy_sine=phase_cmy_sine*180/pi;

% Save magnitude and phase
filemagcmy=['mag_cmy_M' Mach '_k' RedFreq '_a' Ampl];
save(filemagcmy, 'mag_cmy', '-ascii', '-double');
filephasecmy=['phase_cmy_M' Mach '_k' RedFreq '_a' Ampl];
save(filephasecmy, 'phase_cmy', '-ascii', '-double');
filephasecmysine=['phase_cmy_sine_M' Mach '_k' RedFreq '_a' Ampl];
save(filephasecmysine, 'phase_cmy_sine', '-ascii', '-double');

% Save magnitude and phase with respect to alpha
scaled_mag_cmy=mag_cmy/amplitude;
fraction_mag_cmy=mag_cmy(1:end-1)./mag_cmy(2:end);
filescaledmagcmy=['scaled_mag_cmy_M' Mach '_k' RedFreq '_a' Ampl];
save(filescaledmagcmy, 'scaled_mag_cmy', '-ascii', '-double');
filefractionmagcmy=['fraction_mag_cmy_M' Mach '_k' RedFreq '_a' Ampl];
save(filefractionmagcmy, 'fraction_mag_cmy', '-ascii', '-double');
```

B.3 Data collection

B.3.1 Collect aerodynamic coefficients for one Mach number

```
% magnitude_phase_angle_plotter.m

clear all;
close all;
clc;

% Load magnitude and phase of all reduced frequencies
[mag_cl_k0_05, phase_cl_k0_05, real_cl_k0_05, im_cl_k0_05, mag_cmy_k0_05,...
 phase_cmy_k0_05, real_cmy_k0_05, im_cmy_k0_05, D0_05]=unsteady_dataloader_k0_05;
[mag_cl_k0_10, phase_cl_k0_10, real_cl_k0_10, im_cl_k0_10, mag_cmy_k0_10,...
 phase_cmy_k0_10, real_cmy_k0_10, im_cmy_k0_10, D0_10]=unsteady_dataloader_k0_10;
[mag_cl_k0_20, phase_cl_k0_20, real_cl_k0_20, im_cl_k0_20, mag_cmy_k0_20,...
 phase_cmy_k0_20, real_cmy_k0_20, im_cmy_k0_20, D0_20]=unsteady_dataloader_k0_20;
[mag_cl_k0_30, phase_cl_k0_30, real_cl_k0_30, im_cl_k0_30, mag_cmy_k0_30,...
 phase_cmy_k0_30, real_cmy_k0_30, im_cmy_k0_30, D0_30]=unsteady_dataloader_k0_30;
[mag_cl_k0_50, phase_cl_k0_50, real_cl_k0_50, im_cl_k0_50, mag_cmy_k0_50,...
 phase_cmy_k0_50, real_cmy_k0_50, im_cmy_k0_50, D0_50]=unsteady_dataloader_k0_50;
[mag_cl_k0_80, phase_cl_k0_80, real_cl_k0_80, im_cl_k0_80, mag_cmy_k0_80,...
 phase_cmy_k0_80, real_cmy_k0_80, im_cmy_k0_80, D0_80]=unsteady_dataloader_k0_80;

% Store the magnitude and phase of all reduced frequencies into one vector
mag_cl_M0_745=[mag_cl_k0_05(1) mag_cl_k0_10(1) mag_cl_k0_20(1)...
 mag_cl_k0_30(1) mag_cl_k0_50(1) mag_cl_k0_80(1)];
mag_cmy_M0_745=[mag_cmy_k0_05(1) mag_cmy_k0_10(1) mag_cmy_k0_20(1)...
```

```
 mag_cmy_k0_30(1) mag_cmy_k0_50(1) mag_cmy_k0_80(1)];
phase_cl_M0_745=[phase_cl_k0_05(1) phase_cl_k0_10(1) phase_cl_k0_20(1)...
 phase_cl_k0_30(1) phase_cl_k0_50(1) phase_cl_k0_80(1)];
phase_cmy_M0_745=[phase_cmy_k0_05(1) phase_cmy_k0_10(1) phase_cmy_k0_20(1)...
 phase_cmy_k0_30(1) phase_cmy_k0_50(1) phase_cmy_k0_80(1)];
real_cl_M0_745=[real_cl_k0_05(1) real_cl_k0_10(1) real_cl_k0_20(1)...
 real_cl_k0_30(1) real_cl_k0_50(1) real_cl_k0_80(1)];
im_cl_M0_745=[im_cl_k0_05(1) im_cl_k0_10(1) im_cl_k0_20(1)...
 im_cl_k0_30(1) im_cl_k0_50(1) im_cl_k0_80(1)];
real_cmy_M0_745=[real_cmy_k0_05(1) real_cmy_k0_10(1) real_cmy_k0_20(1)...
 real_cmy_k0_30(1) real_cmy_k0_50(1) real_cmy_k0_80(1)];
im_cmy_M0_745=[im_cmy_k0_05(1) im_cmy_k0_10(1) im_cmy_k0_20(1)...
 im_cmy_k0_30(1) im_cmy_k0_50(1) im_cmy_k0_80(1)];
save mag_cl_M0_745 mag_cl_M0_745 -ascii -double
save phase_cl_M0_745 phase_cl_M0_745 -ascii -double
save mag_cmy_M0_745 mag_cmy_M0_745 -ascii -double
save phase_cmy_M0_745 phase_cmy_M0_745 -ascii -double
save real_cl_M0_745 real_cl_M0_745 -ascii -double
save im_cl_M0_745 im_cl_M0_745 -ascii -double
save real_cmy_M0_745 real_cmy_M0_745 -ascii -double
save im_cmy_M0_745 real_cmy_M0_745 -ascii -double
save time_data_last_period_M0_745_k0_05 D0_05 -ascii -double
save time_data_last_period_M0_745_k0_10 D0_10 -ascii -double
save time_data_last_period_M0_745_k0_20 D0_20 -ascii -double
save time_data_last_period_M0_745_k0_30 D0_30 -ascii -double
save time_data_last_period_M0_745_k0_50 D0_50 -ascii -double
save time_data_last_period_M0_745_k0_80 D0_80 -ascii -double
```

B.3.2 Collect data for one DOF

```
% magnitude_phase_angle_plotter_all_M.m

clear all;
close all;
clc;

% Load magnitude and phase for all frequencies and Mach numbers
mag_cl_M0_5 = load('./M0_5/mag_cl_M0_5');
phase_cl_M0_5 = load('./M0_5/phase_cl_M0_5');
mag_cmy_M0_5 = load('./M0_5/mag_cmy_M0_5');
phase_cmy_M0_5 = load('./M0_5/phase_cmy_M0_5');
mag_cl_M0_745 = load('./M0_745/mag_cl_M0_745');
phase_cl_M0_745 = load('./M0_745/phase_cl_M0_745');
mag_cmy_M0_745 = load('./M0_745/mag_cmy_M0_745');
phase_cmy_M0_745 = load('./M0_745/phase_cmy_M0_745');
mag_cl_M0_75 = load('./M0_75/mag_cl_M0_75');
phase_cl_M0_75 = load('./M0_75/phase_cl_M0_75');
```

```
mag_cmy_M0_75 = load('./M0_75/mag_cmy_M0_75');
phase_cmy_M0_75 = load('./M0_75/phase_cmy_M0_75');
mag_cl_M0_755 = load('./M0_755/mag_cl_M0_755');
phase_cl_M0_755 = load('./M0_755/phase_cl_M0_755');
mag_cmy_M0_755 = load('./M0_755/mag_cmy_M0_755');
phase_cmy_M0_755 = load('./M0_755/phase_cmy_M0_755');
mag_cl_M0_76 = load('./M0_76/mag_cl_M0_76');
phase_cl_M0_76 = load('./M0_76/phase_cl_M0_76');
mag_cmy_M0_76 = load('./M0_76/mag_cmy_M0_76');
phase_cmy_M0_76 = load('./M0_76/phase_cmy_M0_76');
mag_cl_M0_765 = load('./M0_765/mag_cl_M0_765');
phase_cl_M0_765 = load('./M0_765/phase_cl_M0_765');
mag_cmy_M0_765 = load('./M0_765/mag_cmy_M0_765');
phase_cmy_M0_765 = load('./M0_765/phase_cmy_M0_765');
mag_cl_M0_8 = load('./M0_8/mag_cl_M0_8');
phase_cl_M0_8 = load('./M0_8/phase_cl_M0_8');
mag_cmy_M0_8 = load('./M0_8/mag_cmy_M0_8');
phase_cmy_M0_8 = load('./M0_8/phase_cmy_M0_8');

% Real and imaginary parts
real_cl_M0_5 = load('./M0_5/real_cl_M0_5');
im_cl_M0_5 = load('./M0_5/im_cl_M0_5');
real_cmy_M0_5 = load('./M0_5/real_cmy_M0_5');
im_cmy_M0_5 = load('./M0_5/im_cmy_M0_5');
real_cl_M0_745 = load('./M0_745/real_cl_M0_745');
im_cl_M0_745 = load('./M0_745/im_cl_M0_745');
real_cmy_M0_745 = load('./0_745/real_cmy_M0_745');
im_cmy_M0_745 = load('./M0_745/im_cmy_M0_745');
real_cl_M0_75 = load('./M0_75/real_cl_M0_75');
im_cl_M0_75 = load('./M0_75/im_cl_M0_75');
real_cmy_M0_75 = load('./M0_75/real_cmy_M0_75');
im_cmy_M0_75 = load('./M0_75/im_cmy_M0_75');
real_cl_M0_755 = load('./M0_755/real_cl_M0_755');
im_cl_M0_755 = load('./M0_755/im_cl_M0_755');
real_cmy_M0_755 = load('./M0_755/real_cmy_M0_755');
im_cmy_M0_755 = load('./M0_755/im_cmy_M0_755');
real_cl_M0_76 = load('./M0_76/real_cl_M0_76');
im_cl_M0_76 = load('./M0_76/im_cl_M0_76');
real_cmy_M0_76 = load('./M0_76/real_cmy_M0_76');
im_cmy_M0_76 = load('./M0_76/im_cmy_M0_76');
real_cl_M0_765 = load('./M0_765/real_cl_M0_765');
im_cl_M0_765 = load('./M0_765/im_cl_M0_765');
real_cmy_M0_765 = load('./M0_765/real_cmy_M0_765');
im_cmy_M0_765 = load('./M0_765/im_cmy_M0_765');
real_cl_M0_8 = load('./M0_8/real_cl_M0_8');
im_cl_M0_8 = load('./M0_8/im_cl_M0_8');
real_cmy_M0_8 = load('./M0_8/real_cmy_M0_8');
```

```
im_cmy_M0_8 = load('./M0_8/im_cmy_M0_8');

% Put everything together into one matrix
mag_cl = [mag_cl_M0_5; mag_cl_M0_745; mag_cl_M0_75; mag_cl_M0_755;...
 mag_cl_M0_76; mag_cl_M0_765; mag_cl_M0_8];
phase_cl = [phase_cl_M0_5; phase_cl_M0_745; phase_cl_M0_75; phase_cl_M0_755;...
 phase_cl_M0_76; phase_cl_M0_765; phase_cl_M0_8];
mag_cmy = [mag_cmy_M0_5; mag_cmy_M0_745; mag_cmy_M0_75; mag_cmy_M0_755;...
 mag_cmy_M0_76; mag_cmy_M0_765; mag_cmy_M0_8];
phase_cmy = [phase_cmy_M0_5; phase_cmy_M0_745; phase_cmy_M0_75; phase_cmy_M0_755;...
 phase_cmy_M0_76; phase_cmy_M0_765; phase_cmy_M0_8];

amp=0.05*pi/180;
real_cl2 = [real_cl_M0_5; real_cl_M0_745; real_cl_M0_75; real_cl_M0_755;...
 real_cl_M0_76; real_cl_M0_765; real_cl_M0_8]./amp;
im_cl2 = [im_cl_M0_5; im_cl_M0_745; im_cl_M0_75; im_cl_M0_755;...
 im_cl_M0_76; im_cl_M0_765; im_cl_M0_8]./amp;
real_cmy2 = [real_cmy_M0_5; real_cmy_M0_745; real_cmy_M0_75; real_cmy_M0_755;...
 real_cmy_M0_76; real_cmy_M0_765; real_cmy_M0_8]./amp;
im_cmy2 = [im_cmy_M0_5; im_cmy_M0_745; im_cmy_M0_75; im_cmy_M0_755;...
 im_cmy_M0_76; im_cmy_M0_765; im_cmy_M0_8]./amp;


% Recreate real and imaginary parts
% First, convert phase back to cosine
phase_cl_cosine = phase_cl-90;
phase_cmy_cosine = phase_cmy-90;
real_cl = mag_cl.*cos(phase_cl*pi/180+pi);
im_cl = mag_cl.*sin(phase_cl*pi/180+pi);
real_cmy = mag_cmy.*cos(phase_cmy*pi/180);
im_cmy = mag_cmy.*sin(phase_cmy*pi/180);

% Save magnitude and phase angle
save mag_cl_pitch mag_cl -ascii -double
save phase_cl_pitch phase_cl -ascii -double
save mag_cmy_pitch mag_cmy -ascii -double
save phase_cmy_pitch phase_cmy -ascii -double

% Save the real and imaginary parts
save real_cl_pitch real_cl -ascii -double
save im_cl_pitch im_cl -ascii -double
save real_cmy_pitch real_cmy -ascii -double
save im_cmy_pitch im_cmy -ascii -double
```

B.3.3 Input data in format for flutter program

```
% input_for_flutter_program_generator.m
```

```
clear all;
close all;
clc;

% Load real and imaginary parts of both degrees of freedom
im_cl_pitch = load('./Oscillating_airfoil/im_cl_pitch');
real_cl_pitch = load('./Oscillating_airfoil/real_cl_pitch');
im_cmy_pitch = load('./Oscillating_airfoil/im_cmy_pitch');
real_cmy_pitch = load('./Oscillating_airfoil/real_cmy_pitch');
im_cl_plunge = load('./Plunging_airfoil/im_cl_plunge2');
real_cl_plunge = load('./Plunging_airfoil/real_cl_plunge2');
im_cmy_plunge = load('./Plunging_airfoil/im_cmy_plunge2');
real_cmy_plunge = load('./Plunging_airfoil/real_cmy_plunge2');

% Convert matrices to the right format per Mach number
k = [0.05; 0.10; 0.20; 0.30; 0.50; 0.80];
% M = 0.5
M0_5 = [k real_cl_plunge(1,:)' im_cl_plunge(1,:)' real_cl_pitch(1,:)'...
 im_cl_pitch(1,:)' real_cmy_plunge(1,:)' im_cmy_plunge(1,:)' real_cmy_pitch(1,:)'...
 im_cmy_pitch(1,:)'];
% M = 0.745
M0_745 = [k real_cl_plunge(2,:)' im_cl_plunge(2,:)' real_cl_pitch(2,:)'...
 im_cl_pitch(2,:)' real_cmy_plunge(2,:)' im_cmy_plunge(2,:)' real_cmy_pitch(2,:)'...
 im_cmy_pitch(2,:)'];
% M = 0.75
M0_75 = [k real_cl_plunge(3,:)' im_cl_plunge(3,:)' real_cl_pitch(3,:)'...
 im_cl_pitch(3,:)' real_cmy_plunge(3,:)' im_cmy_plunge(3,:)' real_cmy_pitch(3,:)'...
 im_cmy_pitch(3,:)'];
% M = 0.755
M0_755 = [k real_cl_plunge(4,:)' im_cl_plunge(4,:)' real_cl_pitch(4,:)'...
 im_cl_pitch(4,:)' real_cmy_plunge(4,:)' im_cmy_plunge(4,:)' real_cmy_pitch(4,:)'...
 im_cmy_pitch(4,:)'];
% M = 0.76
M0_76 = [k real_cl_plunge(5,:)' im_cl_plunge(5,:)' real_cl_pitch(5,:)'...
 im_cl_pitch(5,:)' real_cmy_plunge(5,:)' im_cmy_plunge(5,:)' real_cmy_pitch(5,:)'...
 im_cmy_pitch(5,:)'];
% M = 0.765
M0_765 = [k real_cl_plunge(6,:)' im_cl_plunge(6,:)' real_cl_pitch(6,:)'...
 im_cl_pitch(6,:)' real_cmy_plunge(6,:)' im_cmy_plunge(6,:)' real_cmy_pitch(6,:)'...
 im_cmy_pitch(6,:)'];
% M = 0.8
M0_8 = [k real_cl_plunge(7,:)' im_cl_plunge(7,:)' real_cl_pitch(7,:)'...
 im_cl_pitch(7,:)' real_cmy_plunge(7,:)' im_cmy_plunge(7,:)' real_cmy_pitch(7,:)'...
 im_cmy_pitch(7,:)'];

% Save the real and imaginary parts
```

```
save M0_5_fully_turbulent_2 M0_5 -ascii -double
save M0_745_fully_turbulent_2 M0_745 -ascii -double
save M0_75_fully_turbulent_2 M0_75 -ascii -double
save M0_755_fully_turbulent_2 M0_755 -ascii -double
save M0_76_fully_turbulent_2 M0_76 -ascii -double
save M0_765_fully_turbulent_2 M0_765 -ascii -double
save M0_8_fully_turbulent_2 M0_8 -ascii -double
```

B.4 Flutter program

```
  program f2dof
c+====================================================================+
c+ Carsten Hippe / Nicolas Verdon                                     +
c+--------------------------------------------------------------------+
c+ Programm zur Berechnung der Flattergrenze 2 Freiheitsgrade        +
c+====================================================================+
c       Externe Programme aus IMSL Bibliothek :                       +
c               EVCCG : Lsung eines komplexen Eigenwertproblems      +
c               LINCG : Invertierung einer komplexen Matrix           +
c               MATMUL: Multiplikation komplexer Matrizen             +
c--------------------------------------------------------------------+
c
character*80 input_file(100),outd1,outd2,outf1,outf2
real*16 c,ma,In,ka,xih,gamh,xia,gama,xa
real*16ra,sig2,wa,gam,Su,Ttot,R
        real*16 err,Fi_min,Fi_max
real*16 v1(100),v2(100),v3(100),v4(100),v5(100)
      real*16 v6(100),v7(100),v8(100),v9(100)
        real*16 Mach,as,V,rho_u,rho_o,zmach(100)
        real*16 mu,k,dk,damp1(500),damp2(500),freq1(500),freq2(500)
real*16 fdamp1(500,500),fdamp2(500,500)
        real*16 rho(500),Fi(500),drho,w1,w2,w3,w4,w5,w6,w7,w8
integer i,j,z,resol,n_freq,ind,ind2
complex D(2,2),Da(2,2),M(2,2),mat_K(2,2),A(2,2),inv_K(2,2)
        complex AERO(2,2),mat_KM(2,2),mat_tot(2,2)
        complex lambda(2),lambda_it(2)
      complex vp(2,2),vp_it(2,2),mat_KD(2,2),inv_KD(2,2),mat_tot2(2,2)
complex a1,a2,a3,a4,ii
c
parameter (xih=0.0043)
parameter (Pi=3.14159)
parameter (gamh=0.0086)
parameter (xia=0.0015)
parameter (gama=0.0030)
parameter (xa=0.0420)
parameter (ra=0.1828**2)
```

```
parameter (sig=0.6991**2)
ii=(0,1)
c
c+++++++Strukturparameter++++++++++++++++++++++++++++++++++++++++++++++
c
c=0.3
ma=26.268
In=0.079
ka=6.646E+03
wa=SQRT(ka/In)
c xih=0.0043
c gamh=xih*2
c gama=xia*2
c xia=0.0015
c xa=0.0420
c ra=0.1828
c sig2=sig**2
c
c+++++++Aerodynamikparameter++++++++++++++++++++++++++++++++++++++++++
gam=1.4
Su=110.4
Ttot=Su/0.365
R=287
c+++++++Eingabe Machzahlen
c+++++++        je Machzahl eine Matrix der aerodynamischen Derivativa
c       here from file :
c       no of reduced frequencies
c       no of Mach numbers
c       vector of Mach numbers
c       Name of aerodynamic data files (one for each Mach number)
open(UNIT=90,file='f2dof_input',status='old')
read(90,*) n_freq
read(90,*) num_mach
do imach=1,num_mach
   read(90,*) zmach(imach)
   enddo
do imach=1,num_mach
   read(90,*) input_file(imach)
   enddo
c
c
c-------------------------------------------------------
c+++++++Schleife ueber alle Machzahlen
do imach=1,num_mach
c-------------------------------------------------------
   Mach = zmach(imach)
c
```

```
c+++++++solver control++++++++++++++++++++++++++++++++++++++++++++++++++++
c (Set the precision with err & the range of flutter indices)
c
err=0.0001
resol=50
Fi_min=0.0
Fi_max=0.4
c
c+++++++unsteady aerodynamic datas+++++++++++++++++++++++++++++++++++++++
c+++++++in order : redfrequency, Lh, Lalf, Mh, Malf
c++++++++++++++++++++++++++++++++++++++++++++++++++++++++++++++++++++++++
c
c n_freq=5
c
open(UNIT=10,file=input_file(imach),status='old')
do i=1,n_freq
read(10,*)v1(i),v2(i),v3(i),v4(i),v5(i),v6(i),v7(i),v8(i),v9(i)
      end do
close(UNIT=10)
c
c+++++++Aufstellen der Systemmatrizen++++++++++++++++++++++++++++++++++++
c
c=======Massenmatrix====================================================
c
DATA M/(1,0),(xa,0),(xa,0),(ra,0)/
c
c=======Steifugkeitsmatrix==============================================
c
DATA mat_K/(sig,0),(0,0),(0,0),(ra,0)/
c
c=======Daempfungsmatrix Da=D*K=========================================
c
DATA D/(0,gamh),(0,0),(0,0),(0,gama)/
Da=matmul(D,mat_K)
c
CALL LINCG (2,mat_K,2,inv_K,2)
mat_KM=matmul(inv_K,M)
CALL EVCCG (2,mat_KM,2,lambda,vp,2)
c write(*,*)lambda
c
c+++++++Schallgeschwindigkeit++++++++++++++++++++++++++++++++++++++++++++
c
as=sqrt(gam*R*Ttot*(1/(1+0.5*Mach**2*(gam-1))))
V=Mach*as
rho_o=Fi_max**2*(ma*wa**2)/(Pi*V**2)
rho_u=Fi_min**2*(ma*wa**2)/(Pi*V**2)
drho=(rho_o-rho_u)/resol
```

```
c
c++++++++Schleife ueber den Bereich des Flatterindex Fi
c       ====================================================================
do i=1,resol
c-------------------------------------------------------------------------
   rho(i)=rho_u+drho*i
c-------------------------------------------------------------------------
   mu=ma/(0.25*Pi*rho(i)*c**2)
c-------------------------------------------------------------------------
   Fi(i)=2*V/(sqrt(mu)*c*wa)
c
c++++++++++Schleife ueber Freiheitsgrade
c          ================================================================
   do j=1,2
c-------------------------------------------------------------------------
      k=wa/sqrt(lambda(j))*c/V
      dk=1
c       ============================================================
      niter=0
      do
                           niter=niter+1
c            print*,i,j,niter,dk
           if(niter.ge.20) exit
         if (dk.LE.err) exit

c
c++++++++Interpolation der aerodynamischen Derivativa++++++++++++++++++++
c
        vlo=v1(1)
vup=v1(n_freq)
   if(k.lt.vlo) then
      ind1=1
                      ind2=2
      END IF
   if(k.gt.vup) then
      ind2=n_freq
      ind1=n_freq-1
      END IF
   if(k.ge.vlo .and. k.le.vup) then
      do kk=1,n_freq-1
      if(k.ge.v1(kk) .and. k.le.v1(kk+1)) ind1=kk
      enddo
      ind2=ind1+1
      END IF
      quot=(k-v1(ind1))/(v1(ind2)-v1(ind1))
c
w2=v2(ind1)+(v2(ind2)-v2(ind1))*quot
```

```
w3=v3(ind1)+(v3(ind2)-v3(ind1))*quot
w4=v4(ind1)+(v4(ind2)-v4(ind1))*quot
w5=v5(ind1)+(v5(ind2)-v5(ind1))*quot
w6=v6(ind1)+(v6(ind2)-v6(ind1))*quot
w7=v7(ind1)+(v7(ind2)-v7(ind1))*quot
w8=v8(ind1)+(v8(ind2)-v8(ind1))*quot
w9=v9(ind1)+(v9(ind2)-v9(ind1))*quot
c
a1=w2+w3*ii
a2=w6+w7*ii
a3=w4+w5*ii
a4=w8+w9*ii
AERO(1,1)=a1
AERO(2,1)=a2
AERO(1,2)=a3
AERO(2,2)=a4
c-----------------------------------------------------------------------
         A=2/(Pi*mu*k**2)*AERO
c-----------------------------------------------------------------------
 mat_KD=mat_K+Da
 CALL LINCG (2,mat_KD,2,inv_KD,2)
 mat_tot2=matmul(inv_KD,M+A)
 CALL EVCCG (2,mat_tot2,2,lambda_it,vp_it,2)
c
 dk=abs(k-wa/sqrt(real(lambda_it(j)))*c/V)
         k=wa/sqrt(real(lambda_it(j)))*c/V
      end do
c             ============================================================
c       write(*,*)i,j,k,lambda_it,aimag(lambda_it(1)),sqrt(lambda_it(1))
c       write(*,*)mu
c             ============================================================
      if (j.EQ.1) then
 damp1(i)=2*Pi*aimag(sqrt(lambda_it(1)))/real(sqrt(lambda_it(1)))
  freq1(i)=wa/real(sqrt(lambda_it(1)))
c             ------------------------------------------------------------
      elseif (j.EQ.2) then
c             ------------------------------------------------------------
 damp2(i)=2*Pi*aimag(sqrt(lambda_it(2)))/real(sqrt(lambda_it(2)))
  freq2(i)=wa/real(sqrt(lambda_it(2)))
      endif
c       ============================================================
   end do
c          ============================================================
end do
c       ============================================================
c
open(UNIT=20,file='damping_output.dat',status='unknown')
```

```
open(UNIT=30,file='frequen_output.dat',status='unknown')
   do i=1,resol
      write(20,21) Fi(i),damp1(i),damp2(i)
      write(30,21) Fi(i),freq1(i),freq2(i)
      fdamp1(imach,i)=damp1(i)
      fdamp2(imach,i)=damp2(i)
  21   FORMAT(5(e15.5))
c
         end do
c
write(20,6020)
write(30,6020)
 6020 format(1x)
c
enddo
c
close(UNIT=20)
close(UNIT=30)
c
c+++++Daempfung d(Mach,Fi) in Tecplot Format
c*********************************************************
      open(96,file='fluterdiagram.plt',form='formatted')
      write(96,6019) num_mach, resol
 6019 format('Title = "Damping(Ma,Fi)" '/
     &       'Variables = "Ma" "Fi" "damp1" "damp2"'/
     &       'zone i=',i3,', j=',i3,', f=point')
c
      do j=1,resol
         do i=1,num_mach
            write(96,9696) zmach(i),Fi(j),fdamp1(i,j),fdamp2(i,j)
 9696     format(4f15.8)
    enddo
    enddo
c*********************************************************
c
end
```

B.5 Compute flutter boundary

```
% flutter_plotter.m

clear all;
close all;
clc;
```

```
% Load damping and frequency
damping = load('damping_output.dat');
frequency = load('frequen_output.dat');
no = 50;
Fi = damping(1:no,1);
M = [0.5 0.745 0.75 0.755 0.76 0.765 0.8];

% Load real and imaginary parts of generalised forces
forces_M0_5=load('M0_5_fully_turbulent_2');
forces_M0_745=load('M0_745_fully_turbulent_2');
forces_M0_75=load('M0_75_fully_turbulent_2');
forces_M0_755=load('M0_755_fully_turbulent_2');
forces_M0_76=load('M0_76_fully_turbulent_2');
forces_M0_765=load('M0_765_fully_turbulent_2');
forces_M0_8=load('M0_8_fully_turbulent_2');
forces_M0_5=forces_M0_5(:,2:end);
forces_M0_745=forces_M0_745(:,2:end);
forces_M0_75=forces_M0_75(:,2:end);
forces_M0_755=forces_M0_755(:,2:end);
forces_M0_76=forces_M0_76(:,2:end);
forces_M0_765=forces_M0_765(:,2:end);
forces_M0_8=forces_M0_8(:,2:end);
forces_k0_20=[forces_M0_5(3,:); forces_M0_745(3,:); forces_M0_75(3,:);...
 forces_M0_755(3,:); forces_M0_76(3,:); forces_M0_765(3,:); forces_M0_8(3,:)];
forces_k0_30=[forces_M0_5(4,:); forces_M0_745(4,:); forces_M0_75(4,:);...
 forces_M0_755(4,:); forces_M0_76(4,:); forces_M0_765(4,:); forces_M0_8(4,:)];
forces_k0_50=[forces_M0_5(5,:); forces_M0_745(5,:); forces_M0_75(5,:);...
 forces_M0_755(5,:); forces_M0_76(5,:); forces_M0_765(5,:); forces_M0_8(5,:)];

% Make zero vector
zeroxvec = linspace(0.05, 0.4, no);
zerovec = zeros(no,1);

% Make matrices per Mach number
M0_5_damp = damping(1:no,:);
M0_745_damp = damping(no+1:2*no,:);
M0_75_damp = damping(2*no+1:3*no,:);
M0_755_damp = damping(3*no+1:4*no,:);
M0_76_damp = damping(4*no+1:5*no,:);
M0_765_damp = damping(5*no+1:6*no,:);
M0_8_damp = damping(6*no+1:7*no,:);
damp_plunge = [M0_5_damp(:,2) M0_745_damp(:,2) M0_75_damp(:,2) M0_755_damp(:,2)...
 M0_76_damp(:,2) M0_765_damp(:,2) M0_8_damp(:,2)];
damp_pitch = [M0_5_damp(:,3) M0_745_damp(:,3) M0_75_damp(:,3) M0_755_damp(:,3)...
 M0_76_damp(:,3) M0_765_damp(:,3) M0_8_damp(:,3)];

M0_5_freq = frequency(1:no,:);
```

```
M0_745_freq = frequency(no+1:2*no,:);
M0_75_freq = frequency(2*no+1:3*no,:);
M0_755_freq = frequency(3*no+1:4*no,:);
M0_76_freq = frequency(4*no+1:5*no,:);
M0_765_freq = frequency(5*no+1:6*no,:);
M0_8_freq = frequency(6*no+1:7*no,:);
freq_plunge = [M0_5_freq(:,2) M0_745_freq(:,2) M0_75_freq(:,2) M0_755_freq(:,2)...
 M0_76_freq(:,2) M0_765_freq(:,2) M0_8_freq(:,2)];
freq_pitch = [M0_5_freq(:,3) M0_745_freq(:,3) M0_75_freq(:,3) M0_755_freq(:,3)...
 M0_76_freq(:,3) M0_765_freq(:,3) M0_8_freq(:,3)];

% Find the flutter index at which the damping is zero
sign_damp = sign(damp_plunge);
diff_damp = diff(sign_damp);
for j=1:7
for i=1:length(diff_damp);
    if diff_damp(i,j)==2
        index(j)=i;
        Fiflutter1(j)=Fi(index(j));      % Take the last negative value of Fi where
        Fiflutter2(j)=Fi(index(j)+1);  % flutter occurs
        dampflutter1(j)=damp_plunge(index(j),j);    % Compute damping at flutter
        dampflutter2(j)=damp_plunge(index(j)+1,j);
        dampflutterpitch1(j)=damp_pitch(index(j),j);
        dampflutterpitch2(j)=damp_pitch(index(j)+1,j);
        freqflutter1(j)=freq_plunge(index(j),j);
        freqflutter2(j)=freq_plunge(index(j)+1,j);
        freqflutterpitch1(j)=freq_pitch(index(j),j);
        freqflutterpitch2(j)=freq_pitch(index(j)+1,j);
    end
end
end
% Use linear interpolation to find Fiflutter
arm1=zeros(1,7)-dampflutter1;
arm2=dampflutter2-zeros(1,7);
Fiflutter=(Fiflutter1.*arm2+Fiflutter2.*arm1)./(arm1+arm2);

% Compute frequency and damping at flutter
dampplungeflutter=(arm1.*Fiflutter1+arm2.*Fiflutter2)./(Fiflutter1+Fiflutter2);
damppitchflutter=...
(dampflutterpitch1.*Fiflutter1+dampflutterpitch2.*Fiflutter2)./(Fiflutter1+Fiflutter2);
freqplungeflutter=...
(freqflutter1.*Fiflutter1+freqflutter2.*Fiflutter2)./(Fiflutter1+Fiflutter2);
freqpitchflutter=...
(freqflutterpitch1.*Fiflutter1+freqflutterpitch2.*Fiflutter2)./(Fiflutter1+Fiflutter2);

% Compute the eigenvalues at flutter
c=0.3;
```

```
v=M*sqrt(1.4*287*273.15);
redfreqplungeflutter=freqplungeflutter.*c./v;
redfreqpitchflutter=freqpitchflutter.*c./v;

% Compute the generalised airloads at flutter
for i=1:length(redfreqplungeflutter)
    if redfreqplungeflutter(i)>0.2&&redfreqplungeflutter(i)<0.3
        diffk0_30(i)=0.3-redfreqplungeflutter(i);
        diffk0_20(i)=redfreqplungeflutter(i)-0.2;
        for j=1:length(forces_k0_20)
            airloads(i,j)=(forces_k0_20(i,j).*diffk0_30(i)...
+forces_k0_30(i,j).*diffk0_20(i))./(diffk0_20(i)+diffk0_30(i));
        end
    elseif redfreqplungeflutter(i)>0.3&&redfreqplungeflutter(i)<0.5
            diffk0_50(i)=0.5-redfreqplungeflutter(i);
            diffk0_30(i)=redfreqplungeflutter(i)-0.3;
            for j=1:length(forces_k0_30)
                airloads(i,j)=(forces_k0_30(i,j).*diffk0_50(i)...
   +forces_k0_50(i,j).*diffk0_30(i))./(diffk0_30(i)+diffk0_50(i));
            end
    end
end
for i=1:length(redfreqpitchflutter)
    if redfreqpitchflutter(i)>0.3&&redfreqpitchflutter(i)<0.5
            diffk0_50(i)=0.5-redfreqpitchflutter(i);
            diffk0_30(i)=redfreqpitchflutter(i)-0.3;
            for j=1:length(forces_k0_30)
                airloadspitch(i,j)=(forces_k0_30(i,j).*diffk0_50(i)...
   +forces_k0_50(i,j).*diffk0_30(i))./(diffk0_30(i)+diffk0_50(i));
            end
    end
end
clh=airloads(:,1)+airloads(:,2)*1i;
cmh=airloads(:,5)+airloads(:,6)*1i;
cla=airloadspitch(:,3)+airloadspitch(:,4)*1i;
cma=airloadspitch(:,7)+airloadspitch(:,8)*1i;

% Compute magnitude and phase of airloads
mag_clh=abs(clh);
phase_clh=atan2(imag(clh),real(clh))*180/pi+180;
mag_cla=abs(cla);
phase_cla=atan2(imag(cla),real(cla))*180/pi-180;
mag_cmh=abs(cmh);
phase_cmh=atan2(imag(cmh),real(cmh))*180/pi;
mag_cma=abs(cma);
phase_cma=atan2(imag(cma),real(cma))*180/pi;
```

Appendix C

Steady Flow Simulations with Deformed Airfoil Geometries

C.1 Determination of new airfoil geometry

C.1.1 Polynomials used to approximate the deformation of the airfoil

The general equations of the polynomials that were used to determine the new airfoil contour with angle of attack correction are given by:

$$\text{Upper surface: } \Delta z_{\text{def.}} = a_u x^5 + b_u x^4 + c_u x^3 + d_u x^2 + e_u x + f_u \tag{C.1}$$

$$\text{Lower surface: } \Delta z_{\text{def.}} = a_l x^9 + b_l x^8 + c_l x^7 + d_l x^6 + e_l x^5 + f_l x^4 + g_l x^3 + h_l x^2 + k_l x + m_l \tag{C.2}$$

The coefficients corresponding to the polynomials are depicted in tables C.1 and C.2.

M	α (°)	a_u	b_u	c_u	d_u	e_u	f_u
0.5	0	$4.5591 \cdot 10^4$	$-3.4506 \cdot 10^4$	$8.9023 \cdot 10^3$	$-8.9889 \cdot 10^2$	$3.2374 \cdot 10^1$	-0.3597
0.765	0	$7.4650 \cdot 10^4$	$-5.5230 \cdot 10^4$	$1.3911 \cdot 10^4$	$-1.3714 \cdot 10^3$	$4.8831 \cdot 10^2$	-0.5307
0.765	0.2	$7.0796 \cdot 10^4$	$-5.1890 \cdot 10^4$	$1.2847 \cdot 10^4$	$-1.2190 \cdot 10^3$	$3.9506 \cdot 10^1$	-0.4018
0.765	0.4	$7.1874 \cdot 10^4$	$-5.3181 \cdot 10^4$	$1.3374 \cdot 10^4$	$-1.3071 \cdot 10^3$	$4.4811 \cdot 10^2$	-0.4780
0.765	0.6	$7.5551 \cdot 10^4$	$-5.6340 \cdot 10^4$	$1.4387 \cdot 10^4$	$-1.4514 \cdot 10^3$	$5.2907 \cdot 10^1$	-0.5785
0.765	0.8	$6.8500 \cdot 10^4$	$-5.0707 \cdot 10^4$	$1.2752 \cdot 10^4$	$-1.2411 \cdot 10^3$	$4.1446 \cdot 10^1$	-0.4268
0.765	1	$6.9480 \cdot 10^4$	$-5.1423 \cdot 10^4$	$1.3028 \cdot 10^4$	$-1.3020 \cdot 10^3$	$4.6690 \cdot 10^1$	-0.4929

Table C.1: Polynomial coefficients used to obtain the upper surface of the deformed airfoil contour

M	α (°)	a_l	b_l	c_l	d_l	e_l	f_l	g_l	h_l
0.5	0	$-1.0308 \cdot 10^8$	$1.1546 \cdot 10^8$	$-4.9672 \cdot 10^7$	$9.6183 \cdot 10^6$	$-5.6077 \cdot 10^5$	$-7.8602 \cdot 10^4$	$1.3476 \cdot 10^4$	$-7.0900 \cdot 10^2$
0.765	0	$-3.8330 \cdot 10^8$	$4.9877 \cdot 10^8$	$-2.7066 \cdot 10^8$	$7.9344 \cdot 10^7$	$-1.3667 \cdot 10^7$	$1.4231 \cdot 10^6$	$-8.9662 \cdot 10^4$	$3.2260 \cdot 10^3$
0.765	0.2	$-3.0500 \cdot 10^8$	$3.8753 \cdot 10^8$	$-2.0339 \cdot 10^8$	$5.6754 \cdot 10^7$	$-9.0666 \cdot 10^6$	$8.4283 \cdot 10^5$	$-4.5437 \cdot 10^4$	$1.3511 \cdot 10^3$
0.765	0.4	$1.1209 \cdot 10^7$	$-3.0913 \cdot 10^7$	$3.0513 \cdot 10^7$	$-1.5128 \cdot 10^7$	$4.1781 \cdot 10^6$	$-6.5478 \cdot 10^5$	$5.6810 \cdot 10^4$	$-2.6288 \cdot 10^3$
0.765	0.6	$-1.8947 \cdot 10^8$	$2.5131 \cdot 10^8$	$-1.3770 \cdot 10^8$	$4.0087 \cdot 10^7$	$-6.6742 \cdot 10^6$	$6.4543 \cdot 10^5$	$-3.5684 \cdot 10^4$	$9.9642 \cdot 10^2$
0.765	0.8	$-4.2535 \cdot 10^7$	$5.4228 \cdot 10^7$	$-2.6984 \cdot 10^7$	$6.2829 \cdot 10^6$	$-5.8097 \cdot 10^5$	$-1.4842 \cdot 10^4$	$6.3003 \cdot 10^3$	$-4.5908 \cdot 10^2$
0.765	1	$8.2572 \cdot 10^7$	$-1.3760 \cdot 10^8$	$9.6191 \cdot 10^7$	$-3.6784 \cdot 10^7$	$8.3383 \cdot 10^6$	$-1.1291 \cdot 10^6$	$8.8085 \cdot 10^4$	$-3.7286 \cdot 10^3$

M	α (°)	k_l	m_l
0.5	0	$1.2044 \cdot 10^1$	$-6.2956 \cdot 10^{-2}$
0.765	0	$-5.8030 \cdot 10^1$	0.3402
0.765	0.2	$-2.1563 \cdot 10^1$	0.1202
0.765	0.4	$5.5649 \cdot 10^2$	-0.3505
0.765	0.6	$-1.1289 \cdot 10^1$	$4.2786 \cdot 10^{-2}$
0.765	0.8	$1.2011 \cdot 10^1$	$-8.1576 \cdot 10^{-2}$
0.765	1	$7.2707 \cdot 10^1$	-0.4376

Table C.2: Polynomial coefficients used to obtain the lower surface deformed airfoil contour

When these polynomials are added to the undeformed airfoil coordinates, a deformed airfoil with angle of attack correction is obtained, that is, simulations with this airfoil need to be performed at an angle of $-\theta$ degree, which is equivalent to the tangent of the line connecting the first and the last measurement point. It should be noted that the coefficients correspond to the case where x is in m, whereas $\Delta z_{\text{def.}}$ and $\Delta z_{\text{def.+rot.}}$ are in mm. Figure C.1 shows the measured airfoil coordinates as well as the polynomial approximation of the upper surface with and without angle of attack correction at $M = 0.765$ and $\alpha = 0.8°$.

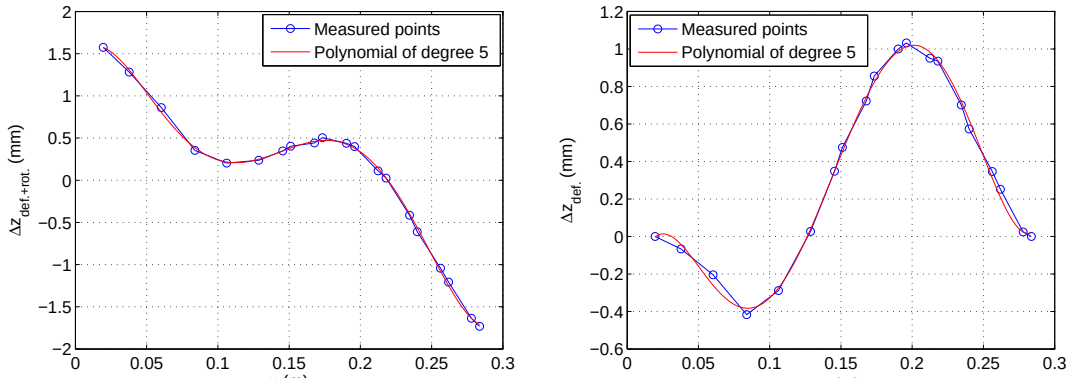

(a) Without angle of attack correction (b) With angle of attack correction

Figure C.1: Measured deformation and polynomial approximations of the upper surface at $M = 0.765$ and $\alpha = 0.8°$

C.1.2 Determine new airfoil contour

```
function [alphau, alphal, newp5, newp5a, newp9, newp9a] = ...
determine_new_contour(datfileu,datfilel)

% Load x- and delta z-values
%A = load('M0_765_a0_uppersurface.dat');
%B = load('M0_765_a0_lowersurface.dat');
A = load(datfileu);
B = load(datfilel);

% Sort the x-values
[xu,inxu] = sort(A(:,1));
[xl,inxl] = sort(B(:,1));

% Now sort the other variables as well
for i=1:length(xu)
    deltazu(i,1) = A(inxu(i),2);
end
for i=1:length(xl)
    deltazl(i,1) = -B(inxl(i),2);          % for lower surface uncomment this
end
```

```
xfineu=xu(1):0.001:xu(end);
xfinel=xl(1):0.001:xl(end);

% Fit polynominals through the points of various degrees
% upper surface
p1u=polyfit([xu(1); xu(end)], [deltazu(1); deltazu(end)],1);
f1u=polyval(p1u,xfineu);
p3u=polyfit(xu,deltazu,3);
f3u=polyval(p3u,xfineu);
p4u=polyfit(xu,deltazu,4);
f4u=polyval(p4u,xfineu);
p5u=polyfit(xu,deltazu,5);
f5u=polyval(p5u,xfineu);
p6u=polyfit(xu,deltazu,6);
f6u=polyval(p6u,xfineu);
p7u=polyfit(xu,deltazu,7);
f7u=polyval(p7u,xfineu);
p8u=polyfit(xu,deltazu,8);
f8u=polyval(p8u,xfineu);
p9u=polyfit(xu,deltazu,9);
f9u=polyval(p9u,xfineu);
p10u=polyfit(xu,deltazu,10);
f10u=polyval(p10u,xfineu);
% lower surface
p1l=polyfit([xl(1); xl(end)], [deltazl(1); deltazl(end)],1);
f1l=polyval(p1l,xfinel);
p3l=polyfit(xl,deltazl,3);
f3l=polyval(p3l,xfinel);
p4l=polyfit(xl,deltazl,4);
f4l=polyval(p4l,xfinel);
p5l=polyfit(xl,deltazl,5);
f5l=polyval(p5l,xfinel);
p6l=polyfit(xl,deltazl,6);
f6l=polyval(p6l,xfinel);
p7l=polyfit(xl,deltazl,7);
f7l=polyval(p7l,xfinel);
p8l=polyfit(xl,deltazl,8);
f8l=polyval(p8l,xfinel);
p9l=polyfit(xl,deltazl,9);
f9l=polyval(p9l,xfinel);
p10l=polyfit(xl,deltazl,10);
f10l=polyval(p10l,xfinel);

% Plot the orginal points and polynominals
figure(1);
plot(xu,deltazu,'bo-');
```

```
hold on;
% upper surface
plot(xfineu,f3u,'r');
plot(xfineu,f4u,'g');
plot(xfineu,f5u,'m');
plot(xfineu,f6u,'c');
plot(xfineu,f7u,'k');
plot(xfineu,f8u,'y');
plot(xfineu,f9u,'--r');
plot(xfineu,f10u,'--g');
plot(xfineu,f1u,'-b');
xlabel('x (m)');
ylabel('\Delta z (mm)');
legend('Orginal points','n = 3','n = 4','n = 5','n = 6','n = 7','n = 8','n = 9',...
'n = 10');

% lower surface
figure(2);
plot(xl, deltazl,'bo-');
hold on;
plot(xfinel,f3l,'r');
plot(xfinel,f4l,'g');
plot(xfinel,f5l,'m');
plot(xfinel,f6l,'c');
plot(xfinel,f7l,'k');
plot(xfinel,f1l,'-b');
xlabel('x (m)');
ylabel('\Delta z (mm)');
legend('Orginal points','n = 3','n = 4','n = 5','n = 6','n = 7');

alphau = atan((deltazu(end)-deltazu(1))/((xu(end)-xu(1))*10^3))*180/pi;
alphal = atan((deltazl(end)-deltazl(1))/((xl(end)-xl(1))*10^3))*180/pi;

% Plot deformation without rotation
% upper surface
f1newu=polyval(p1u,xu);
newdeltazu=deltazu-f1newu;
figure(3);
plot(xu,newdeltazu);

% Evaluate new polynominals
g1u=polyval(p1u,xfineu,'bo-');
g3u=f3u-g1u;
g4u=f4u-g1u;
g5u=f5u-g1u;
g6u=f6u-g1u;
g7u=f7u-g1u;
```

```
% Plot the new polynominals
hold on;
plot(xfineu,g3u,'r');
plot(xfineu,g4u,'g');
plot(xfineu,g5u,'m');
plot(xfineu,g6u,'c');
plot(xfineu,g7u,'k');
xlabel('x (m)');
ylabel('\Delta z corrected for rotation (mm)');
legend('Orginal points','n = 3','n = 4','n = 5','n = 6','n = 7');


% lower surface
f1newl=polyval(p1l,xl);
newdeltazl=deltazl-f1newl;
figure(4);
plot(xl,newdeltazl);

% Evaluate new polynominals
g1l=polyval(p1l,xfinel,'bo-');
g3l=f3l-g1l;
g4l=f4l-g1l;
g5l=f5l-g1l;
g6l=f6l-g1l;
g7l=f7l-g1l;
g8l=f8l-g1l;
g9l=f9l-g1l;
g10l=f10l-g1l;

% Plot the new polynominals
hold on;
plot(xfinel,g3l,'r');
plot(xfinel,g4l,'g');
plot(xfinel,g5l,'m');
plot(xfinel,g6l,'c');
plot(xfinel,g7l,'k');
plot(xfinel,g8l,'y');
plot(xfinel,g9l,'--r');
plot(xfinel,g10l,'--g');
xlabel('x (m)');
ylabel('\Delta z corrected for rotation (mm)');
legend('Orginal points','n = 3','n = 4','n = 5','n = 6','n = 7','n = 8','n = 9',...
'n = 10');

% Load data files
U = load('CAST-10_xyz_coordinates_nach_vermessung_uppersuface.dat');
```

```
L = load('CAST-10_xyz_coordinates_nach_vermessung_lowersuface.dat');
TE = load('CAST-10_xyz_coordinates_nach_vermessung_te_2.dat');

% Sort the x-values
[xu2,ixu2] = sort(U(:,1));
[xl2,ixl2] = sort(L(:,1));
[xte2,ixte2] = sort(TE(:,1));

% Assign sorted x-values
Uvar(:,1) = xu2;
Lvar(:,1) = xl2;
TEvar(:,1) = xte2;

% Now sort the other variables as well
for i=1:length(U)
    Uvar(i,2:size(U,2)) = U(ixu2(i),2:size(U,2));
end
for i=1:length(L)
    Lvar(i,2:size(L,2)) = L(ixl2(i),2:size(L,2));
end
for i=1:length(ixte2)
    TEvar(i,2:size(TE,2)) = TE(ixte2(i),2:size(TE,2));
end

% Upper surface
% Calculate new airfoil contour without angle of attack correction
h1u=polyval(p1u,Uvar(:,1));
k5u=polyval(p5u,Uvar(:,1));
newzu=zeros(size(Uvar,1),1);
for i=1:size(Uvar,1)
if Uvar(i,1)>xu(1)&&Uvar(i,1)<xu(end)
newzu(i)=Uvar(i,3)+k5u(i)/1000;
end
end
for i=1:length(newzu)
    if newzu(i)==0
        newzu(i)=Uvar(i,3)+h1u(i)/1000;
    end
end
newp5=p5u;

% plot old and new airfoil contour without angle of attack correction
figure(5);
plot(Uvar(:,1),Uvar(:,3),'b');
hold on;
plot(Uvar(:,1),newzu,'r');
```

```
% Calculate new airfoil contour with angle of attack correction
h1u=polyval(p1u,Uvar(:,1));
h5u=polyval(p5u,Uvar(:,1))-h1u;
newzua=zeros(size(Uvar,1),1);
for i=1:size(Uvar,1)
if Uvar(i,1)>xu(1)&&Uvar(i,1)<xu(end)
newzua(i)=Uvar(i,3)+h5u(i)/1000;
end
end
for i=1:length(newzua)
    if newzua(i)==0
        newzua(i)=Uvar(i,3);
    end
end
newp5a=[p5u(1) p5u(2) p5u(3) p5u(4) p5u(5)-p1u(1) p5u(6)-p1u(2)];

% plot old and new airfoil contour with angle of attack correction
figure(6);
plot(Uvar(:,1),Uvar(:,3),'b');
hold on;
plot(Uvar(:,1),newzua,'r');
plot(TE(:,1),TE(:,3),'bo');

% Lower surface
% Calculate new airfoil contour without angle of attack correction
h1l=polyval(p1l,Lvar(:,1));
k9l=polyval(p9l,Lvar(:,1));
newzl=zeros(size(Lvar,1),1);
for i=1:size(Lvar,1)
if Lvar(i,1)>xl(1)&&Lvar(i,1)<xl(end)
newzl(i)=Lvar(i,3)+k9l(i)/1000;
end
end
for i=1:length(newzl)
    if newzl(i)==0
        newzl(i)=Lvar(i,3)+h1l(i)/1000;
    end
end
newp9=p9l;

% plot old and new airfoil contour without angle of attack correction
figure(5);
plot(Lvar(:,1),Lvar(:,3),'b');
hold on;
plot(Lvar(:,1),newzl,'r');

% Calculate new airfoil contour with angle of attack correction
```

```
h1l=polyval(p1l,Lvar(:,1));
h9l=polyval(p9l,Lvar(:,1))-h1l;
newzla=zeros(size(Lvar,1),1);
for i=1:size(Lvar,1)
if Lvar(i,1)>xl(1)&&Lvar(i,1)<xl(end)
newzla(i)=Lvar(i,3)+h9l(i)/1000;
end
end
for i=1:length(newzla)
    if newzla(i)==0
        newzla(i)=Lvar(i,3);
    end
end
newp9a=[p9l(1) p9l(2) p9l(3) p9l(4) p9l(5) p9l(6) p9l(7) p9l(8) p9l(9)-p1l(1)...
 p9l(10)-p1l(2)];

% plot old and new airfoil contour with angle of attack correction
figure(6);
plot(Lvar(:,1),Lvar(:,3),'b');
hold on;
plot(Lvar(:,1),newzla,'r');
plot(TE(:,1),TE(:,3),'bo');
```

Appendix D

Grid Independency Studies

In order to check whether the solution obtained from the CFD simulations is independent of the mesh used a grid independency study is usually carried out. Since the grid generator that has been used in this is a hybrid grid generator, the procedure applied here is a bit different than conventional grid convergence studies. All grid independency studies shown here have been performed with TAU.

This chapter will outline the results of the grid independency studies performed with one of the deformed airfoil geometries and with the original airfoil (both steady and unsteady).

D.1 Steady flow simulations with deformed airfoil geometries

The case selected for this grid independency study with one of the deformed airfoil geometries is a transonic steady case with a Mach number of 0.765 and at an angle of attack of 0°. Various grid refinements have been investigated, both for the structured part of the grid as well as for unstructured part. Furthermore, the influence of the size of the domain, that is, the radius of the farfield boundary has also been investigated. The default grid settings were shown in table 5.1.

D.1.1 Structured part

A number of parameters that are thought to influence the solution of the CFD simulations have been varied. The height of the first cell has been varied such that the value of y^+ in the first cell is always smaller than one. Four different values of y^+ have been selected: $y^+ = 1$, $y^+ = 2/3$, $y^+ = 4/9$ and $y^+ = 8/27$. These values were recommended by the AIAA for their fourth CFD Drag Prediction Workshop 4th AIAA CFD Drag Prediction Workshop [2008]. In order to compute the height of the first cell corresponding to these

values of y^+ an estimation of the skin friction coefficient c_f is needed. Here the estimation for a turbulent flat plate boundary layer as proposed by Schlichting [1979] was used:

$$c_f = 0.455 \left(\log_{10} Re\right)^{-2.58}, \tag{D.1}$$

where a logarithmic velocity profile was assumed. Furthermore the number of cells along the airfoil contour has been changed as well. The spacing at the leading and trailing edge was initially already finer as that at the upper and lower surfaces and it has been refined correspondingly with each variation of the length of the cells along the airfoil contour. Furthermore, the number of cells inside the structured layer (in wall-normal direction) has been changed, while keeping the total height of the structured layer the same. Finally, the total height of the structural layer has been varied, while keeping the number of cells in airfoil normal direction the same. The total boundary layer height of a turbulent flat plate is computed as follows (Schlichting [1979]):

$$\delta = \frac{0.371c}{Re^{0.2}}. \tag{D.2}$$

The results of these variations are shown in table D.1.

y^+	Coefficient		
	c_l	c_d	c_{m_y}
1	0.301791 (+1.8%)	0.015845 (-0.1%)	-0.051915 (-2.4%)
$\frac{2}{3}$	0.298708 (+0.8%)	0.015853 (-0.08%)	-0.051237 (-1.0%)
$\frac{4}{9}$	0.296433	0.015866	-0.0507105
$\frac{8}{27}$	0.294020 (-0.8%)	0.015903 (+0.2%)	-0.050286 (+0.8%)
Length of cells along contour (mm)	c_l	c_d	c_{m_y}
4	0.302349 (-7.0%)	0.015149 (-1.6%)	-0.051606 (+9.6%)
2	0.314528 (-3.3%)	0.015288 (-0.7%)	-0.054295 (+4.9%)
1	0.3252798	0.015391	-0.057071
0.5	0.326216 (+0.3%)	0.015398 (+0.05%)	-0.057298 (-0.4%)
Number of layers	c_l	c_d	c_{m_y}
35	0.284042 (-7.0%)	0.0156215 (-2.0%)	-0.048661 (+8.3%)
70	0.305380	0.015933	-0.053063
140	0.312346 (+2.2%)	0.016044 (+0.7%)	-0.054480 (-2.6%)
Structural layer thickness/ boundary layer thickness of flat plate	c_l	c_d	c_{m_y}
1	0.300605 (-1.6%)	0.015762 (-0.1%)	-0.051815 (+2.4%)
1.5	0.3055298 (+0.05%)	0.015908 (-0.2%)	-0.053083 (-0.04%)
2	0.305380	0.015933	-0.053063
0.5	0.306113 (+0.2%)	0.015961 (+0.2%)	-0.053219 (-0.3%)

Table D.1: Force and moments coefficient at $M = 0.765$ and $\alpha = 0°$ for various mesh settings of the structural mesh part

From table D.1 it can be seen that the difference with the $y^+ = 2/3$ and $y^+ = 8/27$ cases is less than one percent. Hence, the grid with a y^+-value of 4/9 in the first cell above the airfoil has been selected for further computations. From the variation in the number of cells along the contour it can be seen that the force and moment coefficients do not change much when the number of cells along the airfoil contour are 2, 1 or 0.5 mm. Therefore the fine case with cells of 1 mm along the contour has been selected for further calculations. Furthermore, it can be seen that the relative error with respect to the 140 layers in the structured part of the grid is a bit larger than in the previous variations of the the number of cells along the airfoil contour and the first cell height. It is however sufficiently small in order to speak of grid independence. Also since the increase in computational costs is large for the 140 layers case compared to the default 70 layers case. Therefore, 70 layers in wall-normal direction have been used. Table D.1 indicates that the height of the structural layer is not that important, at least it is sufficiently high when twice the boundary layer thickness of a flat plate is taken. It is however expected that, when half of the boundary layer thickness is used, severe deviations start to occur. Therefore, taking twice the boundary layer thickness is sufficient. Since at the Mach numbers considered for this deformation study no large separation area is present behind the shock wave.

D.1.2 Unstructured part

To investigate the influence of the unstructured part, the cells in the unstructured part have been made smaller. This was done in such a way that the aspect ratio of the cells stays the same. The importance of this was pointed out by Salas [2006]. Since the unstructured part consist of triangles in two dimensions this means that for the first refinement each triangle is splitted into four triangles and for the second refinement these four triangles are splitted in 16 triangles (compared to the original grid). The original case will be called default, the case with four triangles is called fine and the case with 16 triangles is called extra fine. Derefinement was not possible (with the TAU refinement tool), therefore it cannot be checked whether an even more coarse grid would be sufficient. The force and moment coefficients obtained from the simulations can be found in table D.2.

Coefficient	Default	Fine	Extra fine
c_l	0.305380	0.306192 (+0.3%)	0.305750 (+0.1%)
c_d	0.015933	0.015729 (-1.3%)	0.015613 (-2.0%)
c_{m_y}	-0.053063	-0.053222 (-0.3%)	-0.053067 (-0.008%)

Table D.2: Force and moment coefficient at $M = 0.765$ and $\alpha = 0°$ for various levels of unstructural part refinement

As can be seen from these tables the error made by taking the default grid is less than 2.0% for all coefficients. From this it can be concluded that using the default grid is sufficient.

D.1.3 Farfield boundary

The influence of the farfield boundary has also been investigated. The radius of the farfield boundary is 1000 times the airfoil chord. Table D.3 shows the results obtained with this mesh. As can be seen from this table a farfield boundary of 100 times the airfoil chord is also sufficient, since the differences in the results are small (2.3% or less). Therefore the farfield boundary is be taken to be 100 times the chord length of the airfoil in the simulations used for determination of the flutter boundary (both steady and unsteady).

Radius of farfield boundary	Coefficient		
	c_l	c_d	c_{m_y}
100c	0.296433	0.015866	-0.0507105
1000c	0.294316 (-0.7%)	0.015498 (-2.3%)	-0.051274 (+1.1%)

Table D.3: Force and moments coefficient at $M = 0.765$ and $\alpha = 0°$ for radius of farfield boundary variation

D.2 Steady flow simulations with the original CAST-10 airfoil

A grid independency check has been performed for the fully turbulent case as well as for the simulations with free boundary layer transition with the original CAST-10 airfoil. During this check several grid settings of the structured part of the grid have been changed. As those are expected to influence the results the most (based on the grid independency study performed with the deformed airfoil contour). The default grid used for all simulations has the settings as shown in table 6.1. The first cell height, the number of structured layers and the length of the cells on the airfoil surface (including leading and trailing edge) has been varied. Each of these parameters has been multiplied and divided by two. For the number of cells on the surface this also holds for the leading and trailing edges, that is when the number of cells on the surface is halved, the number of cells at the leading and the trailing edge of the airfoil is also halved.

D.2.1 Fully turbulent simulations

The testcase used for the fully turbulent simulations is: $M = 0.765$ and $\alpha = 0.0°$. Table D.4 shows the force and moment coefficients obtained with the different meshes. From this table it can be seen that the deviations with respect to the default grid are smaller than 2% and therefore the results are grid independent.

y^+	Coefficient		
	c_l	c_d	c_{m_y}
1	0.459383 (+0.8%)	0.014289 (-0.6%)	-0.072461 (+1.1%)
$\frac{1}{2}$	0.455765	0.014378	-0.071673
$\frac{8}{27}$	0.453785 (-0.4%)	0.014416 (+0.3%)	-0.071241 (-0.6%)
Length of cells along contour (mm)	c_l	c_d	c_{m_y}
2	0.451498 (-0.9%)	0.014544 (+1.2%)	-0.070549 (-1.6%)
1	0.455765	0.014378	-0.071673
0.5	0.456614 (+0.2%)	0.0143845 (+0.05%)	-0.071844 (+0.2%)
Number of layers	c_l	c_d	c_{m_y}
50	0.454135 (-0.4%)	0.0143671 (-0.08%)	-0.071305 (-0.5%)
100	0.455765	0.014378	-0.071673
200	0.454468 (-0.3%)	0.014319 (-0.4%)	-0.071324 (-0.5%)

Table D.4: Force and moments coefficient at $M = 0.765$ and $\alpha = 0°$ for various mesh settings of the structural mesh part (fully turbulent)

D.2.2 Free transition simulations

The testcase selected for the grid independency study with free transition is $M = 0.74$ and $\alpha = 0°$. Table D.5 shows the force and moment coefficients obtained with the different meshes at this Mach number.

y^+	Coefficient		
	c_l	c_d	c_{m_y}
1	0.548928 (+0.6%)	0.007896 (-1.3%)	-0.085881 (+0.6%)
$\frac{1}{2}$	0.545471	0.007997	-0.085340
$\frac{8}{27}$	0.543109 (-0.4%)	0.008059 (+0.8%)	-0.084967 (-0.4%)
Length of cells along contour (mm)	c_l	c_d	c_{m_y}
2	-	-	-
1	0.545471	0.007997	-0.085340
0.5	-	-	-
Number of layers	c_l	c_d	c_{m_y}
50	0.544807 (-0.1%)	0.008017 (+0.2%)	-0.085211 (-0.2%)
100	0.545471	0.007997	-0.085340
200	-	-	-

Table D.5: Force and moments coefficient at $M = 0.74$ and $\alpha = 0°$ for various mesh settings of the structural mesh part (free transition)

It should be noted however that for some meshes there were convergence problems. The transition location did not converge for these meshes. Therefore the results of these meshes have been left out in table D.5. Because of these convergence problems the grid

independency study has been repeated at a less critical Mach number ($M = 0.65$ and at $\alpha = 0°$). At this Mach number there were however convergence problems as well. The force and moment coefficient obtained from the simulations with the different meshes at $M = 0.65$ are shown in table D.6.

y^+	Coefficient		
	c_l	c_d	c_{m_y}
1	0.444742 (+0.4%)	0.0074403 (-1.0%)	-0.073773 (+0.4%)
$\frac{1}{2}$	0.443157	0.0075175	-0.073493
$\frac{8}{27}$	0.442499 (-0.2%)	0.007551 (+0.4%)	-0.073370 (-0.2%)
Length of cells along contour (mm)	c_l	c_d	c_{m_y}
2	0.431882 (-2.5%)	0.008257 (+9.8%)	-0.071540 (-2.7%)
1	0.443157	0.0075175	-0.073493
0.5	-	-	-
Number of layers	c_l	c_d	c_{m_y}
50	0.445578 (+0.5%)	0.007459 (-0.8%)	-0.073910 (+0.6%)
100	0.443157	0.0075175	-0.073493
200	-	-	-

Table D.6: Force and moments coefficient at $M = 0.65$ and $\alpha = 0°$ for various mesh settings of the structural mesh part (free transition)

From these tables it can be seen that if converged force and moment coefficients are obtained, the differences between the different meshes are small (typically 1-2%, except for the drag coefficient in case of 2 mm cells along the contour at $M = 0.65$). Since the finer mesh in case of the length of the cells along the contour and the number of structured layers variation did not give converged results, it cannot be concluded that the results are mesh independent. It can however be noted that the results obtained with the coarsest meshes corresponding to these cases are almost identical to those obtained with the original mesh. Therefore it is highly likely that the results are grid independent, unless these meshes are not in the region where one can speak of grid convergence yet.

D.3 Unsteady flow simulations with the original CAST-10 airfoil

In this section the grid independency of the pitching motion with the original CAST-10 airfoil is checked. The settings that have been varied are the same as those in section D.2. The magnitude and phase angle of both lift and moment coefficient are used to determine whether the results are grid independent.

D.3.1 Fully turbulent simulations

The testcase used for is a pitching motion at $M = 0.765$ and $k = 0.30$. The amplitude of the motion is 0.05°. The magnitude and phase angle of the lift and moment coefficient

obtained for the various meshes are shown in table D.7.

	Magnitude (-)		Phase angle (°)	
y^+	c_l	c_{m_y}	c_l	c_{m_y}
1	$4.9728 \cdot 10^{-3}$ (-0.6%)	$3.9465 \cdot 10^{-4}$ (+2.2%)	-16.26 (-2.8%)	-136.61 (+1.0%)
$\frac{1}{2}$	$4.9759 \cdot 10^{-3}$	$3.8623 \cdot 10^{-4}$	-16.71	-135.29
$\frac{8}{27}$	$5.0059 \cdot 10^{-3}$ (+0.6%)	$3.8081 \cdot 10^{-4}$ (-1.4%)	-17.27 (+3.4%)	-137.61 (+1.7%)
Length of cells along contour (mm)	c_l	c_{m_y}	c_l	c_{m_y}
2	$5.0147 \cdot 10^{-3}$ (+0.8%)	$4.2044 \cdot 10^{-4}$ (+8.9%)	-15.90 (-4.8%)	-132.64 (-2.0%)
1	$4.9759 \cdot 10^{-3}$	$3.8623 \cdot 10^{-4}$	-16.71	-135.29
0.5	$4.9769 \cdot 10^{-3}$ (-0.02%)	$3.8238 \cdot 10^{-4}$ (+1.0%)	-16.72 (+0.06%)	-135.70 (+0.3%)
Number of layers	c_l	c_{m_y}	c_l	c_{m_y}
50	$4.9921 \cdot 10^{-3}$ (+0.3%)	$3.8353 \cdot 10^{-4}$ (-0.7%)	-17.05 (+2.0%)	-136.33 (+0.8%)
100	$4.9759 \cdot 10^{-3}$	$3.8623 \cdot 10^{-4}$	-16.71	-135.29
200	$4.9913 \cdot 10^{-3}$ (+0.3%)	$3.8556 \cdot 10^{-4}$ (-0.2%)	-16.65 (+0.6%)	-135.13 (-0.1%)

Table D.7: Magnitude and phase angle of lift and pitching moment coefficient at $M = 0.765$ and $k = 0.30$ for various mesh settings of the structural mesh part (fully turbulent)

From this table it is observed that the differences between the various meshes are small (up to 3%, except in case of 2 mm cells along the surface) and therefore the results are said to be independent of the mesh for meshes which are finer than those with $y^+ = 1/2$, 1 mm cells on the airfoil contour and 100 structural layers.

D.3.2 Free transition simulations

As in the steady case two Mach numbers ($M = 0.74$ and $M = 0.65$) have been used to check the grid independency of the simulations with free boundary layer transition. The results of this investigation using a pitching motion at $k = 0.30$ are shown in tables D.8 and D.9. It should be noted that the meshes that did not converge in the steady simulations have not been used for the unsteady simulations, since it is expected that the inner iterations would not converge either in that case.

Both tables show that the differences between the mesh are much larger than for the fully turbulent simulations. Especially when cells of 2 mm at the surface are used the differences are significant (up to 23%). Furthermore, care also needs to be taken in choosing the y^+ value, as here large deviations occur for the moment coefficient. Hence, the results of the finer meshes are needed in order to be able to conclude that one can speak of grid independency.

	Magnitude (-)		Phase angle (°)	
y^+	c_l	c_{m_y}	c_l	c_{m_y}
1	$5.4513 \cdot 10^{-3}$ (+0.9%)	$1.7770 \cdot 10^{-4}$ (+5.9%)	-36.12 (+2.0%)	-192.50 (+3.8%)
$\frac{1}{2}$	$5.4023 \cdot 10^{-3}$	$1.6778 \cdot 10^{-4}$	-35.42	-185.54
$\frac{8}{27}$	$5.4033 \cdot 10^{-3}$ (+0.02%)	$1.5675 \cdot 10^{-4}$ (-6.6%)	-35.57 (+0.4%)	-181.35 (-2.3%)
Length of cells along contour (mm)	c_l	c_{m_y}	c_l	c_{m_y}
2	-	-	-	-
1	$5.4023 \cdot 10^{-3}$	$1.6778 \cdot 10^{-4}$	-35.42	-185.54
0.5	-	-	-	-
Number of layers	c_l	c_{m_y}	c_l	c_{m_y}
50	$5.3837 \cdot 10^{-3}$ (-0.3%)	$1.6911 \cdot 10^{-4}$ (+0.8%)	-35.17 (-0.7%)	-183.90 (-0.9%)
100	$5.4023 \cdot 10^{-3}$	$1.6778 \cdot 10^{-4}$	-35.42	-185.54
200	-	-	-	-

Table D.8: Magnitude and phase angle of lift and pitching moment coefficient at $M = 0.74$ and $k = 0.30$ for various mesh settings of the structural mesh part (free transition)

	Magnitude (-)		Phase angle (°)	
y^+	c_l	c_{m_y}	c_l	c_{m_y}
1	$4.6509 \cdot 10^{-3}$ (+0.5%)	$3.8088 \cdot 10^{-4}$ (-1.9%)	-7.97 (+0.3%)	-75.02 (-0.2%)
$\frac{1}{2}$	$4.6260 \cdot 10^{-3}$	$3.8825 \cdot 10^{-4}$	-7.95	-75.24
$\frac{8}{27}$	$4.6544 \cdot 10^{-3}$ (+0.6%)	$4.0615 \cdot 10^{-4}$ (+4.6%)	-6.73 (-15.3%)	-75.43 (-0.3%)
Length of cells along contour (mm)	c_l	c_{m_y}	c_l	c_{m_y}
2	$4.7326 \cdot 10^{-3}$ (+2.3%)	$2.9766 \cdot 10^{-4}$ (-23.3%)	-8.80 (+9.7%)	-76.31 (+1.4%)
1	$4.6260 \cdot 10^{-3}$	$3.8825 \cdot 10^{-4}$	-7.95	-75.24
0.5	-	-	-	-
Number of layers	c_l	c_{m_y}	c_l	c_{m_y}
50	$4.6563 \cdot 10^{-3}$ (+0.07%)	$3.6295 \cdot 10^{-4}$ (-6.5%)	-9.16 (+13.2%)	-76.60 (+1.8%)
100	$4.6260 \cdot 10^{-3}$	$3.8825 \cdot 10^{-4}$	-7.95	-75.24
200	-	-	-	-

Table D.9: Magnitude and phase angle of lift and pitching moment coefficient at $M = 0.65$ and $k = 0.30$ for various mesh settings of the structural mesh part (free transition)

Appendix E

Temporal Independency Study

The results obtained from the unsteady flow simulations need to be independent of the timestep used and of the number of inner iterations used. In order to check this a temporal independency study has been performed in which the timestep was varied as well as the number of inner iterations. This chapter shows the results obtained from these studies performed with TAU for both fully turbulent as well as simulations with free boundary layer transition. Results from both pitching and plunging motion are shown.

E.1 Fully turbulent simulations

The testcase that has been used is a pitching/plunging airfoil at a Mach number of 0.765 and a reduced frequency of 0.05. This case was selected because it was thought to be a critical case in terms of Mach number. At this small reduced frequency the motion is very slow and therefore it is important to have a sufficiently small timestep such that all features of the flow are captured.

E.1.1 Pitching motion

Figure E.1 shows the lift and moment coefficient versus the angle of attack for three different NOTPP: 300, 600 and 1200. The number of inner iterations NOII is 400 for all cases shown. The amplitude of the pitching motion is 0.25°.

From these figures it can be seen that the curves lie on top of each other for NOTPP = 600 and NOTPP = 1200. For NOTPP = 300, however, the moment coefficient curve deviates from the other two NOTPP. Hence, for NOTPP = 300, the resulting solution is not yet timestep-independent, that is, the solution changes when the number of timesteps per period is changed. Based on these graphs 600 timesteps per period have been selected for this pitching airfoil test case. This number gives a temporally converged solution and is more efficient than using 1200 timesteps per period.

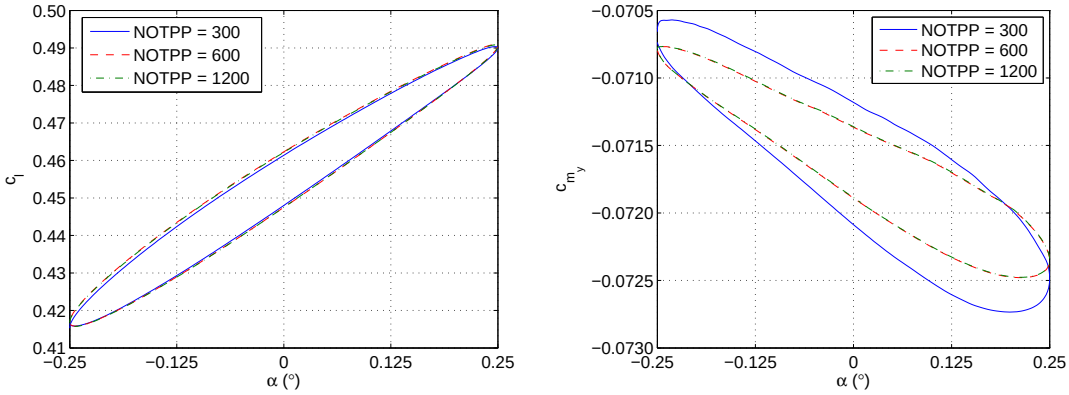

(a) Lift coefficient versus angle of attack

(b) Moment coefficient versus angle of attack

Figure E.1: Lift and moment coefficient versus angle of attack at $M = 0.765$, $k = 0.05$ and NOII $= 400$ for three different NOTPP for pitching motion (fully turbulent)

The magnitude and phase angle of the lift and moment coefficients can also be used in order to determine the temporal convergence. Table E.1 shows these quantities for NOTPP = 300, 600 and 1200.

	Magnitude (-)		Phase angle (°)	
NOTPP	c_l	c_{m_y}	c_l	c_{m_y}
300	$3.7669 \cdot 10^{-2}$ (+0.6%)	$1.0468 \cdot 10^{-3}$ (+25.2%)	-9.86 (-11.9%)	-152.52 (-4.6%)
600	$3.7453 \cdot 10^{-2}$	$8.3578 \cdot 10^{-4}$	-11.19	-159.93
1200	$3.7459 \cdot 10^{-2}$ (+0.02%)	$8.3598 \cdot 10^{-4}$ (+0.02%)	-9.22 (-17.6%)	-158.06 (-1.2%)

Table E.1: Magnitude and phase angle of lift and pitching moment coefficient at $M = 0.765$, $k = 0.05$ and NOII $= 400$ for various NOTPP (fully turbulent)

From this table it can be observed that the changes in magnitude and phase are not really large when the number of timesteps per period is increased. Although the changes from 600 to 1200 NOTPP are smaller than from 300 to 600 (except for the phase angle of the lift coefficient). Therefore, this table confirms that using 600 timesteps per periods is a good compromise between accuracy and efficiency.

The number of inner iterations has also been varied. The same testcase as for the NOTPP investigation has been used. The number of timesteps per period has been fixed at 600. Figure E.2 shows the lift and moment coefficient versus the angle of attack for NOII = 200, 300, 400 and 500.

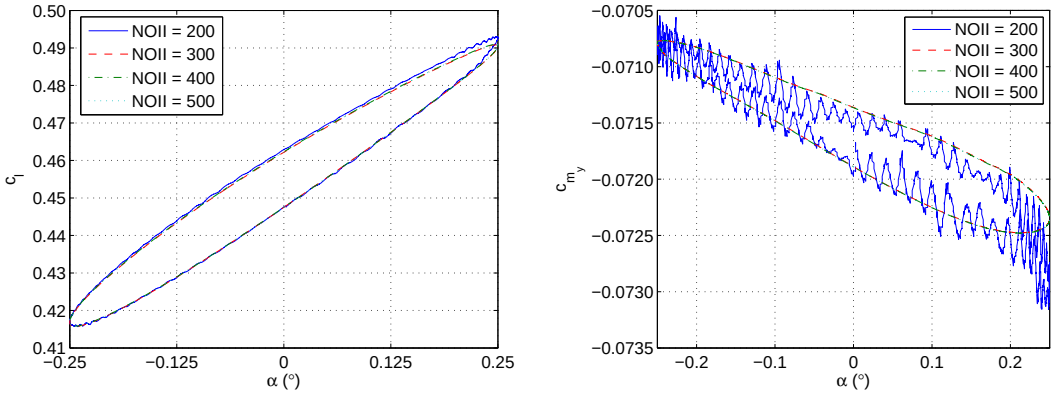

(a) Lift coefficient versus angle of attack

(b) Moment coefficient versus angle of attack

Figure E.2: Lift and moment coefficient versus angle of attack at $M = 0.765$, $k = 0.05$ and NOTPP $= 600$ for four different NOII for pitching motion (fully turbulent)

From these figures it is observed that using 200 inner iterations does not lead to a converged solution. This can be observed from figure E.3, which shows the root-mean square of the density residual in case of 200 inner iterations. It should be noted that at the beginning of each timestep this residual is scaled with the residual of the last inner iteration of the previous timestep (hence it is one at the beginning of each timestep). From this figure it is seen that the residual becomes even larger than one and does clearly not decrease. Hence, the moment coefficient was not converged at each timestep. When this is the case, the next timestep will be started with a non-converged solution of the previous timestep and even if this timestep converges, this leads to wrong results. The results from the other number of inner iterations are approximately on top of each. In order to decide which number would give converged results and is cost-effective, the convergence history of the inner iterations has been looked at. It was seen that when 400 inner iterations are used most timesteps show converged results, hence this number has been used for other simulations of the pitching airfoil.

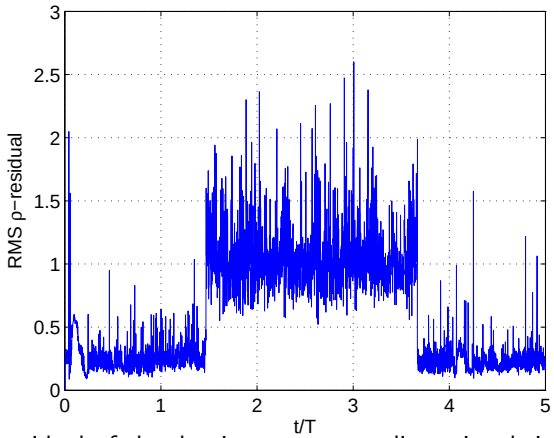

Figure E.3: RMS residual of the density versus non-dimensional time at $M = 0.765$, $k = 0.05$ and $\alpha_m = 0.25°$ (NOTPP $= 600$ and $NOII = 200$)

The magnitude and phase angle of the lift and moment coefficient are shown in table E.2. The changes in magnitude and phase angle with the number of inner iterations are large from 200 to 300 inner iterations. The differences between 300, 400 and 500 inner iterations are not so large (typically less than 1%, except for the phase angle of the lift coefficient when using 500 inner iterations, where the difference is approximately 4%), hence using 400 inner iterations is sufficient.

	Magnitude (-)		Phase angle (°)	
NOII	c_l	c_{m_y}	c_l	c_{m_y}
200	$3.8050 \cdot 10^{-2}$ (+1.6%)	$9.7797 \cdot 10^{-4}$ (+17.0%)	-11.64 (+4.0%)	-167.93 (+5.0%)
300	$3.7470 \cdot 10^{-2}$ (+0.05%)	$8.3516 \cdot 10^{-4}$ (-0.07%)	-11.24 (+0.4%)	-160.05 (+0.08%)
400	$3.7453 \cdot 10^{-2}$	$8.3578 \cdot 10^{-4}$	-11.19	-159.93
500	$3.7491 \cdot 10^{-2}$ (+0.01%)	$8.3674 \cdot 10^{-4}$ (+0.1%)	-10.77 (-3.8%)	-159.60 (-0.2%)

Table E.2: Magnitude and phase angle of lift and pitching moment coefficient at $M = 0.765$, $k = 0.05$ and NOTPP = 600 for various NOII (fully turbulent)

A proper choice of NOTPP and NOII is therefore: NOTPP = 600 and NOII = 400. This choice is valid for $M = 0.765$, $k = 0.05$ and an amplitude of 0.25°, which is relatively large, as the flutter simulations are performed at an amplitude that is five times smaller. Hence, as the testcase used was a very critical testcase, as stated before, this choice of NOTPP and NOII has been extended to other Mach numbers and reduced frequencies, such that the physical timestep is constant.

E.1.2 Plunging motion

For the plunging motion of the airfoil, a similar investigation has been performed. The selected testcase was a plunging airfoil at $M = 0.765$, $k = 0.05$ and the amplitude of the motion was $h_m = 0.005c/k = 0.03$ m. Figure E.4 shows the lift and moment coefficient versus the non-dimensional vertical distance for NOTPP = 300, 600 and 1200.

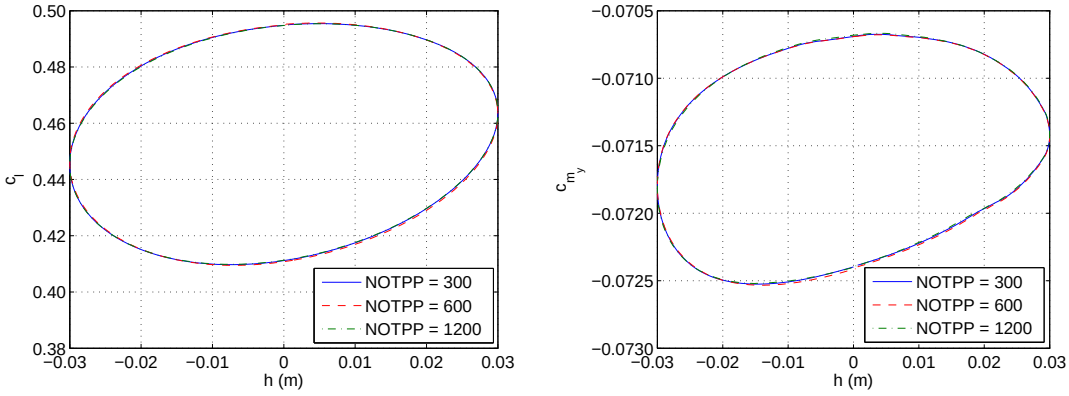

(a) Lift coefficient versus non-dimensional vertical displacement

(b) Moment coefficient versus non-dimensional vertical displacement

Figure E.4: Lift and moment coefficient versus non-dimensional vertical displacement at $M = 0.765$, $k = 0.05$ and NOII = 400 for three different NOTPP for plunging motion (fully turbulent)

From this figure it can be seen that the curves for 600 timesteps per period and 1200 timesteps per period are almost on top of each for both lift and moment coefficient. In order to see the effect of the change in timestep on global quantities, the magnitude and phase angle of the lift and moment coefficient of last oscillation period of these quantities are shown in table E.3.

	Magnitude (-)		Phase angle (°)	
NOTPP	c_l	c_{m_y}	c_l	c_{m_y}
300	$4.2912 \cdot 10^{-2}$ (+0.2%)	$9.0214 \cdot 10^{-4}$ (-0.3%)	77.79 (-0.2%)	-75.83 (-0.5%)
600	$4.28253 \cdot 10^{-2}$	$9.0506 \cdot 10^{-4}$	77.60	-76.22
1200	$4.3086 \cdot 10^{-2}$ (+0.6%)	$9.0309 \cdot 10^{-4}$ (-0.2%)	78.52 (+1.2%)	-75.35 (-1.1%)

Table E.3: Magnitude and phase angle of lift and plunging moment coefficient at $M = 0.765$, $k = 0.05$ and NOII $= 400$ for various NOTPP (fully turbulent)

Based on this table it can be said that the results of the plunging simulation are independent of the number of timesteps used if NOTPP $= 600$, since all differences are about 1% or less. The influence of the number of inner iterations is illustrated in figure E.5 and in table E.4. From which it can be seen that using 400 inner iterations is sufficient to obtain convergence during each timestep. Therefore, for further simulations 400 inner iterations were used for each Mach number and reduced frequency, whereas the timestep obtained with 600 timesteps per period for this testcase has been used for all plunging simulations (see tables 7.1 and 7.2 for the corresponding number of timesteps per period for each testcase).

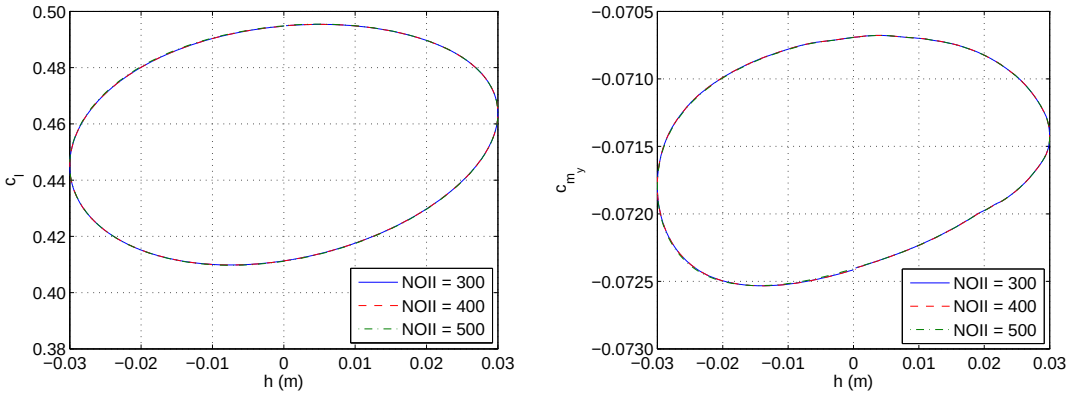

(a) Lift coefficient versus vertical displacement

(b) Moment coefficient versus vertical displacement

Figure E.5: Lift and moment coefficient versus non-dimensional vertical displacement at $M = 0.765$, $k = 0.05$ and NOTPP $= 600$ for three different NOII for plunging motion (fully turbulent)

	Magnitude (-)		Phase angle (°)	
NOII	c_l	c_{m_y}	c_l	c_{m_y}
300	$4.2823 \cdot 10^{-2}$ (-0.005%)	$9.0461 \cdot 10^{-4}$ (-0.05%)	77.60 (0%)	-76.20 (-0.03%)
400	$4.2825 \cdot 10^{-2}$	$9.0506 \cdot 10^{-4}$	77.60	-76.22
500	$4.2923 \cdot 10^{-2}$ (+0.2%)	$9.04509 \cdot 10^{-4}$ (-0.06%)	77.79 (+0.2%)	-75.94 (-0.4%)

Table E.4: Magnitude and phase angle of lift and plunging moment coefficient at $M = 0.765$, $k = 0.05$ and NOTPP $= 600$ for various NOII (fully turbulent)

The timestep independence of the unsteady complex lift and moment coefficients has been demonstrated for a critical flow case. For the pitching and plunging motion with low reduced frequency ($k = 0.05$) and with amplitudes of $0.25°$ and $0.005c/k$, respectively, 600 timesteps per period and 400 inner iterations are sufficient. Hence, the timestep size obtained from using 600 timesteps per period will definitely be enough for the unsteady "production" computations for determination of the flutter boundary as the amplitude chosen for these computations is five times as small as the one used in the current investigation. Furthermore, the number of timesteps per period can be decreased for higher reduced frequencies, which are less critical because of the , such that the physical timestep size is constant.

E.2 Free transition simulations

For the simulations with free boundary layer transition, the testcase used is $M = 0.74$ and $k = 0.30$. It is expected that this case is a critical testcase, since the Mach number is near the quasi-steady peak in lift-curve slope (see figure 6.13) and the reduced frequency is expected to be close to the flutter frequency. Furthermore, because of the very high computational costs involved for low reduced frequencies, this higher reduced frequency of 0.3 was selected.

E.2.1 Pitching motion

In figure E.6 the lift and moment coefficient are plotted versus the angle of attack for three different timesteps, i.e.: NOTPP = 52, 103 and 206. The number of inner iterations has been fixed at 3200. The amplitude used in for these simulations is $\alpha_m = 0.05°$.

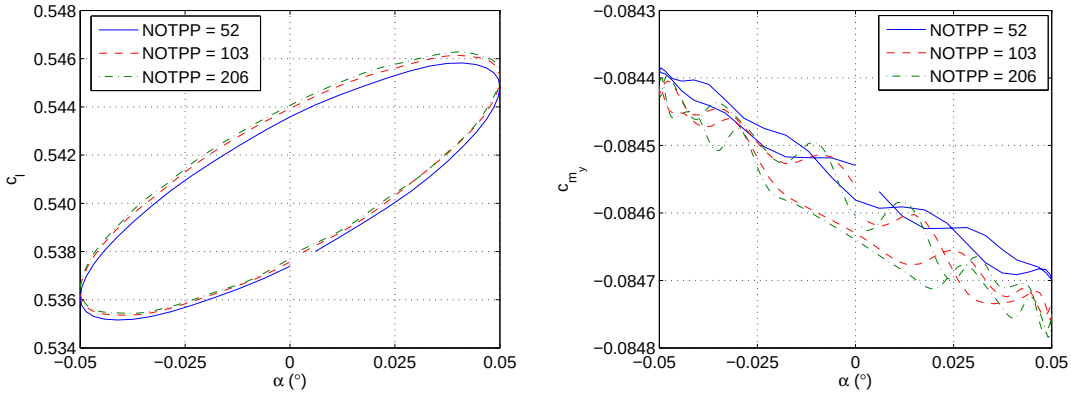

(a) Lift coefficient versus angle of attack

(b) Moment coefficient versus angle of attack

Figure E.6: Lift and moment coefficient versus angle of attack at $M = 0.74$, $k = 0.30$ and NOII = 3200 for three different NOTPP for pitching motion (free transition)

From these figures it can be seen that in case of free transition the curves for NOTPP = 206 and NOTPP = 103 are not on top of each other. For the lift coefficient they are however very close to each other. The curve for NOTPP = 52 is at least not equal to that of NOTPP = 103. For the moment coefficient larger differences appear, the general trends (the small oscillations) for NOTPP = 206 and NOTPP = 103 are however the same. The response of the moment coefficient is clearly non-linear and therefore higher harmonic components will be needed to reconstruct the time signal. The first harmonic can however be used as an approximation. The influence of the number of timesteps per period on the magnitude and phase angle of the lift and moment coefficient is shown in table E.5.

	Magnitude (-)		Phase angle (°)	
NOTPP	c_l	c_{m_y}	c_l	c_{m_y}
52	$5.3284 \cdot 10^{-3}$ (-1.4%)	$1.5411 \cdot 10^{-4}$ (-8.1%)	-34.96 (-1.3%)	-180.10 (-2.9%)
103	$5.4023 \cdot 10^{-3}$	$1.6778 \cdot 10^{-4}$	-35.42	-185.54
206	$5.4284 \cdot 10^{-3}$ (+0.5%)	$1.7462 \cdot 10^{-4}$ (+4.1%)	-35.73 (+0.9%)	-189.15 (+1.9%)

Table E.5: Magnitude and phase angle of lift and pitching moment coefficient at $M = 0.74$, $k = 0.30$ and NOII = 3200 for various NOTPP (free transition)

From this table it is seen that the differences in magnitude and phase angle are relatively small, especially those between NOTPP = 206 and NOTPP = 103, which are all less than 4%. Therefore, as a comprimise between accuracy and efficiency, the number of timesteps per period that has been selected for further computations is 103, which corresponds to 600 timesteps per period at $M = 0.765$ and $k = 0.05$.

The hysteresis loops of the lift and moment coefficient for several numbers of inner iterations are depicted in figure E.7. This figure shows that the hysteresis loops of the lift coefficient obtained at the different NOII (2500, 3200 and 3500) are very close to each

other, whereas for the moment coefficient the small oscillations are a bit different, but the general trends are the same.

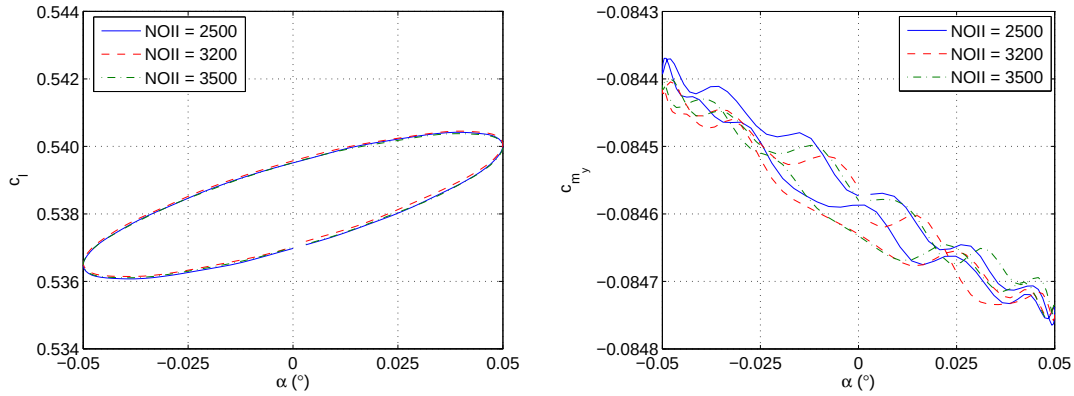

(a) Lift coefficient versus angle of attack

(b) Moment coefficient versus angle of attack

Figure E.7: Lift and moment coefficient versus angle of attack at $M = 0.74$, $k = 0.30$ and NOTPP $= 103$ for three different NOII for pitching motion (free transition)

Table E.6 shows the magnitude and phase angle of the lift and moment coefficient at the various NOII. From this table it can be concluded that when 3200 inner iterations are used, the results are independent of the number of inner iterations, since the differences in magnitude and phase are small (less than 2%, except for the magnitude of the moment coefficient when using 200 inner iterations). Therefore 3200 inner iterations have been used for the unsteady simulations with free boundary layer transition performed with the DLR TAU code. Less inner iterations, for example 400 as in case of the fully turbulent simulations, will not lead to convergence of the lift and moment coefficient at each timestep.

	Magnitude (-)		Phase angle (°)	
NOII	c_l	c_{m_y}	c_l	c_{m_y}
2500	$5.4356 \cdot 10^{-3}$ (+0.6%)	$1.8216 \cdot 10^{-4}$ (+8.6%)	-35.88 (+1.3%)	-186.99 (+0.8%)
3200	$5.4023 \cdot 10^{-3}$	$1.6778 \cdot 10^{-4}$	-35.42	-185.54
3500	$5.3615 \cdot 10^{-3}$ (-0.8%)	$1.6491 \cdot 10^{-4}$ (-1.7%)	-35.70 (+0.8%)	-186.95 (+0.8%)

Table E.6: Magnitude and phase angle of lift and pitching moment coefficient at $M = 0.74$, $k = 0.30$ and NOTPP $= 103$ for various NOII (free transition)

From this investigation it can be concluded that choosing 103 timesteps per period and 3200 inner iterations is a good comprise between accuracy and efficient for the present testcase. Since the testcase used is critical in terms of Mach and reduced frequency, the choices of NOTPP at other Mach numbers and reduced frequencies have been based on the results of this testcase (see table 7.2). It should further be noted that the number of inner iterations needed for simulations with free boundary layer transition is much larger than in case of a fully turbulent boundary layer and therefore the computational costs

are much large (more than 5 times larger).

E.2.2 Plunging motion

Figure E.8 shows the result of the temporal independency study obtained in case of free boundary layer transition for the plunging motion. Three different number of timesteps were again used: NOTPP = 52, 103 and 206, the number of inner iterations used is 3200 and the amplitude of the plunging motion is $h_m = 0.001c/k$.

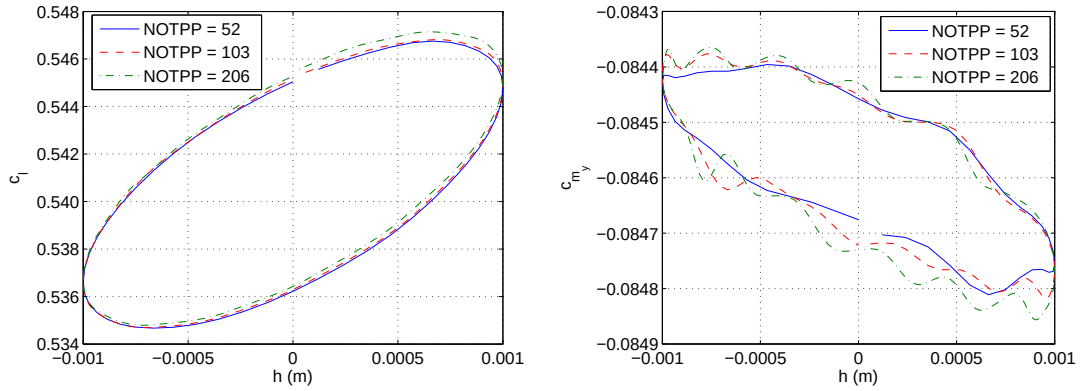

(a) Lift coefficient versus non-dimensional vertical displacement

(b) Moment coefficient versus non-dimensional vertical displacement

Figure E.8: Lift and moment coefficient versus non-dimensional vertical displacement at $M = 0.74$, $k = 0.30$ and NOII = 3200 for two different NOTPP for plunging motion (free transition)

These figures show that minimal differences are present between the hysteresis loops of the lift coefficient. However, the differences are larger for the response of the moment coefficient. By looking at the magnitude (scaled by the amplitude of the motion) and phase angle of the lift and moment coefficient the influence of the timestep can be seen as well, as can be seen from table E.7. The differences between NOTPP = 103 and NOTPP = 206 are larger than those between NOTPP = 52 and NOTPP = 103 (typically more than 1% versus less than 1%, except for the magnitude of the moment coefficient). They are however still sufficiently small, to speak of timestep-independent results.

	Magnitude (-)		Phase angle (°)	
NOTPP	c_l	c_{m_y}	c_l	c_{m_y}
52	$6.0266 \cdot 10^{-3}$ (-0.6%)	$1.9400 \cdot 10^{-4}$ (-7.5%)	47.53 (+0.9%)	-141.37 (0%)
103	$6.0621 \cdot 10^{-3}$	$2.0970 \cdot 10^{-4}$	47.12	-141.37
206	$6.1601 \cdot 10^{-3}$ (+1.6%)	$2.2527 \cdot 10^{-4}$ (+7.4%)	46.55 (-1.2%)	-139.69 (-1.2%)

Table E.7: Magnitude and phase angle of lift and plunging moment coefficient at $M = 0.74$, $k = 0.30$ and NOII = 3200 for various NOTPP (free transition)

The number of inner iterations has been varied as well. Figure E.9 shows the results of

this investigation. The number of timesteps per period used is 103.

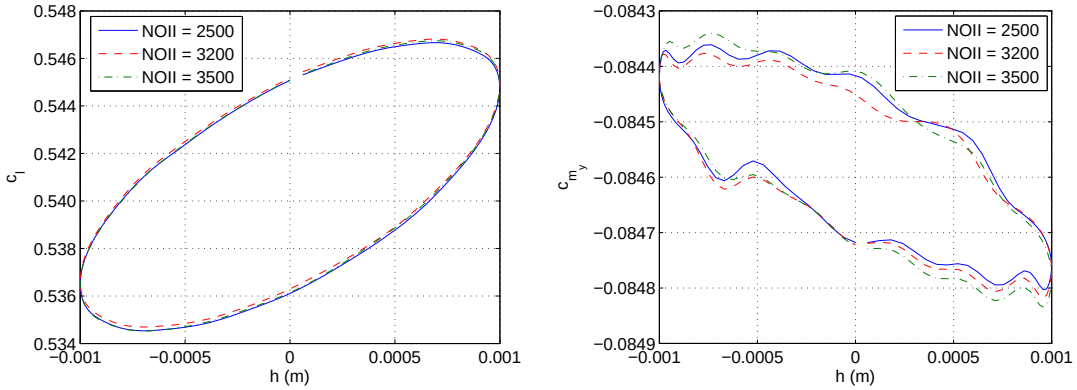

(a) Lift coefficient versus vertical displacement

(b) Moment coefficient versus vertical displacement

Figure E.9: Lift and moment coefficient versus non-dimensional vertical displacement at $M = 0.74$, $k = 0.30$ and NOTPP $= 103$ for three different NOII for plunging motion (free transition)

From these figures it is again observed that, as in case of the NOTPP variation, the response of the lift coefficient is independent of the number of inner iterations used and the response of the moment coefficient shows some variations with each of the number of inner iterations. The same can be seen from table E.8, which shows the magnitude (scaled by the amplitude of the motion) and phase angle of the lift and moment coefficient. Hence, 3200 inner iterations are used for the unsteady simulations with free boundary layer transition.

	Magnitude (-)		Phase angle (°)	
NOII	c_l	c_{m_y}	c_l	c_{m_y}
2500	$6.0735 \cdot 10^{-3}$ (+0.2%)	$2.1275 \cdot 10^{-4}$ (+1.5%)	47.45 (+0.7%)	-138.83 (-2.1%)
3200	$6.0621 \cdot 10^{-3}$	$2.0970 \cdot 10^{-4}$	47.12	-141.37
3500	$6.1086 \cdot 10^{-3}$ (+0.8%)	$2.3347 \cdot 10^{-4}$ (+11.3%)	46.87 (-0.5%)	-141.30 (-0.05%)

Table E.8: Magnitude and phase angle of lift and plunging moment coefficient at $M = 0.74$, $k = 0.30$ and NOTPP $= 103$ for various NOII (free transition)

This investigation has shown that taking 103 timesteps per period and 3200 inner iterations is also sufficient for both pitching and plunging motion at $M = 0.74$ and $k = 0.30$. In order to be consistent this timestep independency check needs to be repeated at a lower reduced frequency. However, efficiency is also an important issue in numerical computations, therefore, the results from the current case have been extended to the simulations needed for determination of the flutter boundary (at different Mach numbers and reduced frequencies, see table 7.2).

Appendix F

Steady Flow Simulations with the Original CAST-10 Airfoil

F.1 Fully turbulent simulations

F.1.1 Pressure and skin friction distributions

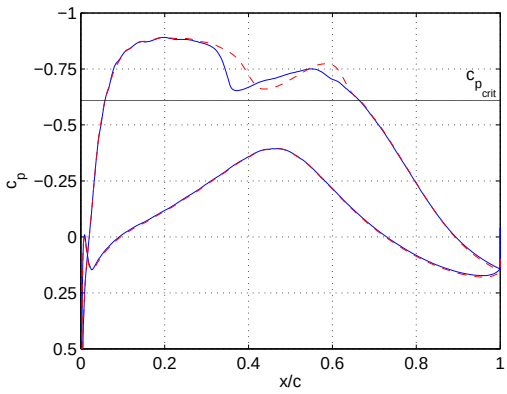

(a) Pressure distribution, $M = 0.745$

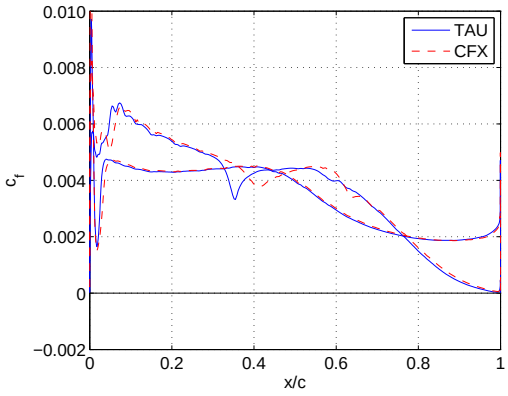

(b) Skin friction distribution, $M = 0.745$

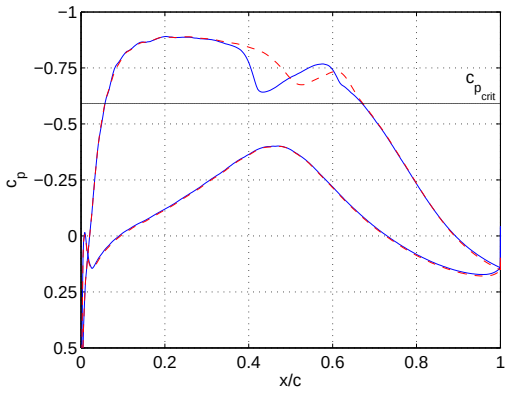

(c) Pressure distribution, $M = 0.75$

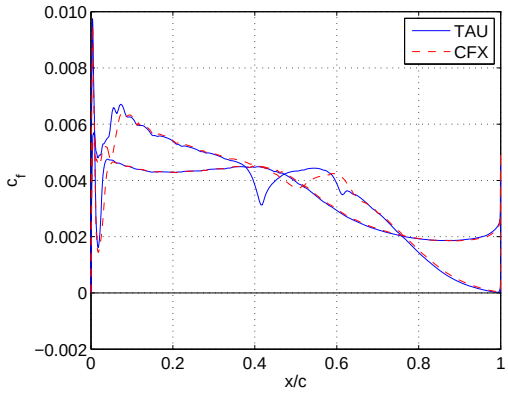

(d) Skin friction distribution, $M = 0.75$

Figure F.1

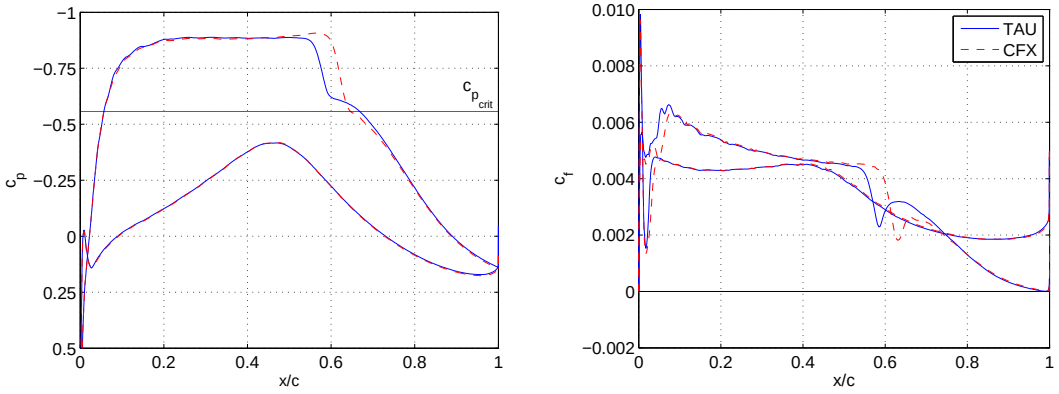

(e) Pressure distribution, $M = 0.76$ (f) Skin friction distribution, $M = 0.76$

Figure F.1: Pressure and skin friction distributions on the CAST-10 airfoil with a fully turbulent boundary layer at $M = 0.745$, $M = 0.75$ and $M = 0.76$

F.1.2 Force and moment coefficients

	TAU			CFX		
M	c_l	c_d	c_{m_y}	c_l	c_d	c_{m_y}
0.745	0.437437	0.012891	-0.066857	0.449799	0.012757	-0.069065
0.75	0.44215	0.013056	-0.067245	0.455651	0.0128951	-0.0696114
0.76	0.455462	0.013558	-0.069799	0.464924	0.0139019	-0.0730934

Table F.1: Force and moment coefficients for the CAST-10 airfoil at $M = 0.745$, $M = 0.75$ and $M = 0.76$ and $\alpha = 0°$ (fully turbulent)

F.2 Free transition simulations

F.2.1 Pressure and skin friction distributions

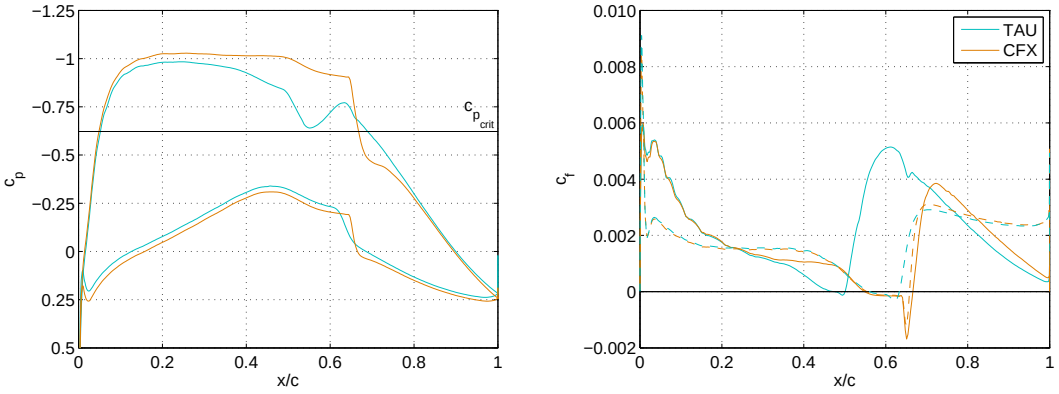

(a) Pressure distribution, $M = 0.74125$ (b) Skin friction distribution, $M = 0.74125$

Figure F.2

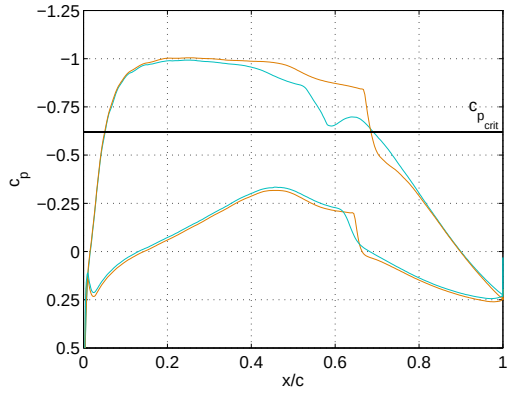

(c) Pressure distribution, $M = 0.741875$

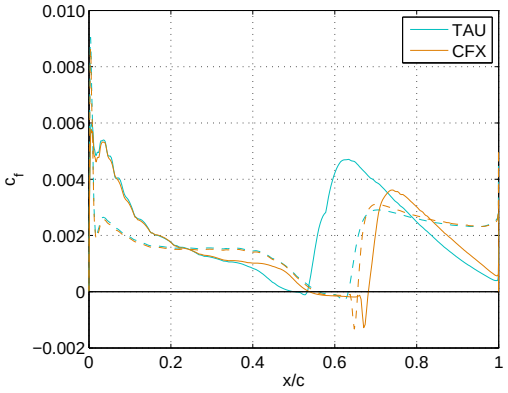

(d) Skin friction distribution, $M = 0.741875$

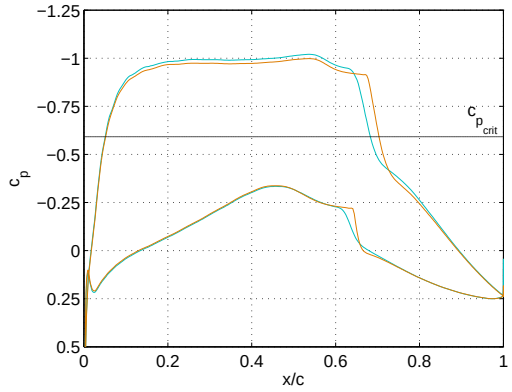

(e) Pressure distribution, $M = 0.75$

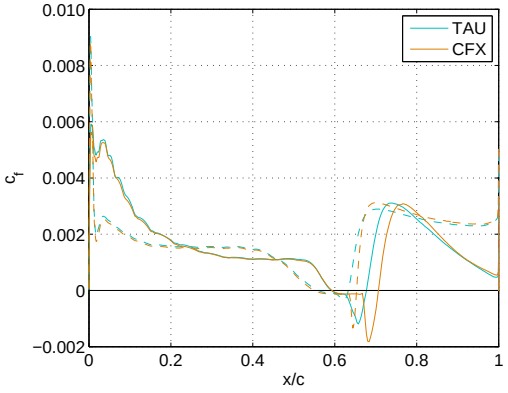

(f) Skin friction distribution, $M = 0.75$

Figure F.2: Pressure and skin friction distributions on the CAST-10 airfoil with free boundary layer transition at $M = 0.74125$, $M = 0.741875$ and $M = 0.75$

F.2.2 Force and moment coefficients

	TAU			CFX		
M	c_l	c_d	c_{m_y}	c_l	c_d	c_{m_y}
0.74125	0.56986	0.0077293	-0.0876656	0.6396	0.006022	-0.1087
0.741875	0.5756663	0.00747653	-0.090057	0.6213	0.00713	-0.1102
0.75	0.614374	0.008128	-0.100045	0.60594	0.008990	-0.10951

Table F.2: Force and moment coefficients for the CAST-10 airfoil at $M = 0.74125$, $M = 0.741875$ and $M = 0.75$ and $\alpha = 0°$ (free transition)

Appendix G

Unsteady Flow Simulations with the Original CAST-10 Airfoil

G.1 Fully turbulent simulation

G.1.1 Pitching motion

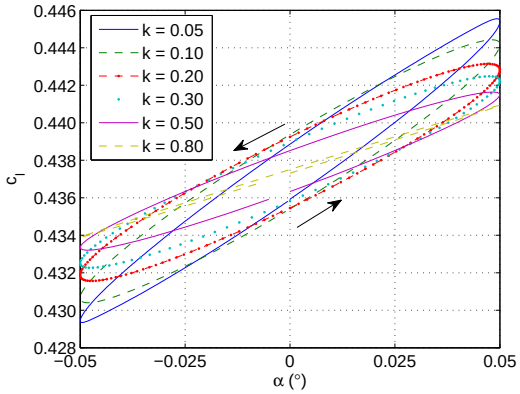

(a) Lift coefficient versus angle of attack $M = 0.745$

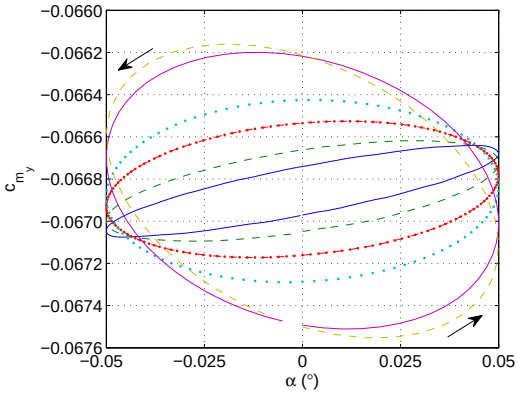

(b) Moment coefficient versus angle of attack $M = 0.745$

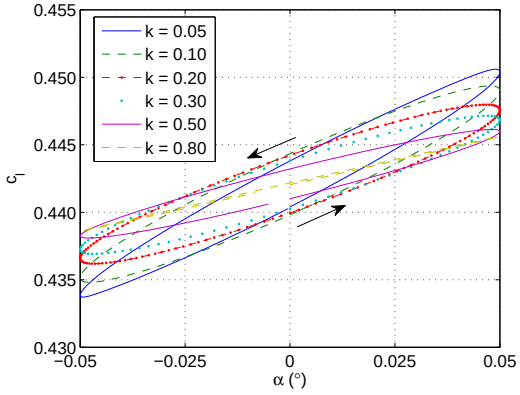

(c) Lift coefficient versus angle of attack $M = 0.75$

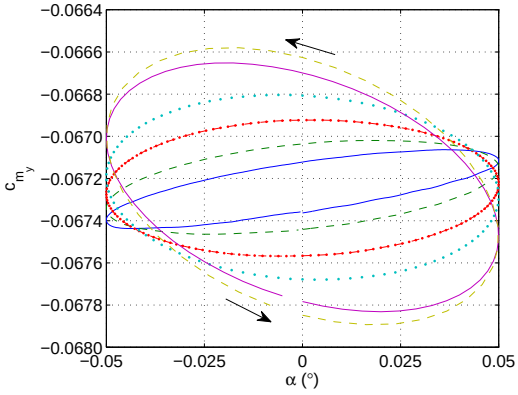

(d) Moment coefficient versus angle of attack $M = 0.75$

Figure G.1

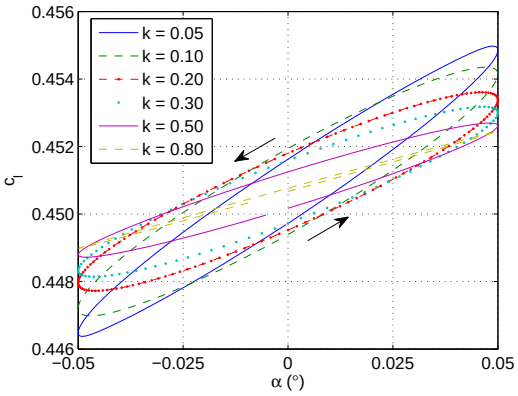

(e) Lift coefficient versus angle of attack $M = 0.76$

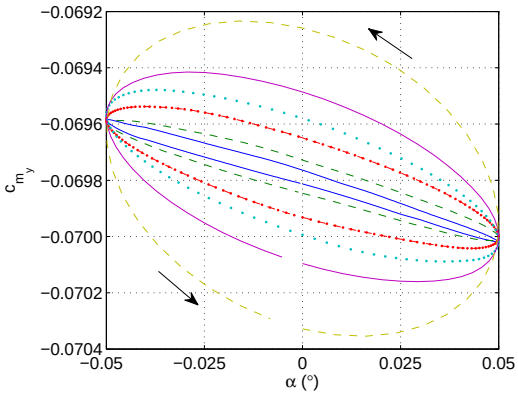

(f) Moment coefficient versus angle of attack $M = 0.76$

Figure G.1: Lift and moment coefficient versus angle of attack for the pitching motion at $M = 0.745$, 0.75 and 0.76 (fully turbulent)

G.1.2 Plunging motion

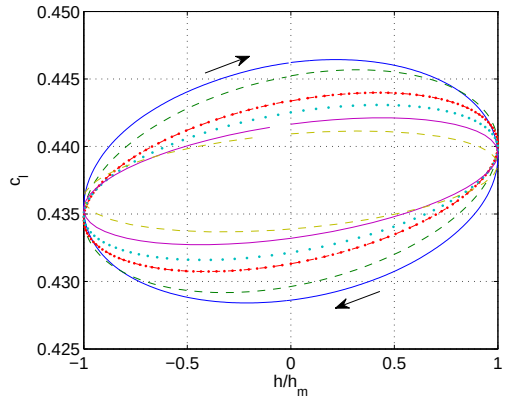

(a) Lift coefficient versus non-dimensional displacement $M = 0.745$

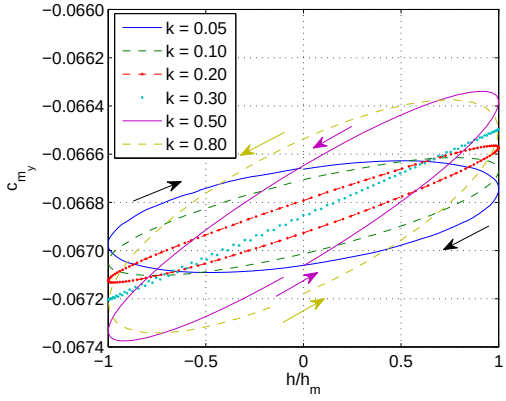

(b) Moment coefficient versus non-dimensional displacement $M = 0.745$

Figure G.2

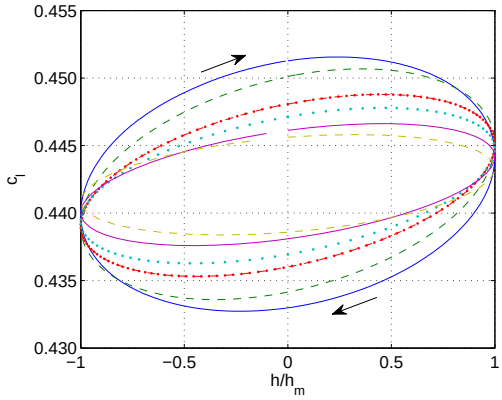

(c) Lift coefficient versus non-dimensional displacement $M = 0.75$

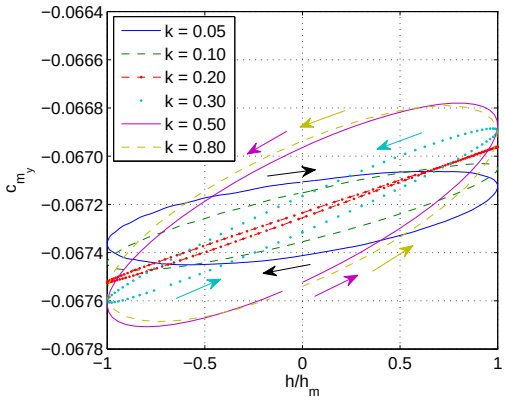

(d) Moment coefficient versus non-dimensional displacement $M = 0.75$

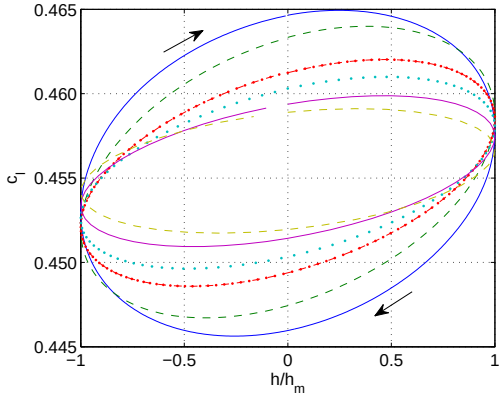

(e) Lift coefficient versus non-dimensional displacement $M = 0.76$

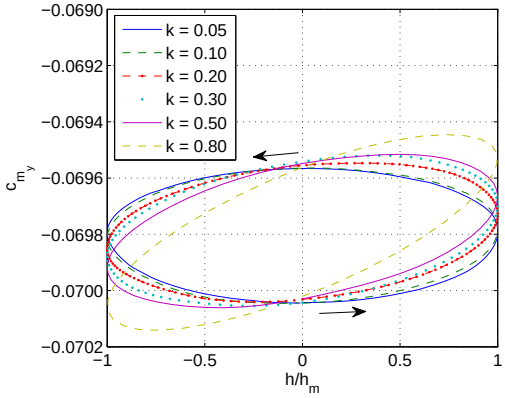

(f) Moment coefficient versus non-dimensional displacement $M = 0.76$

Figure G.2: Lift and moment coefficient versus non-dimensional vertical displacement for the plunging motion at $M = 0.745$, 0.75 and 0.76 (fully turbulent)

G.2 Free transition simulations

G.2.1 Pitching motion

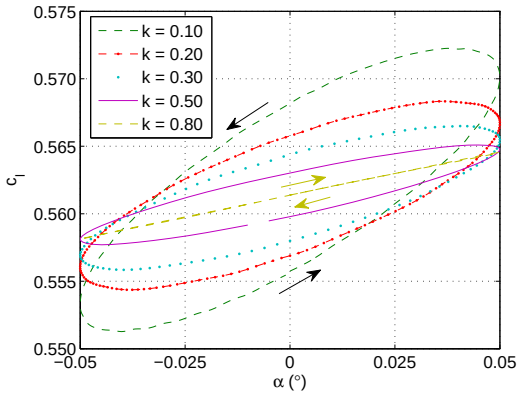

(a) Lift coefficient versus angle of attack $M = 0.74125$

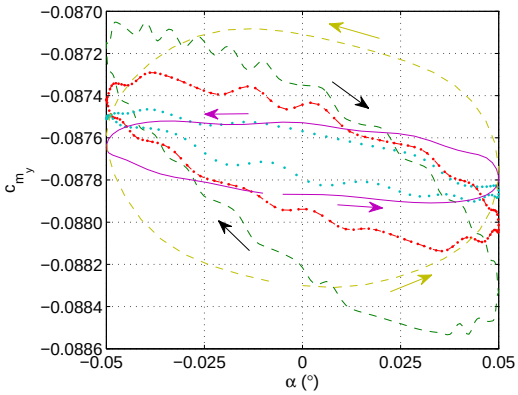

(b) Moment coefficient versus angle of attack $M = 0.74125$

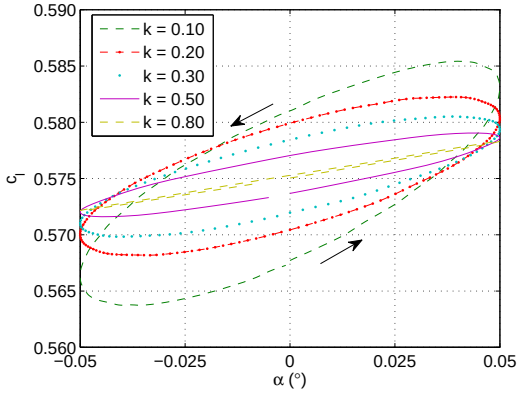

(c) Lift coefficient versus angle of attack $M = 0.741875$

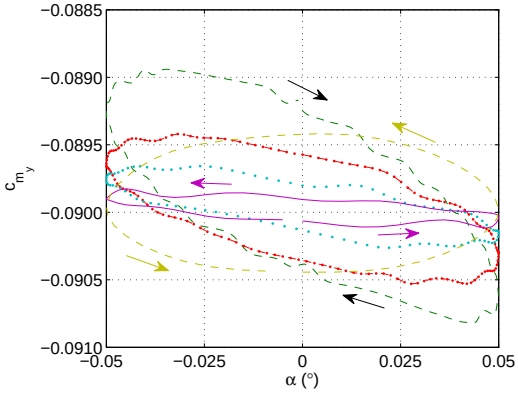

(d) Moment coefficient versus angle of attack $M = 0.741875$

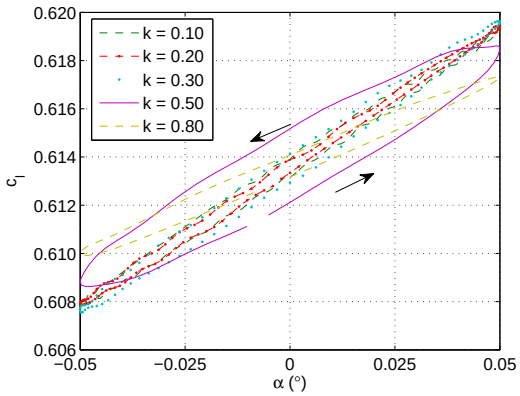

(e) Lift coefficient versus angle of attack $M = 0.75$

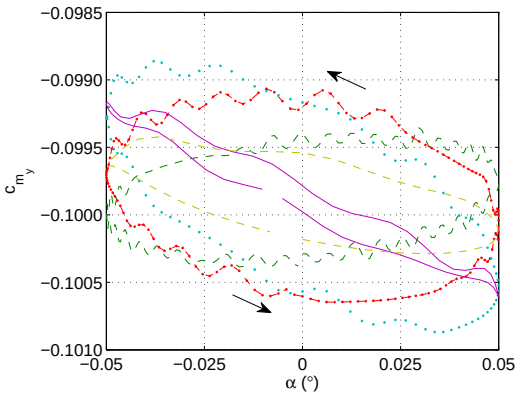

(f) Moment coefficient versus angle of attack $M = 0.75$

Figure G.3: Lift and moment coefficient versus angle of attack for the pitching motion at $M = 0.74125$, 0.741875 and 0.75 (free transition)

G.2.2 Plunging motion

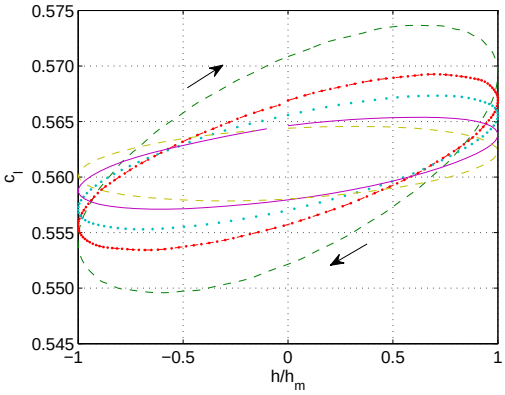

(a) Lift coefficient versus non-dimensional displacement $M = 0.74125$

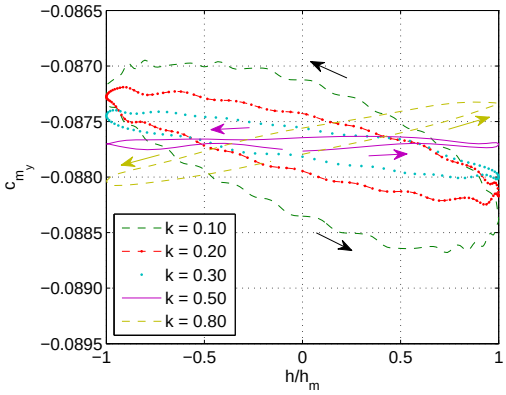

(b) Moment coefficient versus non-dimensional displacement $M = 0.74125$

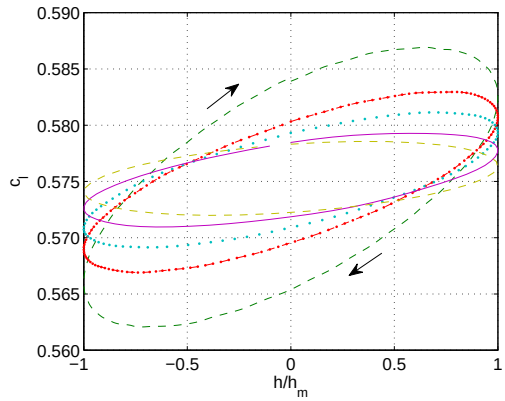

(c) Lift coefficient versus non-dimensional displacement $M = 0.741875$

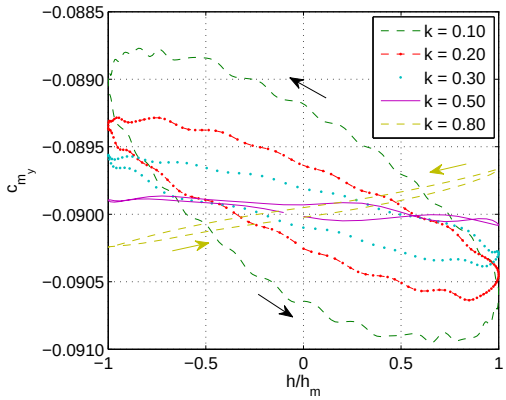

(d) Moment coefficient versus non-dimensional displacement $M = 0.741875$

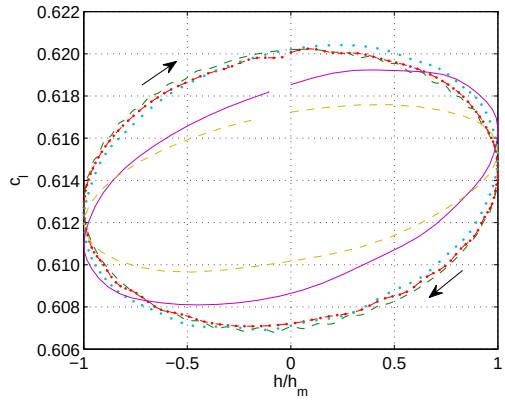

(e) Lift coefficient versus non-dimensional displacement $M = 0.75$

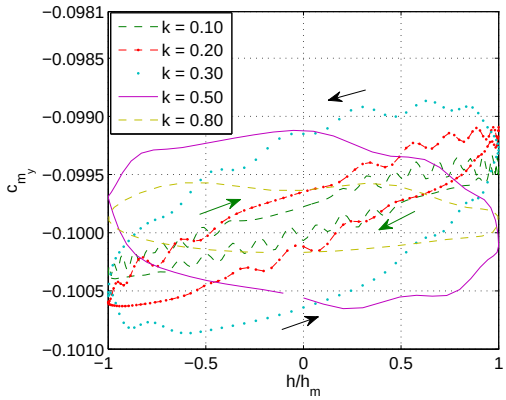

(f) Moment coefficient versus non-dimensional displacement $M = 0.75$

Figure G.4: Lift and moment coefficient versus non-dimensional vertical displacement for the plunging motion at $M = 0.74125$, 0.741875 and 0.75 (free transition)